Observations of Magnetic Fields and Clustering Functions in Prestellar Cores

by

David Nutter

A thesis submitted to the

University of Wales

for the degree of

Doctor of Philosophy

January 2004

ProQuest LLC
789 East Eisenhower Parkway
P.O. Box 1346
Ann Arbor, MI 48106-1346

ACKNOWLEDGMENTS

First and foremost, I would like to thank Hannah for her love, support and friendship over the last three years. I thank Dr. Derek Ward-Thompson for giving me the opportunity to take part in this exciting research, and for all his help and support over the course of the PhD.

I would also like to thank the members past and present, of the Star Formation research group here at Cardiff, especially Dr. Simon Goodwin, Dr. Jason Kirk, and Prof. Ant Whitworth.

Many thanks must also go out to the friends I have made here over the years, especially Iain Brown and Emma Pearce, and all the guys in the terminal room who have kept me sane. An extra note of thanks to Tim Waskett for his help over the years.

I would like to acknowledge and thank the collaborators I have worked with during my PhD, including Prof. Dick Crutcher, Dr. Philippe André, Dr. Jonathan Rawlings and Dr. Matt Redman. A special note of thanks to Dr. Jane Greaves for putting up with many emails on Friday afternoons asking 'Exactly how does polarimetry work again?'

A big thank-you to the computing support staff here at Cardiff, especially Dr. Rodney Smith, and also the support staff of the JCMT, for support during and after many observing runs.

Finally, a thank-you to my parents, for their love and support both before and during the PhD, without which, I would never have made it here in the first place.

Figures 4.2 and 4.10 include photographic data obtained using The UK Schmidt Telescope. The UK Schmidt Telescope was operated by the Royal Observatory Edinburgh, with funding from the UK Science and Engineering Research Council, until 1988 June, and thereafter by the Anglo-Australian Observatory. Original plate material is copyright © the Royal Observatory Edinburgh and the Anglo-Australian Observatory. The plates were processed into the present compressed digital form with their permission. The Digitized Sky Survey was produced at the Space Telescope Science Institute under US Government grant NAG W-2166.

IRAS 100 μm data in Figures 3.3, 4.1, 4.2 and 4.10 courtesy of NASA IPAC/Jet Propulsion Laboratory.

This publication makes use of data products from the Two Micron All Sky Survey, which is a joint project of the University of Massachusetts and the Infrared Processing and Analysis Center/California Institute of Technology, funded by the National Aeronautics and Space Administration and the National Science Foundation.

ABSTRACT

In this thesis, I present SCUBA polarimetry data of three prestellar cores, L1544, L43 and L183. I also present SCUBA scan-map observations of three molecular clouds, Orion B, L1689, and RCrA.

I use the Chandrasekhar-Fermi technique to measure the magnetic field strength in L1544, L43 and L183, and find that each core is approximately magnetically critical or slightly supercritical.

I measure the core mass function for prestellar cores in the Orion B molecular cloud and find that above 1 $M_{\odot}$, the data are best fitted by a power-law of the form $dN/d\log M \propto M^{-1.5}$. The mass function has a peak at approximately 1 $M_{\odot}$. This core mass function is comparable with the Salpeter slope of $M^{-1.35}$.

I also determine the mean surface density of companions $\Sigma_c(\theta)$ for the Orion B region, and find that it is best fitted by a power law of the form $\Sigma_c(\theta) \propto \theta^{-0.3}$. This is smaller than the slope of $\theta^{-0.6}$ that is typically found for young stars in most molecular clouds. However, this slope is consistent with my data at the extreme limits of my 1σ error bars. My value of $\Sigma_c(\theta) \propto \theta^{-0.3}$ is comparable with the slope of $\theta^{-0.2}$ that is found for the nearby Orion Trapezium association.

I find that the L1689 molecular cloud has a comparable rate of star formation to the neighbouring and more massive L1688. In addition, the star formation in L1689 occurs in a number of filaments that are parallel both to each other, and to similar filaments in L1688. I conclude that these observations indicate that the star formation is being influenced by the nearby Sco OB2 association.

I compare the RCrA data to previous surveys of the region, and discover a previously unknown Class 0 source.

Contents

List of Figures

List of Tables

Chapter 1

An Introduction to Star Formation

1.1 Introduction

Star formation is one of the most important processes in the Universe. Without it, the Universe would be a very dull and lonely place. The stars have generated almost all of the elements in the Universe that are more massive than helium, and so have made our very existence possible.

The mechanism of star formation generates the mass distribution of stars, and also determines the rate at which stars form in the Galaxy. These have a dramatic effect on the evolution of the region in which the star formed, and on the Galaxy as a whole. Low mass stars evolve very slowly, and lock up matter. Massive stars are extremely luminous, and input a large amount of energy into the Galaxy in the form of energetic winds, ionising radiation and supernovae shocks. This energy

has a dramatic effect on the interstellar medium, by sweeping up large volumes of gas and dust, which can become dense enough to form more stars.

The fate of stellar clusters in which massive stars are always formed depends crucially on the degree and rapidity of the removal of gas by the massive stars. On a larger scale, the evolution of the Galaxy can be affected by the ejection of gas by supernovae into the intergalactic medium.

Finally, the heavy elements from which we and our planet are made, are formed within stars, and the formation of planets from these heavy elements depends on the detailed conditions of the star formation process.

It is therefore important to understand how stars are formed and why they have the properties that have made our existence possible. We must also have a good understanding about how stars are formed, in order to interpret the observations of many branches of astronomy, from cosmology and galaxy evolution, to planet formation.

In this chapter, I discuss our current understanding of low mass star formation. I will not discuss the specifics of high mass star formation, which occurs in a qualitatively different manner, and is more difficult to observe due to the large distance to high mass star-forming regions.

In Section 1.2, I summarise the properties of the youngest stellar objects, protostars, and how they evolve towards the main sequence. In Section 1.3 I discuss relevant parameters such as the density profile, temperature and lifetime of prestellar cores, which are the progenitors of protostars. Different theories of the evolution of prestellar cores are discussed in Section 1.4. Techniques for measuring the interstellar magnetic field are given in Section 1.5. Methods of measuring the

masses of molecular clouds and cores are discussed in Section 1.6. Finally the stellar initial mass function is introduced in Section 1.7.

1.2 Protostellar Evolution

1.2.1 The Birthplace of Stars

It is now well accepted that stars are formed in the dense regions of the interstellar medium (ISM), which are known as giant molecular clouds (GMCs). This was made apparent by the association of the youngest optically visible stars, T-Tauri stars, with molecular clouds (Herbig, 1977; Jones & Herbig, 1979).

T-Tauri stars were first discovered by Joy (1945) and the class was named after the prototype star in Taurus. They are notable for their irregular variability, strong Hα emission and lithium absorption, ultraviolet and infrared continuum excesses, and association with nebulosity. Subsequent work has shown that associations of T-Tauri stars are often seen with short lived O-associations (Ambartsumian, 1947), and are therefore themselves young. In addition, studies have shown that the radial velocity (Herbig, 1977) and proper motions (Jones & Herbig, 1979) of T-Tauri stars in Taurus are consistent with the bulk motion of the cloud itself. This confirms that T-Tauri stars are very young, and are born in molecular clouds.

After subsequent observations at a variety of wavelengths, the classification has been separated into classical T-Tauri stars (CTTS) that have similar properties to the prototype star, and weak-line T-Tauri stars (WTTS), which exhibit less Hα emission, and often have an X-ray counterpart.

GMCs are concentrated in the Galactic spiral arms, and are probably formed by the compression of gas as it enters the denser region of a spiral arm (e.g. Williams, Blitz, & McKee, 2000). The masses of GMCs are typically $\sim 10^5 - 10^6$ $M_\odot$, with diameters of ~ 50 pc. The high densities ($N_{H_2} \simeq 10^2$ cm^{-3}) lead to the formation of molecules on the surfaces of dust grains and they are subsequently evaporated into the gas phase. The high column density shields the cloud interior, and prevents the gaseous molecules from being photo-dissociated by the interstellar UV radiation. At these high densities, cooling by collisionally excited molecules and dust, together with the shielding, cause the cloud interior to be very cold (Goldsmith & Langer, 1978), with typical temperatures (away from internal heating sources) of $\sim 10 - 20$ K. This low temperature reduces the thermal support of the cloud, and fragments become gravitationally unstable and collapse to form stars. The conditions required for gravitational instability are discussed further in Section 1.6.2.

1.2.2 The Youngest Stars

The initial product of the gravitational collapse of a cloud fragment is a protostar. A protostar exists from the moment of the creation of a central hydrostatic object at the cloud centre. Part of the remainder of the cloud fragment (hereafter called the circumstellar envelope) accretes onto a circumstellar disk, and from there on to the surface of the protostar. As this occurs, the protostar increases in mass at the expense of the circumstellar envelope.

There are a number of observational signatures that reveal the presence of a protostar within its parent cloud, such as molecular outflows, centimetre wavelength continuum emission, or evidence of an internal heating source (e.g. André,

Ward-Thompson, & Barsony, 2000). Molecular outflows are usually seen by the emission of CO that has been swept up by the wind from the protostar, and are generally bipolar in nature (e.g. Snell, Loren, & Plambeck, 1980; Bachiller, 1996). They are often coincident with Herbig-Haro (HH) objects, which are the optical counterpart of the outflow and are seen by emission of shocked H_2 (Herbig & Jones, 1981). Centimetre emission can arise from free-free emission at the accretion shock on the protostar surface, or from the shocks associated with HH objects. In both cases, the emission arises from gas ionised by short wavelength radiation from material heated by the shock (Bertout, 1983; Bontemps, André, & Ward-Thompson, 1995; Gibb, 1999). An infrared source is only seen when the protostar is relatively evolved and has become less embedded.

Protostars have been divided into 4 distinct classes (Lada, 1987; André, Ward-Thompson, & Barsony, 1993) that make up an evolutionary sequence between the time of formation of a central hydrostatic object, to the young star's transition to the main sequence. These classes are known as Class 0, I, II and III respectively.

1.2.3 Class 0 Protostars

Class 0 protostars are the youngest protostellar objects, and have accreted less than 50% of their final mass. They were discovered observationally by André et al. (1993) following a submillimetre survey of the ρ Oph A star-forming clump. They had previously not been detected as they are not visible in the infrared.

The protostar is surrounded by a massive circumstellar envelope, which is centrally peaked and has a density profile of $\rho(r) \propto r^{-p}$, where $p \sim 1.5 - 2$ (Ladd et al., 1991; Motte et al., 1998; Motte & André, 2001). This profile holds until the

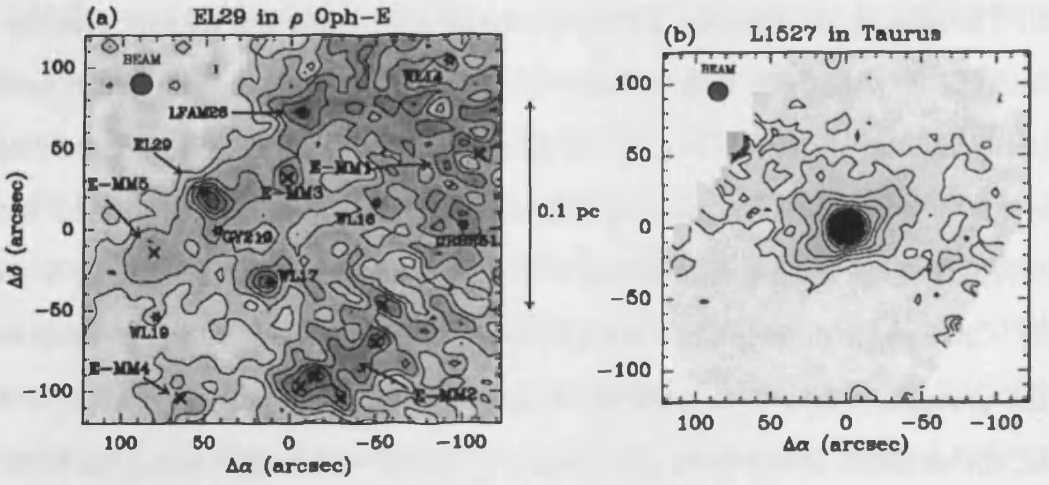

Figure 1.1: (a) & (b). A comparison between (a) the clustered region around the Class I source EL-29 in ρ Ophiuchi, and (b) the more isolated L1527 Class 0 source in Taurus. Nearby YSOs and density enhancements are marked with stars and crosses respectively in (a). Both regions were mapped at 1.3 mm using the IRAM 30 m telescope. Both figures are plotted to the same linear scale, as shown by the 0.1 pc bar (Motte et al., 1998).

envelope merges with the ambient cloud medium. The radius of cut-off depends crucially on the environment of the protostar. In isolated star-forming regions such as the Taurus-Auriga molecular cloud, the large separations between protostars mean that each object has a large volume from which to accrete material. As a result, the envelope does not merge with the cloud until a radius of 10000 – 15000 AU (Motte & André, 2001). In more clustered regions like ρ Ophiuchi, the envelope merges with the ambient cloud and other protostellar envelopes at a much smaller radius of $\leq$ 5000 AU (Motte et al., 1998). This is illustrated very well in Figure 1.1 (Motte et al., 1998), which compares the region around the Class I source EL-29 in ρ Ophiuchi with the L1527 Class 0 source in Taurus (Figures 1.1(a) and 1.1(b) respectively).

Class 0 protostars can be distinguished observationally from more evolved protostars by their large submillimetre luminosity (L_{smm}) compared to their bolo-

metric luminosity (L_{bol}) (André et al., 1993). The submillimetre luminosity is measured longward of 350 μm, and is proportional to the mass of the circumstellar envelope. The bolometric luminosity is derived mostly from accretion of material onto the central protostar:

$$L_{bol} = \frac{GM_{\star}\dot{M}_{acc}}{R_{\star}}, \tag{1.1}$$

where $M_{\star}$ is the mass of the central object, $\dot{M}_{acc}$ is the accretion rate, $R_{\star}$ is the protostellar radius and G is the gravitational constant. André et al. (1993) used Equation 1.1 to estimate $M_{\star}$ based on the measured value of L_{bol}. The ratio L_{smm}/L_{bol} can therefore be used to infer $M_{env}/M_{\star}$. Assuming a constant accretion rate of a_{eff}^3/G where a_{eff} is the effective sound speed (e.g. Stahler, Shu, & Taam, 1980), and an approximately constant protostellar radius of $R_{\star} \simeq 3$ $R_{\odot}$ (Stahler et al., 1980), André et al. calculated that a protostar with $M_{env} \simeq M_{\star}$ will have $L_{smm}/L_{bol} \geq 0.005$. Recent work has indicated that the accretion rate is not constant with time. This is discussed later in this section.

The youth of Class 0 protostars is further indicated by the detection of infall signatures in molecular lines shapes, towards many Class 0 objects (e.g. Walker et al., 1986; Gregersen et al., 1997). A sufficiently optically thick emission line will exhibit self-absorption at the mean velocity of the cloud. This double peaked profile is often seen to have a brighter blue component, which can indicate that infall is occurring in the cloud. An explanation for this is illustrated in Figure 1.2 (Zhou et al., 1993), which shows a protostar surrounded by a gas cloud. The cloud material is hotter at the centre due to the heating effect of the protostar. The emission from the near-side of the cloud is redshifted relative to the mean cloud velocity. From this half of the cloud, we preferentially detect radiation emitted from the cold part of the cloud furthest from the protostar. The reverse is true in the other half of the cloud, and we preferentially see emission from the hotter

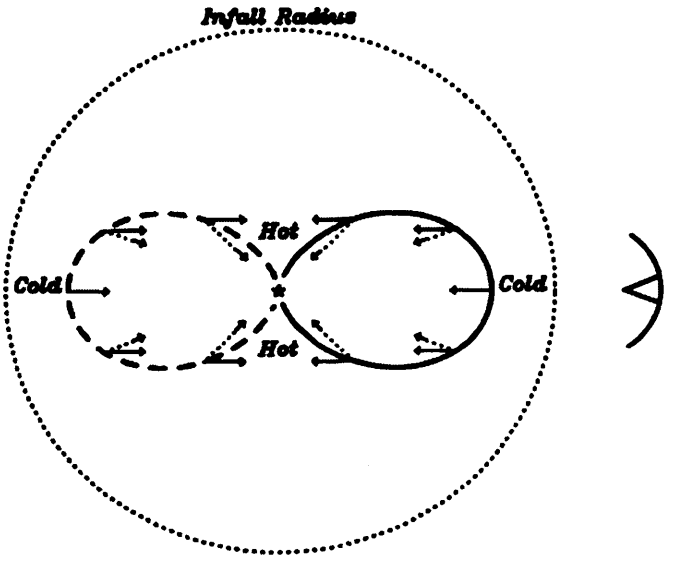

Figure 1.2: An explanation for the asymmetric line profile from an infalling cloud (Zhou et al., 1993). See text for discussion.

part of the cloud. The blue component of the double peaked profile is therefore brighter than the red component (Zhou, 1992; Ward-Thompson et al., 1996). An optically thin observation is also needed to confirm that the double peaked profile is not simply due to two clouds along the same line of sight.

1.2.4 Protostellar Evolution

Following an infrared survey of the ρ Ophiuchi molecular cloud (Lada & Wilking, 1984), Lada (1987) classified the embedded stars into three Classes (I, II and III) based on the slope ($\alpha_{\rm IR}$) of their spectral energy distributions (SEDs) between 2 and $10 - 25\mu$m:

$$\alpha_{\rm IR} = \frac{{\rm d}\log(\lambda F_\lambda)}{{\rm d}\log(\lambda)}. \tag{1.2}$$

The authors interpreted these classes as an evolutionary sequence.

Class I sources have an SED that is broader than a blackbody (see Figure 1.3(a)) and rises between 2 and 25 μm ($\alpha_{\rm IR} > 0$). They are interpreted as relatively evolved protostars surrounded by a diffuse low mass envelope with $M_\star > M_{env}$. Their SED consists of a contribution from the central protostar (shown as a dashed line on Figure 1.3(a)), and a significant contribution from the envelope at longer wavelengths. Using the same technique as described in Section 1.2.3, Gregersen et al. (2000) observed indications of an infalling envelope in a number of Class I sources.

Class II sources have an SED that is either flat or has a small negative slope between 2 and 25 μm ($-1.5 < \alpha_{\rm IR} < 0$). They are visible in the optical and correspond to classical T-Tauri stars. Their SED resembles a blackbody with significant infrared excess — see Figure 1.3(b). This excess is due to an optically thick disk around the young star. The circumstellar envelope has either accreted onto the disk, or has been dispersed by winds and outflows from the star.

The SEDs of Class III sources resemble a reddened blackbody (see Figure 1.3(c)), and decline steeply between 2 and 25 μm ($\alpha_{\rm IR} < -1.5$). The identified Class III objects correspond to weak-line T-Tauri stars. They are interpreted as having a disk that is lower in mass than that of a Class II, and is optically thin due to dust coagulation into planetesimals, or clearing by already formed planets.

The complete evolutionary sequence can be categorised by the property T_{bol}, which is the temperature of a blackbody with the same mean frequency as the observed SED (Chen et al., 1995, 1997). Using this notation, Class 0 protostars have $T_{bol} < 70$ K, Class I protostars have $70 < T_{bol} < 650$, Class II sources have $650 < T_{bol} < 2880$, and Class III objects have $T_{bol} > 2880$.

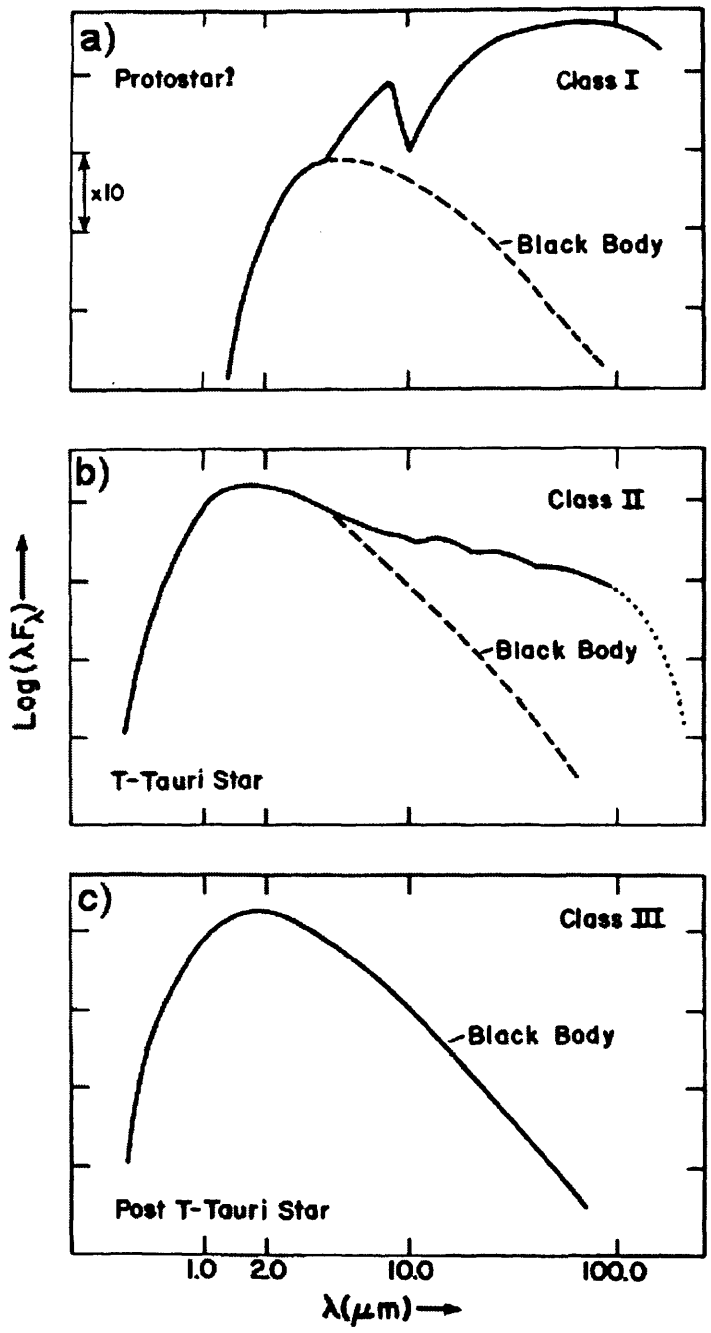

Figure 1.3: Diagrams of the SEDs of Class I, II and II YSOs. The SED of Class I sources is dominated by a cool circumstellar envelope. Class II sources have a blackbody with a considerable infrared excess due to a circumstellar disk. The SED of Class III sources is that of a reddened blackbody (Lada, 1987).

1.2.5 Decreasing Accretion Rate with Time

It is well recognised that young stellar objects (YSOs) are the driving source of outflows (e.g. see the review by Bachiller, 1996). In a study of the outflow activity of a number of Class 0 and Class I sources, Bontemps et al. (1996) showed that the outflow momentum flux F_{CO} of Class 0 sources is typically an order of magnitude above the linear relation between F_{CO} and L_{bol} that holds for Class I sources. In addition, Bontemps et al. found that F_{CO} was well correlated with the envelope mass M_{env} for the complete sample of Class 0 and Class I sources. Interpreting the change in M_{env} as evolutionary, this implies that outflow power decreases with time. Most explanations for the generation of the outflow from a YSO involve the accretion of material from the circumstellar envelope as the energy source for the outflow. Therefore the reduced outflow power could be caused by a reduction in the accretion rate with time. This conclusion has important consequences for the initial conditions of protostellar collapse, which are discussed in Section 1.3.

1.2.6 Protostellar Lifetime

The lifetime of the different protostellar stages is usually determined by counting the relative numbers of each class of object in a region (e.g. André et al., 2000). Wilking, Lada, & Young (1989) estimated the lifetime of Class II objects, by calculating the Kelvin-Helmholtz contraction time for each star since the end of the accretion phase. The average calculated age was $\sim 4 \times 10^5$ yr. Greene et al. (1994) determined that in the ρ Ophiuchi cloud, there are between 1/4 and 3/4 as many Class I sources as Class IIs, and therefore estimated the lifetime of Class I sources to be $\sim 2 \times 10^5$ yr. The low number of Class 0 sources in ρ Ophiuchi (Motte et al., 1998) (2 compared to 15–30 Class I sources) indicates that the lifetime of

Class 0 protostars is approximately 1/10 that of Class I protostars, or $\sim 2 \times 10^4$ years. These lifetimes are based on small number statistics and are only order of magnitude estimations.

The shorter lifetime of Class 0 sources, is consistent with the result of Bontemps et al. (1996) that the Class 0 accretion rate is higher than that of a Class I protostar. Bontemps et al. attempted to quantify the accretion rate based on the measured outflow momentum flux. They calculated the outflow mass loss rate $\dot{M}_W$ from $F_{\rm CO}$, and hence calculated the accretion rate $\dot{M}_{acc}$ for the Class 0 and Class I sources in their sample. They assumed the relation $\dot{M}_W = 0.1\dot{M}_{acc}$, in agreement with a number of theoretical predictions (e.g. Shu et al., 1994; Pelletier & Pudritz, 1992).

These calculations yielded accretion rates of $\sim 10^{-5}$ $M_\odot yr^{-1}$ for Class 0 sources, and $\sim 10^{-6}$ $M_\odot yr^{-1}$ for Class I sources. Therefore a 1 $M_\odot$ star would be in the Class 0 phase for $\sim 5 \times 10^4$ years, and in the Class I phase for $\sim 5 \times 10^5$ years (see also Whitworth & Ward-Thompson 2001).

1.3 Prestellar cores

In order to understand the process of star formation, it is important to know from what protostars are formed, and how that pre-protostellar (or prestellar for brevity) object evolves into a protostar. In this section, I will review the properties of prestellar cores, the fragments of cloud that have been identified to be the precursors of protostars. These are extremely important objects and studying their properties indicates the relative importance of the different aspects of the physics controlling star formation. A prestellar core is defined as a gravitationally

bound core that has not yet formed a protostellar object at the centre.

1.3.1 History

The identification of a prestellar core came after more than a decade of research. Myers, Linke, & Benson (1983) selected $\sim$ 90 regions of high optical extinction in the Palomar Observatory Sky Survey (POSS) plates. In each region, they observed the extinction maxima in ^{13}CO and $C^{18}O$ with a resolution of 1.9′. These observations revealed dense cores with average masses and sizes of 10 – 250 $M_\odot$ and 0.4 – 4 pc respectively.

A follow-up survey of the same positions using ammonia lines found denser condensations within the CO cores (Myers & Benson, 1983). The ammonia cores have average masses and sizes of 0.5 – 10 $M_\odot$ and 0.05 – 0.3 pc respectively. The positions of the ammonia cores in the Taurus molecular cloud were correlated with the positions of T-Tauri stars. In addition, the number of dense cores was seen to be consistent with the expected number of new T-Tauri stars that would form over the next 2×10^5 years, the typical core freefall time. This analysis was based on the T-Tauri lifetime estimates discussed in Section 1.2.6. These results led Myers & Benson to conclude that most (if not all) of the dense cores would form T-Tauri stars in the next 10^6 years.

Beichman et al. (1986) compared the positions of the dense cores detected in CO and NH_3 with the Infrared Astronomical Satellite (IRAS) point source catalogue (Beichman et al., 1985). They found that approximately 50% of the cores were associated with an IRAS detection. Of the cores with an IRAS point source, roughly one third were found to be visible at optical wavelengths and

correspond to T-Tauri stars. Beichman et al. (1986) suggested that the cores with an IRAS detection but no optical counterpart could either be deeply embedded YSOs, or accreting protostars. The cores with no IRAS detections were termed 'starless', and were identified as the possible sites of future star formation.

Ward-Thompson et al. (1994) surveyed 21 of the closer starless cores in ^{13}CO at higher resolution using the JCMT. Peaks of column density were detected for 17 cores. Continuum photometric observations of these peaks were made at 450μm, 800 μm and 1.1 mm using the UKT-14 bolometer receiver on the JCMT, and at 1.3 mm using the IRAM telescope. Five of the strongest detections were also mapped at 800 μm. Each of the cores has a mass that is comparable to or larger than its virial mass, indicating that they are gravitationally bound. However there is no evidence for a central protostar. The luminosity of the sources is too low to be powered by accretion onto a central object, but is consistent with thermal emission due to heating by the interstellar radiation field (Ward-Thompson et al., 2002). In addition, the cores are less centrally condensed than cores with IRAS sources, indicating that they are at an earlier evolutionary stage. This evidence led to Ward-Thompson et al. calling the cores pre-protostellar, a name that was subsequently shortened to prestellar.

1.3.2 Density Profile

The density profile can be calculated from the flux density profile according to the following (Adams, 1991). If the temperature, density and flux density profiles are $T(r) \propto r^{-q}$, $\rho(r) \propto r^{-p}$, and $S(\theta) \propto \theta^{-m}$, then the exponents are related by the expression $m = p + q - 1$. Ward-Thompson et al. (1994) found that the density profiles of the 5 mapped prestellar cores were more centrally condensed than

constant density spheres, but less condensed than $\rho(r) \propto r^{-2}$ everywhere, which was a prediction of the Shu (1977) model of protostellar collapse (see Section 1.4). Instead, the observations indicated that the density profiles of prestellar cores are flatter ($\rho(r) \propto r^{-1.25}$) at the centre, and steepen to $\rho(r) \propto r^{-2}$ beyond a radius of $\sim$ 4000 AU. These profiles are calculated using the assumption that the cores are isothermal (i.e. $q = 0$). This is discussed in the following section.

Subsequent maps of prestellar cores made with improved resolution and sensitivity (André, Ward-Thompson, & Motte, 1996; Ward-Thompson, Motte, & André, 1999) confirmed the conclusions of Ward-Thompson et al. (1994) that the density profile is significantly flatter than $\rho(r) \propto r^{-2}$ at the centre. Depending on the de-projection hypothesis, the results indicate that the central density profile is $\rho(r) \propto r^{-1.2}$ if the core is prolate, and $\rho(r) \propto r^{-0.4}$ if the central region is oblate.

Mid-infrared absorption studies have allowed the cores to be mapped at higher resolution than the millimetre and submillimetre studies allow. Bacmann et al. (2000) mapped 24 prestellar cores at 7 μm with a resolution of 6″ using ISOCAM on board the Infrared Space Observatory (ISO) satellite. Their results were consistent with the flattened inner density profile observed in the millimetre maps, and also showed that for a number of cores, the density profile steepens further to between $\rho(r) \propto r^{-3}$ and $\rho(r) \propto r^{-4}$ beyond a radius of $\sim$ 10000 – 15000 AU.

Alves, Lada, & Lada (2001) mapped the structure of the Bok globule Barnard 68 (an isolated low mass core), by measuring the near-infrared extinction of a large number of background stars. From these observations, they determined the column density along each line of sight. They found that the column density, plotted as a function of radius, is well described by a critically stable Bonner-Ebert sphere. A Bonner-Ebert sphere is an isothermal sphere that is confined by external pressure,

and supported against gravity by internal pressure (Ebert, 1955; Bonnor, 1956). The stability of the sphere is determined by the ratio of the core radius to the radius of the region exhibiting a flatter density profile. Alves et al. used this fit to to conclude that Barnard 68 is currently in a state of equilibrium.

This interpretation was questioned by Ballesteros-Paredes, Klessen, & Vázquez-Semadeni (2003). They found that in numerical simulations, a significant number of cores resembled stable Bonner-Ebert spheres, even though the cores were actually far from equilibrium. The fitting procedure also yielded core temperatures that were a factor of 2 – 3 different from the temperature of the simulation.

Models of protostellar collapse predict that the accretion rate is constant if the density profile at the beginning of collapse is $\rho(r) \propto r^{-2}$ everywhere (e.g. Foster & Chevalier, 1993). As discussed in Section 1.2.5, this is not consistent with observations. Henriksen, Andre, & Bontemps (1997) proposed that the flattened inner density profile could be a direct cause of the decreasing accretion rate inferred by Bontemps et al. (1996). Henriksen et al. modelled the collapse of a number of prestellar cores with density profiles made up of a 3-part power-law. The effect of a flattened inner profile on the collapse was to cause the initial accretion rate to be significantly elevated compared to models without the flattened profile.

Whitworth & Ward-Thompson (2001) modelled a prestellar core as a Plummer-like sphere, which has a steep power-law density profile at large radii and a flattened profile at lower radii. The authors found that as well as being consistent with the observed density profile and the decreasing accretion rate (and hence the relative lifetimes of Class 0 and Class I protostars), the model also explained the infall rates seen towards L1544 (Tafalla et al., 1998; Williams et al., 1999), an observation that most other models have not successfully explained.

1.3.3 Core Temperature

Prestellar cores are well shielded from the interstellar radiation field by the surrounding molecular cloud, and unlike protostellar envelopes, they do not have a central heating source. They are consequently very cold. This is indicated in Figure 1.4, which shows the prestellar core L1544 at 90 and 200 μm made with the ISOPHOT instrument on board ISO (Ward-Thompson et al., 2002). The lack of a detection at 90 μm indicates that the temperature of the emitting material is significantly colder than 30 K, as a blackbody at 30 K has a peak at around 100 μm.

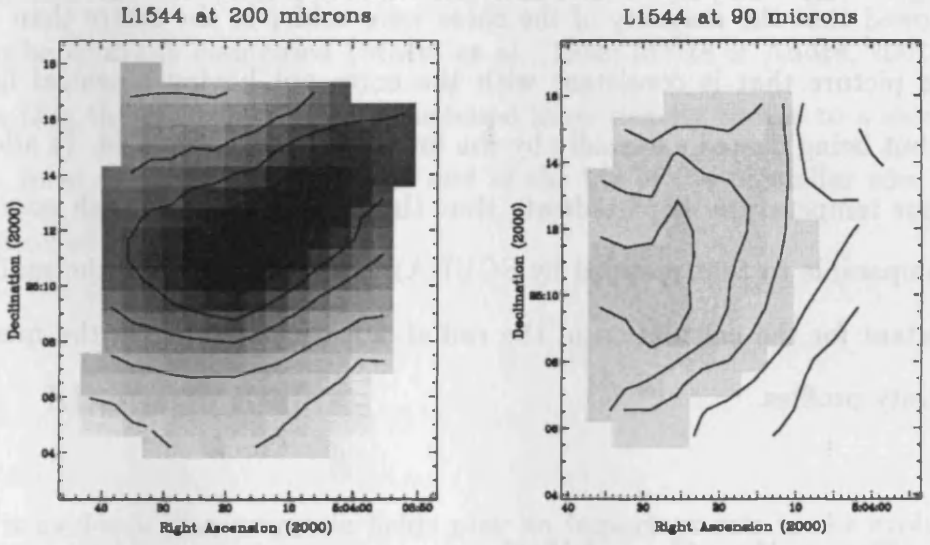

Figure 1.4: ISOPHOT maps of the prestellar core L1544 at 90 and 200 μm (Ward-Thompson et al., 2002).

Ward-Thompson et al. (2002) plotted the SEDs of a number of prestellar cores, based on data at wavelengths of 90, 170, 200, 450, 850 and 1300 μm. They fitted modified blackbody functions of the form:

$$F_\nu = B_{\nu,T}(1 - e^{-\tau_\nu})\Omega, \tag{1.3}$$

where F_ν is the measured flux density, $B_{\nu,T}$ is the Planck function at frequency ν and temperature T, Ω is the solid angle of the source, and τ_ν is the optical depth at frequency ν. τ_ν was assumed to scale as ν^β, where β is the dust emissivity index. The cores were best fitted by a single temperature of between 10 and 15 K.

The ISOPHOT data were also used to calculate colour temperature maps to estimate the temperature at each position in the map. To do this, the 170 and 200 μm maps are ratio-ed in the following way:

$$\frac{F_{\nu_1}}{F_{\nu_2}} = \frac{\nu_1^{3+\beta}[e^{h\nu_2/kT} - 1]}{\nu_2^{3+\beta}[e^{h\nu_1/kT} - 1]}. \tag{1.4}$$

This showed that the majority of the cores were colder in the centre than at the edges, a picture that is consistent with the cores not having a central heating source, but being heated externally by the interstellar radiation field. In addition, the colour temperature maps indicate that the central region of each core (on a scale comparable to that mapped by SCUBA) is approximately isothermal. This is important for the calculation of the radial density profiles from the measured flux density profiles.

1.3.4 Prestellar Core Lifetime

As was discussed for the different YSO classes, the lifetimes of prestellar cores are generally estimated by counting the relative numbers of objects at different evolutionary states (e.g. André et al., 2000). Beichman et al. (1986) found an approximately equal number of ammonia cores with and without IRAS sources. Using the lifetime of the embedded phase (based on the age of the youngest visible T-Tauri star), they estimated the lifetime of the prestellar phase to be approximately 10^6

years. Jessop & Ward-Thompson (2000) repeated this analysis for a number of different clouds, and found that the prestellar lifetime t_p decreases with the central density $n(H_2)$, and the data are best fitted by the relation $t_p \propto n(H_2)^{-0.85\pm0.15}$. They noted that this is consistent with the predictions of models of core evolution, in which the core is partially ionised by cosmic rays, and is supported against collapse by magnetic fields. These models are discussed in more detail in Section 1.4.3.

All prestellar cores mapped at high enough resolution have shown an inner flattened density profile (Ward-Thompson et al., 1994; André et al., 1996; Ward-Thompson et al., 1999; Kirk, 2002). Protostellar envelopes, however, are generally seen to be centrally condensed (Motte et al., 1998; Motte & André, 2001). This implies that the transition, from a flattened inner density profile to a steep inner profile, must occur very close to the end of the life of the prestellar core (Ward-Thompson et al., 1999).

1.3.5 Magnetic Fields

There is evidence that magnetic fields play an important role in the evolution of prestellar cores. Theoretical magnetic models of core evolution reproduce a number of the observed features of prestellar cores. These include the flattened inner density profile (e.g. Ward-Thompson et al., 1994), the steep density profiles at large radii (Bacmann et al., 2000), the anti-correlation of core lifetime with central density (Jessop & Ward-Thompson, 2000), and the rapid evolution from the flattened density profile to a centrally condensed one (Ward-Thompson et al., 1999). These theoretical models require the strength of the magnetic field. However, this is not well constrained observationally.

To date, the only measurements of the magnetic field strength are through low resolution Zeeman measurements, which do not sample the high density cores. These are discussed further in Section 1.5.3. Polarimetry maps indicate the direction of the magnetic field, but do not directly yield the strength. In Chapter 3, I use a technique to calculate the field strength in the plane of the sky for three prestellar cores using polarimetry observations.

Observations of the field direction in prestellar cores using the polarimetry observations (Ward-Thompson et al., 2000) have indicated that the field does not lie in the direction predicted by quasi-static magnetic models. This is covered in more detail in Chapter 3.

1.4 Theories of Prestellar Evolution

As discussed above, young stars are associated with clumps of dense gas in molecular clouds. There have been a number of theories proposed to explain the formation of these clumps. One such theory is that of gravitational instability, which was first suggested by Newton in 1692. The idea was developed further by Jeans (1929), who showed that in an isothermal medium of constant density, there exists an equilibrium between self-gravity, internal pressure and external pressure. Clumps of gas more massive than a critical value will collapse, and clumps less massive than this will expand. The equilibrium mass that neither contracts nor expands has become known as the Jeans mass $M_{\rm J}$:

$$M_{\rm J} \simeq 5.5 \frac{c^3}{G^{3/2}\rho^{1/2}}, \tag{1.5}$$

where c is the isothermal sound speed, G is the gravitational constant, and ρ is the initial density.

Random motions in the cloud will create regions that are more dense than the average density. If such a region has a mass greater than M_J, it will contract, and the density fluctuation will be amplified. Clumps that are much more massive than M_J will be dominated by their self-gravity and will therefore collapse on a freefall time t_{ff}:

$$t_{ff} = \left(\frac{3\pi}{32G\rho}\right)^{\frac{1}{2}}. \tag{1.6}$$

Alternatively, turbulent shocks have been used to explain the formation of thermally supercritical clumps. The role of turbulence in molecular clouds is discussed in Section 1.4.4.

The pressure that supports the clumps against gravity is thermal pressure, therefore a clump of gas that is unstable to gravitational collapse is known as thermally supercritical. This is the basic requirement of the star formation process. A number of different analytic and numerical models have been proposed to explain *how* star formation proceeds. These differ in many ways, and are dominated by different physics, such as gravity, pressure, turbulence or magnetic fields. In this section, I discuss some of these theories.

1.4.1 Similarity Solutions

A number of self-similar analytical solutions have been suggested (e.g. Larson, 1969; Penston, 1969; Shu, 1977; Hunter, 1977; Whitworth & Summers, 1985). These solutions solve the equations of self-gravitating gas dynamics and thermal balance,

whilst removing the temporal and spatial boundary conditions to infinity (Whitworth & Summers, 1985). This is done for computational convenience, and to remove the influence of arbitrary boundary conditions on the results.

The most often quoted similarity solution was known for a while as the 'standard' theory of spontaneous isolated star formation (Shu, 1977). This model takes the elegant (if physically unrealistic) singular isothermal sphere (SIS) as the starting point for protostellar collapse. The SIS is described by a density profile of $\rho \propto r^{-2}$ everywhere. This state is arrived at quasi-statically (i.e. with negligible acceleration), and magnetic fields have been used to explain the gradual evolution of a core to an SIS.

The collapse of the SIS is instigated by the formation of a point mass (at time $t = 0$) at the centre of the core. An expansion wave proceeds outwards to the core edge at the sound speed a. The material within the wavefront is in freefall collapse, and has a density profile of $\rho \propto r^{-1.5}$. The material outside the wavefront is stationary and has the pre-collapse density profile of $\rho \propto r^{-2}$. A consequence of the SIS is that the accretion rate is constant, with a value of a^3/G, where G is the gravitational constant. As discussed in the preceding section, neither the degree of central condensation, nor the constant accretion rate are seen observationally.

The Larson-Penston (LP) collapse solution (Larson, 1969; Penston, 1969) differs in that the collapse begins with a compression wave that propagates inwards from the surface of the core to the centre. When the wave reaches the centre, a point mass is formed and the wave is reflected into an expansion wave. Consequently there is already significant infall at $t = 0$ when the central point mass is formed.

Hunter (1977) identified yet more discrete solutions, and also performed numerical simulations. He found that the collapse resembled the LP solution more closely than that of Shu. This result was also found by Foster & Chevalier (1993), who noted that to achieve a constant accretion rate, the radius of the flat central region of the core at $t = 0$ must be smaller than 0.05 times the core radius.

Whitworth & Summers (1985) showed that rather than there being discrete self-similar solutions, as had been previously assumed by Larson (1969), Penston (1969) and Shu (1977), there is a 2-dimensional continuum of solutions. The solutions can be categorised into 'intrinsically unstable clouds', which behave in a similar manner to that described by the LP solution, 'intrinsically stable clouds', which require an external trigger to promote collapse, and 'unnatural solutions' such as the Shu solution. Whitworth & Summers conclude that the large number of solutions increases the likelihood of an acceptable similarity solution being found from realistic (and hence varied) conditions. Of the three solution types, Whitworth & Summers found that the unstable cloud is the more realistic, and therefore concur with the conclusions of Hunter (1977) and Foster & Chevalier (1993).

Whitworth et al. (1996) showed that the creation of the SIS is unfeasible. It requires that the core be unperturbed by collisions with other cores for a longer time than is reasonable given the velocity dispersion of the cores. If the effects of a magnetic field are included, then the creation of the SIS is even more unlikely, as the field slows down the evolution of the core, thus making an external perturbation more likely. In addition, the collapse of an SIS does not easily form binary star systems, without external perturbations, (which if present, would prevent the SIS from forming in the first place). This difficulty in forming binaries is not consistent with observations, which indicate that the majority of young stars are part of binary

or higher multiple systems (e.g. Ghez, Neugebauer, & Matthews, 1993).

1.4.2 Additional Cloud Support Mechanisms

Zuckerman & Palmer (1974) noted that the Galactic star formation rate is significantly lower than expected, given the total mass of gas in molecular clouds in the Galaxy, and the typical freefall time of a molecular cloud. This agrees with the low star formation efficiency of GMCs, which typically have masses of $10^4 - 10^6$ $M_\odot$, and form open clusters of stars with a total mass less than 10^3 $M_\odot$.

Therefore there must either be additional support mechanisms within molecular clouds, or molecular clouds must have lower lifetimes than the 10^7 years that was previously believed. Two potential sources of cloud support are magnetic fields and turbulence. These are discussed in Sections 1.4.3 and 1.4.4 respectively. The question of reduced cloud lifetime is considered in Section 1.4.5.

1.4.3 Magnetic Fields and Ambipolar Diffusion

There is now considerable evidence that magnetic fields permeate the interstellar medium. These are discussed in Section 1.5. They were proposed to play an important part in the evolution of molecular clouds as early as 1956 by Mestel & Spitzer.

Magnetic fields have been shown to be capable of providing support against gravity, and therefore preventing the collapse of a thermally supercritical molecular cloud (Mouschovias, 1976a,b). The origin of this support is that a partially ionised gas (ionised by either UV photons or cosmic rays) experiences resistance against

crossing magnetic field lines due to the Lorentz force. Friction between the ions and the neutrals slows down the gravitational contraction of the cloud in directions perpendicular to the magnetic field lines, forming a flattened structure.

Depending on the strength of the magnetic field, the cloud can contract in a direction perpendicular to the field direction, by dragging the field lines. This occurs until the the magnetic tension is in equilibrium with the cloud's self-gravity. In this equilibrium state, a cloud is known as magnetically critical.

If the cloud is magnetically subcritical and therefore held in place by the field, the magnetic flux must be removed before the cloud can collapse further. This is achieved through the process of ambipolar diffusion, where the neutrals flow past the ions and thus collapse continues (Mestel & Spitzer, 1956).

The time-scale for the collapse of a sub-critical core t_{AD} is modified from the freefall time t_{ff} by the time-scale for collisions between neutrals and ions t_{ni} according to the following (e.g. Mouschovias & Ciolek, 1999):

$$t_{AD} \simeq \frac{t_{ff}^2}{t_{ni}}. \tag{1.7}$$

This time-scale is reduced as the density increases, because the enhanced shielding reduces the rate of ionisation from energetic photons (Mouschovias, 1979). Therefore as the cloud evolves and the central density increases, the contracting core becomes separated from the outer envelope, which is effectively held in place by the field.

The critical mass $M_{B,crit}$ that can be supported by a magnetic flux Φ is given by:

$$M_{B,crit} = c_1 \Phi G^{-\frac{1}{2}}, \tag{1.8}$$

where c_1 is a constant between 0.13 (Mouschovias & Spitzer, 1976) and $1/2\pi$ (0.16 — Nakano & Nakamura, 1978).

A magnetically subcritical cloud evolves quasi-statically until enough mass has built up in the centre for a supercritical core to form. At this point the field can no longer support the weight of the cloud, and dynamic collapse sets in.

A large number of detailed numerical simulations of cores evolving according to ambipolar diffusion have been performed over the last 20 years (e.g. Fiedler & Mouschovias, 1992; Ciolek & Mouschovias, 1994; Ciolek & Basu, 2000). These have made a number of assumptions and predictions that can be compared to observations. For ambipolar diffusion to be important, the cloud must be initially magnetically subcritical. To determine if this is applicable in real molecular clouds, the mass and the magnetic field strength are required. The mass of molecular clouds is relatively easy to measure, and can be done by measuring the integrated flux of an optically thin species. However, measuring the magnetic field strength is considerably more difficult.

The most common way of measuring the field strength is by using the Zeeman effect. This technique is described in Section 1.5.3. Crutcher (1999) collated Zeeman measurements of a number of molecular clouds, and calculated the mass to flux ratio for each of them. He found that in most cases, the clouds were supercritical with a mass to flux ratio of 2 (in units of the critical value). This implies that the clouds are not supported by magnetic fields. However, as discussed in Section 1.5.3 the Zeeman effect is not an ideal technique for measuring the field strength. An alternative method is discussed in Section 1.5.4, and is used to estimate the field strength of three prestellar cores in Chapter 3.

The predicted time for the core to evolve through ambipolar diffusion to the formation of a supercritical core is $\sim 10^7$ years (e.g. Ciolek & Mouschovias, 1994). This can be compared to the estimated lifetime of prestellar cores of $\sim 10^6$ years (see Section 1.3.4 above). Therefore if the models are correct, by the time prestellar cores are detected they have almost formed a supercritical core. The predicted central density at this time is also in agreement with the observations of prestellar cores (e.g. André et al., 1996).

The models also make predictions about the density profile of the core at different times. The profile is characterised by a flat inner region and a power-law outer region, in general agreement with observation. André et al. (1996) compared the density profile of the prestellar core L1689B to the Ciolek & Mouschovias (1994) model and found that to support the core would require a field strength of ~ 80 μG. This is higher than the field strengths commonly measured using the Zeeman effect in an object of this mass (Crutcher, 1999), though as mentioned above, the Zeeman effect is not an ideal method for determining the field strength.

A number of other predictions of ambipolar diffusion models such as infall speed, density profile and field morphology have been compared with the prestellar core L1544. These comparisons have shown that whilst the models predict some of the observed features, no models can yet account for all of the observations. This is discussed in detail in Section 3.3.

1.4.4 Turbulent Cloud Support

Molecular clouds are generally observed to have non-thermal motions (e.g. Myers, 1983), as evidenced by their broad molecular line profiles. These motions

(hereafter called turbulence) will supplement the support of the cloud. However hydrodynamic turbulence is expected to shock and dissipate on a time-scale comparable with the cloud freefall time-scale of $\sim 10^6$ years (e.g. Mac Low et al., 1998). Therefore in order to provide support over the cloud's lifetime ($\sim 10^7$ years), the turbulence must be continually re-injected. A number of sources of turbulence have been suggested, including Galactic shear on large scales, supernovae shocks on intermediate scales and stellar outflows from young stars on small scales (e.g. Norman & Ferrara, 1996).

An alternative suggestion was that turbulence in a magnetised medium, or magneto-hydrodynamic (MHD) turbulence was more long lived (Arons & Max, 1975). Unlike sonic compressive waves, transverse oscillations along the field lines (Alfvén waves) do not involve collisions between clumps of gas, and are therefore less dissipative and more long lived. In order for this mode of oscillation to be important, the thermal pressure must be small compared to the magnetic pressure, which is equivalent to the Alfvén speed being much higher than the sound speed. This is generally observed to be the case, and though the gas motions are usually seen to be supersonic, they are typically sub-Alfvénic (e.g. Myers & Goodman, 1988).

Recent numerical studies however, have indicated that transverse Alfvén waves can be converted into compressive motions, which are rapidly dissipated (e.g. Mac Low et al., 1998; Stone, Ostriker, & Gammie, 1998). If these studies are correct, then either the turbulence is continually re-injected, or molecular clouds only survive for $\sim 10^6$ years. The latter possibility is discussed in the following section.

1.4.5 Molecular Cloud Lifetimes

In an effort to explain the low Galactic star-forming rate, Elmegreen (2000) commented that one third of clusters in the Large Magellanic Cloud (LMC) that are younger than 10 Myr are still associated with gas, and essentially no clusters older than this showed evidence of any associated gas. This implies that clouds only last for ~ 3 Myr once star formation has begun. In addition, few molecular clouds are observed that do not have associated stars, the only exception to this being the Maddalena-Thaddeus cloud (Maddalena & Thaddeus, 1985). Therefore molecular clouds must be created, form their stars and be dissipated in only a few Myr. This removes the need for long-lived turbulent or magnetic support. Elmegreen (2000) argued that the low Galactic star-forming rate is due to the fact that clouds are not long-lived so the majority of gas in a molecular cloud is never dense enough to form stars.

1.5 Measuring Interstellar Magnetic Fields

The evidence for interstellar magnetic fields was first discovered over 50 years ago when Hall (1949) and Hiltner (1949) independently detected the polarisation of starlight. The observation that the degree of polarisation was correlated with reddening, lead to the suggestion that the polarisation was caused by dust grains that are aligned by the magnetic field, and preferentially absorb one component of the background radiation. The magnetic field was first measured directly by observing the Zeeman effect in 21 cm HI spectra (Verschuur, 1969).

As discussed in the previous section, the role of the magnetic field may be

crucial to the process of star formation. It is therefore important to measure its properties observationally. In this section, I discuss the different observational techniques that are used for measuring interstellar magnetic fields. These include polarimetry (Section 1.5.1), and two methods for measuring the strength of the magnetic field, the Zeeman effect, and the Chandrasekhar-Fermi technique (Sections 1.5.3 and 1.5.4 respectively).

1.5.1 Polarimetry

Polarimetry is the study of linearly or circularly polarised light. After the discovery that starlight could be polarised by dust grains along the line of sight, Davis & Greenstein (1951) suggested that elongated spinning dust grains could be aligned perpendicular to the local magnetic field. These aligned grains would preferentially absorb the component of the background radiation that was parallel with the grains' long axis, leading to the transmitted light being partially polarised in a direction perpendicular to the grain axis and parallel to the magnetic field. Since then a number of theories have been proposed to explain what causes the grains to spin, and why they align perpendicular to the magnetic field. These are discussed in Section 1.5.2

Optical polarimetry has been used primarily to map the large scale magnetic field of our own and other galaxies (e.g. Axon & Ellis, 1976). These studies have shown that the magnetic field lines tend to lie along the galactic spiral arms (e.g. Ward-Thompson, 1987). Polarimetry has also been used to map the magnetic field at the periphery of molecular clouds, where the extinction is low, and background stars can still be detected (e.g. Vrba, Strom, & Strom, 1976b). However, the high extinction at the centre of molecular clouds puts these regions beyond the reach of

optical polarimetry.

One solution to this is to use the same technique in the infrared where the opacity is lower (e.g. Wilking et al., 1979). However, recent research has suggested that this method does not probe the field in the centres of molecular clouds (Goodman et al., 1995). These authors argue that the degree of polarisation does not increase with extinction in the cloud centre. Also the polarisation shows no correlation with the cloud structure, and shows a similar morphology to the optical polarisation map of the outskirts of the cloud. They blame this on a possible change in grain size or geometry at high density, as the polarisation efficiency for absorption polarimetry is highly dependent on grain properties. They conclude that the map is probably sampling the foreground polarisation caused by dust in the same regime as that sampled in the optical map.

Fortunately, the thermal radiation emitted by aligned grains is also polarised. This was first successfully mapped in the far-infrared by Cudlip et al. (1982) and in the submillimetre by Hildebrand, Dragovan, & Novak (1984). The emission is optically thin and can therefore be used to probe the centres of molecular clouds. The degree of polarisation has also been shown to correlate with the morphology of high density filaments (e.g. Matthews, Wilson, & Fiege, 2001). This indicates that the technique is sampling the magnetic field in the cloud centre. Unlike in absorption polarimetry, the radiation is polarised in a direction parallel to the grain's long axis. This is discussed in the following section.

1.5.2 Grain Alignment

Davis & Greenstein (1951) suggested that rotating paramagnetic grains in a mag-

netic field will experience a torque that aligns them such that their long axis is perpendicular to the field. A paramagnetic material consists of numerous permanent atomic dipoles that are normally independent, but line up when an external magnetic field is applied. This causes the material to have a magnetisation M (magnetic moment per unit volume) that is aligned with the external field. For a spinning grain, the time taken to induce the magnetisation results in a component ($M_\perp$) perpendicular to the magnetic field. A torque between $M_\perp$ and $\boldsymbol{B}$ aligns the rotation axis of the grain with the magnetic field.

A spinning triaxial grain will have a rotational energy E_r and a total angular momentum J given by Equations 1.9 and 1.10 (Purcell, 1979):

$$E_r = \frac{1}{2}(I_x\Omega_x^2 + I_y\Omega_y^2 + I_z\Omega_z^2), \tag{1.9}$$

$$J = (I_x^2\Omega_x^2 + I_y^2\Omega_y^2 + I_z^2\Omega_z^2)^{\frac{1}{2}}, \tag{1.10}$$

where $\Omega_{x,y,z}$ and $I_{x,y,z}$ are the angular velocities and moments of inertia in the x, y, and z directions. The coordinates of the grain are defined such that the x axis is the grain's long axis, and $I_x < I_y < I_z$.

The rotational energy of the grain can be dissipated through paramagnetic absorption (Davis & Greenstein, 1951). This is the resistance of the material to aligning the atomic dipoles. Mechanical stresses can also cause dissipation of energy (Purcell, 1979). These occur by the centrifugal forces acting on the imperfectly elastic grain. However the total angular momentum is always conserved. This will cause Ω_z to increase at the expense of Ω_x and Ω_y, until $\Omega_x = \Omega_y = 0$ and the grain is spinning around its shortest axis. The thermal emission from the grain will therefore be partially polarised parallel to the grain's long (x) axis, which is perpendicular to the direction of the magnetic field.

for molecular hydrogen is on the surface of grains. Adsorbed atomic hydrogen is free to move around the grain surface until it collides with another hydrogen atom, and forms H_2 in an exothermic reaction that liberates 4.5 eV. The H_2 is ejected from the grain and the grain recoils. If the molecules are ejected preferentially from specific sites, the grain will spin up and potentially achieve a very high rotation rate.

1.5.3 Zeeman effect

The standard technique for measuring the interstellar magnetic field strength uses the Zeeman effect, which is the splitting of a species' electronic energy levels in an external magnetic field. An electron bound to an atom can be described by a series of quantum numbers. The principal quantum number (n) describes the shell that the electron is in, where n can be any positive integer greater than 0. The orbital angular momentum quantum number (l) can take any integer between 0 and $n-1$, and dictates the shape of the electron's wave-function. The magnetic quantum number (m_l) can be any integer between $-l$ and l. The energy levels defined by this quantum number are degenerate unless the atom is in a magnetic field. In a magnetic field, adjacent levels become separated by $\mu_B B$, where $\mu_B = e\hbar/2m$ and B is the field strength. This is illustrated in Figure 1.5. In this example, the spectral line (shown in Figure 1.5 as a red line) splits from a singlet '1' to a triplet '2,3,4' state.

Typical interstellar magnetic fields are very weak (of the order microgauss to milligauss), therefore the separation of the spectral lines is typically below 1 kHz, and is therefore not resolvable. However if the magnetic field is parallel to the line of sight, the spectral lines that make up the triplet are polarised in different

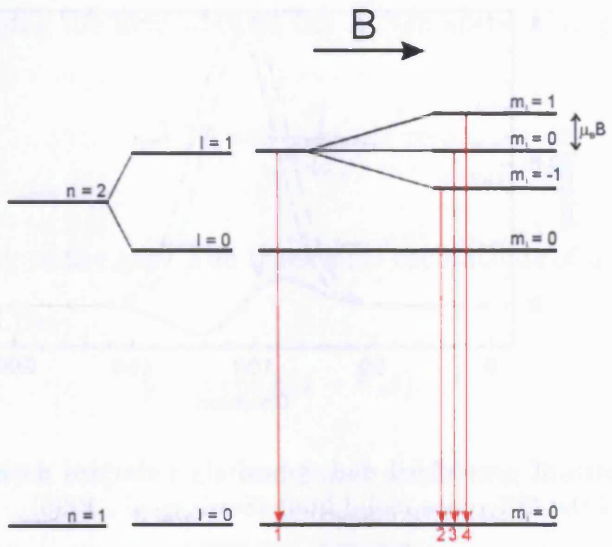

Figure 1.5: Diagram illustrating the splitting of an energy level in a magnetic field.

ways. In the example given above, line 3 is linearly polarised and lines 2 and 4 are circularly polarised with opposite senses. Observing the left and right handed circularly polarised light and finding the difference, should yield a differential signal that is measurable, as shown in Figure 1.6 (Sault et al., 1990). If the magnetic field is perpendicular to the line of sight, all the lines are linearly polarised, therefore this technique is only a measure of the line of sight field component.

The Zeeman effect was first observed in the interstellar medium by Verschuur (1969) in HI absorption towards the Taurus molecular cloud. However, HI is not a good species to observe the Zeeman effect in the denser regions of molecular clouds, where the majority of the hydrogen is molecular. OH lines at 18 cm are a better tracer in these regions, and the Zeeman effect has been observed in emission towards Barnard 1 using the 305 m Arecibo telescope (Goodman et al., 1989). However, Zeeman observations with this tracer are limited by the low spatial resolution (3′ with the Arecibo telescope), caused by the low frequency (1666 MHz) of the lines. Additionally the fractional abundance of OH decreases at high density

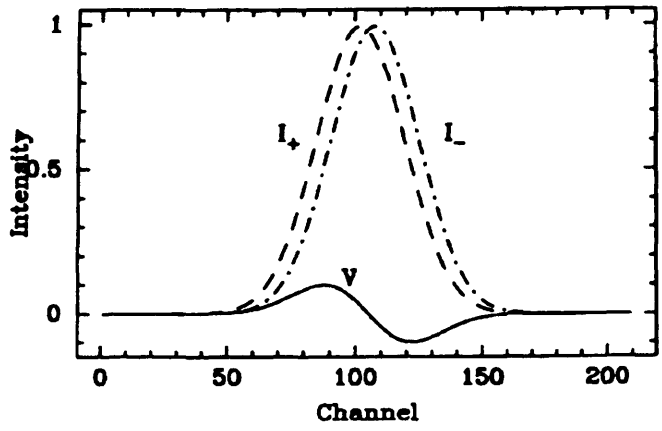

Figure 1.6: Spectra of unresolved and oppositely polarised emission (dashed and dot-dashed lines) and the difference (solid line) (Sault et al., 1990)

because its formation mechanism requires ionising photons. The (1-0) transition of CN at 113 GHz (2.65 mm) is a much more promising transition to observe the Zeeman effect with, as the higher frequency allows much higher spatial resolution. To date, CN Zeeman detections have been made towards the high mass star-forming regions OMC1 and DR21OH (Crutcher et al., 1999), and data for lower mass objects should become available as detector technology improves.

1.5.4 Chandrasekhar-Fermi method

Polarimetry observations of the magnetic field do not yield the magnitude of the magnetic field B directly, though Chandrasekhar and Fermi (1953) proposed that the dispersion of polarisation vectors can be used to estimate the plane of sky magnetic field strength B_{pos}. Their derivation is as follows and relies on the assumptions that the magnetic field is frozen into the gas and that the gas motion is isotropic.

Signals travel along the field lines at the Alfvén speed $V_{\rm A}$, given by:

$$V_A = \frac{B}{\sqrt{(4\pi\rho)}}, \tag{1.11}$$

where ρ is the density of the gas. The transverse oscillations of a field line (Alfvén waves) are described by:

$$y = a\cos k(x - V_A t). \tag{1.12}$$

Differentiating this with respect to x and t and combining the results gives:

$$V_A^2 \overline{\left(\frac{\delta y}{\delta x}\right)^2} = \overline{\left(\frac{\delta y}{\delta t}\right)^2}, \tag{1.13}$$

where $\delta y/\delta t$ is equal to the one dimensional velocity dispersion δv, and $\delta y/\delta x$ is equal to the dispersion of the polarisation vectors $\delta\theta$. Combining Equations 1.11 and 1.13, the magnetic field strength is given by:

$$B = \sqrt{(4\pi\rho)}\frac{\delta v}{\delta\theta}, \tag{1.14}$$

with B measured in G, ρ in gcm^{-3}, δv in cms^{-1} and $\delta\theta$ in radians.

The velocity dispersion δv is in the plane of the sky. While it is not possible to measure this quantity, it is assumed to be equal to the dispersion along the line of sight, which is measurable through molecular line observations. The assumption that the molecular line observations trace the same material as the polarised emission is also made. The validity of this assumption is discussed below. Hence the magnetic field strength can be estimated from the dispersion in the polarisation measurements.

There are many potential problems with the technique, the most obvious being

that any large scale structure in the magnetic field will cause the measured $\delta\theta$ to be an overestimate. This must be dealt with in each individual case. The averaging of different turbulent cells, either in the plane of the sky (caused by insufficient angular resolution) or along each line of sight (obviously unavoidable), both decrease the measured $\delta\theta$. Numerous cells along the line of sight have been inferred by modelling the dispersion of position angles towards molecular clouds on a larger scale (Myers & Goodman, 1991).

In order to investigate the usefulness of the Chandrasekhar-Fermi technique, and to quantify the above effects, simulated observations of molecular cloud models have been performed (Ostriker, Stone, & Gammie, 2001; Heitsch et al., 2001) with a variety of conditions. It was demonstrated that the technique can measure B_{pos} under certain conditions if a multiplicative factor of ~ 0.5 is included. This factor takes into account non-uniform density structure and sampling multiple cells along the line of sight. Ostriker et al. (2001) show that the technique is valid for their strong field model only, where the mean magnetic energy is greater than the turbulent magnetic energy.

Including this calibration factor and converting ρ into the hydrogen volume density (Equation 1.16) and δv into the FWHM line width, $\Delta V = \sqrt{8 \ln 2}\delta v$, Equation 1.14 becomes:

$$B_{pos} = 9.3\sqrt{n(H_2)}\frac{\Delta V}{\delta\theta}, \tag{1.15}$$

with B_{pos} measured in μG, $n(H_2)$ in cm^{-3}, ΔV in kms^{-1} and $\delta\theta$ in degrees.

The density is converted into the molecular hydrogen volume density using the fractional abundances given in Table 1.1. For simplicity these values assume that matter is comprised of molecular hydrogen, atomic helium and heavier elements

Table 1.1: Mass fractions and number fractions of H_2, He and O_2 (representing heavy elements), based on meteoritic data (Anders & Grevesse, 1989).

Species	H_2	He	O_2
Mass of species (m_H)	2	4	32
Mass fraction	0.706	0.275	0.019
Number fraction	0.836	0.163	0.001

(represented by molecular oxygen).

$$\begin{aligned} \rho &= [n(H_2) \times 2m_H] + [n(He) \times 4m_H] + [n(O) \times 32m_H], \\ &= [n(H_2) \times 2m_H] + [0.195n(H_2) \times 4m_H] + [0.0017n(H_2) \times 32m_H], \\ &= 2.8m_H n(H_2). \end{aligned} \tag{1.16}$$

It must be kept in mind when interpreting the results that the technique only measures B_{pos}, which varies with the inclination angle (i) as $B\cos i$. However, the addition of a line of sight component that is equal to the two (equal) plane of sky components only increases B to $1.22B_{pos}$.

In Chapter 3 I use this technique to measure the magnetic field strength in the plane of the sky for three prestellar cores, L1544, L43 and L183.

1.6 Mass Estimates of Molecular Clouds and Cores

In this section, I discuss the techniques used in this thesis for calculating the masses of prestellar cores and protostellar envelopes. I will concentrate on the calculation of mass based on the continuum radiation that arises from the thermal emission of dust grains. At the temperatures of molecular cloud interiors, this radiation is

emitted in the submillimetre wavelength range.

There are alternative techniques for measuring cloud masses, such as spectral line emission from molecular species. However, this radiation is frequently not optically thin, and the molecules are subject to chemical processing and depletion onto the cold surfaces of dust grains (e.g. Redman et al., 2002).

1.6.1 Determining Masses from Submillimetre Observations

In order to determine the mass of astronomical objects from thermal dust emission, we make the assumption that it is optically thin. The following derivation of the dust mass is based on that by Hildebrand (1983).

The total flux at frequency ν received from N grains is given by:

$$F(\nu) = N\left(\frac{\sigma_g}{D^2}\right) Q(\nu)B(\nu,T), \tag{1.17}$$

where D is the distance to the grains, σ_g is the cross-sectional area of a grain, $Q(\nu)$ is the grain emissivity and $B(\nu,T)$ is the Planck function at temperature T:

$$B(\nu,T) = \frac{2h\nu^3}{c^2}\left[e^{\frac{h\nu}{kT}} - 1\right]^{-1}, \tag{1.18}$$

where h is Planck's constant, k is the Boltzmann constant and c is the speed of light. The fraction σ_g/D is the solid angle subtended by a single grain, and $Q(\nu)B(\nu,T)$ is the energy emitted by the grain at frequency ν and temperature T.

The mass of dust is given by:

$$M_d = V_d\rho_g = Nv_g\rho_g, \tag{1.19}$$

where V_d is the total volume of the dust, v_g is the volume of a single grain, and ρ_g is the typical density of a grain. If the grain radius is a, the grain volume is given by:

$$v_g = \frac{4}{3}\pi a^3 = \frac{4}{3}\sigma_g a. \tag{1.20}$$

Note that this is only strictly true for spherical dust grains, but is a good approximation nonetheless.

Combining Equations 1.17, 1.19 and 1.20 yields:

$$M_d = \left(\frac{F(\nu)D^2}{B(\nu,T)}\right)\left(\frac{4\rho_g a}{3Q(\nu)}\right). \tag{1.21}$$

The first term in Equation 1.21 contains parameters that can be determined observationally. The second term is equal to the inverse of κ_d, the grain mass absorption coefficient.

Hildebrand (1983) assumed values for a and ρ of 0.1 μm and 3 gcm^{-3} respectively. The value for ρ is based on the known densities of graphite and silicates, the probable components of interstellar dust. Mathis, Rumpl, & Nordsieck (1977) found that the interstellar extinction is best fitted by grains with a size distribution centred around 0.1 μm.

The emissivity is more difficult to determine. Whitcomb et al. (1981) measured the UV and 125 μm optical depths for an interstellar cloud. The cloud needed to have an A_V that was low enough that UV flux from a background star could be detected, and high enough to measure the emission from the cloud at 125 μm. The ratio of optical depths is equal to the ratio of the extinction efficiencies ($Q_{ext,UV}/Q_{ext,125}$), and was found to be approximately 4000, with an uncertainty of a factor of 4.

The extinction efficiency is equal to the ratio of the extinction and geometric cross-sections:

$$Q_{ext} = \frac{\sigma_{ext}}{\sigma_{geom}} = \frac{\sigma_{abs} + \sigma_{scat}}{\sigma_{geom}}. \quad (1.22)$$

At UV wavelengths, both the σ_{scat} and σ_{abs} are equal to σ_{geom}, therefore the extinction efficiency is equal to 2. At infrared wavelengths, scattering is negligible, so σ_{ext} is equal to σ_{abs}. The extinction efficiency is therefore equal to the absorption efficiency, which by Kirchoff's law is equal to the emissivity. This value can be extrapolated to longer wavelengths if the wavelength dependence β of the emissivity is known. This is generally assumed to be ~ 1 at IR wavelengths ($\lambda < 200\mu$m), and ~ 2 at sub-mm wavelengths (Hildebrand et al., 1977; Whitcomb et al., 1981; Hildebrand, 1983). This method yields a value for $\kappa_{d,850\mu m}$ of 0.8 cm^2g^{-1}.

κ_d can also be determined experimentally. Agladze et al. (1994) measured the absorption coefficient for crystalline and amorphous forsterite (Mg_2SiO_4) in the laboratory. They found values for $\kappa_{d,850\mu m}$ of 1.6 cm^2g^{-1} and 0.6 cm^2g^{-1} for crystalline and amorphous material at a temperature of 20 K. The experiment also provided a direct measurement of β, which was found to be equal to 1.3.

Both the observational and experimental techniques yield a $\kappa_{d,850\mu m}$ that is larger than the canonical value of 0.6 cm^2g^{-1} (Draine & Lee, 1984), which was calculated for bare graphite grains in the diffuse interstellar medium. There are a number of possible explanations for the larger value of κ_d in cold, dense molecular clouds. Volatile materials could freeze on to the grain surfaces to form ice mantles, and grains could agglomerate and form 'fluffy' structures.

Ossenkopf & Henning (1994) modelled the effects of coagulation and freeze-out on κ_d for silicate grains. They found that mantle formation occurs rapidly compared to coagulation, and both effects increase the absorption coefficient. For

volume densities of 10^5 cm^{-3} that are typical of prestellar core environments, their models predict a $\kappa_{d,1.3mm}$ of 0.8 cm^{2}g^{-1} with an uncertainty of a factor of 2. Extrapolating this value to 850 μm yields a $\kappa_{d,850\mu m}$ of 1.9 cm^{2}g^{-1} using the canonical far infrared β of 2, and a $\kappa_{d,850\mu m}$ of 1.4 cm^{2}g^{-1} using the $\beta = 1.3$ that is recommended by Agladze et al. (1994).

Each of these methods has some drawbacks. The Whitcomb et al. (1981) method involves assuming that κ_d is the same in the dense cloud being studied, as it is in a less dense cloud for which the UV extinction can be measured. It also requires extrapolating Q_{ext} over a large range of wavelengths. The laboratory studies of Agladze et al. (1994) only consider one type of grain material, and do not take into account icy mantles or grain coagulation. Modelling studies also make a number of assumptions regarding the grain composition. However, even taking into account all of these uncertainties, measuring the thermal dust emission remains the most reliable way of determining the mass of molecular cloud cores. The alternative is measuring the optically thin emission from molecular species, which are subject to an unknown amount of chemical processing and depletion out of the gas phase.

In this thesis, I will use the value of $\kappa_{d,850\mu m} = 1.4$ cm^{2}g^{-1} recommended by Ossenkopf & Henning (1994) for densities of 10^5 gcm^{-3} and a β of 1.3. This is within the uncertainty of the value predicted by Whitcomb et al. (1981), and can be reproduced in the laboratory with a mixture of crystalline and amorphous silicate (Agladze et al., 1994). The gas mass can then be calculated using the canonical gas to dust ratio of 100 (Hildebrand, 1983).

1.6.2 Virial Masses

To determine whether or not an object is gravitationally stable, its virial mass can be calculated. The virial theorem states that the sum of twice the internal kinetic energy $\mathcal{T}$, the gravitational potential energy $\mathcal{W}$, and the magnetic energy $\mathcal{M}$ is equal to zero for a cloud or fragment of cloud that is in equilibrium, i.e.:

$$2\mathcal{T} + \mathcal{W} + \mathcal{M} = 0. \tag{1.23}$$

If the sum of these terms is greater than zero, the cloud will expand. If is less that zero, it will contract.

The kinetic energy $\mathcal{T}$ is due to both thermal and the non-thermal components, and is generally determined from the linewidths of emission lines from molecular species:

$$\mathcal{T} = \frac{3}{2} M\sigma^2, \tag{1.24}$$

where M is the mass of the core and σ is the one-dimensional velocity dispersion:

$$\sigma = \frac{\Delta V_{\overline{m}}}{\sqrt{8 \ln 2}} \tag{1.25}$$

and $\Delta V_{\overline{m}}$ is the linewidth of a particle of mean mass ($2.33 m_H$).

The velocity dispersion is generally measured using a tracer molecule of significantly larger mass than $2.33 m_H$. $\Delta V_{\overline{m}}$ must therefore be converted from the measured linewidth ΔV_{mol} using (e.g. Caselli et al., 2002):

$$\Delta V_{\overline{m}}^2 = \Delta V_{mol}^2 + 8 \ln 2 \frac{kT}{m_H} \left(\frac{1}{2.33} - \frac{1}{m_{mol}} \right), \tag{1.26}$$

where m_{mol} is the mass of the molecular tracer in atomic mass units, T is the temperature and k is the Boltzmann constant.

The gravitational potential energy for a uniform density sphere is given by:

$$\mathcal{W} = \frac{-3GM^2}{5R}, \tag{1.27}$$

where G is the gravitational constant and M and R are the measured mass and radius respectively of the cloud fragment being considered.

The magnetic energy is given by:

$$\mathcal{M} = \frac{B^2V}{2\mu_0}, \tag{1.28}$$

where B is the magnetic field strength, V is the volume of the fragment and μ_0 is the permeability of free space.

In order to determine the relative importance of these three terms for a typical prestellar core, the L183 core is considered. The data for this core are presented in Chapter 3. The velocity dispersion is measured using N_2H^+ emission (Caselli et al., 2002). The mass and dimensions of the core are determined from submillimetre maps (Kirk, 2002). The field strength is estimated using the Chandrasekhar-Fermi technique discussed above. The three terms for L183 are given in Table 1.2. This analysis indicates that the core is gravitationally bound, and that kinetic support against gravity is more important than the magnetic support, though the magnetic support is not insignificant. This is consistent with the result of Ward-Thompson et al. (2000) that both magnetic and turbulent pressure is important in the support of the core. This is discussed further in Section 3.1.

Table 1.2: The virial parameters for the prestellar core L183

Virial parameters	
$\mathcal{T}$	1.8×10^{35} J
$\mathcal{W}$	-4.6×10^{35} J
$\mathcal{M}$	0.6×10^{35} J
$2\mathcal{T} + \mathcal{W} + \mathcal{M}$	-0.5×10^{35} J

1.7 The Initial Mass Function

The final mass of each star is determined by the conditions at the time of its formation. The distribution of stellar masses at birth is referred to as the initial mass function (IMF). As discussed at the beginning of this chapter, the stellar IMF has dramatic consequences for the evolution of the parent molecular cloud, the interstellar medium, and the evolution of the Galaxy. Therefore a knowledge of the IMF is important for an understanding of most aspects of Galactic astronomy. In addition, the mass to light ratio of distant galaxies depends on the IMF, and understanding its universality is therefore important for the study of cosmology.

In order to establish the form of the IMF, stellar masses must be determined. These cannot be measured directly, and must be inferred from a star's luminosity. To do this, the relation between stellar mass, age and luminosity must be well understood. This is known as the mass-luminosity relation, and also depends on the star's metallicity and its speed of rotation (e.g. Kroupa, 2002). This mass-luminosity relation must also account for unresolved binary companions. The inferred mass function (which is known as the present-day mass function – PDMF) must then be corrected for stars that have evolved off the main sequence.

The first estimate of the IMF was published by Salpeter (1955), who found that between 0.4 and 10 $M_\odot$, the solar neighbourhood IMF $\zeta(\log m)$ is a power-law

with the form $\zeta(\log m) \propto m^{-1.35}$. Since that seminal research, the IMF has been measured for a variety of different environments, and the range of masses has been extended by an order of magnitude in each direction. However no-one has yet disproved Salpeter's original result.

The high mass side of the IMF has been shown to be consistent with the Salpeter slope up to the most massive stars ($m \sim 120$ $M_\odot$ — Massey, 1998). However, these surveys are by necessity, of more distant regions, and often do not account for the binary fraction. The true IMF may therefore be steeper than the measured value (Kroupa, 2001a). The scatter in the measurements of the IMF slope in this mass range is quite large with a 1σ error of ~ 0.7. This could indicate either an inherent variation in the IMF, or simply the level of accuracy of the observational techniques.

For lower mass stars, the mass function does not continue to rise with the same slope. Between ~ 0.08 and ~ 0.5 $M_\odot$, the slope of the IMF is -0.3 ± 0.5 (Kroupa, 2001b). These surveys are generally limited to nearby stars, and therefore the binary fraction is accounted for. At masses below ~ 0.08 $M_\odot$, the IMF appears to turn over, with a slope of approximately 0.5 (Luhman & Rieke, 1999; Najita, Tiede, & Carr, 2000; Martín et al., 2000)

A great deal of effort has recently been put into determining whether or not the IMF is universal. There is some evidence that exotic regions have top-heavy IMFs, for example the starburst galaxy NGC 3603 has a mass function with a slope of -1.7 above 3 $M_\odot$ (Eisenhauer et al., 1998). However, most of these exotic regions are difficult to observe. In more typical environments, there is no significant difference in the IMFs measured for the local neighbourhood, more distant open clusters, or very old globular clusters. There is an indication that the position of

the peak of the IMF may depend weakly on metallicity, but this is by no means proven (Chabrier, 2003).

The origin of the IMF is still very much an open question, although it is clearly determined at the star formation stage. It has been suggested that it originates in the manner in which a cloud fragments (e.g. Chabrier, 2003). Alternative suggestions are that the final mass of each star is determined by dynamical effects such as competitive accretion (e.g. Bonnell et al., 2001) or accretion being stopped by outflows from the young star (e.g. Shu, Adams, & Lizano, 1987; Velusamy & Langer, 1998). Another explanation is that the final mass depends simply on the reservoir of gas available to the accreting protostar (e.g. Bacmann et al., 2000).

Motte et al. (1998) measured the mass spectrum of prestellar cores in the ρ Ophiuchi molecular cloud, and found that the core mass spectrum resembled the stellar IMF. This indicates that the IMF is determined by the fragmentation of the cloud, and not by other effects such as competitive accretion or dynamical feedback. However, using smoothed particle hydrodynamics (SPH) simulations, Goodwin, Whitworth, & Ward-Thompson (2004) have shown that the IMF in the Taurus molecular cloud can be explained by convolving the core mass spectrum with the mass spectrum of stars that are formed in each core. The latter mass spectrum is dominated by effects such as competitive accretion and dynamical ejection. These two results are not necessarily incompatible, as it has already been shown in Section 1.2.3 that the two star-forming regions are very different.

In Chapter 5, I measure the core mass spectrum for prestellar cores in the Orion B molecular cloud, and compare the result to the IMF, and to previously measured core mass functions for that region.

1.8 Summary and Thesis Overview

In this chapter, I have discussed our current understanding of the star formation process. I have described the observed characteristics of prestellar cores and protostars, and discussed how these observations have increased our knowledge of star formation. I have given an overview of the competing theories that try to explain how and why stars form with the properties that we observe.

I have explained the different methods that can be employed to measure the interstellar magnetic field. The technique used in this thesis to measure the masses of prestellar cores and protostellar envelopes has been explained. Finally I have introduced the stellar initial mass function, and described the different possible underlying causes.

In Chapter 2, I describe the instrumentation and data reduction techniques used in the final three chapters. In Chapter 3, I discuss the polarimetry data of three prestellar cores, L1544, L43 and L183. I use the Chandrasekhar-Fermi technique to determine the magnetic field strength in these cores, and compare this with the predictions of different models.

I introduce large area submillimetre maps of three molecular clouds, Orion B, L1689 and RCrA in Chapter 4. I describe the data reduction methods used for each region. I also discuss the source extraction techniques that were used to determine the flux density of each source in the maps.

The submillimetre scan-maps are analysed in Chapter 5. A comparison with the literature data for each of the regions is conducted, and the nature of each source ascertained. The core mass function for the Orion B data is calculated

and compared with the IMF and other submillimetre maps of the region. The clustering of the sources in Orion B is also investigated and compared to the way in which young stars are observed to be clustered.

The current star formation activity in the L1689 molecular cloud is compared to that in the neighbouring and more massive cloud L1688. The RCrA map is analysed and a new Class 0 protostar is identified.

The results of the thesis are summarised in Chapter 6, and the final conclusions are presented.

Chapter 2

Data Acquisition and Reduction

In this Chapter, I discuss the telescope and instrumentation used to obtain the data analysed in Chapters 3, 4 and 5. I also describe the standard data reduction routines, and introduce some new techniques for reducing noise in the data.

2.1 Instrumentation

The data described in this thesis are in the submillimetre wavelength range. At these wavelengths, the atmosphere is effectively opaque due to attenuation by water vapour. However, at very high, dry sites, atmospheric windows open at some frequencies and allow up to 80% transmission in good conditions. One such site is the summit of Mauna Kea, an extinct volcano in Hawaii. The atmospheric transmission as a function of wavelength for Mauna Kea is given in Figure 2.1 (Holland et al., 1999). This graph represents the transmission through a precipitable water vapour content of 1 mm, typical of good conditions at the site.

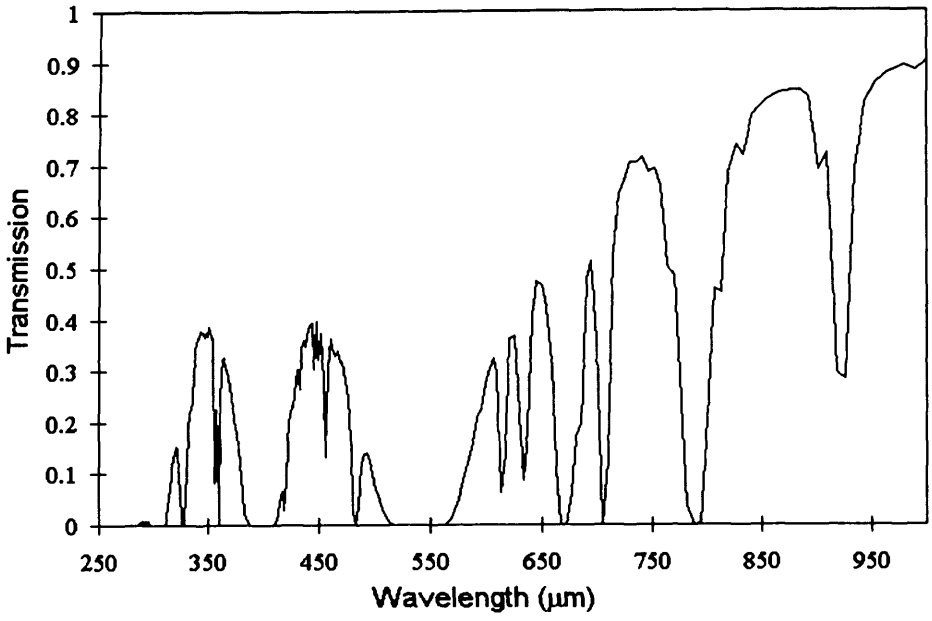

Figure 2.1: The transmission of the atmosphere as a function of wavelength in the submillimetre range (Holland et al., 1999).

2.1.1 The James Clerk Maxwell Telescope

The summit of Mauna Kea is the location of the James Clerk Maxwell Telescope (JCMT), the world's largest telescope dedicated to submillimetre astronomy (Phillips, 2002). At an altitude of 4092 m, it is above 97% of the atmospheric water vapour. It operates in the wavelength range of 200 μm to 2 mm. The primary mirror has a diameter of 15 m, giving diffraction limited resolutions of $\sim 7''$ and $\sim 14''$ at the principal operating wavelengths of 450 and 850 μm. The JCMT is a Cassegrain/Nasmyth telescope on an Altitude-Azimuth mount with a rotating tertiary mirror to direct the beam to the different instruments. There are two types of instruments, heterodyne receivers for measuring spectral line emission from molecular species, and SCUBA (Submillimetre Common User Bolometer Array), a continuum camera primarily used for mapping the thermal emission from interstellar and circumstellar dust. Both types of instrument feature additional

hardware for measuring the polarisation state of the incoming radiation. Each heterodyne receiver is optimised for a different atmospheric window, while SCUBA contains filters which allows use in all of the main windows. The JCMT is funded by the UK (55%), Canada (25%) and the Netherlands (20%), and is managed by the Joint Astronomy Centre (JAC) based in Hilo, Hawaii.

2.1.2 SCUBA

SCUBA is composed of two bolometer arrays, and is mounted on the left-hand Nasmyth focus (Holland et al., 1999). It can be used for photometry, deep imaging or wide-field mapping. The principal emitter of submillimetre radiation is cold dust (below 30 K), therefore the majority of objects studied with SCUBA are seen through their dust component. These include objects at different stages of the star-formation process, from prestellar cores (Ward-Thompson et al., 1994) and protostars (André et al., 1993) to the protoplanetary disks around young stars (Holland et al., 1998). Further afield in distant galaxies, starlight is processed by dust and re-emitted in the far-IR and submillimetre wavelength range (Eales et al., 1999). In some heavily obscured starburst galaxies, very little optical light escapes, and submillimetre surveys are currently the only way to detect them (Cowie, 2003). This wavelength range is therefore crucial for the study of galaxy formation and evolution (e.g. Webb et al., 2003). SCUBA is also changing the perceived view about the origins of dust from a stellar wind dominated picture, to one in which supernovae play an important role (Dunne et al., 2003).

A bolometer is the most sensitive type of broadband detector in the submillimetre wavelength range. It determines the energy input by measuring the increase in temperature caused by incoming photons (Holland, Duncan, & Griffin, 2002).

The basic design has an absorber of specific heat capacity C, in thermal contact with a fixed temperature heat sink. Incident energy (E) causes the temperature of the absorber to rise by:

$$\Delta T = \frac{E}{C}. \tag{2.1}$$

The temperature change causes the resistance and therefore the voltage across the device to change.

The bolometers are arranged in two hexagonal close-packed arrays, which are termed the long wave (LW) and short wave (SW) arrays. These arrays are illustrated in Figure 2.2 (Holland et al., 1999). The feedhorns of each array are designed such that the LW and SW arrays are optimised for use at 850 μm and 450 μm respectively. Both arrays have approximately the same field of view of diameter 2.3′ (the SW array is slightly smaller), and can be used simultaneously with the use of a dichroic beam splitter. There are also three bolometers that allow single pixel photometry at the longer wavelengths of 1.1, 1.3 and 2 mm.

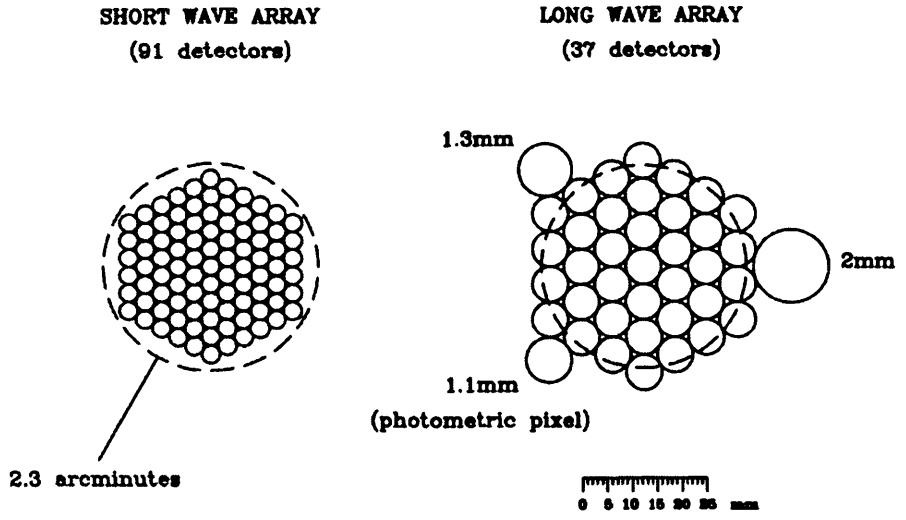

Figure 2.2: The bolometer arrangement of SCUBA, showing the SW and LW arrays, and the 3 photometric pixels. The 2.3′ LW field of view is overlaid on both arrays (Holland et al., 1999).

Each bolometer is significantly smaller than the diffraction spot of the incoming radiation, therefore the bolometers are coupled to the incoming beam using conical feedhorns (Holland et al., 2002). For maximum efficiency, the feedhorns have a diameter of $2F\lambda$, where λ is the wavelength of the incoming radiation, and F is the focal ratio of the optics. This causes the image plane to be under-sampled by a factor of 16. 16 telescope pointings are therefore needed to create a fully sampled image. This is achieved by jiggling the telescope secondary mirror or rastering the array, both of which are explained in detail in Section 2.3.

2.1.3 Sensitivity

The sensitivity of a bolometer is given by its noise equivalent power (NEP), which is the power absorbed that produces a signal to noise ratio of unity (Holland et al., 2002). The NEP is limited by the photon noise from the sky, and the intrinsic properties of the bolometer. The intrinsic NEP is caused by Johnson noise (the random fluctuations in the bolometer) and phonon noise (the quantisation of the phonons that transport energy to the bolometer's heat sink).

In order to maximise the sensitivity of the bolometers, the two intrinsic contributions are made as small as possible. Phonon noise is proportional to T, the temperature of the bolometer, and Johnson noise is proportional to $T^{\frac{1}{2}}$, so cooling the detectors to very low temperatures is crucial to achieve background limited sensitivity. To this end, the bolometers are cooled to 100 mK using a dilution refrigerator housed in a liquid helium dewar at a temperature of 4 K.

As a result of the large bandwidth employed by bolometer detectors, the sensitivity is degraded due to background power loading, which heats the bolometer.

This can be minimised by increasing the thermal conductance (G) between the absorber and the heat sink, which has the added effect of reducing the response time ($\tau_r = C/G$). However this has the effect of increasing NEP_{phonon}, so a compromise must be reached. The total NEP is therefore given by:

$$NEP^2_{total} = NEP^2_{photon} + NEP^2_{johnson} + NEP^2_{phonon} + NEP^2_{loading}. \quad (2.2)$$

The actual sensitivity achieved when making astronomical observations is given by the NEFD (noise equivalent flux density), which is the flux density that produces a signal to noise of unity in one second of integration, and is given by:

$$NEFD = \frac{NEP}{\eta_c \eta_t A_e \Delta v e^{-\tau A}} \quad (2.3)$$

where η_c is the chopping efficiency, η_t is the telescope efficiency, A_e is the collecting area, Δv is the bandwidth of the filter and $e^{-\tau A}$ is the atmospheric transmission at airmass A. Achieving this NEFD requires that the sky noise (caused by fluctuations in emission by the atmosphere — see Sections 2.2 and 2.4.6) be completely removed.

2.1.4 The SCUBA Polarimeter

In order to measure the polarisation state of the incoming radiation, the UK-Japan polarimeter is placed in the SCUBA beam. The design of the polarimeter is shown schematically in Figure 2.3, and is based on a rotating half-waveplate in front of a fixed analyser. The waveplate is composed of birefringent quartz of a thickness that retards the component of the radiation perpendicular to the waveplate axis by 180° (Greaves et al., 2003). The net effect on the radiation passing through the waveplate is to mirror the polarisation direction about the waveplate axis. As a

result of this, as the waveplate rotates, the angle of polarisation seen by the analyser rotates at twice the rotation rate of the waveplate (Berry & Gledhill, 2001). The analyser is composed of 10 μm etched copper on a mylar substrate, which transmits one component of the radiation and reflects the other. The SCUBA bolometers therefore detect a signal modulated by a sine wave. The technique used to determine the polarisation state of the incoming radiation is described in Section 2.5.

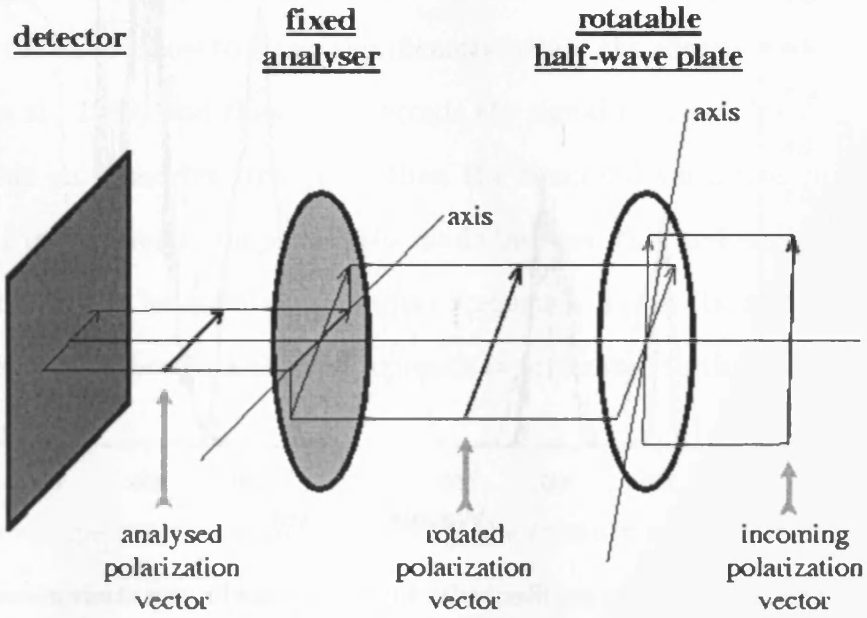

Figure 2.3: Schematic of the JCMT polarimeter (Berry & Gledhill, 2001).

2.2 The Submillimetre Atmosphere

The observable wavelengths are determined by the atmospheric transmission windows at 850, 750, 600, 450 and 350 μm as illustrated in Figure 2.1. There is also a small window at 200 μm that opens under extremely good conditions (Walker

et al., 2003). A rotating drum of bandpass filters designed to match these windows allows different wavelengths to be selected. As both the LW and SW arrays can be used simultaneously, the windows can be accessed in pairs, allowing observations at 850/450 μm or 750/350 μm. The frequency response of the filters normalised to the atmospheric transmission in each window is shown in Figure 2.4, overlaid on the atmospheric transmission profiles.

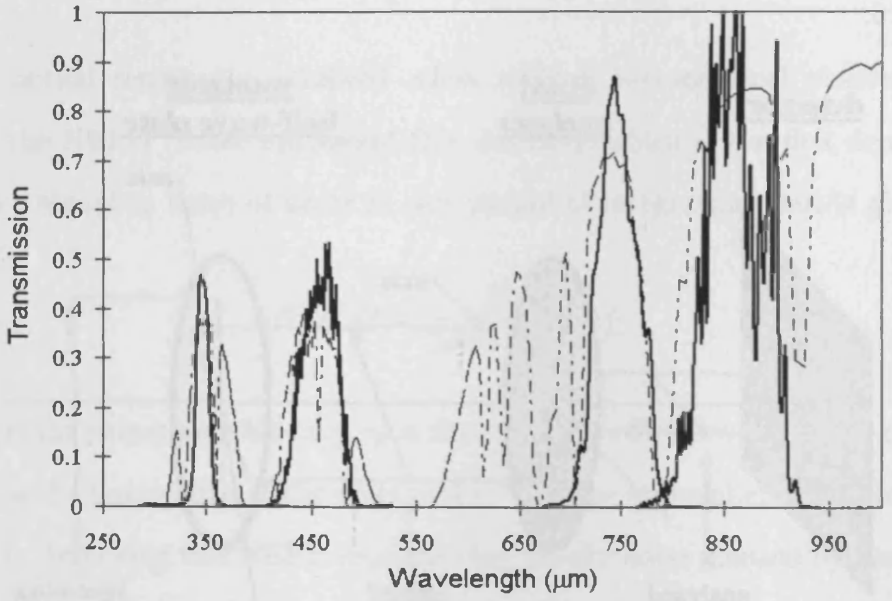

Figure 2.4: The SCUBA filter profiles (solid lines) overlaid on the atmospheric transmission profile (dashed line). Each filter has been scaled arbitrarily to match the atmospheric window (Holland et al., 1999).

As well as attenuating submillimetre radiation, the atmosphere emits thermal radiation at these wavelengths. This sky emission generally has an intensity that is many orders of magnitude greater than the astronomical radiation being studied, and has large spatial and temporal variations. The standard way to remove sky emission in infrared and submillimetre astronomy is to chop and nod the telescope (e.g. Glass, 1972; Papoular, 1983). Chopping is done by oscillating the secondary

mirror in a square wave pattern to place the array alternately on the source and a nearby area of blank sky. The sky emission can then be largely removed by subtracting the 'sky' beam from the 'source' beam, so long as the sky emission is correlated across both beams. For this to be successful, the distance between the two beams (the chop throw) should be as small as possible.

For photometry of point sources, a chop throw of 30 - 40″ is recommended, although when mapping sources larger than this, a larger chop throw is required. Increasing the chop throw to 2′ can significantly reduce the effectiveness of chopping (Holland et al., 1999) and therefore degrade the signal to noise. Ideally, chopping should occur on a shorter time-scale than the temporal variations in the atmosphere, but in practice a compromise is made between this and engineering issues such as reliability. The standard chopping frequency is $\sim$ 8 Hz, and can be made in any direction, although a chop in azimuth is preferable so that both beams see the same airmass.

The telescope is also nodded by moving the primary mirror such that the sky beam becomes the source beam, and the source beam sees a new area of sky, on the opposite side of the source. The reason for this is primarily to remove any asymmetries between the two beams and linear gradients in sky emission, as well as to compensate for differences in path length. The primary mirror is nodded at a rate of $\sim$ 0.1 Hz.

This technique of chopping and nodding removes the majority of the sky noise, but some residual noise is generally still present due to differences in atmospheric emission in the two beams. This noise should be correlated across the arrays and can therefore be removed with post-observation data processing (see Section 2.4.6).

2.3 Observing Modes

2.3.1 Photometry

The standard observing mode for point sources is photometry mode. Photometry observations can be made using both arrays simultaneously or any of the three longer wavelength pixels individually. Chopping and nodding are employed to remove sky noise from the signal as described in the previous section. When using the arrays, the residual sky noise is removed by subtracting a sky signal calculated using the off-source bolometers.

2.3.2 Jiggle-mapping

Jiggle-mapping is generally used for mapping extended sources that are smaller than the field of view, though can also be used for surveying larger fields (Eales et al., 2000). The technique is called jiggle-mapping because the arrays are moved relative to the beam by jiggling the secondary mirror in order to fully sample the arrays.

The jiggle pattern used depends on the wavelengths being observed. If a single array is being used (generally the LW array), a 16 point jiggle pattern is required — shown in Figure 2.5(a). This gives Nyquist sampling of the array ($\sim 6''$ for the LW array and $\sim 3''$ for the SW array). If both arrays are used, a 64 point jiggle pattern is needed to simultaneously sample the space between the LW bolometers and still achieve Nyquist sampling of the SW array — see Figure 2.5(b).

The arrays are sampled at a rate of 128 Hz, though data are only recorded

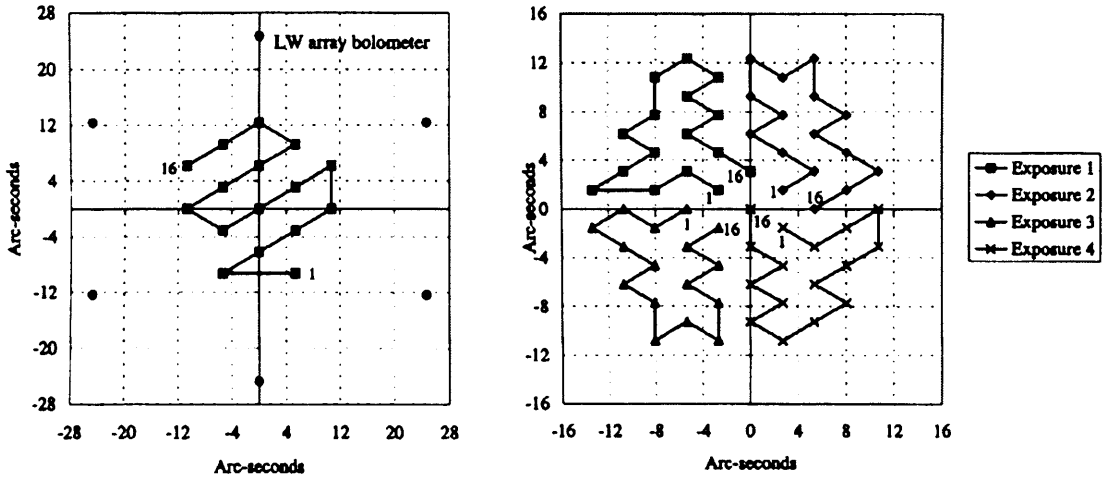

Figure 2.5: (a) & (b). The jiggle patterns required to fully sample (a) a single array (16 point jiggle), or (b) both arrays (64 point jiggle) (Holland et al., 1999).

every one second. The variance of these 128 points is calculated and recorded as a measure of the quality of the observation. Each position in the jiggle pattern is given one second of integration, half of which is off-source as a result of the chopping. The telescope is then nodded and the pattern repeated with a new off-source position (see Section 2.2). The 16 and 64 point jiggle-maps therefore take 32 and 128 seconds respectively plus overheads to complete. A 64 point jiggle-map is split up into four exposures, each executed in the same way as a 16 point jiggle-map. The reason for this is that nodding after the complete 64 point jiggle pattern is too infrequent to effectively cancel the beam asymmetry.

The time taken to achieve a signal to noise ratio of σ is given by:

$$t = 16\left[\frac{NEFD\sigma}{F}\right]^2, \tag{2.4}$$

where F is the flux density of the source (Matthews, 2003). The factor of 16 is introduced because each pixel is only sampled for $1/16^{\text{th}}$ of the time due to the jiggle pattern. This equation holds for the 64-point jiggle-map because both the

sampling density and the time taken are higher by a factor of four.

2.3.3 Scan-mapping

The scan-mapping technique is used for mapping sources that are larger than the field of view of the instrument. The array is rastered across the sky, forming a strip, which is several arc-minutes long and the width of the array. The rectangular scan-map is completed by making additional strips. The length of one scan is limited to $20'$ by the data acquisition hardware, although the maximum size of the scan-map is approximately $10' \times 10'$ as the scans are generally at an angle to the map. This is illustrated in Figure 2.6.

Nyquist sampling in the direction perpendicular to the scan direction is achieved for both arrays by scanning the array at an angle of $15.5° + N \times 60°$ to the hexagonal array, where $N = 0 \rightarrow 5$. Figure 2.7 illustrates how scanning at these angles allows the space between neighbouring bolometers to be sampled. Along the scan direction, the sampling is governed by the scanning rate. A rate of $24'' \, s^{-1}$ together with a data acquisition rate $\sim$ 8 Hz yield a sample spacing of $\sim 3''$, which fully samples both arrays. It is possible to increase the scanning rate and so make larger maps, although this causes the SW array to be under-sampled.

The time taken to obtain a signal to noise ratio of σ for a source of flux density F is given by:

$$t = \frac{(x + L)W}{d^2 N} \left[\frac{NEFD\sigma}{F}\right]^2 \tag{2.5}$$

where L and W are the length and width of the scan-map, d is the sample spacing and N is the number of bolometers (Matthews, 2003). x is a small amount that is added to each scan length to allow for overlap with neighbouring scan-maps, and

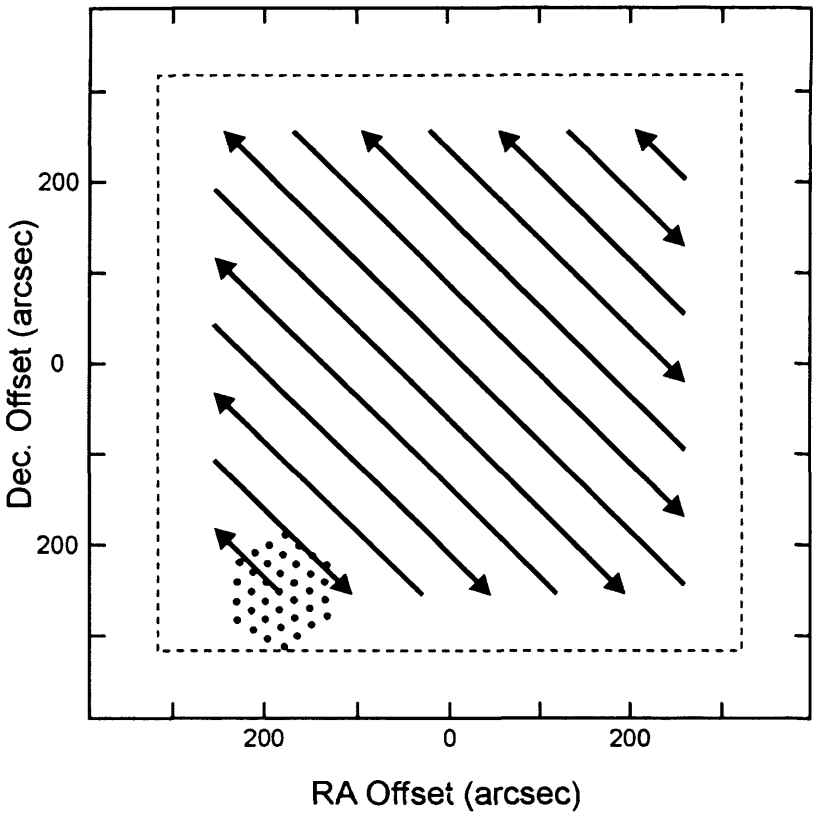

Figure 2.6: Diagram of a scan-map. The dashed line shows the extent of the scan-map. The footprint of the array is shown at the lower left hand corner. The arrows show the path traced by the centre of the array.

is usually equal to the size of the array. The first term in Equation 2.5 gives the fraction of time that any one pixel is being observed for, which is the number of pixels in the map divided by the number of bolometers.

Two position chopping at a rate of $\sim$ 8 Hz is employed to remove sky emission. The large angular size of the map and the limitation on the size of the chop throw, means that it is not possible to chop onto an area outside the map. A small chop throw ($< 1'$) is therefore used as this removes the sky contribution most efficiently.

The disadvantage of chopping onto a different area of the image, is that each source appears as positive and negative signal in the map. the positive signal is

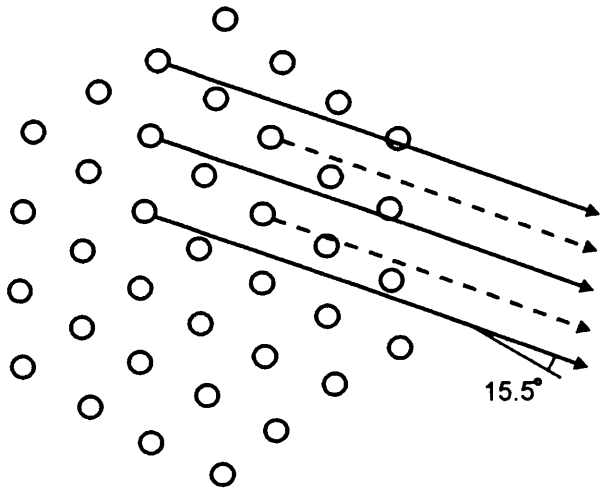

Figure 2.7: Schematic of the LW array illustrating how specific scan directions allow the array to be fully sampled.

seen when the 'source' beam passes over the source, while the negative signal is caused by the 'sky' beam passing over it. The positive and negative sources are separated by the chop throw. This is known as a dual-beam or differential map and is illustrated in Figure 2.8.

This method of observation is effectively convolving the astronomical signal with a dual beam function. In the limit of infinite telescope resolution, this function comprises a positive and negative δ function separated by x_0, the chop throw, — illustrated in 1D in Figure 2.9(a). Realistically the δ function is convolved with the telescope beam, which can be approximated to a Gaussian — see Figure 2.9(b).

Convolution theory states that the Fourier transform ($\mathcal{FT}$) of a convolution of two functions, is equal to the product of the $\mathcal{FT}$s of the two functions (see Appendix A). Therefore dividing the image by the dual beam function in Fourier space should deconvolve the dual beam function, and reconstruct the image.

In one dimension, the dual δ function $d(x)$, and its Fourier transform $D(k)$

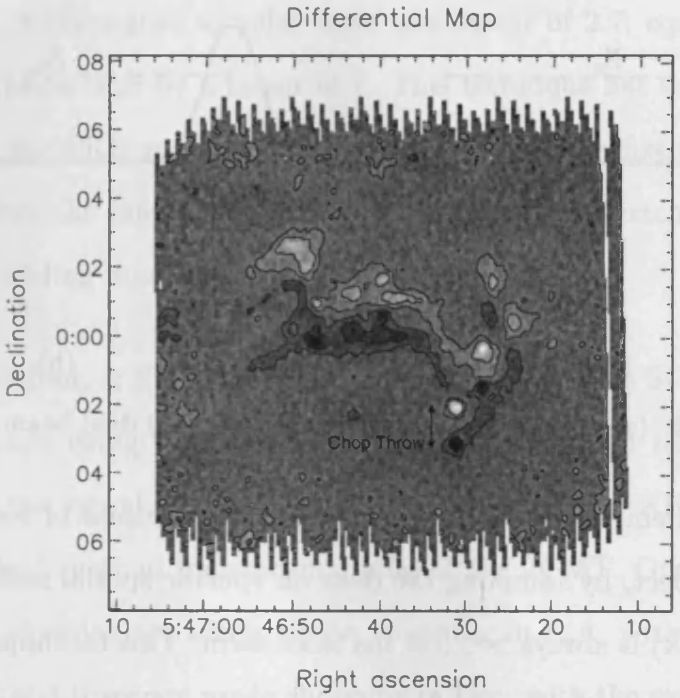

Figure 2.8: An example of a differential map.

are given by:

$$d(x) = \delta(x + \frac{x_0}{2}) - \delta(x - \frac{x_0}{2}), \tag{2.6}$$

$$\begin{aligned} D(k) &= \int_{-\infty}^{\infty} \delta(x + \frac{x_0}{2}) e^{-2\pi i k x} - \delta(x - \frac{x_0}{2}) e^{-2\pi i k x} dx, \\ &= e^{2\pi i k (x_0/2)} - e^{-2\pi i k (x_0/2)}, \\ &= 2i \sin(\pi k x_0). \end{aligned} \tag{2.7}$$

However, dividing the $\mathcal{FT}$ of the image by this function will amplify the noise in the image on spatial frequencies of the inverse chop throw and its harmonics, i.e.:

$$k = 0, \frac{\pm n}{x_0}, \tag{2.8}$$

where n is any integer.

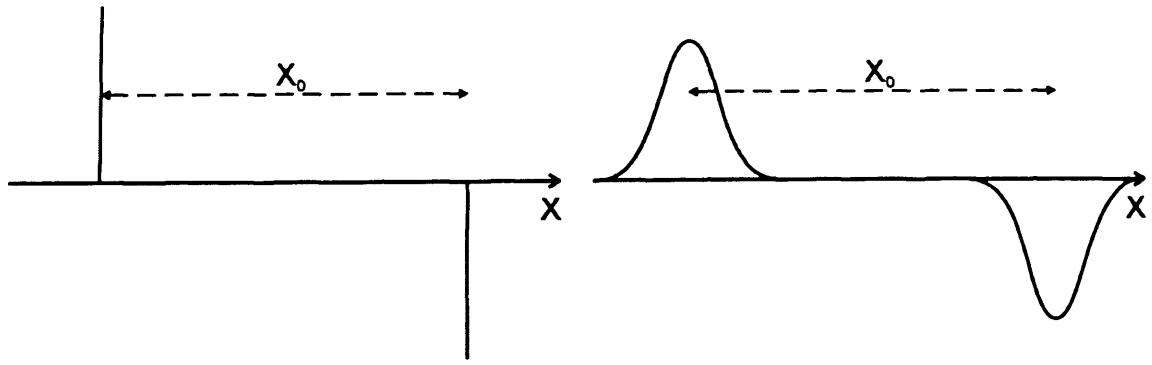

(a) (b)

Figure 2.9: (a) & (b). (a) Dual δ function, and (b) dual beam function.

Emerson, Klein, & Haslam (1979) proposed a method of reducing the magnitude of this effect, by sampling the data on specific spatial scales such that the amplitude of $D(k)$ is always $> 0.5 \times$ the maximum. This technique (known as the EKH method) was initially used for scan-maps, though it has several drawbacks. The technique involves chopping in the direction of the scan, which must be in azimuth to provide the optimal sky cancellation. Each scan must then be restored individually. It is necessary for every object in the scan to appear in both the positive and negative beams, or an error will be propagated along the scan. The scan must therefore extend completely off any extended sources. The requirement that the scan be made in azimuth, together with sky rotation means that a scan cannot be extended at a later time.

Emerson (1995) suggested an alternative technique of reconstructing multiple beam data. It involves making four maps, two of which are made chopping in one direction with two chop throws, and two in the orthogonal direction with the same two chop throws. Each map has its dual beam function deconvolved as described above. The maps are then combined in Fourier space, weighting each spatial frequency by a^2, where a is the amplitude of $D(k)$.

Emerson showed that for simulated data, this method of observation provides

an improvement in the signal to noise ratio of a factor of 2.7, equivalent to a reduction in integration time by a factor of 7. This technique has several additional advantages over the EKH method. The chop directions are fixed in celestial coordinates, therefore the mapped region of sky can easily be extended or the map made deeper by adding more maps before the reconstruction.

Jenness, Lightfoot, & Holland (1998) used the method with SCUBA and found that the map made using the new 'Emerson II' method did have a significant improvement in the signal to noise ratio, compared to the EKH method. This is now the standard method for scan-mapping at the JCMT. Generally six maps are made, three of which are made whilst chopping in R.A. with chop throws of 20″ ,30″ and 65″ , and three are made chopping in Dec. with the same chop throws. An alternative set of chop throws are 30″ , 44″ and 68″ . These sets of chop throw are chosen because the harmonics of the inverse chop throws (i.e. the spatial frequencies for which $D(k) = 0$) do not coincide.

2.3.4 Polarimetry

Polarimetric data can be taken using each of the three observing modes, though only the jiggle-map and photometry polarimetry modes are currently fully commissioned. In each case, 16 standard observations are made, rotating the waveplate by 22.5° between each. This allows the polarisation parameters to be calculated as described in Section 2.5. Polarimetry observations are strongly dependent on the stability of the atmosphere over the time taken to complete the observation (see Section 2.5.5). Polarimetric jiggle-mapping is therefore generally carried out with a 16 point jiggle-map as opposed to the 64 position pattern, which takes four times longer to complete. Also, the instrumental polarisation has not been fully

characterised for the SW array, so the 64 point pattern is not required.

The time taken to achieve a signal to noise σ in the percentage polarisation is similar to Equation 2.4, and is given by the following equation (Greaves et al., 2003):

$$t = \frac{4}{\eta} \times 16 \left[\frac{NEFD\sigma}{pF}\right]^2, \tag{2.9}$$

where η is the transmission of the waveplate and p is the percentage polarisation. The additional factor of four is included because four waveplate positions are needed to completely characterise the polarisation as discussed in Section 2.5.1. Half the photons received by the telescope are reflected by the analyser, though the effect this has on the integration time is cancelled by the noise in the polarisation percentage being $1/\sqrt{2}$ that of a single intensity observation.

2.4 Data Reduction

The technique used for reducing the data made with using the different observing modes is very similar, and is carried out using the SCUBA Users Reduction Facility (SURF — Jenness & Lightfoot, 2000). Polarimetric jiggle-map data are reduced using the same method as for standard jiggle-maps, with the addition of the instrumental polarisation step 2.4.3. Additional steps after the reduction are required to extract the polarisation parameters, and are described in Section 2.5.3

Scan-map data are reduced in a similar manner. The method for removing correlated sky-noise differs (Section 2.4.6), and additional steps are required to remove baselines (Section 2.4.5), and to deconvolve the dual beam function whilst combining maps made with different chop configurations (Section 2.4.8).

2.4.1 Reduce Switch and Flatfield

The SURF routine REDUCE_SWITCH is used to subtract the 'sky' beam from the 'source' beam, thereby eliminating the majority of the sky emission. For jiggle-maps, the 'sky' beams should not contain any astronomical flux, therefore after this subtraction, the data should be wholly positive, and contain only residual sky noise that can be removed later (see Section 2.4.6). In scan-map data however, each object gives rise to a positive and negative image, as the 'source' and 'sky' beams respectively are scanned across it. After this routine has been run, and for the majority of the reduction (up to the regrid stage — see Section 2.4.7) the data are in the form of a time-series for each bolometer. Flatfielding is carried out to correct for fixed differences between the different bolometers.

2.4.2 Atmospheric Extinction

Radiation is attenuated as it passes through the atmosphere according to Beer's law:

$$I = I_0 e^{-\tau \sec z}, \tag{2.10}$$

where I is the measured intensity, I_0 is the intensity incident at the top of the atmosphere, τ is the optical depth of the atmosphere, and z is the zenith angle. τ can be determined by measuring I at a range of elevations and plotting $\ln I$ against airmass ($\sec z$) to yield a gradient of $-\tau$. However, this requires making observations of an object over the course of several hours and also assumes a very stable atmosphere, a condition that is almost certainly not held.

Skydips estimate the zenith optical depth much more quickly by measuring the emission from the sky as a function of elevation. This emission can be characterised

by a brightness temperature (J_{meas}), which is the temperature of a blackbody that emits at the same intensity as that measured. J_{meas} is composed of two components, arising from the sky and the telescope itself, which are described by different temperatures, J_{sky} and J_{tel} respectively (Hazell, 1991):

$$J_{meas} = (1 - \eta)J_{tel} + \eta J_{atm}(1 - e^{-\tau A}), \tag{2.11}$$

where η is the efficiency of the telescope and A is the airmass. This picture is complicated by τ not being constant across the filter's passband and requires the addition of a 'bandwidth factor' (b), where $1 - b$ is the fraction of the filter bandwidth that is opaque due to atmospheric absorption. Hence Equation 2.11 becomes:

$$J_{meas} = (1 - \eta)J_{tel} + \eta J_{atm}(1 - be^{-\tau A}). \tag{2.12}$$

Fitting the data to Equation 2.12 allows τ to be calculated. The advantage of a skydip is that the optical depth is measured at the same azimuth and wavelength as the observations. However, the overheads involved preclude carrying out a skydip more than every one to two hours.

The nearby Caltech Submillimeter Observatory (CSO) has a tipping radiometer that takes a skydip every ten minutes. It operates at 225 GHz (1.25 mm) and measures the optical depth at a fixed azimuth. The records of τ measured at 850 and 450 μm and 225 GHz over a number of years have allowed the formulation of empirical relations between τ_{225}, τ_{850} and τ_{450} (Archibald et al., 2002). These relations are presented in Table 2.1. The two filter sets correspond to the original filters (450N:850N), and the wider bandwidth filters (450W:850W) installed in December 1999.

Table 2.1: The empirical relations between τ_{225}, τ_{850} and τ_{450}, for both narrow and wide bandwidth filters (Archibald et al., 2002).

	$\tau_Y = a(\tau_X - b)$			
Filters	τ_Y	τ_X	a	b
450N:850N	τ_{850}	τ_{225}	3.99 ± 0.02	0.004 ± 0.001
	τ_{450}	τ_{225}	23.5 ± 0.2	0.012 ± 0.001
	τ_{450}	τ_{850}	5.92 ± 0.04	0.032 ± 0.002
450W:850W	τ_{850}	τ_{225}	4.02 ± 0.03	0.001 ± 0.001
	τ_{450}	τ_{225}	26.2 ± 0.3	0.014 ± 0.001
	τ_{450}	τ_{850}	6.52 ± 0.08	0.049 ± 0.004

The scatter in individual measurements taken with the CSO radiometer is high, though a polynomial fit to the data gives the longer time-scale trends that have been shown to agree with optical depths determined using the JCMT skydips. The CSO τ data can therefore be used to track changes in the optical depth that are missed by the more infrequent JCMT skydips.

A recent addition to the range of techniques used to track the atmospheric opacity, is the JCMT radiometer. The emission from an atmospheric water line of wavelength 1.6 mm is measured, and the water vapour content is estimated by modelling the line shape. The radiometer is installed in the receiver cabin and takes data from the main beam, therefore the optical depth is estimated along the line of sight. Data are collected every 6 seconds, allowing the stability of the atmosphere to be monitored on a much shorter time-scale than is possible with skydips or the CSO radiometer.

When the atmospheric opacity is known, the SURF routine EXTINCTION is used to apply a correction factor to the data, so that it represents the flux density received above the atmosphere.

2.4.3 Instrumental Polarisation

The polarisation measured by SCUBA is affected by an instrumental polarisation IP, which arises from the optics and the Gore-Tex membrane that protects the antenna (Greaves, 1999). The IP has been measured for each of the LW array bolometers by observing the emission from planets that is assumed to be unpolarised at these wavelengths. Initially, Saturn was used, though observations of Uranus and Mars have produced consistent results (Greaves, 2000). The IP is elevation dependent, with both the IP angle and percentage scaling linearly with elevation.

To remove the effects of the IP, an intensity is subtracted from that recorded by each bolometer. The intensity to be subtracted is calculated from a knowledge of the IP for that bolometer, the elevation of the source, and the waveplate angle.

2.4.4 Removal of Spikes and Noisy Bolometers

Some bolometers in the array are considerably more noisy than others. It is generally recommended that the entire time-series from these bolometers is removed, even though their contribution to the final map is given a low weight due to the high standard deviation of the data. This process can be labourious because frequently, when viewing the data, only one bolometer is obviously 'bad', even though there may be three or four bolometers that need removing. This is a result of the dynamic range of the image being dominated by the noisiest bolometer. Selecting and removing the noisy bolometers can be automated to some degree, for example by calculating the standard deviation of the data recorded by each bolometer. However the results should be checked manually as bright sources in the data will

also increase the apparent standard deviation.

As well as removing all data taken with the noisy bolometers, there are numerous spikes that must be removed. Spikes that occur on a fast time scale compared with the 128 Hz data acquisition rate, are removed by the SCUBA transputers before the data are recorded. Spikes that last longer are not detected in this manner, and must be removed in the data reduction. There are a number of routines provided for despiking (Jenness & Lightfoot, 2000). In all cases, the level of clipping (N) can be specified by the user.

The SURF routines SIGCLIP and SCUCLIP clip any data further from the mean than N sigma. In the case of sigclip, the statistics are calculated from the entire observation, therefore the data will tend to be clipped from the inherently noisier bolometers. Scuclip however calculates statistics for each bolometer in turn. In both cases, each time a spike is removed, the statistics are recalculated and the process iterated. For data with only weak sources, scuclip can be used quite effectively. However, bright sources such as planets can be falsely identified as spikes and removed. When reducing jiggle-map data, the bright sources can be temporarily blanked while performing the clip, but the nature of scan-map observations does not allow this.

The DESPIKE routine regrids the data on to a rectangular grid representing the true sky positions of each data point. The data are partitioned into cells, and despiked by clipping any data points that are more than N sigma from the mean in that cell. This routine is more reliable near bright sources, as the source itself is less likely to be clipped.

The DESPIKE2 routine is used for scan-map data and compares each point

to the previous and subsequent data-points along the scan. The data are flagged if this difference is greater than N sigma from the mean difference. In order to confirm the detection of a spike, the data are smoothed along the scan direction and the process repeated for the flagged data. A spike will behave differently from a real source, as the increase in signal is localised to a single data point.

2.4.5 Baseline Removal

This stage is only required from reducing scan-map data. This is because scan-map observations involve 2-position chopping, in which one beam is always 'on' and the other is always 'off'. This is different from the photometry and jiggle-map observations, where the 'on' and 'off' beams are switched around by the nod. If there is a net difference in the sky emission between the two beams, there will be a DC offset in the signal, which must be removed.

With the EKH method of scanning, this offset is not a problem, as the telescope is usually chopped in azimuth, which causes the least differential emission. Also the telescope is chopped along the scan, so all sources in the scan should be detected in both the positive and negative beams. The average signal along the scan should therefore be zero, and any difference from this is corrected automatically.

When using the Emerson II technique however, chopping is carried out in celestial coordinates. This causes the two beams to see a different airmass, therefore there is likely to be some degree of differential emission. In addition, each individual scan need not have a mean of zero, because a bright source may only appear in one of the two beams. Therefore the scan cannot necessarily have its mean subtracted to account for the offset.

Figure 2.10 shows the first 500 measurements taken with the LW bolometers 1–20, both before and after the baseline removal (Figures 2.10(a) and 2.10(b) respectively). The removed baseline is shown in Figure 2.10(c). The grey scale indicates the voltage recorded by the bolometer for each measurement. The ends of each scan are shown as white horizontal lines. It is clear that the DC offset between the different bolometers has been largely eliminated by the operation.

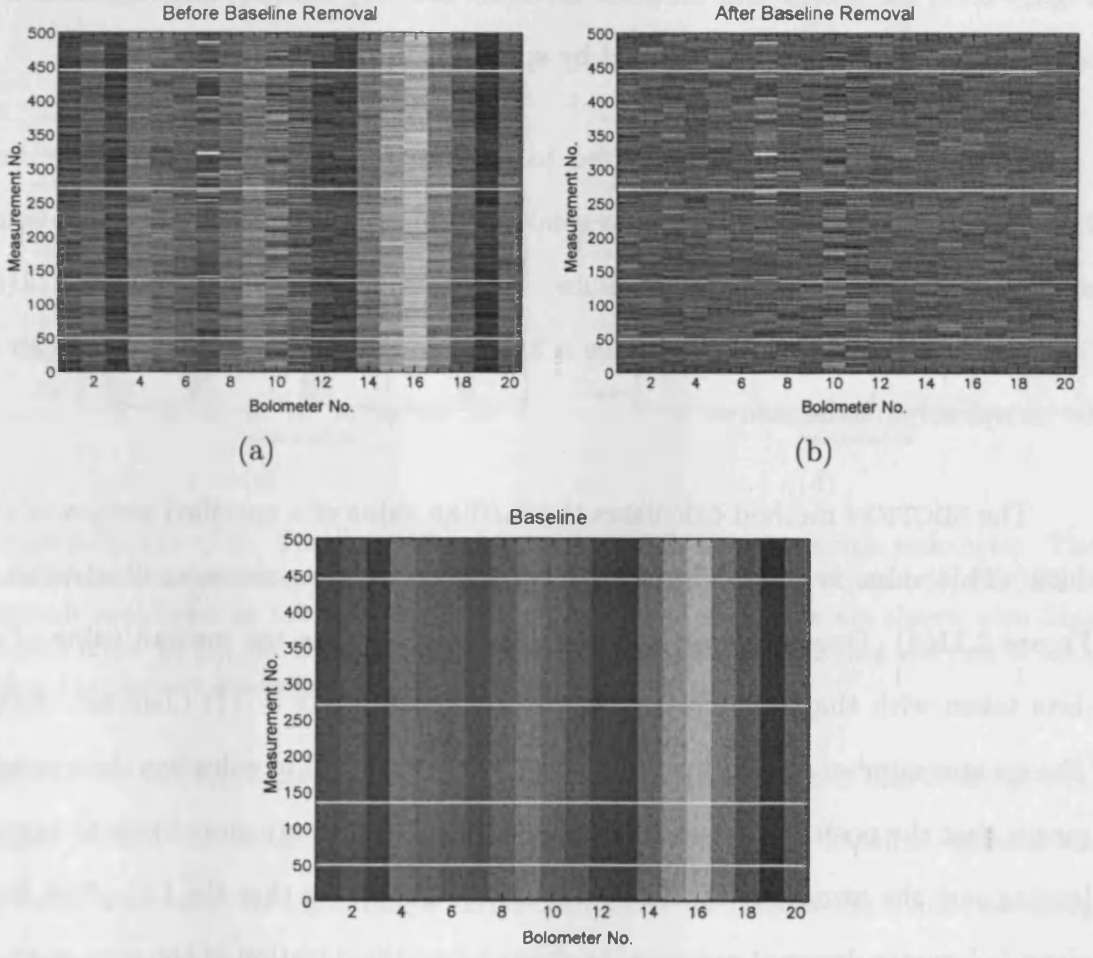

Figure 2.10: (a), (b) and (c). The first 500 measurements of a scan-map (approximately one quarter of the map) for the LW bolometers 1–20. (a) shows the data before a baseline is removed. (b) shows the data after the baseline has been removed using the MEDIAN method. (c) shows the calculated baselines. The white horizontal lines indicate the ends of each scan.

Baselines are removed using the SURF command SCAN_RLB, which can use a number of different methods. The MEAN and MEDIAN methods simply subtract the mean or median value of each scan, from that scan. These are illustrated in Figures 2.11(a) and 2.11(b) respectively, which shows the first 500 measurements taken by a single bolometer. The blue vertical lines indicate the edges of each scan, and the red horizontal lines show the calculated baseline. As is clear from Figure 2.11, the MEAN and MEDIAN methods are very similar, although MEDIAN is recommended as it is less affected by spikes in the data.

The LINEAR method can be used to remove sloping baselines. This is done by calculating the median value of a small section of data at the end of each scan, and interpolating between these values. An example is shown in Figure 2.11(c). This method only works if the source is small enough for the ends of each scan to be completely off the source.

The SECTION method calculates the median value of a specified section of the data. This value is then subtracted from the entire time-series as illustrated in Figure 2.11(d). One recommended method is to calculate the median value of all data taken with that bolometer (specified using SECTION = {}) (Jenness, 2000). The greater number of measurements used by this method to calculate the average, means that the positive and negative astronomical signals are more likely to cancel, leaving just the atmospheric effects. Figure 2.10(c) shows that the DC offset for a given bolometer does not appreciably change over the duration of the scan-map. If this were not the case, the SECTION method would not correctly remove the offset.

A great deal of care is needed when removing the baselines, as artefacts can be produced if an inappropriate method is used. This is discussed in detail in Sections 4.2.2 and 4.3.2. If none of the standard methods produces satisfactory

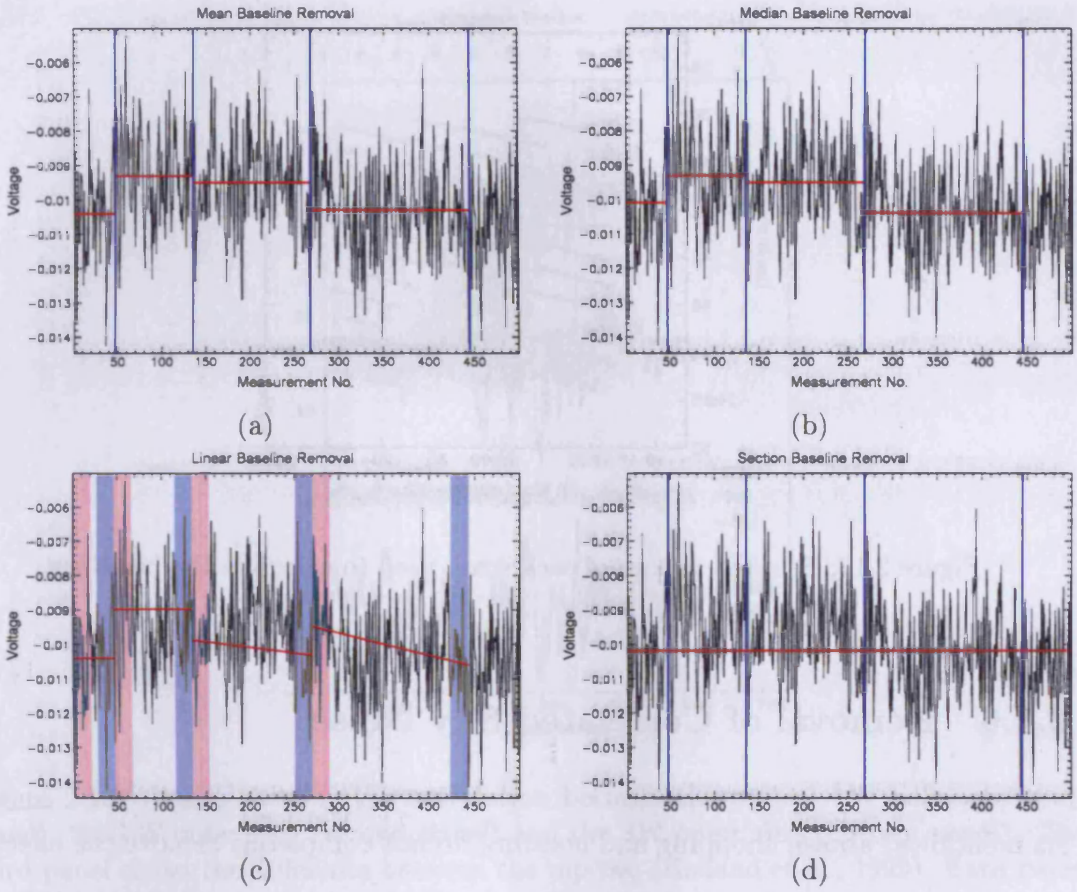

Figure 2.11: (a) – (d). The first 500 measurements taken with a single bolometer. The baselines calculated using the (a) MEAN, (b) MEDIAN, (c) LINEAR, and (d) SECTION methods are shown as red horizontal lines. The ends of each scan are shown with blue vertical lines. In (c), the measurements used to calculate the beginning and end of each linear baseline are shaded red and blue respectively.

results, the SECTION method can be used to calculate baselines based on specific ranges within the data. This can be used to optimise the baseline calculation for each scan-map, by including a large number of measurements whilst avoiding any areas with significant amounts of astronomical signal. This is however a time consuming task, as the measurement numbers at the ends of each section of scan must be determined manually. An example of scans used for this technique is given in Figure 2.12. I have named this the SUB-MEDIAN method.

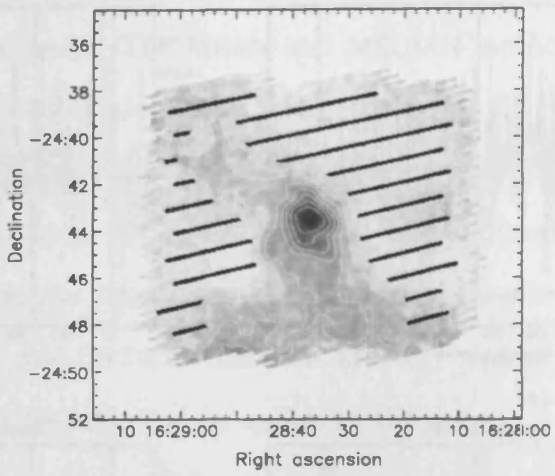

Figure 2.12: Selected regions of each scan, used to calculate the baselines.

2.4.6 Removal of Correlated Sky Noise

As mentioned above, chopping and nodding do not completely remove the effect of the atmospheric emission on the data, because the two beams have slightly different paths through the atmosphere. However the variation in emission is correlated across the array because all bolometers sample the same atmospheric paths (three, as a result of chopping and nodding). This variation is usually referred to as correlated sky noise.

If some bolometers are off-source and therefore only sampling the variable emission from the atmosphere, the variation can be characterised and removed from all of the bolometers, thereby eliminating the correlated sky noise. This is demonstrated in Figure 2.13, which compares the signal in the central LW pixel (top panel), with the median signal from the outer ring of pixels, termed 'LW sky' (panel 2). The two traces are obviously correlated, and the difference between the two (panel 3) clearly shows that the noise is substantially reduced. The fourth

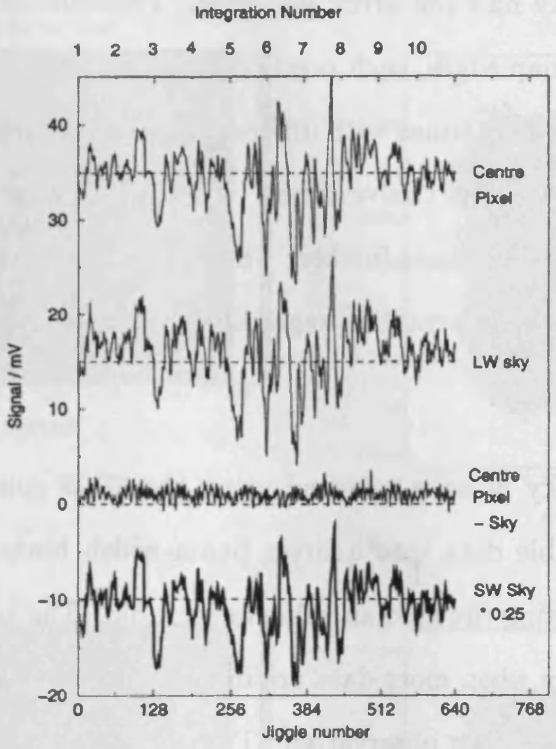

Figure 2.13: Traces showing the correlation between the central LW bolometer (top panel), the LW outer ring (second panel) and the SW outer ring (bottom panel). The third panel shows the difference between the top two (Holland et al., 1999). Each panel is offset by an arbitrary amount for comparison.

panel shows the median signal from the outer ring of the SW array, demonstrating that the sky emission is also correlated between the two wavelengths.

When data are taken in scan-map mode, the rastering field of view means that no bolometers are off-source for the whole map. Each bolometer therefore sees a time varying signal as a result of the array scanning across the source, as well as the fluctuations in sky emission. It is therefore not so easy to remove the correlated sky noise.

The key to removing this degeneracy lies in the multiple observations made at each position. As was shown in Figure 2.6, each scan is offset from the previous

scan by approximately half the array footprint. Therefore in any one map, with the exception of the map edges, each position is scanned twice. In addition to this, the map area is covered six times with different chop configurations. Each position is therefore sampled at least twelve times. If multiple or overlapping scan-maps are made, this coverage increases further. The sky emission being correlated across the array provides more information regarding which signals are astronomical in origin.

The correlated sky noise is removed using the SURF routine CALCSKY. This bins all of the available data into quarter beam-width bins, and a model of the source is calculated using the median value in each bin. The accuracy of the model increases substantially when more data are included in the calculation. The model is then subtracted from each observation. The correlated sky noise is determined by calculating the mean value of all of the bolometers from each measurement in the time-series. This value is then subtracted from the original data.

Figure 2.14 demonstrates the effectiveness of the strategy, by showing a scan-map of L1689B, before and after the skynoise removal. This example shows the data from a single scan-map, though the source model was made using the data from three overlapping scan-maps. Each point in the model is therefore made up of up to 36 measurements.

2.4.7 Regridding and Mosaicing

The REBIN routine is used to transform the data from the form of a time-series for each bolometer, to a rectangular grid. The grid size and pixel-scale are user definable, and the grid can be in one of numerous coordinate systems, including

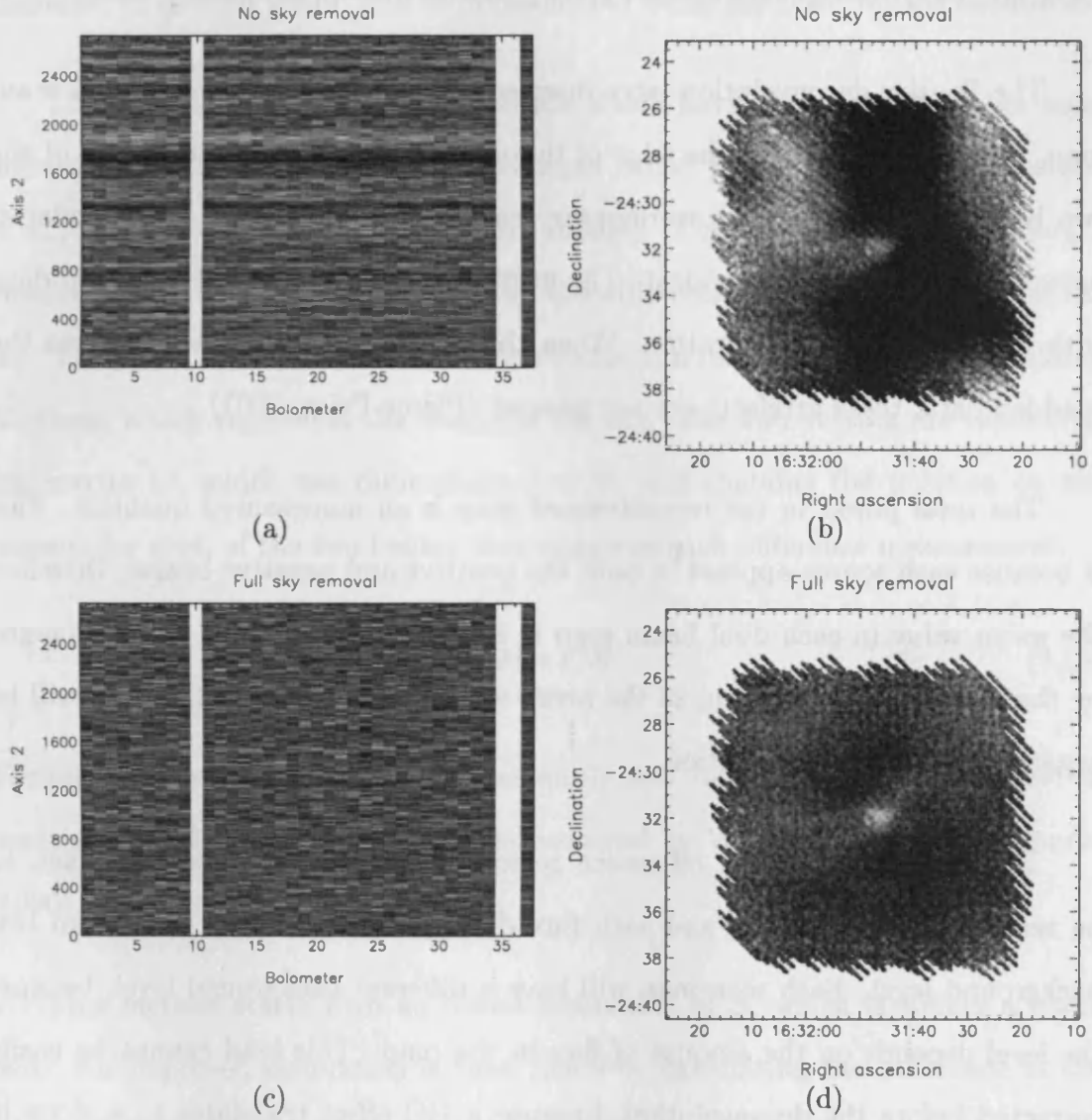

Figure 2.14: (a) – (d). A scan-map of L1689B (a & b) before, and (c & d) after the skynoise is removed using CALCSKY. (a) and (c) show the data as bolometer signal along the x axis and measurement number on the y axis. Correlated sky noise affects all bolometers simultaneously and is therefore manifested as horizontal signals that can be clearly seen in (a). (b) shows the effect of the sky-noise on the map. The noise is mostly on large spatial scales, where the map is the least sensitive. (c) and (d) demonstrate the improvement in both the time-series and the map.

RA/Dec., Nasmyth, Alt-Az, and a coordinate frame centred on a planet. Various weighting functions can be used to combine multiple measurements made at the same position, including Gaussian and linear (conical) functions. Alternatively the data can be combined with a simple median, though this is only recommended if

there are many data-points in each pixel (Sandell, Jessop, & Jenness, 2001).

The Fourier deconvolution introduces edge effects to the reconstructed scan-map. These are caused by the edge of the map being covered by only one of the two beams. If two partially overlapping scan-maps are coadded, the boundaries between the two maps are evident. The REBIN routine can be used to co-add data with the same chop configuration. When the dual beam is deconvolved from the coadded data, these artefacts are not present (Pierce-Price, 2001).

The total power in the reconstructed map is an unmeasured quantity. This is because each source appears in both the positive and negative beams, therefore the mean value in each dual beam map is zero. The mean value is not changed by the Fourier deconvolution, so the areas of low flux density in the map will be negative after the deconvolution.

The mean value of the off-source region of each map is therefore taken to be zero point of that map, and each flux density must be made relative to this background level. Each scan-map will have a different background level, because the level depends on the amount of flux in the map. This level cannot be easily corrected before the deconvolution, because a DC offset translates to a slope in the map after deconvolution. Therefore the background level must be measured for each region of the final map, and the flux density measurements made relative to this.

2.4.8 Deconvolving the Differential Beam

The last stage of the scan-map reduction is to remove the differential nature of the data. The standard method of doing this is to use the Emerson II method

discussed in Section 2.3.3. This is implemented using the Surf routine REMDBM.

There are a number of other methods which have been suggested, the most promising of which is an iterative technique called Matrix Inversion (Johnstone et al., 2000a). Each scan-map can the thought of as an vector $\boldsymbol{D}$ containing I measurements, each measurement being the difference between two points on the sky. The desired outcome of the reconstruction is a rectangular grid $\boldsymbol{S}$ containing N pixels, which represents the image of the sky. The two vectors are related by the matrix $\boldsymbol{C}$, which has dimensions $I \times N$, and contains the position on the rectangular grid, of the two beams that comprise each difference measurement.

$$\boldsymbol{D} = \boldsymbol{C}\boldsymbol{S} \tag{2.13}$$

The matrix $\boldsymbol{C}$ is too large to be inverted easily, and Johnstone et al. (2000a) use an iterative method based on a technique proposed by Wright, Hinshaw, & Bennett (1996).

This method starts with an initial estimation of $\boldsymbol{S}$, which is simply a blank field. An improved estimation is then made by calculating the difference in the values of $\boldsymbol{D}$ that are separated by the chop throw. This difference is then averaged with the previous estimate of $\boldsymbol{S}$. The process is iterated until the solution converges. In the absence of noise, this produces the exact result with relatively few iterations. A simple example of this is given in Appendix B.

Johnstone et al. (2000a) compare this method to the Fourier deconvolution method, and also a maximum entropy technique. They show that both the matrix inversion and the Fourier deconvolution methods produce acceptable results, both for synthesised images and real data. The authors find that their matrix inversion

method is less susceptible to edge effects than the Fourier deconvolution method, and copes better with maps containing variable noise levels. However, the software is not yet publicly available.

Johnstone et al. (2000a) found that the maximum entropy technique they used, fails to properly reconstruct a synthesised image with no added noise. The authors argue that maximum entropy methods are not useful techniques for reconstructing dual beam data, as the technique generally requires the total flux in the map to be known. This is an unmeasured quantity in dual beam data.

2.4.9 Calibration

As discussed in Section 2.1.2, bolometers measure incident radiation by a change in voltage caused by heating of the bolometer. The measurements must therefore be calibrated by observing objects of known brightness.. The exception to this is polarimetry mapping, which does not need to be calibrated because only relative changes in intensity are required to determine the degree and angle of linear polarisation.

The primary calibrator sources used by the JCMT are the planets Uranus and Mars. Planets are ideal used because their brightness is well understood. Jupiter and Saturn are not used because of their large angular size, and Neptune is currently in the same portion of the sky as Uranus, is less bright, and only has a slightly smaller angular size.

If these are not available, secondary calibrators are used. These are either protostellar sources (e.g. IRAS 16293-2422 and NGC 2071IR) or protoplanetary nebulae (e.g. IRC+10216 and CRL618). However, some of these are variable, and

some are surrounded by faint extended emission (Sandell, 1994). The calibrator sources have been calibrated using Mars and Uranus, and the variable sources have well understood light curves, resulting from a large number of observations (Jenness et al., 2002).

Calibrating is carried out at least twice per shift, allowing linear interpolation between the two calibrations over the night. More observations throughout the night would be preferable, but the advantages must be weighed against the increased overhead cost.

The JCMT uses a segmented primary mirror. The individual segments can be adjusted to optimise the shape of the mirror. However, there are always small deviations in the shape from a perfect parabola. These are manifested as a time varying error beam, which can be approximated to a broad Gaussian that is convolved with the main beam.

There are two different ways to calibrate maps, either in Jy/beam or Jy/aperture. For point sources it is recommended that the calibration be done in Jy/aperture (Sandell et al., 2001). To do this, the voltage in equally sized apertures is measured on both the source and the calibrator. The flux density of the source (S_{source}) is given by:

$$S_{source} = V_{source}\frac{S_{tot}}{V_{cal}} \tag{2.14}$$

where V_{source} and V_{cal} are the integrated voltages within the source and calibrator apertures respectively, and S_{tot} is the total flux density of the calibrator.

For the primary calibrators, S_{tot} is obtained using the FLUXES program, which calculates the planetary position, and hence the flux density received. Each planet was calibrated relative to Mars, which has the best understood emission at sub-

millimetre wavelengths.

The flux density received from the secondary calibrators has been determined using a large number of observations (Jenness et al., 2002) made over a number of years. The values of the peak and integrated flux within a 40″ aperture are given Sandell (2002). The fraction $\frac{S_{tot}}{V_{cal}}$ is known as the flux conversion factor (FCF), and is different for different sized apertures. When this method of calibration is used, there is no need to worry about the error beam, because the same fraction of radiation is scattered from the primary beam to the error beam for equal sized apertures.

If calibrating this way, the angular size of the calibrator source must be small compared with the aperture. If the Earth-Mars distance is small, Mars is extended in the JCMT beam, and is therefore unsuitable for this type of calibration unless a large aperture is used. Some of the secondary calibrators are also extended relative to the beam (Sandell et al., 2001).

For studying extended objects, the recommended method is to calibrate in Jy/beam (Sandell et al., 2001). To do this, the flux density received from the calibrator is required, and the fraction of this that couples with the telescope beam. The total flux density for the primary calibrators is provided by the FLUXES program, which also calculates the angular diameter of the planet (D).

The coupling of the flux with the beam is given by:

$$S_{beam} = \frac{S_{tot}}{K}, \tag{2.15}$$

where the coupling constant K is given by:

$$K = \frac{x^2}{1 - e^{-x^2}}, \tag{2.16}$$

and x is:

$$\frac{D}{1.2\theta_A}. \tag{2.17}$$

θ_A is the FWHM of the primary beam, and can be measured from the map of the calibrator, or from a weighted average of a number of pointing sources. If a primary calibrator is used, its angular size must be deconvolved from the measured FWHM (θ_m):

$$\theta_A = \left(\theta_m^2 - \frac{ln2}{2}D^2\right)^{0.5}. \tag{2.18}$$

The FCF can then be calculated using:

$$\text{FCF} = \frac{S_{beam}}{V_{peak}}, \tag{2.19}$$

where V_{peak} is the peak voltage in the calibrator map. Multiplying the source map by the FCF will calibrate the map in Jy/beam.

For calibrator sources, S_{beam} is quoted directly (Sandell, 2002), therefore the FCF can be calculated simply by dividing this value by the peak flux density from the secondary calibrator map.

When measuring the flux density in an aperture from a map calibrated in Jy/beam, the measured value must be divided by the beam integral for a Gaussian, which is equal to $1.134\theta_A^2$. In addition, a correction must be made for the flux lost to the error beam. This correction can be calculated by multiplying the calibrator map by the FCF, and measuring the flux density in an aperture placed over the

Table 2.2: The error beam correction factor (EBCF) calculated using a number of different sized apertures. The total flux density for Uranus at the time of this observation is 62.9 Jy.

Aperture radius	15″	30″	45″	60″	75″
Measured flux density (Jy)	64.9	73.6	78.0	79.8	80.9
EBCF	1.03	1.17	1.24	1.27	1.29

calibrator. A larger aperture will increase the measured flux density. Table 2.2 gives an example of the error beam correction factor (EBCF) for a number of different sized apertures placed over a map of Uranus.

The flux density of the source measured using an aperture, must therefore be divided by the EBCF for that aperture.

2.5 Polarimetry

2.5.1 Theory

We can describe electromagnetic radiation (travelling along the z axis) as a superposition of two orthogonal waves whose electric field vectors are described as:

$$E_x(z,t) = E_{0,x}\cos(kz + wt), \tag{2.20}$$

$$E_y(z,t) = E_{0,y}\cos(kz + wt + \zeta), \tag{2.21}$$

where ζ describes the phase difference between the two waves (Hecht, 1998). If the radiation is polarised, the amplitudes of the two waves ($E_{0,x}$ and $E_{0,y}$) and the phase difference are constant for a period that is long compared to the wave

oscillation period.

If ζ is equal to zero or π, the resultant wave oscillates in a fixed plane and the radiation is said to be linearly polarised. The amplitude of the resultant wave (E_0) and the angle of this plane relative to the $x-z$ plane are functions of the ratio of $E_{0,x}$ and $E_{0,y}$. If ζ is not equal to zero or π, the resultant wave oscillates in a plane that rotates around the z axis, and the radiation is elliptically polarised. The submillimetre emission we are concerned with here is linearly polarised and it is this form of polarisation that is discussed below.

We can measure the polarisation properties of radiation by observing through a polarising analyser, which only transmits radiation vibrating parallel to its principal plane (Serkowski, 1974). If polarised light passes through an analyser such that the angle between the electric field of the radiation and the principal plane of the analyser is θ, the amplitude of the transmitted wave is:

$$E(\theta) = E_0 \cos\theta, \tag{2.22}$$

and the intensity (S) observed is:

$$S(\theta) = E_0^2 \cos^2\theta. \tag{2.23}$$

In general, astronomical radiation is not 100% polarised, but consists of a polarised component (I_p) and an unpolarised component (I_u), the total intensity being the sum of the two. To characterise the polarisation state of the measured light, observations must be made with different values of θ. As θ is changed by rotating the analyser, the unpolarised component remains constant, and the polarised component varies sinusoidally. This is shown graphically in Figure 2.15.

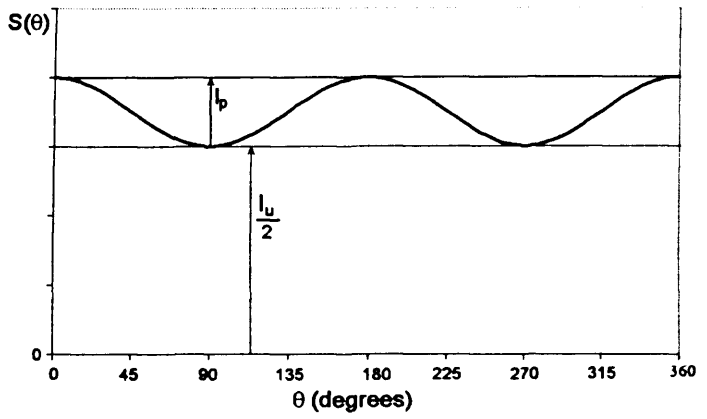

Figure 2.15: The relation between the transmitted intensity and the angle between the principal plane of the analyser and the electric vector of the radiation.

Two observations, sampling orthogonal components of linearly polarised radiation, will measure (Berry & Gledhill, 2001):

$$S_0(\theta) = I_p \cos^2\theta + \frac{I_u}{2}, \tag{2.24}$$

$$\begin{aligned} S_{90}(\theta) &= I_p \cos^2(90-\theta) + \frac{I_u}{2}, \\ &= I_p \sin^2\theta + \frac{I_u}{2}, \end{aligned} \tag{2.25}$$

and the Stokes Q parameter is defined as the difference between these two quantities:

$$Q = S_0 - S_{90} = I_p \cos 2\theta. \tag{2.26}$$

Measuring the intensity of two additional orthogonal components separated from the previous two by 45° gives us the Stokes U parameter in a similar manner:

$$S_{45}(\theta) = I_p \cos^2(\theta+45) + \frac{I_u}{2}, \tag{2.27}$$

$$\begin{aligned} S_{135}(\theta) &= I_p \cos^2(90-\theta+45) + \frac{I_u}{2}, \\ &= I_p \sin^2(\theta+45) + \frac{I_u}{2}, \end{aligned} \tag{2.28}$$

$$U = I_{45} - I_{135} = I_p \sin 2\theta. \quad (2.29)$$

The third Stokes parameter I, is the total intensity and is found using:

$$I = S_0 + S_{90} = I_p + I_u. \quad (2.30)$$

From the three Stokes parameters, the polarised intensity (I_p), the percentage polarisation (P) and the orientation of the plane of polarisation θ can be calculated using the following:

$$I_p = \sqrt{Q^2 + U^2}, \quad (2.31)$$

$$P = (I_p/I) \times 100\%, \quad (2.32)$$

$$\theta = 0.5 \arctan\left(\frac{U}{Q}\right). \quad (2.33)$$

2.5.2 Astronomical Polarimetry

For the purposes of astronomical polarimetry, we want to measure the position angle of the polarised light relative to a fixed direction on the plane of the sky, so we define Q and U such that S_0 is measured in a plane that is parallel with the direction to the north celestial pole. The intensity transmitted through an analyser is:

$$S(\phi_A) = I_p \cos^2(\theta - \phi_A) + \frac{I_u}{2}, \quad (2.34)$$

where ϕ_A is the analyser angle, measured from the analyser's principal axis to the north celestial pole, and θ is the angle from the electric vector to the north celestial pole. Expanding the $\cos^2$ term and combining with Equations 2.26 and

2.29, Equation 2.34 becomes:

$$S(\phi_A) = \frac{1}{2}\left[I + Q\cos 2\phi_A + U\sin 2\phi_A\right]. \tag{2.35}$$

If S is measured as a function of ϕ_A, the Stokes parameters can be fitted, allowing the determination of I_p and θ.

ϕ_A is calculated from the waveplate angle ϕ_{WP}, which is measured relative to an arbitrary zero position. The angle between this zero position and the north celestial pole is therefore needed. This angle changes with time due to the rotation of the sky, and is a function of the elevation of the source and the parallactic angle.

2.5.3 Calculating the Stokes Parameters

Once the data have been reduced and regridded, we can calculate the Stokes parameters discussed in Section 2.5.1. There are two methods for doing this, the main difference being the point at which the data from multiple observations are added together. The data are in the form of a series of maps, with each observation comprising 16 jiggle-maps, each map differing from the previous by a rotation of the waveplate of 22.5°.

When using method 1, all observations are regridded into a single data cube containing N jiggle-maps, where N is equal to the number of observations multiplied by 16. The analyser angle (ϕ_A) is calculated for each map, and the Stokes parameters are calculated for each position in the map by fitting a modified version of Equation 2.35 to the time-series of data (Serkowski, 1974; Sparks & Axon, 1999):

$$S(\phi_A) = \frac{t}{2}\left[I + \epsilon\left(Q\cos 2\phi_A + U\sin 2\phi_A\right)\right], \tag{2.36}$$

where t and ϵ are the transmission and efficiency respectively of the polarimeter and are measures of the quality of the polariser, such that a perfectly good polariser will have $t = 1$ and $\epsilon = 1$, and a perfectly bad polariser (e.g. a piece of glass) will have $t = 2$ and $\epsilon = 0$ (Sparks & Axon, 1999).

The fit is performed at each position by minimising χ^2 over the entire dataset:

$$\chi^2 = \frac{1}{2}\sum_i^N \left[\frac{(S_i(\phi_A) - S_i'(\phi_A))^2}{\sigma_i^2}\right], \tag{2.37}$$

where $S_i(\phi_A)$ is calculated from Equation 2.36 using the current best estimates of the Stokes parameters. $S_i'(\phi_A)$ is the data for the i'th map and σ_i is the variance associated with $S_i'(\phi_A)$. The variance is based on the dispersion of the 128 values measured in a 1 second integration (see Section 2.3.2). The Stokes parameters are calculated at each position and variances are recorded based on the quality of the fit.

Method 2 differs from the previous in that the Stokes parameters are calculated for each observation separately. Each observation consists of 16 waveplate positions, within which is a four-fold degeneracy. This degeneracy is caused by the analyser angle rotating at twice the rate of the waveplate angle, therefore a 360° rotation of the waveplate rotates the analyser angle by 720° . Also polarisation vectors are not true vectors, but have a 180° degeneracy.

Equivalent data from each observation are stacked into a single file, resulting in four stacks for each observation. The variance for each position in the stacked image is the standard error of the four values. In the same way as the previous method, the Stokes parameters at each position are calculated by fitting Equation 2.36 to the four data points, with the uncertainty in each Stokes parameter calculated

from the input variances, rather than the fit. This is repeated for each observation. Each set of I, Q and U maps (one per observation) is coadded to produce the final data cube.

This technique is recommended over the former one as the noise in the I, Q and U maps does not integrate down correctly with Method 1 when multiple observations are made (Greaves et al., 2003).

2.5.4 Polarisation Parameters

From the coadded maps of Q, U and I, the parameters P, I_p and θ can be calculated. The relations between these are given in Section 2.5.1, though in practice, a more rigorous method is used.

The percentage polarisation is calculated using:

$$P = \left(q^2 + u^2 - \Delta\right)^{\frac{1}{2}} \times 100\%, \tag{2.38}$$

$$\sigma_P = \left(\left[\frac{q^2\sigma_q^2 + u^2\sigma_u^2}{q^2 + u^2}\right] \times 100\%\right)^{\frac{1}{2}}, \tag{2.39}$$

where q and u are the normalised Stokes parameters:

$$q = \frac{Q}{I}, \qquad \sigma_q = \left(\frac{\sigma_I^2 q^2 + \sigma_Q^2}{I^2}\right)^{\frac{1}{2}}, \tag{2.40}$$

$$u = \frac{U}{I}, \qquad \sigma_u = \left(\frac{\sigma_I^2 u^2 + \sigma_U^2}{I^2}\right)^{\frac{1}{2}}, \tag{2.41}$$

and Δ is to remove the statistical bias, introduced because the normally distributed noise in q and u translates to a positive polarisation percentage (Garcia, 1995). The debias term (Δ) was originally proposed by Wardle & Kronberg (1974) and is a

weighted mean of the variances in q and u (σ_q and σ_u respectively):

$$\Delta = \frac{(q^2\sigma_q^2) + (u^2\sigma_u^2)}{q^2 + u^2}. \tag{2.42}$$

The polarised intensity can then be calculated using:

$$I_p = 0.01(P.I), \tag{2.43}$$

$$\sigma_{I_p} = \left((q^2 + u^2)\sigma_I^2 + I^2\left[\frac{q^2\sigma_q^2 + u^2\sigma_u^2}{q^2 + u^2}\right]\right)^{\frac{1}{2}}, \tag{2.44}$$

and the angle between the polarisation vector and the direction to the north celestial pole can be obtained from:

$$\theta = 0.5 \arctan\left(\frac{U}{Q}\right). \tag{2.45}$$

The uncertainty in the angle (s_θ) is given by the following equation (Hildebrand et al., 2000):

$$s_\theta = \frac{\sigma_P}{2P}. \tag{2.46}$$

Equations 2.38 to 2.46 are derived in Appendix C

2.5.5 Improving Signal to Noise

Whilst reducing the polarimetry data, it became apparent that some observations (a set of 16 jiggle-maps with one complete rotation of the waveplate) contained more noise than others, and their removal improved the quality of the data. Alternatively some of the data within an observation can be discarded if they are inconsistent with the consensus of the rest of the data.

One way to decide whether or not an observation is likely to be bad is to look at the weather log for the night. One might expect poorer data to be taken when the atmospheric water vapour level was higher. However, for polarimetry data, it is not so much the level of τ that causes problems, but the stability. It is easy to see why this is the case, as the polarimetric information is obtained by comparing measurements taken some minutes apart. If the sky opacity changed in those minutes, the information obtained will be incorrect. Tracking the sky opacity on a fast enough time-scale should allow the stability to be determined. However, the CSO radiometer is not updated often enough to be useful in this regard and the JCMT's line of sight radiometer was not operational when most of the data discussed here were taken. It is therefore necessary to determine the quality of the data from the data themselves.

2.5.6 Discarding Bad Observations

If there is sufficient signal to noise in each observation, then each one can be compared with the whole, and it is relatively straightforward to find the bad data. However for weak sources such as prestellar cores, the signal in a single observation is too low to do this and a more indirect approach must be taken.

The polarisation parameters were calculated for a subset of data omitting a small number of randomly selected observations, but containing enough to contain significant signal. A measure of the quality of the reconstruction (q_f) was determined, and this was recorded along with the list of omitted observations. The process was repeated a large number of times, and an average q_f was calculated for each observation. This enabled a ranking of the observations, because for a particular observation, a large q_f would mean that better reconstructions were made

when it was omitted.

The criterion selected for determining q_f was δP, the measurement uncertainty in P:

$$\delta P = \sigma_p^2 = 100^2 \left(\frac{q^2\sigma_q^2 + u^2\sigma_u^2}{q^2 + u^2} \right). \tag{2.47}$$

Each reduced map contains a distribution of δP's, (one for each vector) and a good quality reconstruction will have a larger proportion of low δP's. q_f was calculated by dividing the number of vectors with $\delta P < 5\%$, by the number with $\delta P > 5\%$. The 5% was chosen because for a good reconstruction, 5% marked the boundary between the main distribution and the high δP tail.

Once the observations are ranked, a series of reconstructions can be made, each reconstruction having the next worst observation subtracted. If q_f is calculated for each of these reconstructions, it should increase as the worst observations are removed, and start to decrease when good observations start to be removed, the peak indicating the optimal reconstruction. An example of the improvement made with this technique is shown in Figure 2.16. Figure 2.17 demonstrates the correlation between the quality of the data and the stability of the atmospheric opacity. The worst quality observations identified by this technique were all made in the second shaded block where the weather is clearly much more unstable.

2.5.7 Discarding Bad Data within an Observation

An alternative to throwing away entire observations that have been deemed bad, is to discard only parts of some observations. This can be done by coadding the Stokes IQU data for each observation more carefully. Advantages of this type of technique are that only the data that are inconsistent with the average are

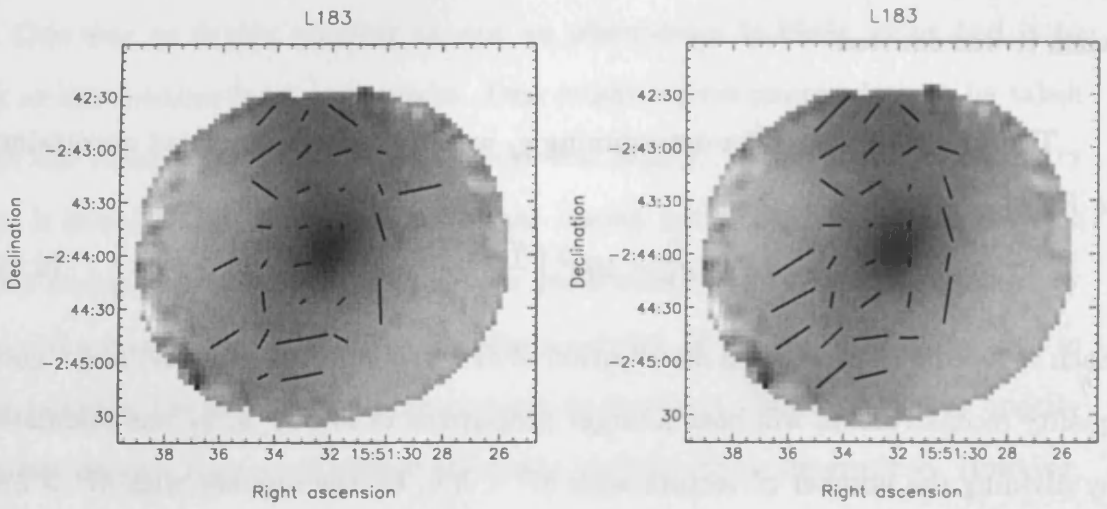

Figure 2.16: (a) & (b). Figure showing the improvement made to a polarisation map of L183 by omitting the worst quality data.

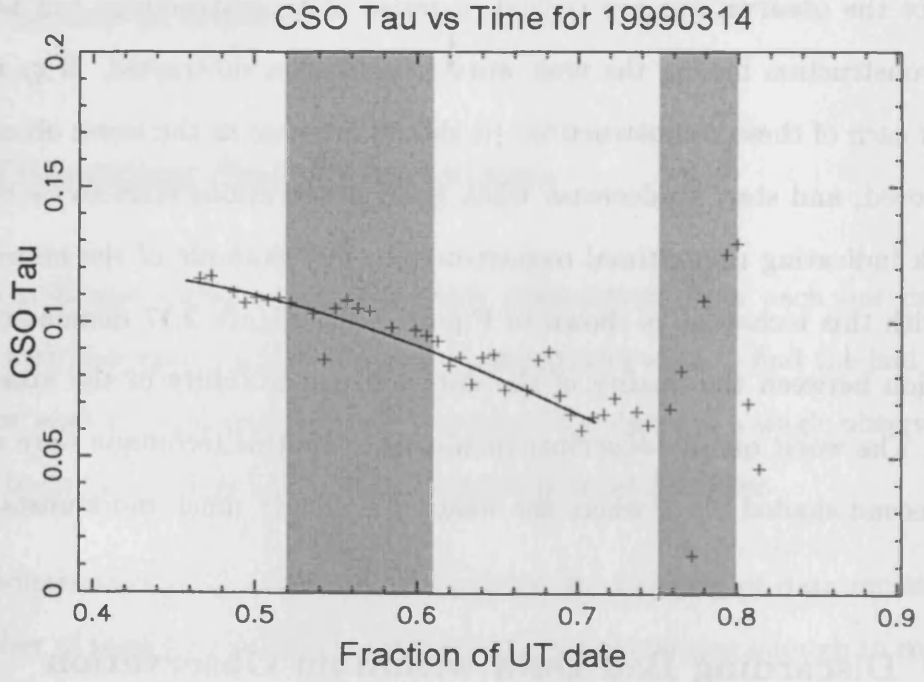

Figure 2.17: Figure showing the τ_{225} as a function of the UT date, for 14th Mar 1999. The crosses are the CSO τ values, the line is a polynomial fit to the τ values, and the shaded areas are where polarimetry data was taken.

discarded. Also, the estimated quality is based on the consistencies in the Q and U values directly, rather than their estimated uncertainties.

SCUBA samples data with a spatial frequency of 6″ in an 850 μm 16 point jiggle-map. Since the beam at 850 μm is approximately 14″, there are a number of correlated pixels within each beam. This, coupled with the large number of observations made, introduces a number of degeneracies. The Q, U and I values should be comparable for a given position in all observations and the average value for each position should be comparable to the other values within a beam.

In the standard reduction method, the Q, U and I values for each pixel are combined using a weighted mean and a polarisation vector is calculated. These are binned to produce a single vector for each beam. These vectors are then discarded if certain criteria are not met. A better method is to discard bad data before performing the averaging, so that the final vectors only contain consistent data and are more likely to make the final cut.

Figure 2.18 highlights some problems with the standard method. The Figure plots the Stokes Q parameter for a single (6″) position, measured in 25 observations. The error bars on the plot are the calculated variances for each point (see Section 2.5.3). One of the points (marked 'O') is obviously erroneous, though the calculated uncertainty is particularly low. This causes a weighted mean (marked 'm1') to be heavily skewed by the erroneous point. Clipping the data at 1σ from a standard mean before combining the observations removed this problem, and the mean Q for the clipped data (marked 'm2') is more believable. It should be stressed at this point that Figure 2.18 does not portray typical data. The data for the majority of positions analysed do not contain these highly weighted outliers, though they were seen on a number of occasions.

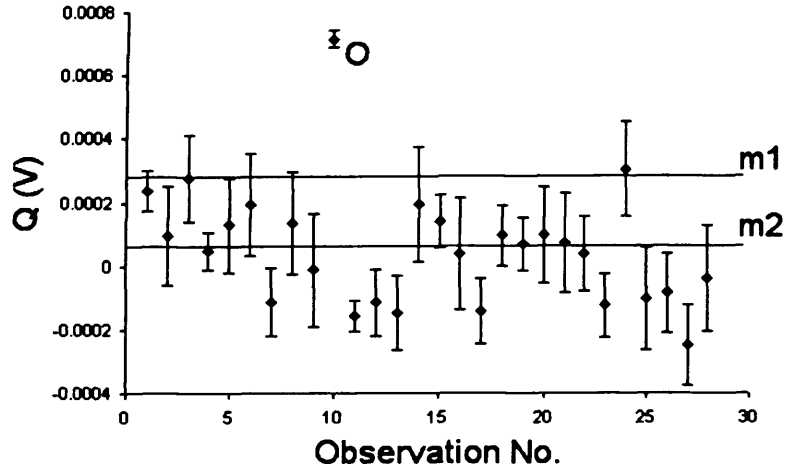

Figure 2.18: Figure plotting the Stokes Q parameter measured for a single pixel in 25 observations. The error bars indicate the variances calculated as described in 2.5.3. Discarding points that are more than 1σ from the mean changes the value of a weighted mean from 'm1' to 'm2'.

Figure 2.19 shows the improvement in consistency in the data, by comparing the Q and U values for each position in a 2×2 grid of $6''$ pixels. Each point in these should be comparable as the square of pixels is smaller than than the beam size. By applying this method, the standard deviation of these points has decreased by more than a factor of three. The error bars plotted in Figure 2.19 are calculated from the variances of each of the observations that made the 1σ cut discussed above.

2.6 Summary

In this chapter, I have introduced the telescope and instrumentation used to obtain the data described in the following chapters. The atmospheric conditions at the telescope and the strategies used to minimise their effect on the data were

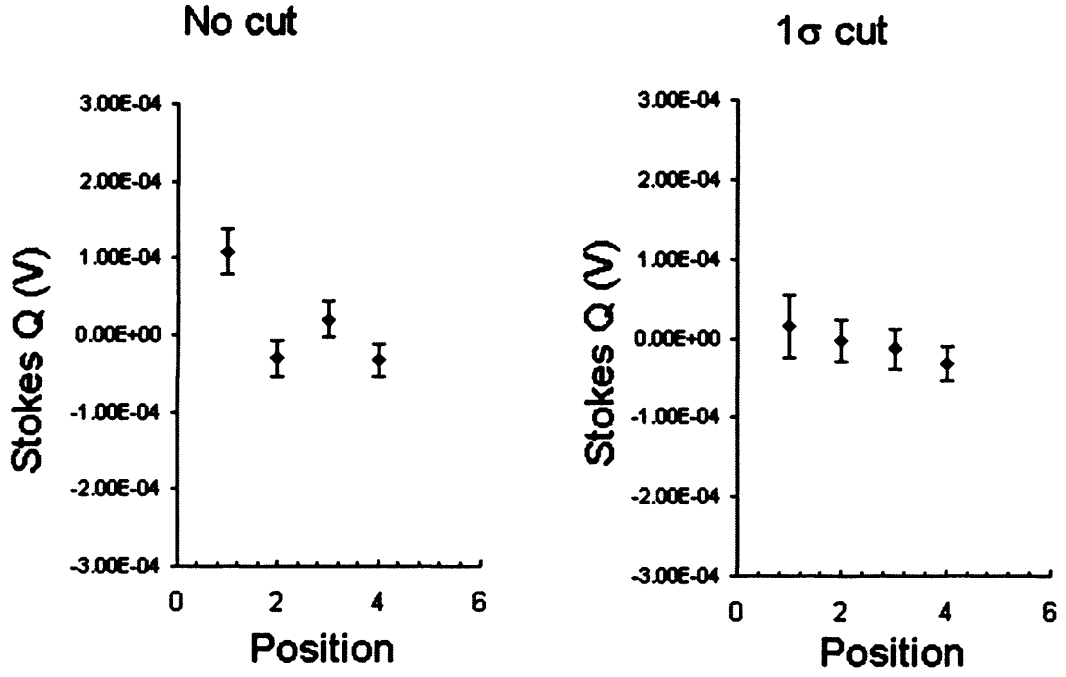

(a) (b)

Figure 2.19: (a) & (b). Figure showing the improvement in consistency for 4 correlated 6″ pixels when a 1σ cut is applied to the data

discussed. The different modes of data acquisition were described, including jiggle-mapping and scan-mapping. The data reduction process was described in detail, with emphasis on the reduction of scan-map data. Finally, the theory and practice of submillimetre polarimetry was discussed, including the strategies I have developed to remove the effects of the atmosphere from the data.

Chapter 3

Measuring the Magnetic Field in Prestellar Cores

3.1 Introduction

If we wish to understand the underlying physics controlling star formation, it is important to determine the role played by the magnetic field. In order to do this, the morphology and strength of the field must be determined observationally. As discussed in Chapter 1, measuring the polarisation state of thermal dust emission can yield information about the direction of the magnetic field, though the field strength is not measured directly. To determine the morphology of the magnetic field at the onset of protostellar collapse, Ward-Thompson et al. (2000) carried out the first polarimetry observations of prestellar cores, using SCUBA and the UK-Japan polarimeter on the JCMT. These instruments are described in detail in Chapter 2.

The three cores observed by Ward-Thompson et al. (2000) were L1544, L183 and L43. They are a subset of the dense cores observed by Myers et al. (1983). They each have no associated IRAS point source (Beichman et al., 1986), and were therefore termed starless cores. Observations of the continuum dust emission were made by Ward-Thompson et al. (1994), and the high central density of some cores led to them being termed 'prestellar'.

Ward-Thompson et al. (2000) found that the magnetic field in each of the cores was uniform in direction, and offset from the core's minor axis by 30° - 45°. They compared the polarisation maps with the results of simulations of magnetised clouds, carried out by Ostriker, Gammie, & Stone (1999). These simulations make predictions about the morphology of the magnetic field for clouds with different magnetic field strengths. They quantified the field strength using the parameter β, which is defined as the ratio of the thermal pressure P_{th} to the magnetic pressure P_{mag}:

$$\beta = \frac{P_{th}}{P_{mag}} = \frac{c^2\rho}{V_A^2\rho} = \frac{c^2}{B^2/4\pi\rho}, \tag{3.1}$$

where c is the sound speed, V_A is the Alfvén speed, B is the magnetic field strength, and ρ is the density.

Clouds with $\beta \ll 1$ are dominated by the magnetic field, and the field lines remain unperturbed throughout the evolution of the cloud. Material flows along the field lines to form elongated structures with the minor axis parallel with the magnetic field. Clouds with $\beta > 1$ are dominated by turbulence, which tangles the field lines. Clouds with an initial β between 0.1 and 1 have fairly uniform field lines, but there can be an offset between the field direction and the minor axis. The polarisation maps made by Ward-Thompson et al. (2000) are therefore most compatible with the intermediate regime ($\beta = 0.1 \rightarrow 1$), where neither the

magnetic field nor the turbulence is dominant.

In this Chapter, I present further polarimetry observations of L183, and use the Chandrasekhar-Fermi technique to infer the plane of sky magnetic field strength for the three cores. I also calculate the mass to magnetic flux ratio in order to evaluate whether or not the prestellar cores are magnetically subcritical or supercritical. These results are compared with the different theoretical models discussed in Chapter 1.

3.2 Observations and Data Reduction

Polarimetry observations of L183 and L43 were carried out on the nights of 1999 March 14^{th} and 15^{th}. Observations of L1544 were made on 1999 September 13^{th}, 15^{th} and 16^{th}. L183 was observed for a further three shifts on the nights of 2002 February 14^{th} – 17^{th}. All observations were made between 01:30 and 09:30 Hawaiian Standard Time.

Each observation was carried out by making sixteen 16-point jiggle maps, rotating the waveplate by 22.5° between each map, as described in Chapter 2. Chopping and nodding were employed to remove the majority of the sky noise (see Section 2.2). Pointing checks were carried out approximately every hour, using planets, secondary calibrator sources or pointing sources. The telescope pointing was found to be better than $\pm 2''$ and $\pm 3''$ in azimuth and elevation respectively.

The sky opacity at 850 μm was calculated using a polynomial fit to the 225 GHz CSO τ data, and converting τ_{225} to τ_{850} using the empirical relations described in Section 2.4.2. Skydips taken at regular intervals through the nights were used

Table 3.1: The observational details, including pointing sources used. 1:16293-2422, 2:Uranus, 3:CRL618, 4:1514-241, 5:IRC+10216, 6:1510-089. † Observations on this night were made in two blocks, separated by a 3 hour gap. Though the opacity of the atmosphere was lower on average in the second block, it was extremely unstable (see Figure 2.17), therefore the data were discarded.

Source name	UT date	Pointing sources	No. of observations	Observations used	Average τ_{225}
L43	1999 Mar 14	1,2	14	14	0.08
	1999 Mar 15	1,2	15	0	0.06
L183	1999 Mar 14	1,2	9	7	0.10†
	1999 Mar 14	1,2	5	0	0.07†
	1999 Mar 15	1,2	15	13	0.06
	2002 Feb 14	1,4	11	0	0.13
	2002 Feb 15	1,4,5	32	26	0.06
	2002 Feb 16	4,5,6	27	24	0.06
	2002 Feb 17	2,5,6	29	28	0.05
L1544	1999 Sep 13	3	21	0	0.08
	1999 Sep 15	3	9	9	0.07
	1999 Sep 16	3	18	0	0.06

to corroborate the τ values used. The details of the observations, including the number of observations made, the pointing sources used, and the average τ_{225} for the duration of the observations are given in Table 3.1.

3.2.1 Data Reduction

The data presented in this Chapter were reduced as described in Chapter 2. In each case, method 2 was used for co-adding the data, (i.e. the Stokes parameters were calculated before the observations were co-added — see Section 2.5.3). The data were reduced in subsets to check that they were reproducible.

In the case of the L43 and L1544 data, the atmospheric conditions on some nights were deemed 'bad', and the data were therefore not included. Examples of

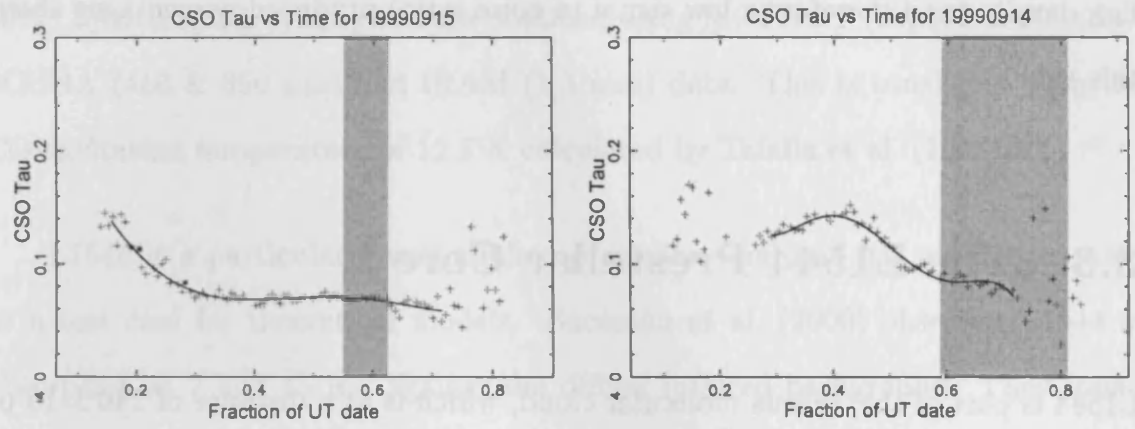

(a) (b)

Figure 3.1: (a) & (b). Figures showing the atmospheric opacity, as measured by the CSO water vapour monitor. The crosses are the $\tau_{225\mathrm{Ghz}}$ data, the line is a polynomial fit, and the shaded areas are when polarimetric data were obtained. (a) is indicative of a 'good' night, while (b) indicates a 'bad' night (see text for discussion).

the conditions on nights that were deemed 'good' and 'bad' are shown in Figures 3.1(a) and 3.1(b) respectively. The quality of polarimetry data is affected more by the variation in atmospheric opacity than by the absolute value. Therefore the standard deviation of the τ_{225} values was calculated for the time period during which each set of data was acquired. If the standard deviation in τ_{225} was greater than 0.01, then the data were discarded.

The quality of the L183 data was treated in a more detailed way, by removing bad observations from each night as described in Section 2.5.6. The number of observations used for each source are given in column 5 of Table 3.1.

The polarisation vectors were clipped at a level of 2σ, to remove vectors with a poor signal to noise ratio. Around the edges of the map, there is insufficient signal for the data to be fitted by Equation 2.35. This tends to generate anomalous values of Q and U that produce vectors with an unphysically high percentage polarisation. As a result, these vectors are not removed by a signal to noise cut, and so a cut of $P > 20\%$ is used. This value was chosen as only regions of the map with a low

flux density (and therefore a low signal to noise ratio) produced percentages above this value.

3.3 The L1544 Prestellar Core

L1544 is part of the Taurus molecular cloud, which is at a distance of 140 ± 15 pc (Elias, 1978). This estimate is based on the degree of reddening of stars on the line of sight (a large jump in reddening occurs at the distance of the cloud), and also distance estimates of stars thought to be associated with the cloud. The L1544 core is located towards the east of the molecular cloud at RA (1950) = $5^h\,01^m\,15^s$, Dec. (1950) = $25°\,06'\,40''$. The uncertainty in the distance to L1544 is primarily due to the unknown position of the core within the cloud along the line of sight. Assuming the cloud depth is the average of the two plane of sky dimensions, this uncertainty is ± 25 pc.

The mass of L1544 has been measured by mapping the emission from dust and molecular species. Ward-Thompson et al. (1999) measured a core mass of 3.2 $M_\odot$ over an area of 0.09×0.05 pc, using the MPIfR 1.3 mm bolometer array at the IRAM 30 m telescope. Kirk (2002) obtained a mass of 2.5 ± 1 $M_\odot$ at 850 μm over an area of 0.1×0.1 pc using the SCUBA camera at the JCMT. Tafalla et al. (1998) mapped the L1544 region in optically thin $C^{18}O(1-0)$, and determined a core mass of 8 $M_\odot$. The mass derived from the CO map was obtained by measuring the integrated flux density over a larger area than the dust maps (0.22×0.14 pc), therefore it is unsurprising that the mass is larger. The method used to calculate the mass of an object from its thermal dust emission was discussed in Section 1.6.1.

The dust temperature of the L1544 core was calculated as 10 ± 3 K (Kirk,

2002) by fitting a greybody to data obtained using ISOPHOT (90, 170 & 200 μm), SCUBA (450 & 850 μm) and IRAM (1.3 mm) data. This is consistent with the CO excitation temperature of 12.5 K calculated by Tafalla et al. (1998).

L1544 is a particularly well studied prestellar core, and has often been used as a test case for theoretical models. Bacmann et al. (2000) observed L1544 in absorption at 7 and 15 μm against the diffuse infrared background. They found that the density profile becomes very steep at large radii (10000 - 30000 AU). They compared the density profile to that predicted by a number of ambipolar diffusion models, and found that the best fit was given by the B_{UV} model of Ciolek & Mouschovias (1995) at time t_2.

The time-scales for the B_{UV} model are defined such that the density increases by a factor of 10 between each of the times t_0, t_1 ... t_6. The initial central density is defined to be 2.6×10^3 cm^{-3}, therefore by time t_2, the central density is approximately equal to the observed value in prestellar cores. By t_2 the core has evolved for approximately 1.2×10^7 years.

The B_{UV} model is initially very magnetically subcritical, although by time t_2, diffusion of the neutrals through the field lines has increased the central mass to flux ratio, forming a supercritical core. The model incorporates UV ionisation, which increases the ionisation rate in the outer parts of the cloud. These outer layers therefore receive a greater degree of magnetic support and remain subcritical, leading to the sharp edges in the cloud. The initial value of β for this model is 0.04, which is lower than the range $0.1 \rightarrow 1$ suggested by the observations of Ward-Thompson et al. (2000).

After formation of the supercritical core, the magnetic field strength in the

B_{UV} model increases with decreasing radius, as a result of the field lines being dragged by the ions. At time t_2, the field strength is predicted to be $\sim$ 50 μG at a radius of 0.04 pc (the approximate scale of our polarimetry map) decreasing to $\sim$ 35 μG at larger scales.

In order to compare these predicted magnetic field strengths with observed values, the inclination angle of the core must be known. Ciolek & Basu (2000) found that an angle of 20° between the magnetic field direction and the plane of the sky reproduced the observed axis ratio, if the shape of the core is the same symmetric oblate spheroid as that predicted by their ambipolar diffusion model. Using this inclination angle, the line of sight component of the field at large scales ($\geq$ 0.1 pc) is predicted to be 12 μG. This scale is similar to that probed by Zeeman measurements. Crutcher & Troland (2000) measured the Zeeman effect in L1544 using the 18 cm line of OH. They measured a field strength along the line of sight of 11 μG, which is consistent with the prediction of the B_{UV} model.

Tafalla et al. (1998) carried out observations of L1544 using several atomic and ionic molecular line tracers. The line profiles of some species showed self-absorption with a brighter blue peak. The authors used this to infer that the foreground absorbing gas is redshifted compared to the background emitting gas, indicating infall. By fitting a simple two-layer model to the data, they inferred an infall rate of 0.1 kms^{-1}. They claimed that this rate of infall was too high to be explained by ambipolar diffusion models. Williams et al. (1999) made higher resolution maps using the BIMA interferometer, and measured a similar rate of infall over a much smaller spatial scale.

Ciolek & Basu (2000) argued that the B_{UV} model could reproduce these infall rates, at least on the small scale observed by Williams et al. (1999). They agreed

that if the central density in the model was set to the observed peak value, the infall rate is lower than that predicted by the B_{UV} model. However, at later times ($\geq t_3$), the infall rates are consistent with those observed. At these later times, the central density is higher than that observed. However, the observations cannot resolve this central region, and the density averaged over a region matching the telescope resolution is consistent with the observed peak density.

Ciolek & Basu (2000) conceded that the B_{UV} model underestimates the infall rate on the larger scale observed by Tafalla et al. (1998). They therefore designed a model ($B_{UV-L1544}$) specifically to reproduce the parameters observed by Tafalla et al. (1998) and Williams et al. (1999). This model has initial conditions that are closer to being magnetically critical, through having a lower initial magnetic field strength and a higher initial central density.

On the large scales probed by Zeeman observations, the $B_{UV-L1544}$ model predicts a magnetic field strength of 20 μG. Assuming an inclination angle of 20°, the line of sight field strength is predicted to be 7 μG. This is lower than the value observed using the Zeeman effect (Crutcher & Troland, 2000), however, the inclination angle is poorly constrained. On the smaller scale of the polarimetry maps, this model predicts a field strength that is only slightly smaller than that predicted by the B_{UV} model.

The initial value of β for the $B_{UV-L1544}$ model is 0.4, which is consistent with the observations made by Ward-Thompson et al. (2000). However, the model does not agree with the data of Bacmann et al. (2000) as it does not reproduce the observed sharp edges and large density contrasts. Only models that are initially highly subcritical can reproduce these.

Table 3.2: A summary of the predictions of two ambipolar diffusion models, with comparisons to the observed parameters. ‡1 Both B_{pos} and B_{los} are given assuming an inclination angle of 20° (Ciolek & Basu, 2000). B_{los} is quoted at a scale of 0.1 pc to be comparable with Zeeman observations. ‡2 B_{pos} is quoted at a scale of 0.04 pc to be comparable with estimates of the field strength made from our polarimetry data.

Models & Observations	Observable parameters or predictions				Consistency with models	
	B_{los}‡1	B_{pos}‡2	β	Sharp Edges	B_{UV}	$B_{UV-L1544}$
B_{UV}	12 μG	47 μG	0.04	Yes	N/A	N/A
$B_{UV-L1544}$	7 μG	37 μG	0.4	No	N/A	N/A
Ward-Thompson	–	–	$0.1 \rightarrow 1$	–	No	Yes
Crutcher	11 μG	–	–	–	Yes	No
Tafalla	–	–	–	–	No	Yes
Bacmann	–	–	–	Yes	Yes	No
Williams	–	–	–	–	Possibly	Yes

To summarise, there are no models that can simultaneously fit all of the data. The initially subcritical B_{UV} model matches the absorption data of Bacmann et al. (2000) and the line of sight magnetic field strength measured using the Zeeman effect. It can also be argued to be consistent with the molecular line data of Williams et al. (1999). However, it is not consistent with the infall velocities measured by Tafalla et al. (1998), and the value of β is too low to agree with the data of Ward-Thompson et al. (2000). The $B_{UV-L1544}$ model fits the molecular line data of Tafalla et al. and Williams et al. and the magnetic field morphology measured by Ward-Thompson et al., but cannot reproduce the sharp edges seen in the infrared absorption data of Bacmann et al. This is summarised in Table 3.2.

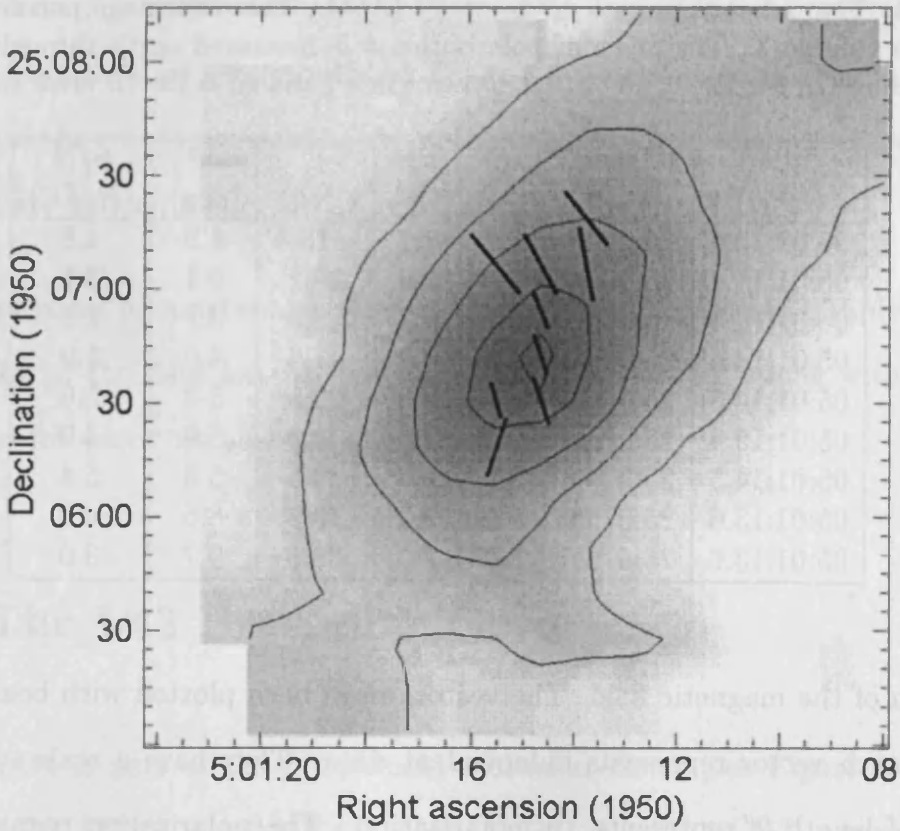

Figure 3.2: Polarisation map of the L1544 prestellar core. The grey-scale and contours show the Stokes I map, with contours at 64, 128, 192, 256 and 304 mJy/beam. The vectors have been rotated through 90° to show the direction of the magnetic field (Ward-Thompson et al., 2000).

3.3.1 Data

Figure 3.2 shows our data of L1544. The grey-scale and contours depict the Stokes I map (total flux density), and the overlaid vectors indicate the direction of the magnetic field. Data obtained in polarimetry mode are not photometrically calibrated, therefore a calibrated jiggle-map of L1544 (Kirk, 2002) was used to calibrate the Stokes I map. The contours are placed at 64, 128, 192, 256 and 304 mJy/beam. Polarimetry yields vectors that are perpendicular to the magnetic field, as discussed in Section 1.5.2, therefore the vectors have been rotated by 90° to show the

Table 3.3: The polarisation measurements of L1544. The percentage polarisation P is quoted in column 3. The angle of polarisation θ is measured north through east. All vectors above 2σ are listed. δP is the 1σ error in P, and $\delta\theta$ is the 1σ error in θ.

RA (1950)	Dec. (1950)	P (%)	δP (%)	θ (deg)	$\delta\theta$ (deg)	S/N ($P/\delta P$)
05:01:15.4	25:06:20	8.2	1.7	−18.4	5.9	4.8
05:01:15.4	25:06:32	4.4	1.4	15.1	9.1	3.1
05:01:14.5	25:06:32	6.2	0.8	18.9	3.7	7.8
05:01:14.5	25:06:44	5.3	0.9	17.4	4.9	5.9
05:01:14.5	25:06:56	5.0	0.9	22.9	5.2	5.6
05:01:15.4	25:07:08	9.7	2.0	39.8	5.9	4.9
05:01:14.5	25:07:08	8.6	1.6	28.5	5.3	5.4
05:01:13.6	25:07:08	9.5	2.2	10.5	6.6	4.3
05:01:13.6	25:07:20	8.6	2.9	38.3	9.7	3.0

direction of the magnetic field. The vectors have been plotted with beam spacing so that each vector represents independent data. They have a scale such that a vector of length 2″ represents 1% polarisation. The polarisation parameters are given in Table 3.3.

Figure 3.2 shows that the core is elongated with an aspect ratio of ~ 2. The core retains this aspect ratio for the majority of the dynamic range of the map. Along its greatest dimension, the core is marginally larger than the field of view, with the edge of the field approximately at the 20% peak-intensity contour. The major axis has a position angle of $-38° \pm 5°$, measured north through east. This does not appear to change over the length of the core. The FWHM dimensions of the core are $\sim 110'' \times 60''$, corresponding to 0.07×0.04 pc at a distance of 140 pc.

As a result of the low number of observations included in the reduction of L1544 (see Section 3.2.1), there are a small number of polarisation vectors greater than 2σ. The vectors are restricted to but do not fill the 192 mJy/beam (60% peak flux density) contour. With the exception of a single vector to the south of the

core, the direction of the vectors is uniform. The average field direction is $19° \pm 5°$, offset from the core's major axis by $57° \pm 7°$. As discussed in Section 3.1, this implies that the core is not dominated by the magnetic field or the turbulence, but that both are playing a part in the evolution of the core.

The physical parameters for the L1544 core are summarised in Table 3.6, and a discussion of the data for this core is given in Section 3.7, along with the two other cores for which we have polarimetry data.

3.4 The L43 Prestellar Core

The L43 core is part of the ρ Ophiuchi molecular cloud (see Figure 3.3). It is located at RA (1950) = $16^h\,31^m\,44^s$, Dec. (1950) = $-15°\,40'\,45''$, approximately 25 pc north of the main part of the cloud. The distance to L43 is assumed to be the same as the distance to the star ρ Ophiuchi, which is associated with the cloud. This has been measured by Hipparcos as 128 ± 12 pc (Bertout, Robichon, & Arenou, 1999). There is an additional uncertainty in the L43 distance estimate based on the assumed cloud radius of 15 pc. The distance to L43 is therefore taken to be 130 ± 20 pc.

L43 is closely associated with a T Tauri star RNO 91 at RA (1950) = $16^h\,31^m\,38^s$, Dec. (1950) = $-15°\,40'\,50''$ (Cohen, 1980). Mathieu et al. (1988) observed the L43 core and RNO 91 in the near-IR, and also at centimetre and millimetre wavelengths using NH_3 and CS molecular tracers. They compared these to previous observations made using ^{12}CO . The observations revealed a collimated molecular outflow originating from RNO 91, the south-east lobe of which has cleared a cavity to the south of the L43 core. This interpretation is illustrated in Figure 3.4. Mathieu

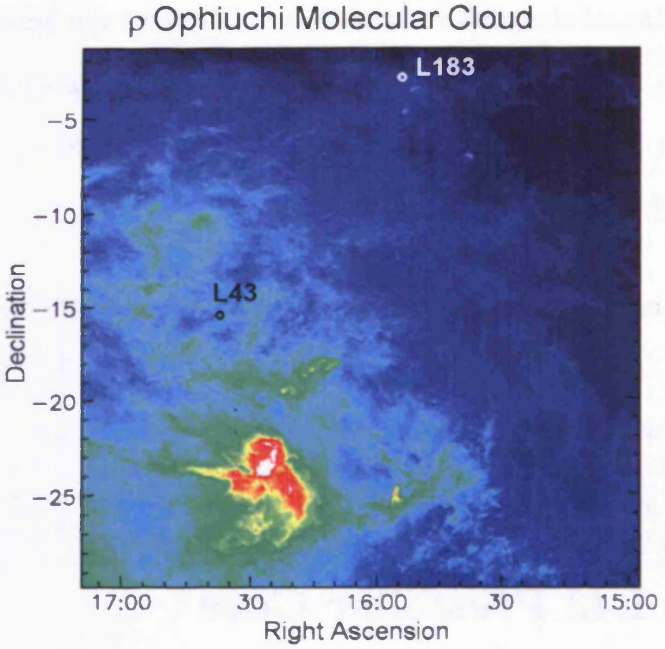

Figure 3.3: The ρ Ophiuchi molecular cloud showing the location of the L43 and L183 prestellar cores. The colour-scale is IRAS 100 μm emission, obtained using the skyview interface (McGlynn, 2003).

et al. suggest that the L43 core is the remnant of a larger core that has already formed one star and is now being partially disrupted by that young star's influence.

The mass of the L43 core was measured by Kirk (2002) using the SCUBA camera to map the thermal dust emission at 850 μm. He obtained a mass of 3 ± 1 $M_\odot$ over an area of 0.09×0.09 pc. A greybody fit based on the SCUBA data and IRAM and ISOPHOT data yielded a temperature of 10 ± 3 K (Kirk, 2002).

3.4.1 Data

Figure 3.5 shows our data of L43. The grey-scale and contours depict the Stokes I map, and the vectors show the direction of the magnetic field. The Stokes I map

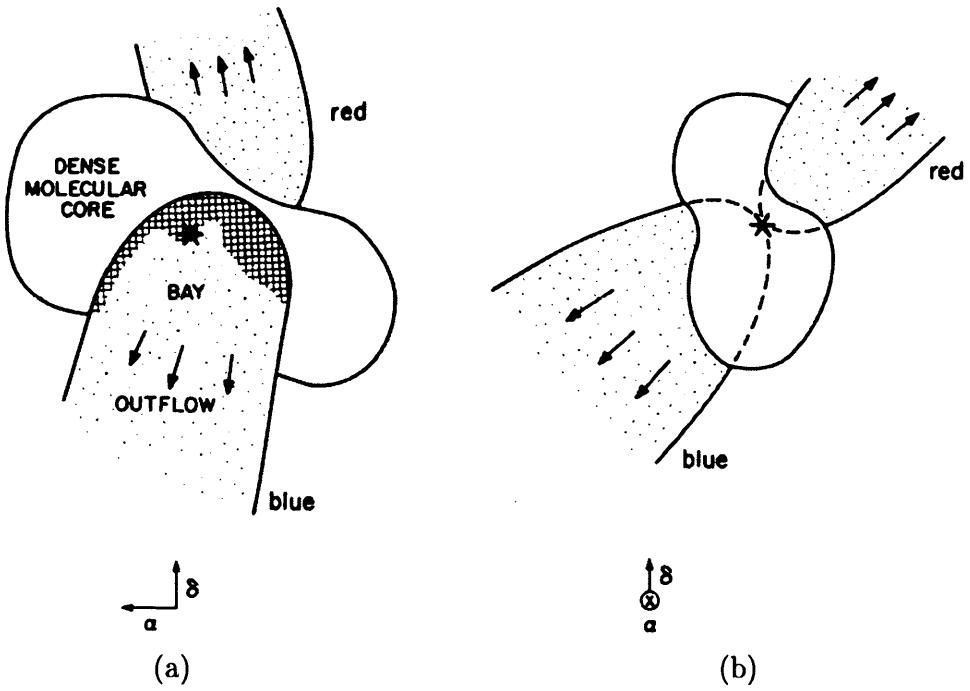

Figure 3.4: (a) & (b). Schematic illustration of the L43 core, the T-Tauri star RNO 91 (marked by "⋆"), and the molecular outflows. (a) The region observed along our line of sight. (b) The system as it might be observed from a direction perpendicular to the outflow direction, approximately 90° west of our line of sight (Mathieu et al., 1988).

was calibrated using a standard jiggle-map (Kirk, 2002). The contours are at 86, 171, 257 and 352 mJy/beam. The vectors have the same spacing and scale as in Figure 3.2, and have also been rotated by 90° . The parameters are given in Table 3.4.

There are two sources shown in Figure 3.5, the L43 prestellar core in the centre of the map, and the T-Tauri star RNO 91 on the western edge. The core is elongated with an aspect ratio of ~ 1.9 and FWHM dimensions of $100'' \times 60''$. The centre of the core is more circular with an aspect ratio of ~ 1.5 at the highest contour shown. The position angle of the core's major axis is $-53° \pm 5°$. The flux density falls off more steeply to the south-west, consistent with the interpretation of Mathieu et al. (1988) that the southern part of the cloud has been cleared by an outflow from RNO 91. The shape of the envelope around the T-Tauri star cannot

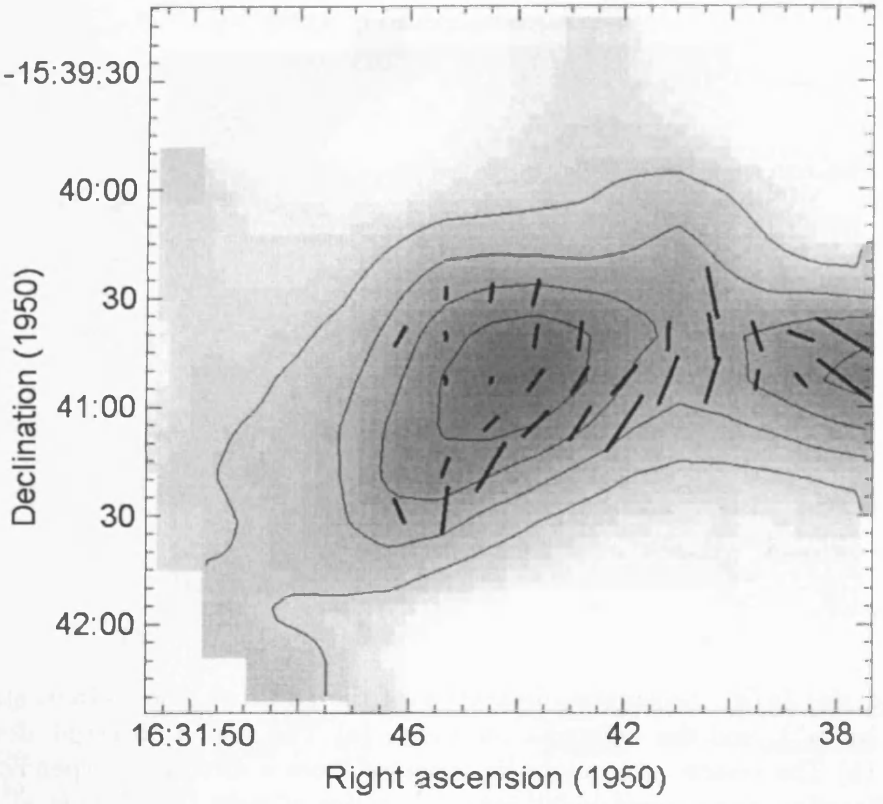

Figure 3.5: Polarisation map of the L43 prestellar core. The grey-scale and contours show the Stokes I map, with contours at 86, 171, 257 and 352 mJy/beam. The vectors have been rotated through 90° to show the direction of the magnetic field (Ward-Thompson et al., 2000).

be determined as it extends beyond the edge of the map. There are more vectors with a signal to noise ratio greater than 2 than in the map of L1544. This is due to L43 being $\sim$ 30% brighter, and the larger number of observations included in the reduction.

There are a number of distinct regions of the map that have different magnetic field properties. At the centre of the core and to the north and east, the field has a position angle of $\sim -21°$ and an average percentage polarisation of 2.4%. To the south of the core, the polarisation is stronger, with an average value of 4.6% and

Table 3.4: The polarisation measurements of L43. The percentage polarisation P is quoted in column 3. The angle of polarisation θ is measured north through east. All vectors above 2σ are listed. δP is the 1σ error in P, and $\delta\theta$ is the 1σ error in θ.

RA (1950)	Dec. (1950)	P (%)	δP (%)	θ (deg)	$\delta\theta$ (deg)	S/N ($P/\delta P$)
16:31:45.4	−15:41:29	7.9	2.3	−6.2	8.3	3.4
16:31:46.2	−15:41:29	2.3	1.0	23.0	12.5	2.3
16:31:44.5	−15:41:17	7.4	0.7	−29.4	2.7	10.6
16:31:45.4	−15:41:17	2.6	0.5	−18.6	5.5	5.2
16:31:42.0	−15:41:05	8.9	2.6	−33.2	8.4	3.4
16:31:42.9	−15:41:05	5.2	0.6	−32.3	3.3	8.7
16:31:43.7	−15:41:05	4.7	0.5	−44.3	3.1	9.4
16:31:44.5	−15:41:05	2.4	0.4	−44.9	4.8	6.0
16:31:37.9	−15:40:53	9.2	1.2	52.8	3.7	7.7
16:31:38.7	−15:40:53	2.2	0.7	41.5	9.1	3.1
16:31:39.5	−15:40:53	2.5	0.6	−9.4	6.9	4.2
16:31:40.4	−15:40:53	6.2	1.0	−16.5	4.6	6.2
16:31:41.2	−15:40:53	6.6	1.4	−22.2	6.1	4.7
16:31:42.0	−15:40:53	5.1	0.7	−40.9	3.9	7.3
16:31:42.9	−15:40:53	4.0	0.4	−31.8	2.9	10.0
16:31:43.7	−15:40:53	3.4	0.3	−36.0	2.5	11.3
16:31:44.5	−15:40:53	0.7	0.3	−13.6	12.3	2.3
16:31:45.4	−15:40:53	0.9	0.4	3.6	12.7	2.3
16:31:37.9	−15:40:41	9.1	3.3	57.9	10.4	2.8
16:31:38.7	−15:40:41	3.5	1.4	70.3	11.4	2.5
16:31:39.5	−15:40:41	4.0	0.7	18.2	5.0	5.7
16:31:40.4	−15:40:41	6.2	0.7	8.6	3.2	8.9
16:31:41.2	−15:40:41	3.7	0.8	−2.5	6.2	4.6
16:31:42.9	−15:40:41	3.7	0.4	−7.1	3.1	9.3
16:31:43.7	−15:40:41	2.9	0.3	−8.9	3.0	9.7
16:31:45.4	−15:40:41	1.0	0.5	3.4	14.3	2.0
16:31:46.2	−15:40:41	2.8	0.9	−28.1	9.2	3.1
16:31:40.4	−15:40:29	7.0	0.9	11.0	3.7	7.8
16:31:43.7	−15:40:29	3.6	0.5	−14.0	4.0	7.2
16:31:44.5	−15:40:29	2.3	0.5	−7.4	6.2	4.6
16:31:45.4	−15:40:29	1.6	0.7	−2.7	12.5	2.3

a position angle of $\sim -33°$. To the west, the field direction bends smoothly round to an angle of $\sim 55°$, and the polarisation increases to an average value of 5.7%, with the peak in polarisation occurring at the saddle between the two sources.

Ward-Thompson et al. (2000) interpreted the field morphology around L43 as being disturbed to the south and west of the core by the molecular outflow. To the north and east, the field remains unaffected by the outflow, and represents the initial state of the magnetic field. This direction is offset from the major axis of the core by $32° \pm 6°$. This result is similar to that obtained for the L1544 core, which is discussed in Sections 3.1 and 3.3.1.

The increase in the degree of polarisation in the outflow could be explained by the grains being aligned by the motions of gas particles streaming past. If this were the case, the polarisation vectors may not be measuring the magnetic field in this region. However, the outflow has not yet penetrated the densest region of the cloud, so the polarisation there should be tracing the magnetic field. Alternatively the observations may be seeing a magnetic field that is being dragged along and distorted by the outflow. Therefore only the vectors that appear to be undisturbed by the outflow are considered when applying the Chandrasekhar-Fermi method. The physical parameters for the L43 core are summarised in Table 3.6, and a discussion of the data for this core is given in Section 3.7, along with the two other cores for which we have polarisation data.

3.5 The L183 Prestellar Core

The L183 cloud is located at RA (1950) = $15^h\,51^m\,32^s$, Dec. (1950) = $-2°\,44'\,00''$, approximately 22° north-west of the ρ Ophiuchi molecular cloud, as illustrated in Figure 3.3. It is part of the L134 complex and is sometimes termed L134N. The distance to L183 has been inferred to be 100 ± 50 pc based on extinction measurements of background stars (Mattila, 1979), and 110 ± 10 pc, using plots of colour-excess versus distance for foreground and background stars (Franco, 1989). A distance of 110 ± 10 pc is therefore used here.

The mass of L183 has been measured using thermal dust emission at 1.3 mm using the MPIfR bolometer array at the IRAM 30 m telescope (Ward-Thompson et al., 1999), and at 850 μm using SCUBA (Kirk, 2002). These observations yielded masses of 1.3 $M_\odot$ over an area of 0.13 × 0.07 pc (1.3 mm), and 1.8 ± 0.6 $M_\odot$ over an area of 0.08 × 0.08 pc (850 μm).

Kirk (2002) found a temperature of L183 of 10 ± 3 K by fitting a greybody to ISOPHOT, SCUBA and IRAM data. A similar study by Lehtinen et al. (2003) gave a lower temperature of 8.2 ± 0.4 K. Pagani et al. (2003) modelled the region as a cold core surrounded by warmer material, and derived a core temperature of 7.6 ± 0.5 K, though this value is based solely on 200 μm ISOPHOT data. The temperature of 8.2 K is compatible with each of these results, and is therefore used in the analysis below.

Infall towards the core of L183 has been observed, using the molecular line tracers CS (2-1) and N_2H^+ (1-0) (Lee, Myers, & Tafalla, 2001). The CS line showed a self-absorbed double peaked profile with a brighter blue peak, the classic signature of infall.

3.5.1 Data

Figure 3.6 shows our data of L183. The background image shows the Stokes I map with contours at 50, 100, 150, 200, 250 and 300 mJy/beam. The polarisation vectors show the percentage polarisation and magnetic field direction, with 1% now represented by a vector of length 1″. The resolution of the I map is approximately 14″, though the vectors have been smoothed to a resolution of 21″ to improve the signal to noise ratio. As described in Section 3.2.1 the vectors have been clipped so that only the significant vectors remain. The polarisation measurements are listed in Table 3.5.

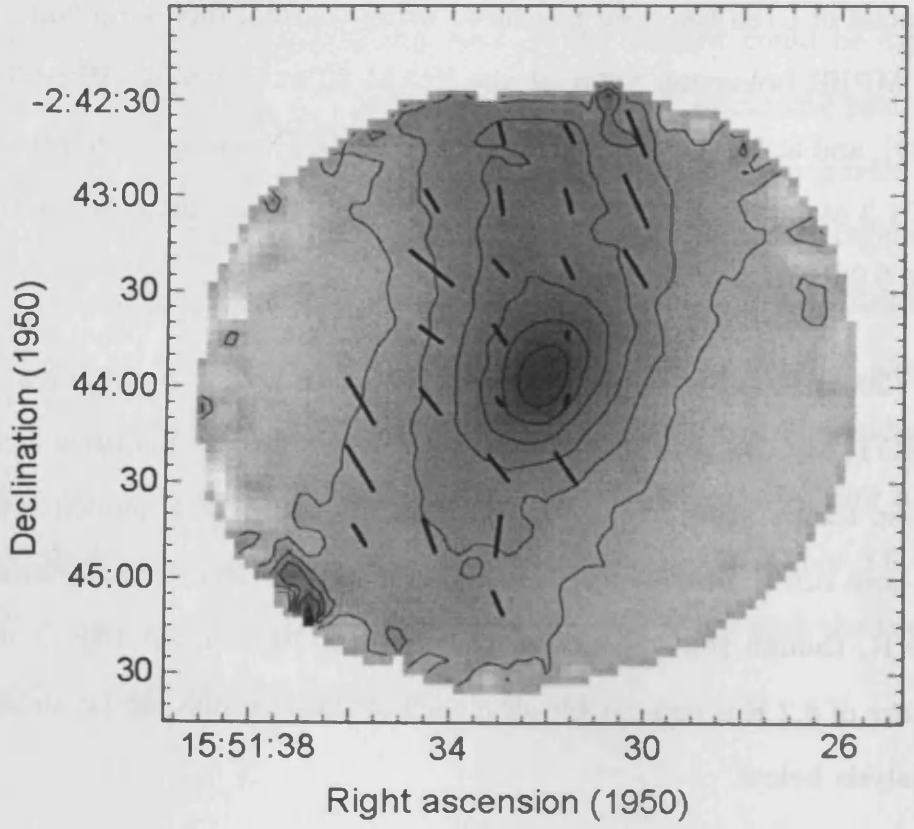

Figure 3.6: Polarisation map of the L183 prestellar core. The grey-scale and contours show the Stokes I map, with contours at 50, 100, 150, 200, 250 and 300 mJy/beam. The vectors have been rotated through 90° to show the direction of the magnetic field.

Table 3.5: The polarisation measurements of L183. The percentage polarisation P is quoted in column 3. The angle of polarisation θ is measured north through east. All vectors above 2σ are listed. δP is the 1σ error in P, and $\delta\theta$ is the 1σ error in θ.

RA (1950)	Dec. (1950)	P (%)	δP (%)	θ (deg)	$\delta\theta$ (deg)	S/N ($P/\delta P$)
15:51:33.0	−2:42:41	6.6	2.1	15.7	9.0	3.2
15:51:31.6	−2:42:41	6.2	2.5	27.7	11.6	2.5
15:51:30.2	−2:42:41	14.9	5.4	22.8	10.4	2.8
15:51:34.4	−2:43:02	7.4	2.4	29.6	9.2	3.1
15:51:33.0	−2:43:02	8.3	1.6	8.9	5.7	5.0
15:51:31.6	−2:43:02	7.2	1.3	15.4	5.2	5.5
15:51:30.2	−2:43:02	17.3	2.9	25.0	4.8	5.9
15:51:34.4	−2:43:23	16.2	4.3	50.4	7.6	3.8
15:51:33.0	−2:43:23	6.5	1.0	40.7	4.3	6.7
15:51:31.6	−2:43:23	6.9	1.3	25.2	5.4	5.3
15:51:30.2	−2:43:23	12.9	2.5	31.8	5.6	5.1
15:51:34.4	−2:43:44	8.0	1.6	53.2	5.7	5.1
15:51:33.0	−2:43:44	6.8	0.8	33.5	3.2	9.0
15:51:31.6	−2:43:44	1.9	0.5	5.2	7.1	4.0
15:51:35.8	−2:44:05	16.3	4.0	30.0	7.0	4.1
15:51:34.4	−2:44:05	9.8	1.7	37.8	4.9	5.8
15:51:33.0	−2:44:05	2.8	0.5	34.2	5.6	5.1
15:51:31.6	−2:44:05	4.2	0.9	−13.9	6.2	4.6
15:51:35.8	−2:44:26	15.7	4.0	30.4	7.3	3.9
15:51:33.0	−2:44:26	9.7	1.3	37.8	3.8	7.4
15:51:31.6	−2:44:26	11.5	2.7	34.5	6.7	4.2
15:51:35.8	−2:44:47	7.2	3.4	29.9	13.5	2.1
15:51:34.4	−2:44:47	10.6	2.4	19.8	6.5	4.4
15:51:33.0	−2:44:47	12.1	2.3	−7.1	5.5	5.3
15:51:33.0	−2:45:08	7.6	2.7	22.5	10.1	2.8

Figure 3.6 shows that the L183 core is elongated in a north-south direction, consistent with previous submillimetre maps of the core (Kirk, 2002). The core extends beyond the edges of the field of view to the north and the south. The flux density at the southern edge of the map is $\sim$ 80 mJy/beam, and at the northern edge is $\sim$ 150 mJy/beam. The FWHM dimensions of the core are $105'' \times 48''$ (0.06×0.03 pc), giving an aspect ratio at this contour of 2.2. The centre of the core becomes progressively more circular, with aspect ratios at the 200 and 300 mJy/beam contours of 1.4 and 1.2 respectively. The major axis of the core has a position angle of $\sim -17°$, measured north through east. The core appears to bend slightly, with the direction of the core's major axis changing from $\sim 0°$ to the north of Dec. (1950) $= -2° 44' 00''$, to $\sim -23°$ south of this line. The intensity falls off more steeply to the west of the core than the east.

From Figure 3.6 it is seen that there are vectors at most points within the 100 mJy/beam contour. The exception to this is to the west of the core where two of the vectors within this contour have been clipped. The polarisation vectors appear to have a lower polarisation percentage in the centre of the core than elsewhere. The implications of this are discussed in Section 3.5.2.

The vector direction is fairly uniform over the core, and indicates an average magnetic field direction of $28° \pm 3°$. It is important to check that there is no systematic change in the direction of the vectors for different regions of the core. This is because the calculation of the magnetic field strength carried out in Section 3.7.3 requires the dispersion of the polarisation vectors. A systematic change in the field direction would increase this dispersion, and so affect the calculated field strength. The average position angle was calculated for two subsets of vectors (northern half and southern half), which are approximately equal in size and are separated by a line at Dec. (1950) $= -2° 44' 00''$. The average position angle to

the north of this line is $29° \pm 3°$, and to the south is $25° \pm 6°$. This difference is approximately 1σ, therefore I conclude that there is no significant change in the direction of the field in the plane of the sky.

The position angle that the major axis of the core makes on the plane of the sky is offset by $\sim 44° \pm 6°$ from the magnetic field direction. This is qualitatively similar to the results obtained for the L1544 and L43 cores, strengthening the argument that the cores are not dominated by either the magnetic field or the turbulence (see Section 3.1). The physical parameters for the L183 core are summarised in Table 3.6.

The theoretical 1σ I_p sensitivity estimated using Equation 2.9, for the 98 observations used in the reduction, is approximately 3 mJy/beam. This value is based on an NEFD of 80 mJyHz$^{-\frac{1}{2}}$, typical of good conditions at the telescope. The observed 1σ I_p sensitivity, averaged over all of the vectors is 3.1 mJy/beam, which is consistent with the theoretical prediction.

The new data for the L183 core confirm the conclusions made by Ward-Thompson et al. (2000), in that the magnetic field direction is uniform over the scale of the map, and offset in direction from the core's minor axis. As discussed in Section 1.5.4, the Chandrasekhar-Fermi technique requires that the magnetic field is not tangled, but has only minor turbulent perturbations on an otherwise uniform field. Therefore the Chandrasekhar-Fermi method can be applied to L183 to measure the field strength in the plane of the sky. This analysis is carried out in Section 3.7.3.

Table 3.6: Summary of the physical parameters of the prestellar cores L1544, L43 and L183, including the position angles (measured north through east) of the core major axis, the average field direction and the offset between them.

	L1544	L43	L183
RA (1950)	05:01:15	16:31:44	15:51:32
Dec. (1950)	25:06:40	−15:40:45	−2:44:00
Distance (pc)	140 ± 25	130 ± 20	110 ± 10
Dust Temperature (K)	10 ± 3	10 ± 3	8.2 ± 0.4
Mass ($M_\odot$)	2.5 ± 1.0	3.0 ± 1.0	1.8 ± 0.6
Major Axis Direction	−38° ± 5°	−53° ± 5°	−17° ± 5°
Field Direction	23° ± 3°	−21° ± 2°	27° ± 3°
Offset	61° ± 6°	32° ± 6°	44° ± 6°

3.5.2 The Central Depolarisation of L183

Figure 3.6 and Table 3.5 show that the percentage polarisation is lower at the centre of the L183 core, where the total intensity is higher. This could indicate an anti-correlation between p and I. Figure 3.7 illustrates this depolarisation more clearly, and shows the minimised χ^2 linear fit to the data.

Depolarisation at higher densities has commonly been seen in polarisation observations of different regions, e.g. OMC-1 (Schleuning, 1998) and OMC-3 (Matthews et al., 2001) in the Orion molecular cloud, L1551 (Lazarian, Goodman, & Myers, 1997) in the ρ Ophiuchi molecular cloud and W51 e1/e2 (Lai et al., 2001). Many possible causes have been suggested, including observational artefacts, unresolved structure in the magnetic field, and a decrease in the efficiency of polarised emission at high density.

One explanation that has been proposed for the depolarisation is that it is a systematic effect introduced by the method of observation. The chopping technique used to remove sky emission (see Section 2.2) involves subtracting a reference beam

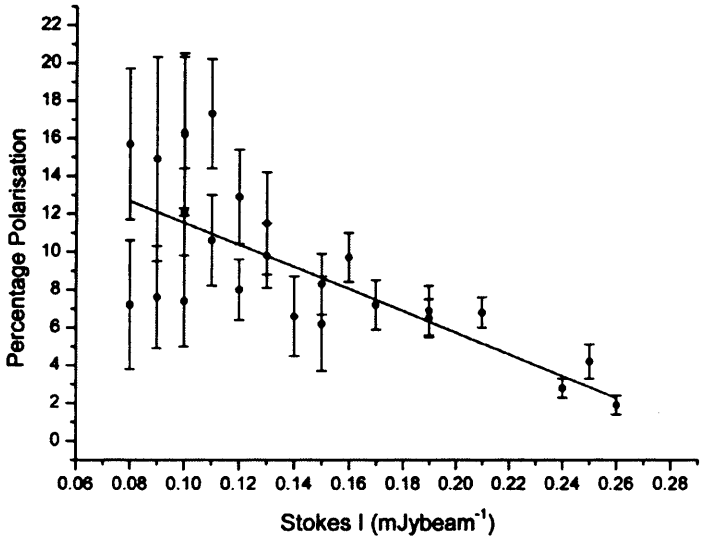

Figure 3.7: Graph showing percentage polarisation of L183 against total intensity, showing a decrease in the polarisation towards the centre of the core. The weighted line of best fit is shown.

from the source beam. If the object being studied is embedded in lower density material, the emission from this material will be subtracted from the source. If this extended emission is polarised, the measured polarisation will be incorrect.

Matthews et al. (2001) carried out a study to quantify this effect by simulating the subtraction of reference beams with different polarisation states from a source beam. They showed that if there is significant polarised flux in the reference beam, and the direction of polarisation is offset in the two beams, then both the measured degree of polarisation and position angle will be incorrect. However, the measured position angle will be a function of the relative flux densities in the two beams and will therefore be expected to change as a function of position in the map. As the position angle is consistent across the polarisation map of L183, this depolarisation mechanism is ruled out.

If the position angle of the polarisation is offset in the source and reference beam by 0° or 90°, the correct position angle will be recovered. However the percentage polarisation will be underestimated or overestimated respectively. Both of these effects will be more significant when the flux in the reference beam is a substantial fraction of the source beam. The effect of the former case will therefore be a depolarisation at lower source intensity, the opposite of what is seen. The latter case will cause an enhanced degree of polarisation at lower source intensity, similar to the observed trend.

Matthews et al. (2001) showed that for depolarisation arising this way, the gradient of a graph of log p vs. log I should decrease towards higher source intensity. Figure 3.8 shows the polarisation data for L183 plotted in this way, with the minimised χ^2 power law shown in grey. Though there is a large amount of scatter in the graph, the gradient does appear to change as a function of I. However, the slope increases towards higher intensity, disagreeing with their prediction.

This increase has been highlighted by calculating the least squares power law fits for the data falling either side of the apparent change in the slope (shown by a dashed line in Figure 3.8). These are plotted as solid black lines. At low intensity, the data are consistent with $p \propto I^0$, whereas at high intensity, the best fit is $p \propto I^{-2}$.

Matthews et al. (2001) also showed that in the extreme case of the reference beam flux density being 25% of the source peak, and the degree of polarisation double that of the source, the slope of the graph is -0.55. This slope is plotted as a dotted line on Figure 3.8 and has too low a gradient to fit the data. I therefore conclude that the depolarisation observed in L183 is not caused by chopping onto polarised extended emission.

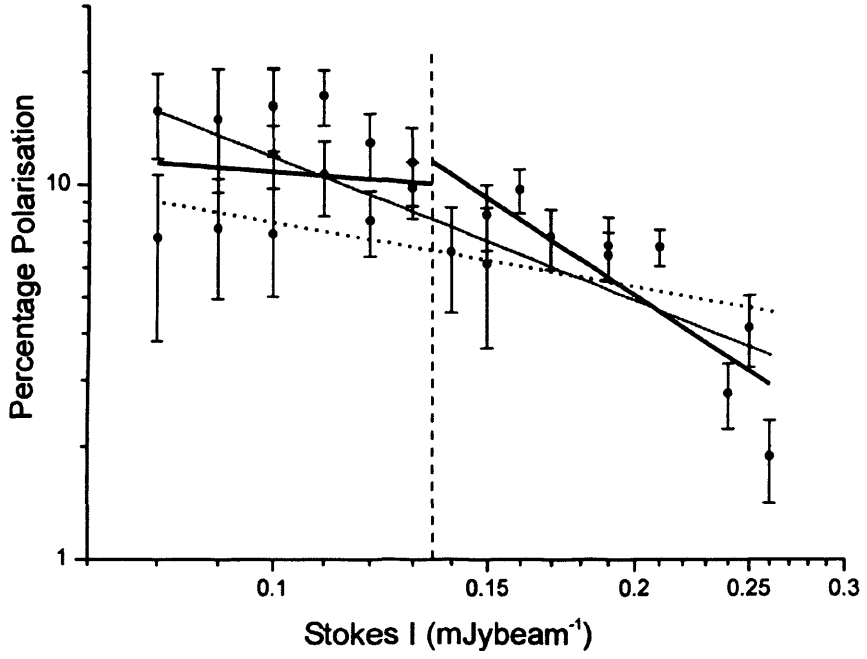

Figure 3.8: Log-Log plot of the percentage polarisation versus Stokes I for the L183 polarimetry data. The grey solid line is a least squares fit to the entire data. The dashed line indicates the position of a possible break. The black solid lines are least squares fits to the low intensity. The dotted line shows the maximum depolarisation that can be explained by a polarised reference beam.

An alternative explanation for the depolarisation, is that a number of different field directions are sampled by the telescope beam. This can be caused by structure in the magnetic field on scales smaller than the beam, or a changing magnetic field along the line of sight.

Depolarisation caused by small scale structure in the telescope beam has been shown observationally for OMC-1 in the orion nebula. This region has been mapped at 100 and 350 μm with resolutions of 35″ and 18″ respectively (Schleuning, 1998) and at 1.3 mm at a resolution of 30″ (Leach et al., 1991). The direction of polarisation is consistent at each wavelength. In each map, the percentage polarisation decreases towards the Kleinmann-Low (KL) nebula, which is the highest

density region. The 100 μm map is shown in the left panel of Figure 3.9.

Rao et al. (1998) mapped the KL nebula with the BIMA array at 1.3 and 3.3 mm, with a beam size of 4.4″ × 2.4″ and 6.8″ × 2.8″ respectively. The 3 mm map is shown in the right-hand panel of Figure 3.9. The BIMA maps show that there is structure in the magnetic field that is unresolved by the maps with poorer resolution. The averaging of the different polarisation angles would cause a decrease in the observed percentage polarisation.

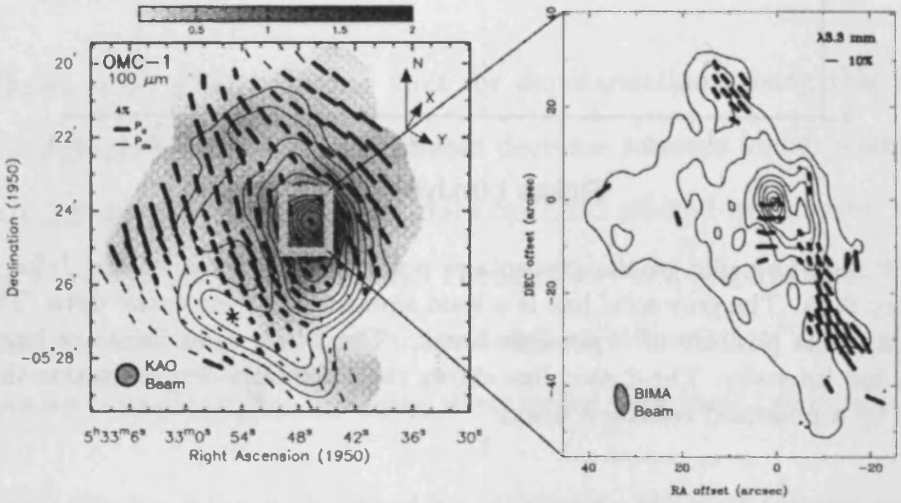

Figure 3.9: Polarisation map of the OMC-1 region showing polarisation vectors, mapped at a resolution of 35″, together with a high resolution (6.8″ × 2.8″) BIMA polarisation map of the emission peak (Weintraub et al., 2000).

If this is the cause of the depolarisation, it appears that there is structure on smaller scales than we can currently resolve. Lai et al. (2002) has observed depolarisation towards the centre of NGC 2024 in the Orion B molecular cloud, with a resolution of 2″.

Polarimetry observations of the OMC-3 filament (Matthews et al., 2001) show depolarisation towards the filament axis that is not restricted to the bright cores embedded along the axis. The authors interpret this depolarisation as arising from

the changing magnetic field along the line of sight caused by a helical field running along the filament.

Although L183 appears to be part of a filament, there is no indication that the level of depolarisation is related to the distance from the filament axis. Therefore we rule this out as an explanation for L183.

The depolarisation could be caused by a change in the properties of the grains in the dense regions of molecular clouds. As discussed in Section 1.5.2, the Davis-Greenstein mechanism for grain alignment requires that the grains be both elongated and spinning. It has been shown that at the high densities of prestellar cores, volatile materials such as CO can condense onto the surface of grains (e.g. Redman et al., 2002). These mantles will tend to make the grains more spherical, which will decrease the polarisation efficiency (Goodman et al., 1995).

As discussed in Chapter 1, in order to align the grains, the alignment time-scale must be shorter than the gas damping time. This condition is less likely to be upheld in the dense regions of clouds for two reasons. The higher density causes an increased rate of collisions between the grains and gas particles, therefore decreasing the gas damping time. Also, the majority of the hydrogen is molecular, therefore the Purcell mechanism for achieving suprathermal rotation will be less efficient. This will reduce the rotation rate of grains and therefore increase the alignment time-scale (Lazarian et al., 1997).

Of these different potential causes for the depolarisation, the most likely seems to be some combination of a number of mechanisms. These are the growth of more spherical grains by adsorption of molecules from the gas phase, reduced alignment efficiency caused by decreased amounts of atomic hydrogen, an increase in the rate

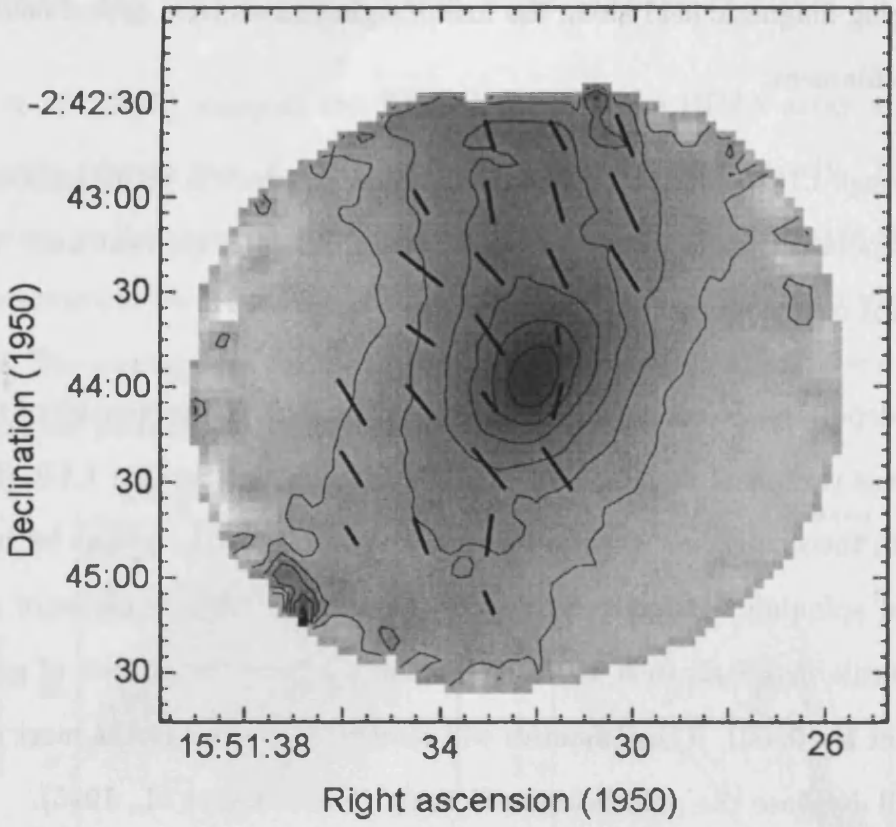

Figure 3.10: Map of the L183 prestellar core showing the polarised intensity. the grey-scale image and contours are as in Figure 3.6. The polarised intensity is given by the length of each vector, with 1″ representing 1 mJy/beam.

of collisional de-alignment, and structure in the magnetic field on scales that are unresolved by the telescope.

The regions of the core from which the polarised emission arises can be investigated by considering a map showing the polarised intensity. Figure 3.10 shows a map of L183, overlaid with vectors of polarised intensity rather than percentage polarisation. The position angle of the vectors show the magnetic field direction. A vector of length 1″ represents a polarised intensity of 1 mJy/beam.

Inspection of Figure 3.10 indicates that there may be a small reduction in the

polarised intensity towards the peak of the total intensity. In order to investigate this, a graph of polarised intensity vs. total intensity is plotted in Figure 3.11. The least squares linear fit to the data does indeed have a negative slope, however, a line with a slope of zero is not a significantly poorer fit.

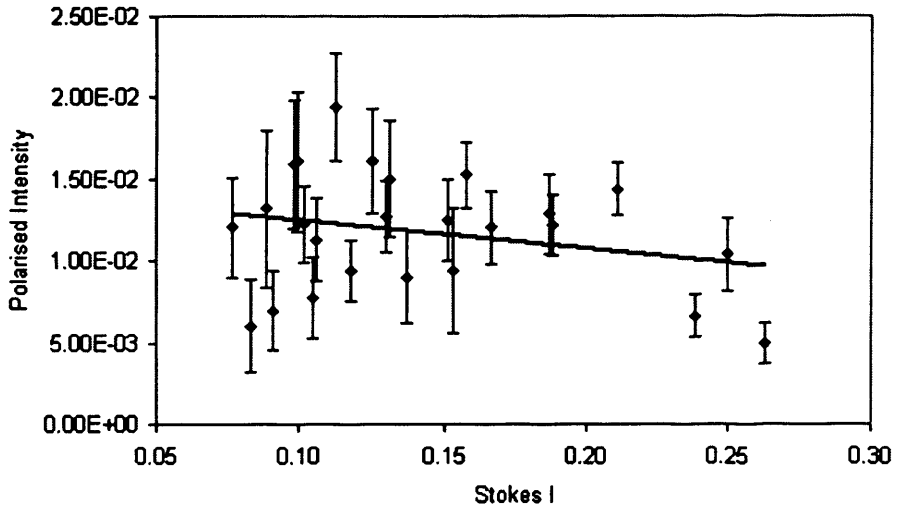

Figure 3.11: Graph showing percentage polarisation against total intensity for L183. The least squares line of best fit is plotted.

If the depolarisation were so severe that the central region of the core was not emitting any polarised flux, then the observed polarised intensity would be due to emission from a shell around a high density 'inner core'. As a result of limb brightening effects, we would not expect the polarised intensity from such a configuration to be centrally peaked.

Though the polarised intensity data for L183 shown in Figure 3.11 are very noisy, it is clear that the polarised intensity is not centrally peaked. We therefore infer that the polarised emission in L183 is probably arising from a thick shell surrounding a small inner core. The size of the inner core is taken as being the 200 mJy/beam contour. The reason for this is that if the vectors that lie within

this contour are removed, the best fit to the remaining data in Figure 3.11 has a positive slope. This structure is used in Section 3.6.1 when calculating the volume density of the region emitting the polarised flux.

There are insufficient vectors in the L1544 map to assess the extent of any depolarising effects, and the influence of the outflow on the morphology of the L43 map makes interpreting any depolarisation more difficult.

3.6 Measuring the Magnetic Field Strength — Theory

The Chandrasekhar-Fermi method can be used to estimate the plane of sky magnetic field strength using polarimetry data (see Section 1.5.4). This technique requires the volume density of the region considered, the turbulent velocity dispersion and the dispersion of the polarisation vectors. In this section, these three parameters are discussed in turn. The technique is applied to the three cores in Section 3.7.

3.6.1 Core Density

The volume number density of hydrogen molecules per m^3, $n(H_2)$, can be calculated if the mass of the cloud is known. Rearranging Equation 1.16, we obtain:

$$n(H_2) = \frac{\rho}{2.8 m_H} = \frac{3M}{4\pi r_1 r_2 r_3} \frac{1}{2.8 m_H}, \tag{3.2}$$

where M is the cloud mass, and $\frac{4}{3}\pi r_1 r_2 r_3$ is the volume of cloud encompassed by the aperture. It is assumed that the line of sight radius (r_3) is the mean of the two radii in the plane of sky (r_1 and r_2). The mass and volume can be calculated from the flux density and radii respectively.

In order to calculate the magnetic field strength, we require the volume density of the region for which we have reliable polarisation vectors. These vectors are generally restricted to the central high density area of the core, as the signal to noise ratio is higher in these regions. The average volume density calculated using the mass and volume of the whole core will therefore be an underestimate.

One way to measure the volume density in this central region is simply to use a smaller aperture. However, Equation 3.2 will yield an overestimate, as the mass is calculated from the flux received from a **cylinder** through the core, whereas the volume is based on a smaller **spheroid**. This is illustrated in Figure 3.12.

Calculating the volume of the central region as a cylinder rather than a spheroid is one way to resolve this inconsistency. The length of the cylinder being the average diameter of the whole cloud on the plane of the sky. This technique should be preferable to calculating the average density over the whole cloud, as it includes a smaller amount of low density material.

Ideally, we would also like to remove the low density material in the foreground and background from our mass estimate, and therefore calculate the density of a small spheroidal core (shaded dark grey in Figure 3.12). Calculating the mass and volume of both the whole core and the cylinder allows us to calculate the density of the (unshaded) region outside the cylinder. Subtracting the volume of the small spheroidal core from that of the cylinder yields the volume of the foreground and

background material (shaded light grey). Assuming that this material has the same density as the region outside the cylinder, we can estimate the mass of the low density material in the cylinder. We can now calculate the mass and volume of the inner core, and use Equation 3.2 to calculate the volume density. The values we find for each core are calculated in Section 3.7.

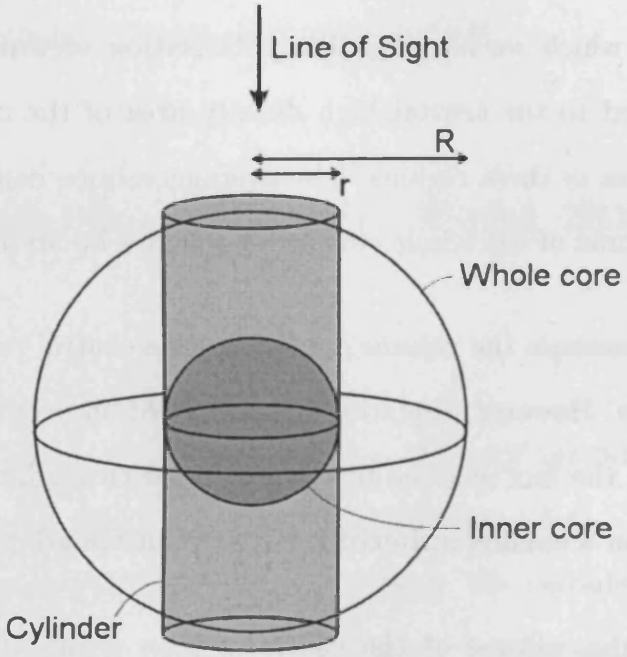

Figure 3.12: Model of a core, showing a large spheroidal core, and the relative volumes of a small inner core and the cylinder from which the flux in a small aperture originates.

3.6.2 Velocity Dispersion

The molecular line used to calculate the line of sight velocity dispersion, is that of the rotation transition N_2H^+ ($J = 1 \rightarrow 0$) at 3.22 mm. N_2H^+ is an ideal molecule for probing the dense interiors of prestellar cores. Like NH_3, it has a high critical density and so only traces the material in the dense cores of clouds. It is not prone to depletion onto grain surfaces, and is therefore generally observed to be centrally

peaked and coincident with the dust continuum peak (e.g. Tafalla et al., 1998). This is shown in Figure 3.13, where the 850 μm SCUBA map is compared to the N_2H^+ map of Caselli et al. (2002). The SCUBA map has been smoothed to the resolution of the N_2H^+ map.

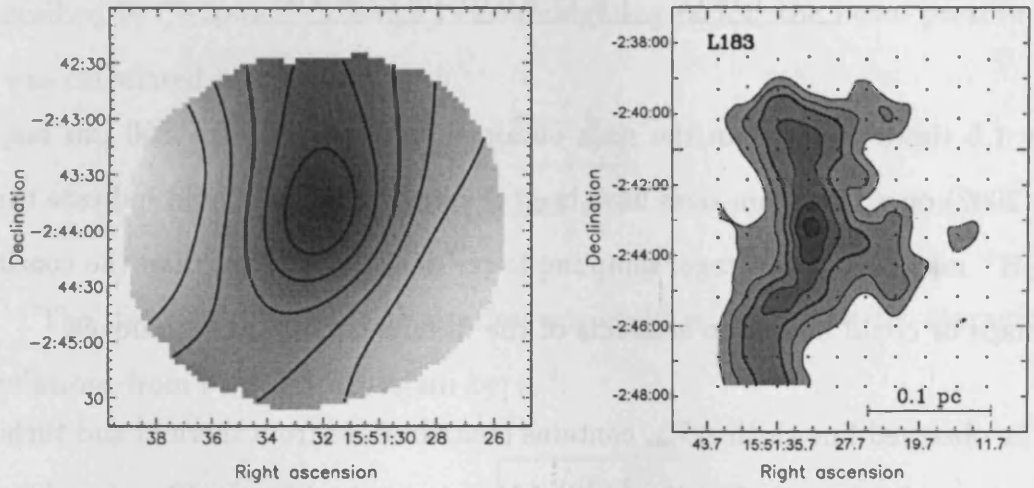

Figure 3.13: (a) & (b). Maps of the L183 prestellar core, made with (a) SCUBA, and (b) the N_2H^+ line (Caselli et al., 2002). The SCUBA map has been smoothed to a resolution of 54″ to be comparable with the molecular line map.

The N_2H^+ ($J = 1 \rightarrow 0$) line contains hyperfine structure as a result of interactions between the spins of the nitrogen nuclei and the unpaired electrons. This creates substructure in the line profile that can be modelled to determine parameters such as the linewidth, excitation temperature and optical depth.

Each of the three cores have been mapped in N_2H^+ using the FCRAO 14 m telescope, with a spatial resolution of 54″ and a spectral resolution of 20 kHz (Caselli et al., 2002). The maps were made with Nyquist sampling for L1544 and L43 and beam sampling for L183. The values for the linewidth used are taken from the peak of the N_2H^+ maps, and are given in Table 3.7.

Caselli et al. (2002) quote the dimensions of the major and minor axes of the cores in their sample after deconvolving the 54″ beam. These sizes are approxi-

Table 3.7: The observed N_2H^+ linewidths, and calculated turbulent linewidth.

Source Name	ΔV_{obs} (kms^{-1})	ΔV_{turb} (kms^{-1})
L1544	0.31 ± 0.01	0.28 ± 0.02
L43	0.36 ± 0.02	0.34 ± 0.03
L183	0.25 ± 0.02	0.22 ± 0.03

mately 1.5 times larger than the sizes obtained from the SCUBA 850 μm maps (Kirk, 2002) once the beam-sizes have been deconvolved. This could indicate that the N_2H^+ maps are on average, sampling lower density material than the continuum maps or could be due to artefacts of the different mapping techniques.

The observed linewidth ΔV_{obs} contains contributions from thermal and turbulent motions. As the turbulent linewidth ΔV_{turb} is required for the Chandrasekhar-Fermi technique, the thermal component should be removed using:

$$\Delta V_{therm} = \sqrt{(8 \ln 2)\frac{kT}{\mu m_H}}, \tag{3.3}$$

$$\Delta V_{turb}^2 = \Delta V_{obs}^2 - \Delta V_{therm}^2, \tag{3.4}$$

(Myers, 1983), where k is the Boltzmann constant, T is the kinetic temperature of the N_2H^+, and μm_H is its molecular mass in kg. At the densities of prestellar cores, the gas and the grains are collisionally thermalised. Therefore the kinetic temperature for each core is assumed to be equal to the dust temperature, which is given in Table 3.6. The observed values of ΔV_{obs} and the calculated value of ΔV_{turb} are given in Table 3.7.

3.6.3 Vector Dispersion

In order to determine the polarisation vector dispersion across the map, the position angle θ and its measurement uncertainty s_θ were calculated for each point as described in Chapter 2. Using s_θ^{-2} as a weighting factor, the mean position angle $\overline{\theta}$ was calculated using:

$$\overline{\theta} = \frac{\sum_i \left(\frac{\theta_i}{S^2_{\theta_i}} \right)}{\sum_i \left(\frac{1}{S^2_{\theta_i}} \right)}. \tag{3.5}$$

The dispersion in the polarisation angles $\delta\theta$ is calculated by averaging the deviations from $\overline{\theta}$, weighting again by s_θ^{-2}:

$$\delta\theta = \sqrt{\frac{\sum_i \left(\frac{(\theta_i - \overline{\theta})^2}{S^2_{\theta_i}} \right)}{\sum_i \left(\frac{1}{S^2_{\theta_i}} \right)}}. \tag{3.6}$$

$\overline{\theta}$ is known more accurately if it is calculated using more vectors. The uncertainty in $\overline{\theta}$ can be calculated using the dispersion $\delta\theta$ and the number of vectors n:

$$\delta\overline{\theta} = \delta\theta/\sqrt{n}, \tag{3.7}$$

Similarly, the uncertainty in the measured dispersion is determined by the number of vectors on which the dispersion is based. Since the mean error in the dispersion of a single vector is given by σ_θ (see below), the uncertainty in the dispersion over all the vectors $\delta_{\delta\theta}$ is given by:

$$\delta_{\delta\theta} = \frac{\sigma_\theta}{\sqrt{n}}. \tag{3.8}$$

We would expect to measure some dispersion in the vectors as a result of noise in the data. In the absence of any intrinsic scatter in the vectors, the spatial dispersion should be equal to the temporal dispersion σ_θ, i.e. the dispersion in the measurement of a single vector as a function of time throughout the observations. We can estimate σ_θ by averaging the measurement uncertainties s_θ, which are based on the variation of the data that makes up each polarisation vector. If $\delta\theta$ is significantly greater than σ_θ, it must be due to the vectors having some real intrinsic scatter.

$$\sigma_\theta = \frac{\sum_i \left(\frac{s_{\theta_i}}{s^2_{\theta_i}}\right)}{\sum_i \left(\frac{1}{s^2_{\theta_i}}\right)}. \tag{3.9}$$

The intrinsic dispersion ($\delta\theta_{int}$) is needed to determine the magnetic field strength and can be obtained from $\delta\theta$ by correcting for the contribution from σ_θ using:

$$\delta\theta_{int} = \sqrt{\delta\theta^2 - \sigma^2_\theta}. \tag{3.10}$$

3.7 Measuring the Magnetic Field Strength — Data

3.7.1 L1544

In order to calculate the volume density for the three cores, photometrically calibrated jiggle-maps were used (Kirk, 2002). As can be seen in Figure 3.2, there are only polarisation vectors in the central region of the core where the flux density is greater than 256 mJy/beam. This region has dimensions on the plane of the sky (assuming a distance of 140 ± 25 pc) of 0.013 ± 0.002 × 0.008 ± 0.001 pc.

The line of sight dimension is assumed to be 0.011 ± 0.003 pc, the average of the dimensions on the sky. The density of this central spheroid was calculated using the method described in Section 3.6.1 and is equal to 3.1×10^5 cm^{-3}.

The measured dispersion for L1544, based on the 9 vectors is 15° ± 2°. The expected dispersion based on the uncertainties in each vector is 5°. Subtracting this from the observed dispersion, yields an intrinsic dispersion of 14° ± 2°. Using an N_2H^+ turbulent linewidth of 0.28 kms^{-1}, Equation 1.15 yields a magnetic field strength of 110 ± 50 μG.

The uncertainty in the measured dispersion is estimated using Equation 3.8. As a result of the low number of vectors for L1544, this uncertainty is known less reliably. This is because the dispersion is more affected by individual vectors that deviate significantly from the mean position angle (e.g. the southern-most vector in Figure 3.2). Therefore it is only taken as an indication of the degree of uncertainty in the dispersion. It is worth noting that increasing this estimated uncertainty by a factor of 4, has only a small effect (a factor of 0.3) on the estimated uncertainty in the magnetic field strength.

Crutcher & Troland (2000) observed the Zeeman effect in 18 cm OH emission, using the Arecibo telescope. They measured a line of sight field strength of 11 μG. At this wavelength, the Arecibo telescope has a 3′ beam, which at the distance of L1544 corresponds to 0.12 pc.

The simplest explanation for this discrepancy is that the direction of the magnetic field is closer to the plane of the sky than to the line of sight. Using the inclination angle of 20° suggested by Ciolek & Basu (2000) (see Section 3.3), the Zeeman measurements imply a total magnetic field strength of 32 μG. This com-

pares to 112 μG calculated using the Chandrasekhar-Fermi method, assuming the same inclination angle. In addition, the ambipolar diffusion models discussed in Section 3.3 predict that at time t_2, the magnetic field strength on a scale of 0.1 pc is approximately 1.5 times smaller than the equivalent strength measured on the scale of these polarisation maps. Taking this into account, the Zeeman observations and the Chandrasekhar-Fermi method disagree by a factor of ~ 2.

Crutcher & Troland (2000) argued that the OH emission does not sample the high density core. Their OH map of L1544 was consistent with the CO maps made by Tafalla et al. (1998), and the same column density was calculated using the different measurements. In addition, the high resolution CO maps show no evidence of the small dense core observed in the submillimetre continuum. If this is the case, then the OH Zeeman measurements would sample the magnetic field at lower densities where the field strength is expected to be lower.

In order to determine the level of support that the core is receiving from the magnetic field, the ratio of the mass to magnetic flux is calculated using:

$$\left[\frac{M}{\Phi}\right]_{measured} = \frac{2.8 m_H n(H_2)(4/3)\pi r_1 r_2 r_3}{B\pi r_1 r_2} = \frac{3.73 n(H_2) m_H r_3}{B}, \tag{3.11}$$

and normalised to the critical mass to flux ratio, calculated using Equation 1.8:

$$\lambda = \frac{[M/\Phi]_{measured}}{[M/\Phi]_{crit}}. \tag{3.12}$$

For L1544, using the Chandrasekhar-Fermi method, λ is equal to 1.0 ± 1, implying that the cloud is approximately critical. Therefore the magnetic field is approximately strong enough to support the core against collapse.

From the Zeeman observations, Crutcher & Troland (2000) found a mass to flux ratio that was 8 times larger than the critical value. However this requires that the magnetic field lies along the line of sight, and they argue that inclination effects could easily bring the mass to flux ratio down to unity.

The B_{UV} model (Ciolek & Mouschovias, 1995) at times t_2 and t_3, and the $B_{UV-L1544}$ model (Ciolek & Basu, 2000) at time t_3, all predict field strengths in the plane of the sky of ~ 40 μG, and mass to magnetic flux ratios of 1–2 times the critical value. These values are consistent with the data presented here (less than 1.5σ difference), if the direction of the field is very close to the plane of the sky.

3.7.2 L43

The polarisation vector dispersion was calculated in the same manner using the same vectors as those used to calculate the mean (see Section 3.4.1). The effect of the outflow from RNO 91 probably precludes the use of the Chandrasekhar-Fermi technique for other regions of the map. The measured dispersion of these vectors is $13° \pm 1°$, with an expected measurement dispersion of $4°$. This yields an intrinsic dispersion of $12° \pm 1°$.

The L43 core has dimensions $0.045 \pm 0.007 \times 0.027 \pm 0.004$ pc. Measuring the flux density within this region, and assuming a line of sight dimension of 0.036 ± 0.009 pc, yields a density of 2.2×10^5 cm^{-3}. A smaller spheroidal region that is coincident with the vectors used, has dimensions of $0.023 \pm 0.003 \times 0.016 \pm 0.002$ pc, with an assumed line of sight dimension of 0.019 ± 0.004 pc. The density for this region, calculated using the method described in Section 3.6.1 is 2.9×10^5 cm^{-3}. This density leads to a magnetic field strength (using Equation 1.15) of 140 ± 50

μG. Using Equations 3.11 and 3.12, λ for the L43 core is 1.3 ± 1 times the critical value. To date there have been no Zeeman observations of the L43 core to compare with this result. However, we note that the calculated values of λ for L1544 and L43 are very similar.

3.7.3 L183

There are reliable polarisation vectors for most areas of the map, therefore all of the submillimetre emitting region appears to contribute to the polarised emission. Hence, the volume density was calculated assuming a simple triaxial spheroidal geometry rather than the model described in Section 3.6.1. The dimensions of this spheroid are $0.037 \pm 0.003 \times 0.018 \pm 0.002$ pc, with an assumed line of sight dimension of 0.028 ± 0.009 pc. The volume density of this spheroid is 2.9×10^5 cm^{-3}.

The measured dispersion of the polarisation vectors in L183 is $15° \pm 1°$. As discussed in Section 3.5.1, there is a small but not significant change in the direction of the magnetic field across the core. It is important to check whether or not this affects the measured dispersion. If the dispersion for each of the two halves of the core was significantly lower than for the whole core, it would not be appropriate to apply the Chandrasekhar-Fermi technique to the data. This is because the dispersion measured for the whole core would be being strongly influenced by the change in direction of the field. The measured dispersion for the northern half of the core (Dec. (1950) $> -2° 44' 00''$) is $13° \pm 1.4°$, and for the southern half (Dec. (1950) $< -2° 44' 00''$) is $18° \pm 1.7°$. These values only differ from the dispersion measured for the whole core at the 2σ level. We therefore maintain that the measured dispersion is caused by turbulent motions in the core, and not by a change in the field direction. The difference in the measured dispersion (if it

is real) could be due to a gradient in the magnetic field strength across the core, though it could equally be caused by a gradient in the level of turbulence.

The measured dispersion of the vectors across the whole core is $15° \pm 1°$. After subtracting a measurement uncertainty of $6°$, the intrinsic dispersion is calculated to be $14° \pm 1°$. Using a volume density of 2.9×10^5 cm^{-3}, an N_2H^+ turbulent linewidth of 0.22 kms^{-1}, and a vector dispersion of $14°$, Equation 1.15 yields a magnetic field strength of 80 ± 25 μG. This yields a mass to flux ratio for the L183 core that is approximately 3 times the critical value.

If the high density inner core is not contributing to the polarised emission, as was discussed in Section 3.5.2, the flux density from this region should not be included in the calculation. The effect of this central region on the density was therefore investigated.

As discussed in Section 3.5.2, the 200 mJy/beam contour is taken to be the boundary of the inner core. The dimensions of this core are $0.01 \pm 0.001 \times 0.007 \pm 0.001$ pc, with an assumed line of sight dimension of 0.008 ± 0.001 pc. The density of this region is calculated as 8.3×10^5 cm^{-3}. The small size of this inner core means that when the mass and volume are removed from from that of the large spheroid, the density of the large spheroid is only decreased to 2.8×10^5 cm^{-3}. In addition, the field strength is proportional to the square root of the volume density, therefore the reduced volume density has no significant effect on the calculated field strength, reducing it by only 2 μG.

Crutcher et al. (1993) observed the Zeeman effect from L183 in emission using the 18 cm OH lines. They found a 3σ upper limit of 16 μG. There are a number of possible reasons for the discrepancy between Zeeman measurement and the result

Table 3.8: Summary of parameters used to calculate the magnetic field strength.

	L1544	L43	L183
Measured dispersion ($\delta\theta$)	15° ± 2°	13° ± 1°	15° ± 1°
Measurement uncertainty (σ_θ)	5°	4°	6°
Intrinsic dispersion ($\delta\theta_{int}$)	14° ± 2°	12° ± 1°	14° ± 1°
Volume density (n(H_2)) ($\times 10^5 cm^{-3}$)	3.1 ± 2.5	2.9 ± 1.8	2.9 ± 1.6
Turbulent linewidth (ΔV_{turb}) (kms^{-1})	0.28 ± 0.02	0.34 ± 0.03	0.22 ± 0.03
Magnetic field strength (B_{pos}) (μG)	110 ± 50	140 ± 50	80 ± 25
Mass to flux ratio (λ)	1.0 ± 1	1.3 ± 1	3.1 ± 2

presented here. These were discussed in Section 3.7.1. The parameters used in the above calculations are given in Table 3.8.

3.8 Summary and Conclusions

In this chapter I have used previously published polarimetry data of L1544, L43 and L183 (Ward-Thompson et al., 2000), together with a new, much deeper map of L183, to measure the dispersion of the magnetic field lines on the plane of the sky. The new polarimetric map of L183 represents the deepest polarimetry map made to date of a prestellar core. The new data have confirmed the conclusions made by Ward-Thompson et al. (2000) that the magnetic field is uniform in direction, and is offset significantly from the core's minor axis.

I have shown that when this result is considered with other observational data of L1544, no theoretical model can satisfactorily explain all of the data. This is summarised in Table 3.2.

I have used the Chandrasekhar-Fermi technique to determine the magnetic field strength in the plane of the sky from the measured dispersion of the polar-

isation vectors. For L1544, L43 and L183, this is equal to 110 ± 50, 140 ± 50 and 80 ± 25 μG respectively. These are larger than the typical line of sight field strengths measured using the Zeeman effect for cores of this mass. However, this is to be expected as the Zeeman observations preferentially sample lower density material. The mass to magnetic flux ratio for the three cores has been determined, and compared to the critical value for magnetic support. These indicate that the cores are either approximately critical or marginally supercritical.

As noted in Chapter 1, the magnetic field strengths measured using this method are projections onto the plane of the sky. For any one cloud, the true field strength could be larger. Over a large enough sample of cores, the true field strength will on average be 22% larger. Consequently, the average value of λ will be reduced by 22%.

The result that the cores may be supercritical is consistent with the observations of infalling material towards L1544 and L183, and especially the evidence that in L1544 both the neutrals and the ions are undergoing infall (Tafalla et al., 1998). Crutcher (1999) compiled all of the Zeeman observations of molecular clouds carried out thus far. He found that the average mass to flux ratio was approximately twice the critical value. This is also consistent with the results presented here.

Ambipolar diffusion models predict the formation of a supercritical core after a period of quasi-static contraction. Our results can be made to be consistent with this picture. However, these observations do not rule out models that are dominated by turbulence, which are magnetically supercritical at all times. Ambipolar diffusion models predict that cores are subcritical earlier in their evolution. Observations of cores at this younger age might be able to distinguish between turbulent and ambipolar diffusion models.

The Chandrasekhar-Fermi technique has been shown to yield magnetic field strengths that are consistent with our current understanding of star formation, and to provide a way of measuring field strengths on a smaller scale than is possible with any other technique.

Chapter 4

Scan-map Observations of Three Molecular Clouds

4.1 Introduction

In this chapter I present scan-map data for three molecular clouds, Orion B, L1689 and RCrA. Each region was mapped at 450 μm and 850 μm. The aspects of the data reduction that are specific to each region are discussed. The features of each map are discussed and the flux density from each object in the maps is measured. The results are analysed in Chapter 5.

4.2 The Orion B Molecular Cloud

The Orion giant molecular cloud is the closest high mass star-forming region (Genzel & Stutzki, 1989). It is located approximately 400 pc from the sun (Brown, de

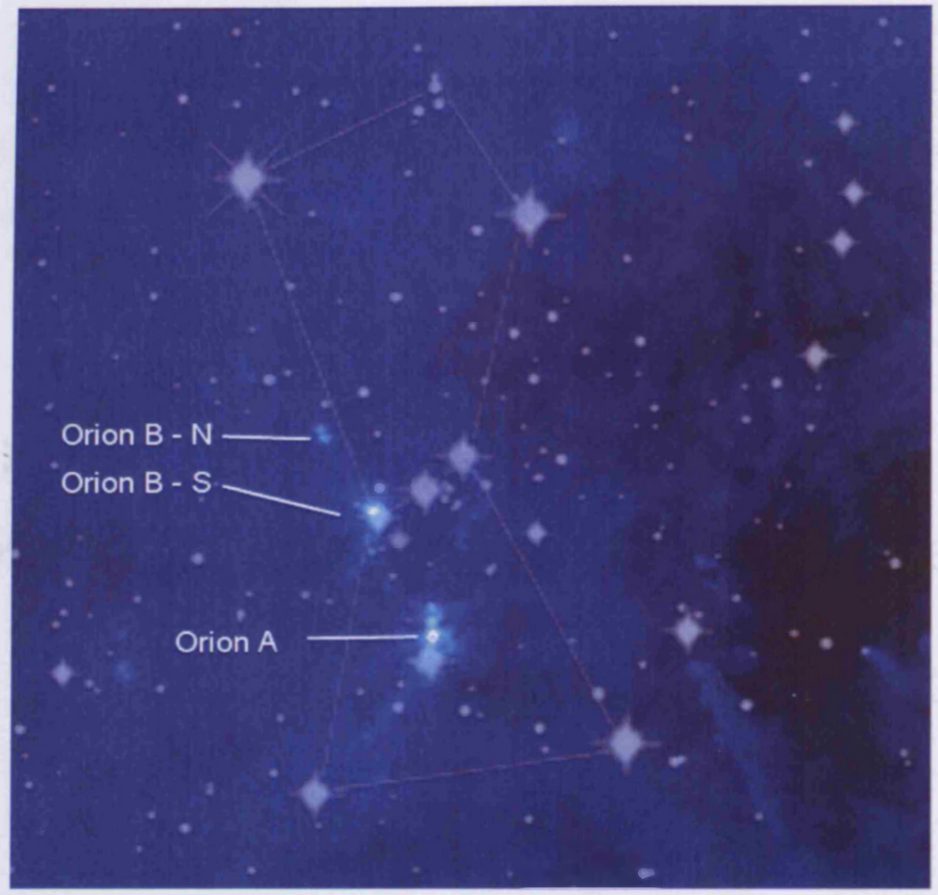

Figure 4.1: The familiar constellation of Orion, overlaid on the 100 μm IRAS data. The Orion A and B molecular clouds are labelled. IRAS images were obtained using the skyview interface (McGlynn, 2003).

Geus, & de Zeeuw, 1994). The molecular cloud is illustrated in Figure 4.1, which shows the IRAS 100 μm map, with the brighter stars of the familiar constellation of Orion overlaid.

The molecular cloud is composed of two parts. The Orion A cloud (L1976) is located in the sword of the Orion constellation. It contains the Orion Nebula (M42), which is the most active site of current star formation in the region, and houses the Trapezium cluster of O and B stars. The Orion B cloud (L1630) lies approximately 5° (35 pc) north of Orion A and is made up of two sub-clouds. The

Orion B south cloud contains the star-forming region NGC 2023/2024, which can be found almost coincident with the eastern-most star in Orion's belt. NGC 2024 is the formation site of the only O stars in Orion B. This part of the cloud is the location of the famous Horsehead nebula. Orion B north is located 2.5° (17 pc) north of NGC 2024, and contains the NGC 2068/2071 and HH24-26 star-forming regions. The data presented in this thesis concern only the Orion B north region, which is hereafter simply called Orion B for brevity.

The distance to the Orion GMC was determined by Brown et al. (1994) using optical photometry of a large number of stars along the line of sight to the cloud. The distance modulus for each star was calculated, and compared to its extinction. The front of the cloud was the point at which the extinction begins to increase more rapidly with distance. This yielded a distance to the near-side of the cloud of ~ 320 pc.

The distance to the rear of the cloud was calculated by comparing the extinction in front of each star (calculated using optical photometry), to the extinction along the entire line of sight (inferred from 100 μm emission). Stars at the back of (or beyond) the cloud, have an equal extinction calculated using both methods. This method yielded a distance of $\sim 500 \pm 30$ pc to the rear of the cloud.

The extent of the cloud along the line of sight of ~ 180 pc is comparable with its size on the plane of the sky, which is ~ 120 pc (assuming an average distance of ~ 400 pc).

4.2.1 Observations

Scan-map observations of the Orion B region were undertaken on the nights of 1998 December 15^{th} – 17^{th}. The observation details are given in Table 4.1. The atmospheric conditions were good on the nights of 1998 December 15^{th} and 16^{th}, with the atmospheric opacity low enough to obtain 450 μm data. On the 17^{th} however, the conditions were considerably worse. This is shown in column 5 of Table 4.1, and the effects are clearly seen in the noise level of the maps (Table 4.2).

The observing strategy was to split the field into six regions and scan-map each region twice. The exception to this was LBS23, which was only mapped once. Each scan-map was carried out as discussed in Chapter 2, by making 6 'sub-maps', each with a different chop configuration. The chop configurations used had chop throws of 20″, 30″ and 65″ in both RA and Dec. The telescope pointing was checked at regular intervals throughout the nights using planets, secondary calibrators and local pointing sources.

The area mapped is illustrated in Figure 4.2, where the scan-mapped regions are overlaid on an optical image with contours of IRAS 100 μm emission. Table 4.1 gives the coordinates of the regions mapped, and the dates each region was observed.

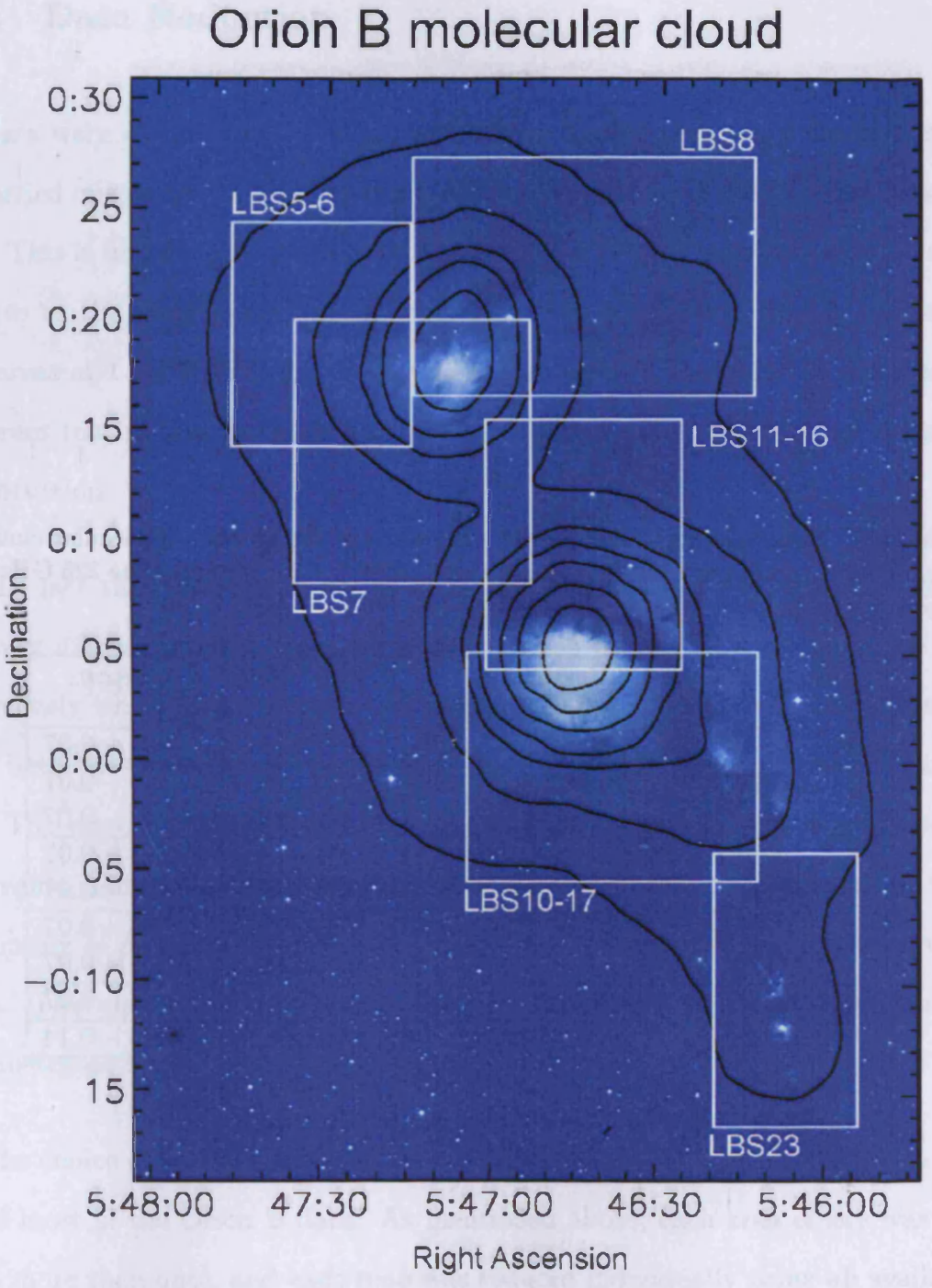

Figure 4.2: Map of the Orion B region showing the scan-mapped areas (white boxes and labels). The background 0.5 μm image is taken from the Digital Sky Survey. The contours are IRAS 100 μm emission at levels of 100, 300, 600, 1000, 1500, 2000 and 2500 $MJySr^{-1}$. Both images were obtained using the skyview interface (McGlynn, 2003).

Table 4.1: The positions of each of the scan-maps of the Orion B molecular cloud. The atmospheric conditions over the course of each night are indicated by the 225 GHz optical depth in column 5.

Region Name	Region Centre		UT Date	τ_{225GHz}
	RA	Dec		
LBS10-17	5:46:40	+0:00:00	1998 Dec 15	0.06 - 0.07
LBS11-16	5:46:40	+0:10:00	1998 Dec 15	0.06 - 0.07
			1998 Dec 16	0.06 - 0.07
LBS7	5:47:15	+0:13:00	1999 Dec 15	0.06 - 0.07
			1998 Dec 16	0.06 - 0.07
LBS5-6	5:47:30	+0:20:00	1999 Dec 15	0.06 - 0.07
			1998 Dec 16	0.06 - 0.07
LBS8	5:46:45	+0:23:00	1998 Dec 16	0.06 - 0.07
LBS23	5:46:10	−0:11:00	1998 Dec 17	0.13 - 0.14

4.2.2 Data Reduction

The data were reduced as described in Chapter 2. For each map, the reduction was carried out using the same method, with the exception of the baseline removal stage. This is because the different baseline removal (SCAN_RLB) routines are very sensitive to the morphology of the map, particularly low level flux density over large areas and regions of flux density near the edges of the map. In some cases a different routine was found to be more appropriate and to give a more accurate reconstruction.

The fact that different methods of removing the baseline can produce maps with very different appearances, means that it can be very difficult to decide unambiguously which reconstruction is the most reliable. Fortunately, most areas of sky in both the Orion B region and the L1689 region were scan-mapped more than once. The reason for this duplication was to improve the signal to noise ratio of each region, though as a by-product it gives an additional constraint on the true distribution of flux density on the sky due to the different scan directions or map offsets. This constraint has proved crucial in the reduction of these data and is well illustrated below.

The choice of baseline removal technique was relatively straightforward in the case of most of the Orion B data. As mentioned above, each area of sky was observed more than once, and each map was reduced individually using all available baseline removal routines. It was immediately apparent that the METHOD=SECTION routine produced maps with notably different morphology from the other techniques on a number of occasions. This is illustrated in Figure 4.3 which shows the LBS10-17 region, reduced using the MEDIAN and SECTION methods respectively.

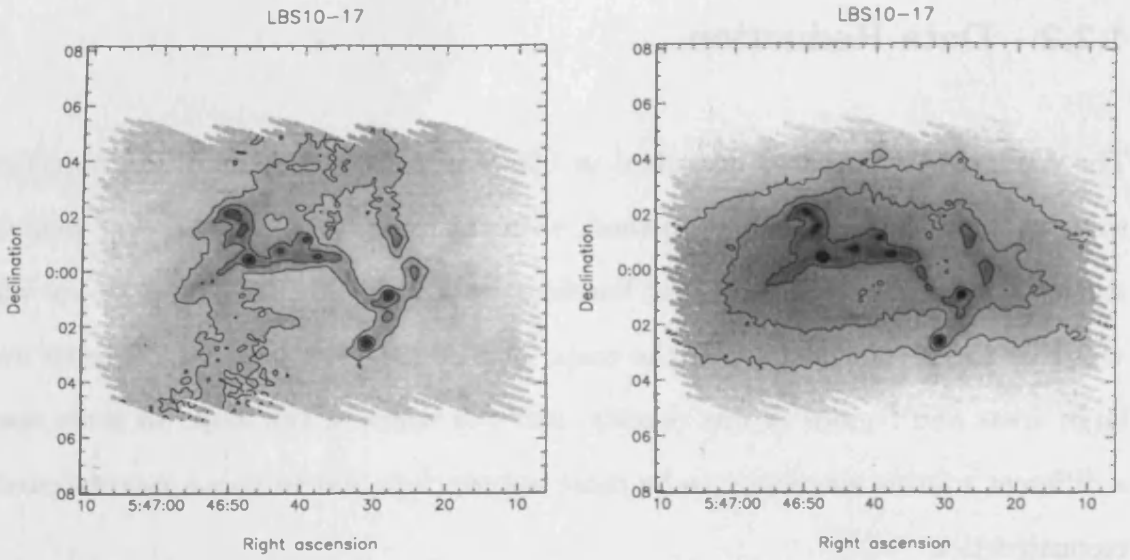

Figure 4.3: (a) & (b). Figures showing the LBS10-17 region reduced with (a) MEDIAN and (b) SECTION methods, illustrating the differences that can occur with different methods.

As can clearly be seen, though the density peaks of the two maps are similar, the level that the peaks sit on is very different. Without additional information it would be difficult to decide which of the two reconstructions is the more accurate. Fortunately a duplicate scan-map of the region allows some ambiguity to be removed, as is demonstrated by Figure 4.4. When all four reconstructions are considered, it is clear that Figure 4.3(b) is anomalous. The SECTION routine produces anomalous results for a number of different maps, in each case the artefact being an area of elevated flux density roughly following the shape of the scan-map itself. This routine was therefore not used at all for the Orion B dataset.

The METHOD=LINEAR routine was also tried with a number of different values for the CHOP parameter (the distance from the end of the scan that is averaged to form one end of a linear interpolation along the scan — see Section 2.4.5). These give essentially the same reconstruction as the MEDIAN routine, but with some 'streaking' along the scan direction (evidence of the direction of the scan in the middle of the map). This is illustrated in Figure 4.5 which compares a

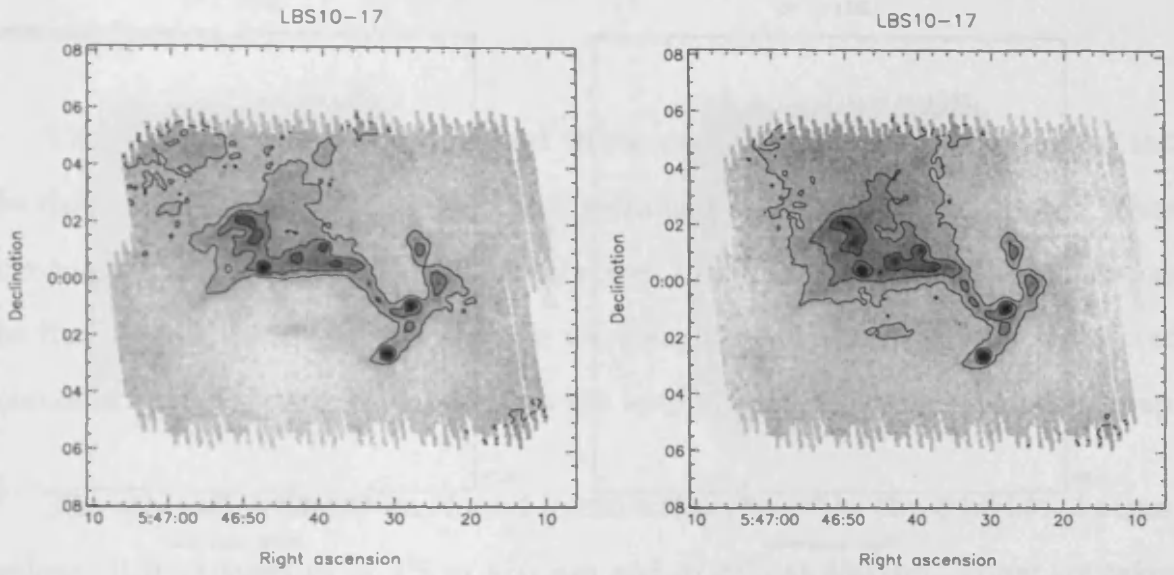

Figure 4.4: (a) & (b). Figures showing a second scan-map of the LBS10-17 region, reduced with (a) MEDIAN and (b) SECTION methods, illustrating how a duplicate scan-map can remove some ambiguity in selecting a reduction technique.

MEDIAN and LINEAR reconstruction. This streaking is less apparent when a larger chop is chosen, but does not go away entirely. This streaking is probably due to incomplete removal of the baselines, caused by too little data being used to calculate each baseline.

Figure 4.5 also shows how flux density at the edge of a map can cause a problem with the reconstruction. The white area above the object at the far south of the map is an area of negative flux density which must be a reduction artefact as this is unphysical. This type of artefact is due to the baseline being fitted incorrectly. In this case it is easy to see why the baseline would be incorrectly fitted if a source is present in the region used to generate the fit. The median routine uses the whole scan to generate the baseline so is less susceptible to these artefacts. As a result of these issues, the MEDIAN routine was used for all of the Orion B data.

As a check on the reproducibility of the data, the flux density from each of the cores was measured for each individual scan-map. This showed that the majority

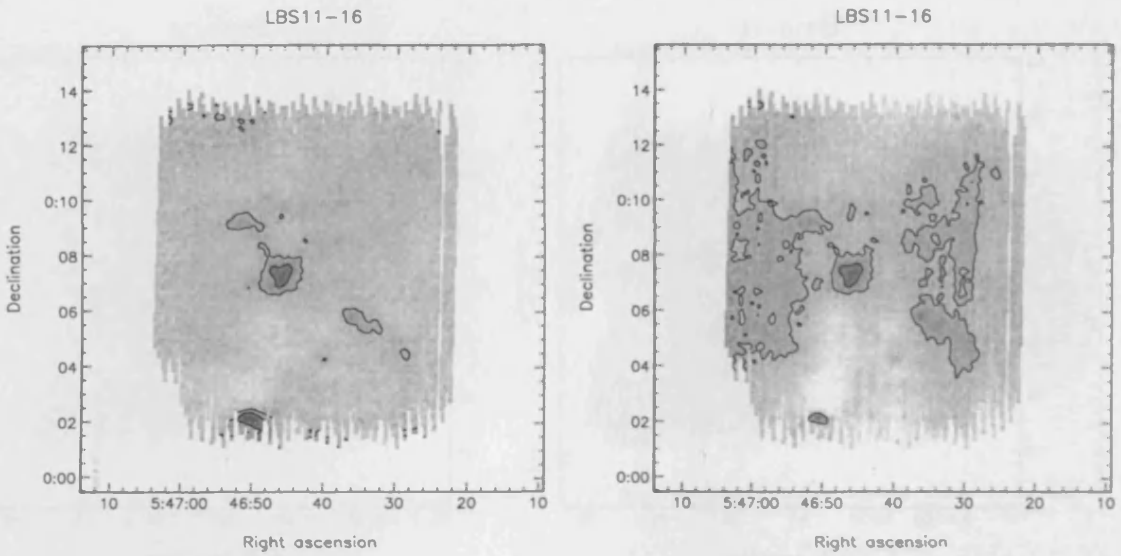

Figure 4.5: (a) & (b). Figures showing a scan-map of the LBS11-16 region, reduced with (a) MEDIAN and (b) LINEAR methods, illustrating reduction artefacts.

of the cores were consistent within 2σ in all scan-maps.

The primary calibrator Uranus was observed each night, and secondary calibrators observed at different times during the night showed that the calibration was consistent. As discussed in Chapter 2, the optimal way of co-adding the data into a single map is to do so before the dual beam is deconvolved. An implication of this is that different parts of the map, that were made on different nights, could potentially have different calibrations. To get round this problem, a number of composite calibration maps were made, using data from different nights. This enabled a map that was composed of data observed on two different nights to be calibrated using a map of Uranus made with data obtained on the same two nights.

Sources that were unresolved at 850 μm in the 14″ JCMT beam were calibrated in Jy/beam. Extended objects were calibrated by measuring the flux within an aperture, and comparing this value to the flux density measured within the same sized aperture on a calibrator map. The choice of aperture size is discussed in

detail in Section 4.5.

The 450 μm maps were smoothed to the resolution of the 850 μm maps, and the data were measured using the same technique as for the 850 μm data. While this does cause a loss of resolution, it increases the signal to noise ratio, and causes the flux density measured for the two wavelengths to be equivalent. Undetected sources are given upper limits based on the level of noise in that region of the map.

The calibration factor was found found to vary over the three nights of observations. It fluctuated by ± 4% at 850 μm and ± 20% at 450 μm. These are taken to be the absolute calibration error on the data.

4.2.3 Data

Figures 4.6 and 4.7 show the reduced data for the Orion B region. The area mapped is approximately 0.2 square degrees, which at the distance of the Orion molecular cloud is equal to ~ 9 pc^2. The maps are made up of a mosaic of six regions, each of which was mapped twice (with the exception of LBS23, which was only mapped once). The names of the regions are marked on the maps.

One of the two scan-maps of the LBS10-17 region has a higher noise level, and when included in the reduction, increases the 1σ noise level by a factor of 2 at 450 μm. This scan-map was therefore left out of the reduction at this wavelength. The LBS23 region is not included in the 450 μm map, because the noise is significantly higher, and none of the sources present in the 850 μm map are detected. The reason for the increased noise level in this region is that conditions were significantly poorer, as shown in Table 4.1.

Table 4.2: Table showing the noise levels for each region of the Orion B maps

Region Name	Region Centre		1σ noise (Jy/beam)	
	RA (2000)	Dec. (2000)	850 μm	450 μm
LBS10-17	5:46:40	+0:00:00	0.028	0.26
LBS11-16	5:46:40	+0:10:00	0.021	0.29
LBS7	5:47:15	+0:13:00	0.021	0.28
LBS5-6	5:47:30	+0:20:00	0.023	0.27
LBS8	5:46:45	+0:23:00	0.027	0.52
LBS23	5:46:10	−0:11:00	0.072	19.00

The 1σ noise levels are given in Table 4.2. These were found by first subtracting a heavily smoothed map to remove the large scale structure. The background offset was calculated by measuring the mean value in the regions away from any sources. When measuring the flux density of any source, the background level appropriate for that map was taken into account.

Figures 4.6 and 4.7 show a number of sources and filaments. The majority of the sources appear to be associated with filaments. The morphology of the two maps is very similar at both wavelengths, and most sources are present in both maps. Some of the fainter filamentary structure that is detected at 850 μm is not seen in the 450 μm map, though this is to be expected as the noise level is higher in the short wavelength map.

We can identify a large number of cores and filaments in the data. The flux densities of the cores that have been detected are given in Table 4.3. The 450 μm data was smoothed to the resolution of the 850 μm data so that the flux values are comparable. This has the added advantage of increasing the signal to noise of the 450 μm data. For both 850 μm and 450 μm, the flux density of unresolved cores is quoted as Jy/14″ beam. The flux density from extended cores is given for the aperture size quoted in the table. Cores that are undetected at 450 μm are given

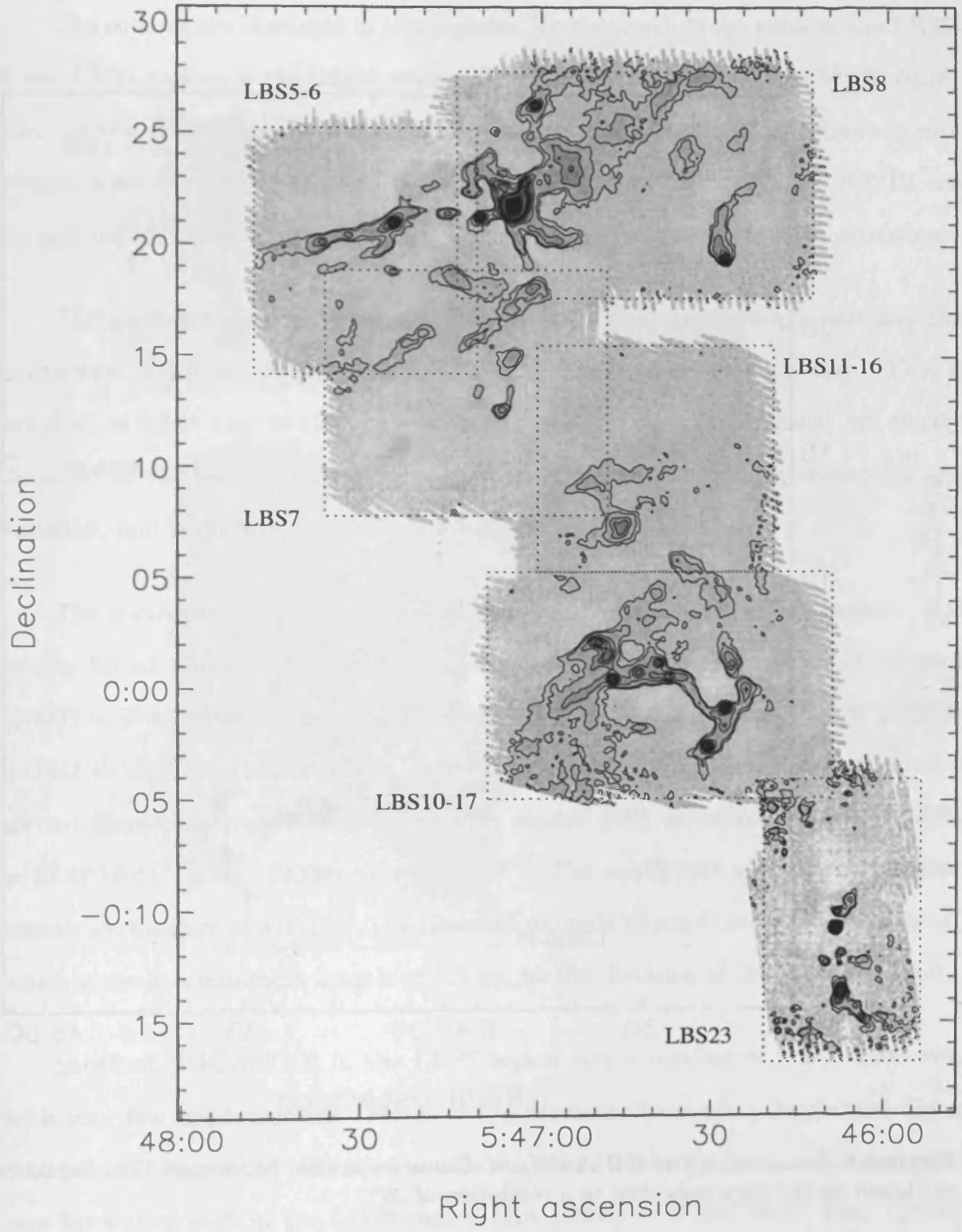

Figure 4.6: Scan-map of Orion B at 850 μm. Contours are 3σ, 5σ, 10σ, 15σ, 20σ, 25σ, 30σ. Contours are based on the map smoothed to a resolution of $18''$.

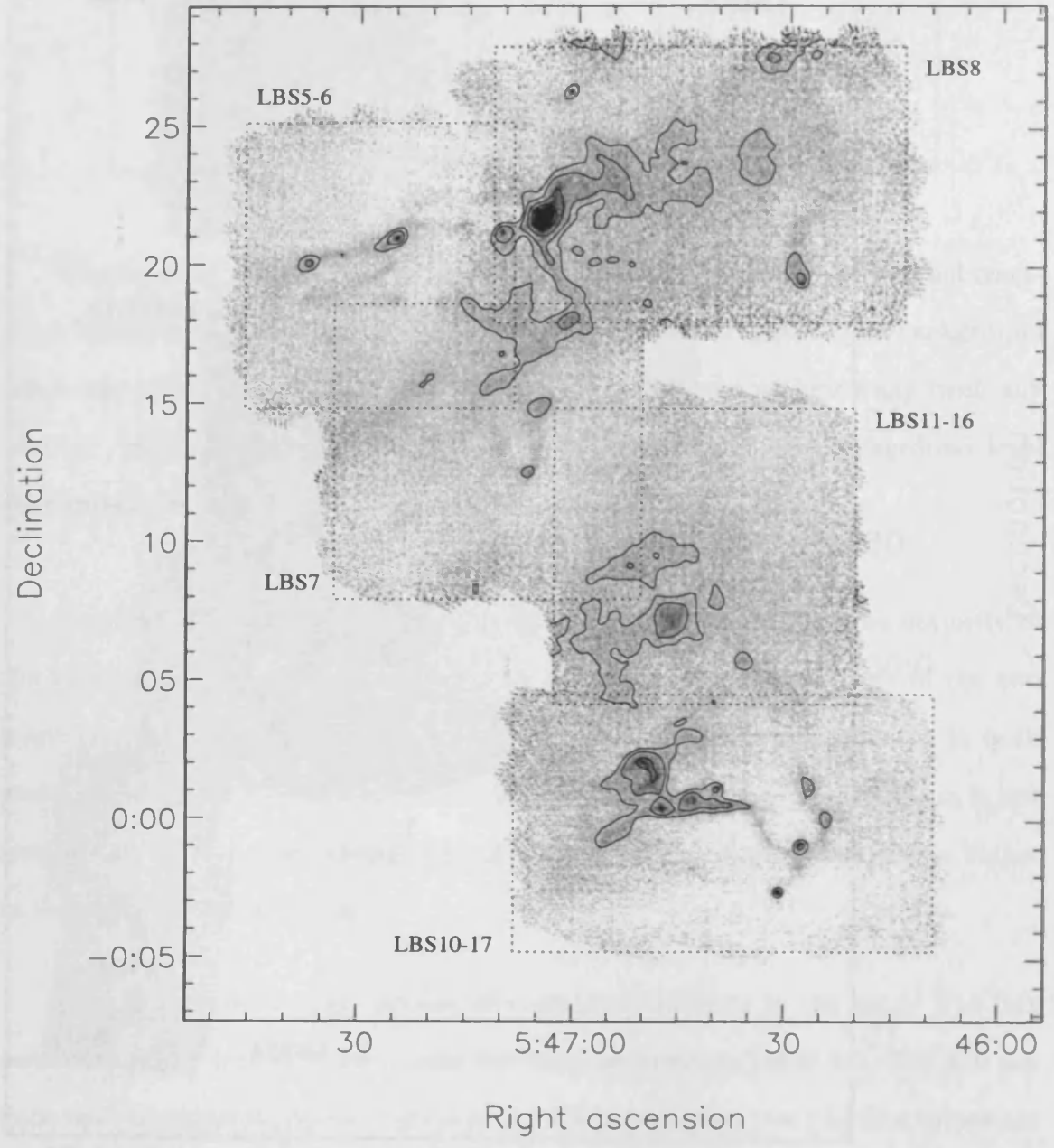

Figure 4.7: Scan-map of Orion B at 450 μm. Contours are 2σ, 3σ, 6σ and 12σ. Contours are based on the map smoothed to a resolution of 25″.

upper limits in units of Jy/14″ beam.

The sources are clustered in two regions. To the north of the map, in the LBS5-6 and LBS8 regions is the bright source NGC-2071IR at RA (2000) = $5^h\,47^m\,04.8^s$, Dec. (2000) = $+0°\,21'\,45''$ (source # 55), which is embedded in a large filament running in a north-west to south-east direction. The morphology of NGC-2071IR can be approximated by a Gaussian, surrounded by a number of low-level extensions.

There are very prominent extensions from the core to the north-east and the south-west, both of which are undetected in the short-wavelength map. This is notable, as other sources that have a similar 850 μm peak flux density, are clearly detected at 450 μm. This is probably caused by contamination by molecular line emission, and is discussed further in Chapter 5.

The north-west side of the filament does not contain many condensations, and is very broad. The filament shows an enhancement in density at coordinates RA (2000) = $5^h\,46^m\,55.0^s$, Dec. (2000) = $+0°\,23'\,30''$, along an axis that is perpendicular to the main filament axis. This is probably simply the superposition of a second filament, which is associated with source #49, at coordinates RA (2000) = $5^h\,47^m\,01.1^s$, Dec. (2000) = $+0°\,26'\,19''$. The south-east side of the filament contains a number of sources. The filament extends beyond the edges of the map, which gives it a minimum length of 2.8 pc, at the distance of the Orion B cloud.

South of NGC-2071IR in the LBS7 region, are a number of broad filaments, with very few condensations. Many of the filaments increase in brightness along their length. This could indicate a source at the end of the filament, as is clearly the case for source #48 in the LBS8 region (RA (2000) = $5^h\,46^m\,28.2^s$, Dec. (2000) = $+0°\,19'\,29''$). Alternatively, the filaments being brighter at one end could be

explained by the filament bending round to lie closer to the line of sight. This second explanation is taken to be the case for the majority of the filaments in the LBS7 region, as the density peaks are very broad, and the increase in their flux density is often gradual along their length. This is illustrated in Figure 4.8.

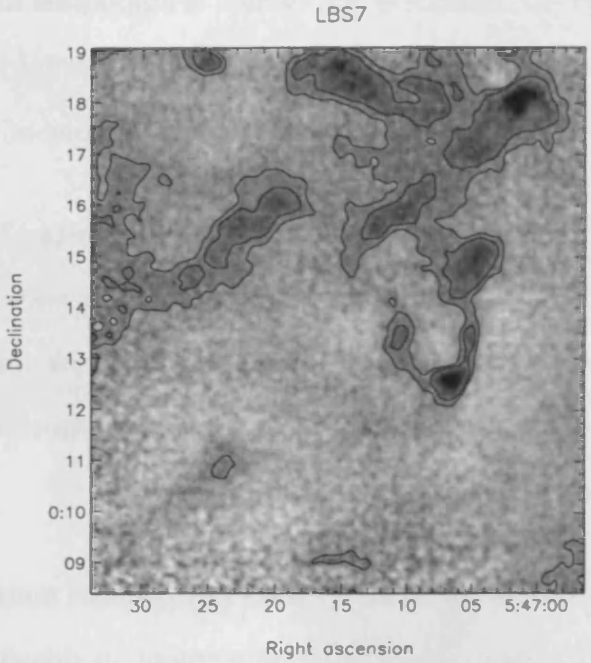

Figure 4.8: An enlargement of the LBS7 region, showing the broad filaments, many of which are not associated with a source.

To the south of the map, in the LBS10-17 region, lie a number of sources, connected by a network of filaments. At the far south of the map, in the LBS23 region, are a number of sources that lie in a line running north-south. Apart from one of the sources being elongated in a north-south direction, there is no direct evidence of the filament itself. This non-detection could be attributed to the noise level being approximately 3 times larger in this region than in the rest of the map. I return to this region in Section 4.5, when I discuss the extraction of further information from the data. The data are then analysed in the following chapter.

Table 4.3: The position and measured flux of each core in the Orion B maps, at 850 μm and 450μm. Column 4 indicates whether or not the core is extended in the 14″ 850 μm JCMT beam. The peak flux is quoted for unresolved sources (columns 6 and 8), and the integrated flux within an aperture is given for extended sources (columns 7 and 9). The aperture size used is given in column 5. 3σ upper limits are quoted for sources that are undetected at 450 μm.

Source ID	RA (2000)	Dec. (2000)	Ext.	Aperture diameter (arcsec)	850 μm		450 μm	
					Peak (Jy/beam)	Int. (Jy)	Peak (Jy/beam)	Int. (Jy)
1	5:46:03.7	−0:14:47	N	–	0.7	–	< 39.3	–
2	5:46:04.9	−0:14:20	N	–	0.5	–	< 39.3	–
3	5:46:07.4	−0:13:38	Y	42	–	2.9	< 39.3	–
4	5:46:03.7	−0:12:12	N	–	0.4	–	< 39.3	–
5	5:46:10.1	−0:12:19	N	–	0.5	–	< 39.3	–
6	5:46:07.6	−0:11:52	N	–	0.5	–	< 39.3	–
7	5:46:08.5	−0:10:45	Y	33	–	3.7	< 39.3	–
8	5:46:08.2	−0:10:03	N	–	0.8	–	< 39.3	–
9	5:46:06.1	−0:09:29	N	–	0.4	–	< 39.3	–
10	5:46:30.9	−0:02:35	Y	32	–	2.4	–	6.1
11	5:46:28.1	−0:01:37	N	–	0.4	–	2.1	–
12	5:46:27.8	−0:00:52	Y	30	–	2.0	–	8.2
13	5:46:24.1	−0:00:01	Y	36	–	1.0	–	5.8
14	5:46:26.7	+0:01:08	N	–	0.5	–	3.1	–
15	5:46:27.4	+0:01:32	N	–	0.3	–	2.5	–
16	5:46:29.3	−0:01:09	N	–	0.4	–	< 0.6	–
17	5:46:32.5	−0:00:38	N	–	0.3	–	1.5	–
18	5:46:33.4	−0:00:11	N	–	0.3	–	1.9	–
19	5:46:35.1	+0:00:34	N	–	0.4	–	2.7	–
20	5:46:37.7	+0:00:35	Y	28	–	1.2	–	7.4
21	5:46:42.5	−0:01:43	N	–	0.2	–	1.2	–
22	5:46:40.5	+0:00:35	N	–	0.4	–	3.4	–
23	5:46:39.4	+0:01:11	Y	28	–	1.3	–	7.4
24	5:46:42.9	+0:00:48	Y	29	–	1.3	–	10.9
25	5:46:47.4	+0:00:26	Y	35	–	2.4	–	13.8
26	5:46:48.2	+0:01:35	Y	34	–	1.9	–	15.8

Table 4.3: continued.

Source ID	RA (2000)	Dec. (2000)	Ext.	Aperture diameter (arcsec)	850 μm		450 μm	
					Peak (Jy/beam)	Int. (Jy)	Peak (Jy/beam)	Int. (Jy)
27	5:46:49.9	+0:02:07	Y	36	–	2.1	–	17.5
28	5:46:40.3	+0:04:16	N	–	0.2	–	2.3	–
29	5:46:28.5	+0:04:26	N	–	0.2	–	< 0.6	–
30	5:46:36.3	+0:05:49	N	–	0.3	–	2.9	–
31	5:46:45.9	+0:07:17	Y	52	–	2.8	–	25.9
32	5:46:51.9	+0:09:13	N	–	0.2	–	< 0.6	–
33	5:47:36.9	+0:20:07	Y	35	–	1.2	–	7.8
34	5:47:32.6	+0:20:24	N	–	0.4	–	3.1	–
35	5:47:25.2	+0:18:49	N	–	0.2	–	1.6	–
36	5:47:24.9	+0:20:59	Y	35	–	2.6	–	13.4
37	5:47:26.4	+0:20:48	N	–	0.5	–	3.6	–
38	5:47:26.2	+0:19:56	N	–	0.3	–	1.9	–
39	5:47:15.3	+0:18:42	N	–	0.3	–	3.0	–
40	5:47:16.0	+0:21:24	N	–	0.4	–	2.2	–
41	5:47:10.5	+0:21:14	Y	28	–	1.5	–	10.8
42	5:47:12.4	+0:22:23	N	–	0.3	–	< 0.5	–
43	5:47:01.7	+0:18:00	Y	32	–	1.2	–	11.4
44	5:47:06.8	+0:12:34	Y	29	–	0.8	–	7.0
45	5:47:04.6	+0:14:59	Y	53	–	1.4	< 0.6	–
46	5:47:10.6	+0:13:23	Y	28	–	0.3	< 0.6	–
47	4:47:05.2	+0:13:29	Y	27	–	0.3	< 0.6	–
48	5:46:28.2	+0:19:29	Y	29	–	1.7	–	11.9
49	5:47:01.1	+0:26:19	Y	32	–	1.7	–	11.6
50	5:47:07.8	+0:25:08	N	–	0.2	–	< 0.6	–
51	5:46:57.2	+0:23:56	N	–	0.4	–	3.6	–
52	5:46:59.1	+0:22:58	N	–	0.3	–	4.3	–
53	5:46:57.2	+0:20:11	N	–	0.4	–	< 1.1	–
54	5:47:06.5	+0:22:35	Y	40	–	2.3	–	–
55	5:47:04.8	+0:21:45	Y	86	–	32.4	–	230.6

4.3 The L1689 Molecular Cloud

The L1689 molecular cloud is part of the ρ Ophiuchi complex, which as discussed in Section 3.4 is located at a distance of 130 $\pm$ 20 pc from the sun. It was first detected by Lynds (1962) in a large study of the dark nebulae detected in the Palomar Observatory Sky Survey plates. The ρ Ophiuchi complex was extensively mapped by Loren (1989) using ^{13}CO at a resolution of 2.4′. The resulting map of the cloud is shown in Figure 4.9. The data showed that the molecular cloud is composed of a number of sub-clouds, the most massive of which is L1688. A number of filamentary clouds (L1709, L1740, L1744, L1755 and L1765) extend from L1688 in a north easterly direction, and are often called the streamers. To the south-east of L1688 lies L1689, which also has filamentary clouds (L1712 and L1729) extending in roughly the same direction. Loren measured masses for L1688 and L1689 of 1447 $M_\odot$ and 566 $M_\odot$ respectively, while the components of the streamers have lower masses of 100–300 $M_\odot$. The direction of the streamers turns to the south at the positions of both L1688 and L1689, forming a horseshoe shape in the case of L1688.

Loren (1989) noted that the morphologies of the two main clouds L1688 and L1689 are similar, in that the star formation in each cloud was concentrated at the western edge. He suggested that this was a result of an interaction with the Sco OB2 association, which lies to the west of the clouds. However, the star formation activity in the two clouds is very different. The star formation efficiency (SFE) of L1688 was calculated to be 34–47% (Wilking & Lada, 1983). L1689 appears to have a much lower SFE (Loren, Wootten, & Wilking, 1990), and as a result, has received less attention than its more active neighbour.

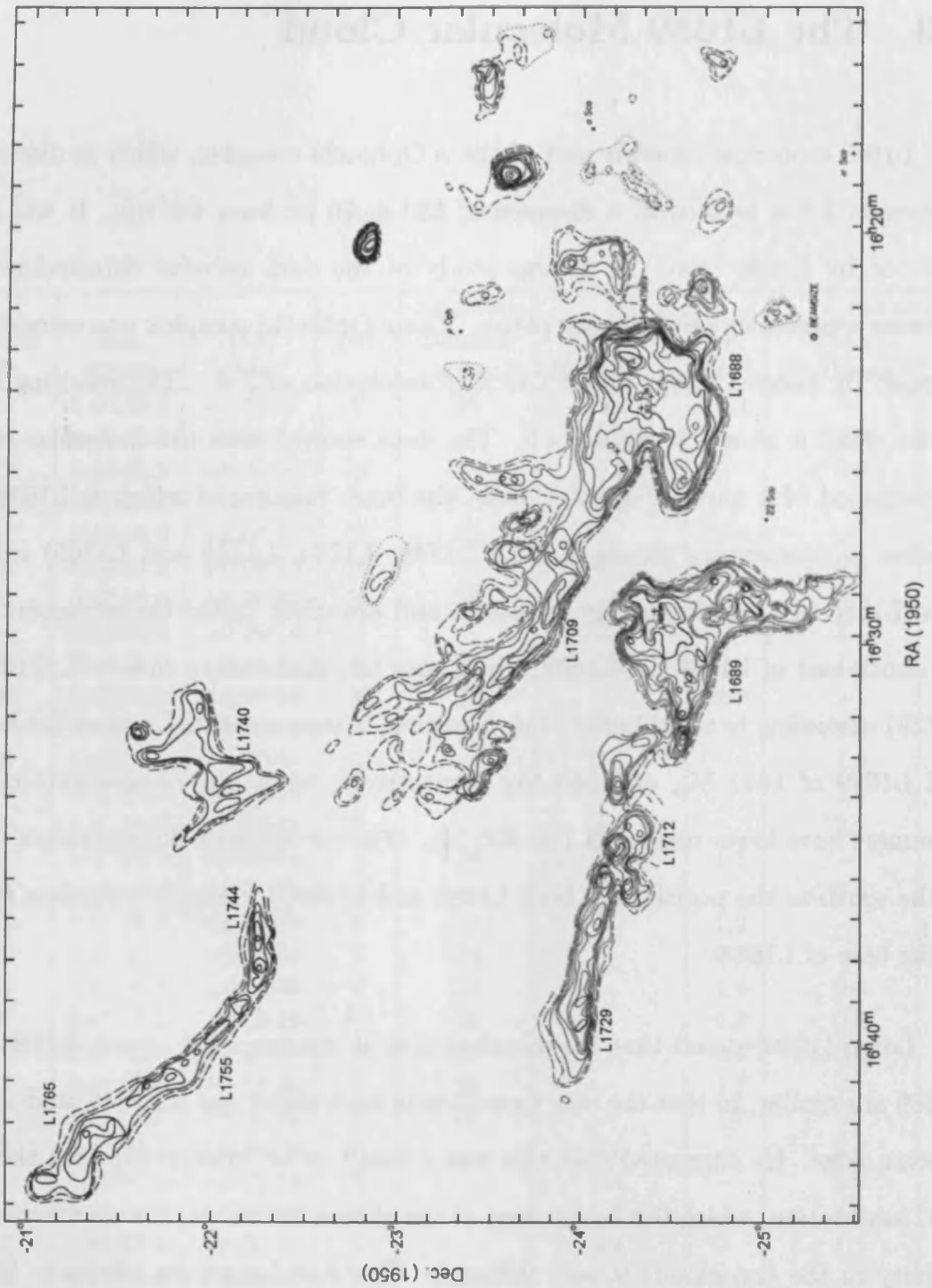

Figure 4.9: ^{13}CO map of the ρ Ophiuchi complex, from Loren (1989). The contour levels give antenna temperatures $T_R^*(^{13}\mathrm{CO})$ of 4, 5, 6, 7, 8, 10, 12, 14, 18 and 20 K. The names of the clouds are marked.

Loren et al. (1990) mapped the L1688, L1689 and L1709 clouds in DCO^+, and discovered a dozen dense clumps, most of which lie in the more massive L1688 cloud. I have chosen to name the objects detected in DCO^+ *clumps* and not *cores*, to avoid confusion with the prestellar cores that are detected in the submillimetre. DCO^+ is only seen in the very cold and dense regions of the cloud, as the molecule is easily dissociated by nearby stars of moderate luminosity. The DCO^+ clumps within L1688 have recently been mapped in the submillimetre continuum to determine the properties of their populations of prestellar and protostellar objects (Motte et al., 1998; Johnstone et al., 2000b). To date, there are no comparable published surveys of the L1689 cloud. In this Section, I discuss a large area SCUBA scan-map survey of the L1689 cloud. The results of this survey are analysed and comparisons with L1688 are made in Section 5.3.

4.3.1 Observations

Scan-map observations of the L1689 region were carried out between 1999 March 9^{th} and 2000 April 12^{th}. The details are given in Table 4.4. The atmospheric conditions were good on all nights. The scan-maps were performed in the same manner as for the Orion B region, though the chop throws used were 30″, 44″ and 68″. These chop throws are believed to give a better spatial frequency coverage. The telescope pointing was checked at regular intervals throughout the nights using planets, secondary calibrators and local pointing sources. The naming system for each scan-map is based either on its 1950 coordinates, or on any previously known sources within the region. The relative position of the different scan-maps is shown in Figure 4.10.

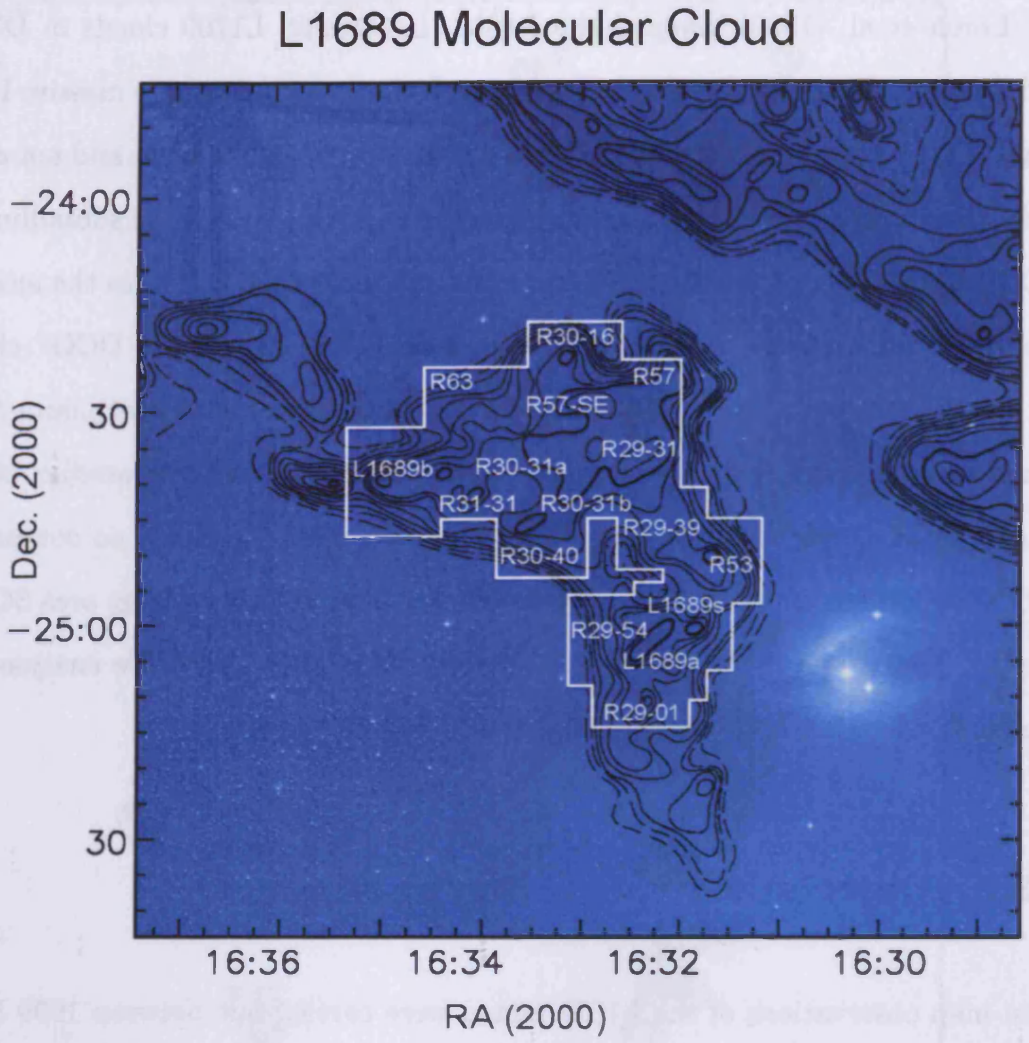

Figure 4.10: A composite map of the L1689 region showing the scan-mapped areas (white outline and labels). The background 0.5 μm image is taken from the Digital Sky Survey, obtained using the skyview interface (McGlynn, 2003). The contours are ^{13}CO emission at $T_R^\star(^{13}\mathrm{CO})$ of 4, 5, 6, 7, 8, 10, 12, 14, 18 and 20 K (Loren, 1989).

4.3.2 Data Reduction

As with the Orion B data, each area of the sky was scan-mapped more than once, though each subsequent scan-map was offset from the previous one to create a mosaic. The reason that this method of mosaicking was used, was to remove

Table 4.4: The positions of each of the scan-maps made of the L1689 molecular cloud. The atmospheric conditions over the course of each night are indicated by the 225 GHz optical depth in column 5.

Region Name	Region Centre		UT Date	τ_{225GHz}
	RA	Dec		
R29-01	16:32:22.7	−25:07:50	1999 Apr 08	0.06 – 0.07
			2000 Apr 10	0.05 – 0.06
L1689a	16:32:12.6	−25:03:21	1999 Aug 08	0.05 – 0.07
			1999 Aug 09	0.06 – 0.08
L1689s	16:31:56.7	−24:58:52	1999 Mar 09	0.07 – 0.11
			2000 Apr 10	0.05 – 0.06
R29-54	16:31:41.4	−24:48:09	2000 Apr 10	0.05 – 0.06
R53	16:31:39.6	−24:49:43	1999 Mar 09	0.07 – 0.11
			2000 Apr 09	0.06 – 0.07
R29-39	16:32:11.5	−24:45:21	2000 Apr 09	0.06 – 0.07
R29-31	16:32:26.1	−24:37:20	2000 Apr 09	0.06 – 0.07
R30-31b	16:33:02.1	−24:37:17	2000 Apr 11	0.05 – 0.06
			1999 Aug 09	0.06 – 0.08
R57	16:32:25.9	−24:28:20	1999 Mar 09	0.07 – 0.11
R57-SE	16:33:17.0	−24:32:16	1999 Mar 09	0.07 – 0.11
			2000 Apr 10	0.05 – 0.06
			2000 Apr 12	0.07 – 0.09
R30-16	16:33:01.9	−24:22:17	2000 Apr 12	0.07 – 0.09
R30-40	16:33:22.3	−24:46:16	2000 Apr 12	0.07 – 0.09
R30-31a	16:33:38.1	−24:37:15	2000 Apr 11	0.05 – 0.06
R31-31	16:34:14.1	−24:37:13	2000 Apr 11	0.05 – 0.06
R63	16:34:01.9	−24:28:13	1999 Aug 08	0.05 – 0.07
			1999 Mar 09	0.07 – 0.11
L1689b	16:34:50.2	−24:38:04	1999 Aug 08	0.05 – 0.07
			1999 Aug 09	0.06 – 0.08
			2000 Apr 11	0.05 – 0.06

artefacts in the map caused by the edges of a scan-map being noisy relative to the centre. Another advantage of this method is that a bright source on the edge of a map will be in the middle of a subsequent map rather than being on the edge of both scan-maps which could cause problems with the baseline removal.

The L1689 data were more difficult to reduce in a reliable way, primarily because the region contains weaker sources. Other than the very bright IRAS 16293, the majority of the sources in L1689 are less than 0.3 Jy/beam, compared to the large number of sources brighter than 0.8 Jy/beam in the Orion B region. The lower flux density means that incorrectly fitted baselines and residual sky-noise are more significant. Also, L1689 contains large areas of extended low level emission comparable in size with the scan-map, which make the baselines difficult to fit.

As a result of these issues, different baseline removal methods are more appropriate for different scan-maps. In the majority of cases, MEDIAN or LINEAR gave more consistent results, though in a small number of cases, SECTION or the more time consuming SUB-MEDIAN methods were used. A reconstruction was deemed inaccurate if the map displayed obvious artefacts such as negative holes or large positive regions tracing the shape of the scan-map (see Figures 4.11(a) and 4.11(b) respectively). Also, if areas on the map differed from the consensus of overlying or surrounding scan-maps by more than 3σ, they were not included.

As is clear from this Section, reducing scan-map data is far from straightforward and should be carried out with great care. The reduction recipes and pipelines that may work reliably for other SCUBA modes such as jiggle-mapping are not appropriate for scan-map data and the data should be reduced using more interactive procedures.

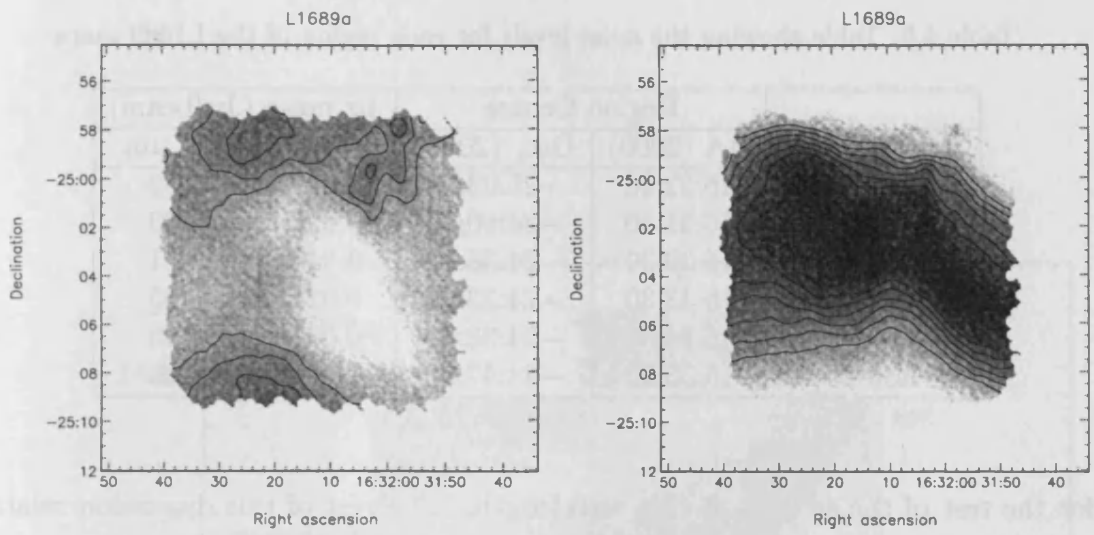

(a) (b)

Figure 4.11: (a) & (b). Figures displaying common map artefacts caused by incorrectly fitted baselines. (a) a negative hole caused by the LINEAR routine, (b) a large positive region caused by the SECTION method.

4.3.3 Data

Figures 4.12 and 4.13 show the reduced data for the L1689 region. Each map is comprised of 26 overlapping scan-maps. The area covered is approximately 0.5 square degrees, which at the distance of L1689, is equal to ~ 2.5 pc^2. Each map has been split up into 6 regions, which are marked on Figures 4.12 and 4.13. The 1σ noise level and the background offset for each of these regions is given in Table 4.5.

Figures 4.12 and 4.13 show that the L1689 region contains both differences and similarities to the maps of Orion B (Figures 4.6 and 4.7). In both regions, the maps consist of filaments with embedded cores. However, in the L1689 maps, there are much fewer sources, and the filaments are noticeably broader (by a factor of ~ 2 after accounting for the different distances to the two regions). From Figure 4.13, it is clear that there is very little detected in L1689 at 450 μm, other than the very bright source IRAS 16293-2422. Therefore only upper limits can be obtained

Table 4.5: Table showing the noise levels for each region of the L1689 maps

	Region Centre		1σ noise (Jy/beam)	
Region Name	RA (2000)	Dec. (2000)	850 μm	450 μm
L1689s	16:32:10	−25:03:00	0.019	0.59
R53	16:31:40	−24:50:00	0.026	2.33
R57	16:32:30	−24:35:00	0.046	1.51
R57-E	16:33:30	−24:33:00	0.024	0.85
L1689b	16:34:50	−24:38:00	0.021	0.53
R30-40	16:33:20	−24:47:00	0.034	1.26

for the rest of the sources at this wavelength. The rest of this discussion relates solely to the 850 μm map.

The flux densities of the L1689 cores are given in Table 4.6. Upper limits are given for most sources at 450 μm. For both 850 μm and 450 μm, the flux density of unresolved cores is quoted in Jy/14″ beam. The flux density from extended cores is given for the aperture size quoted in the table.

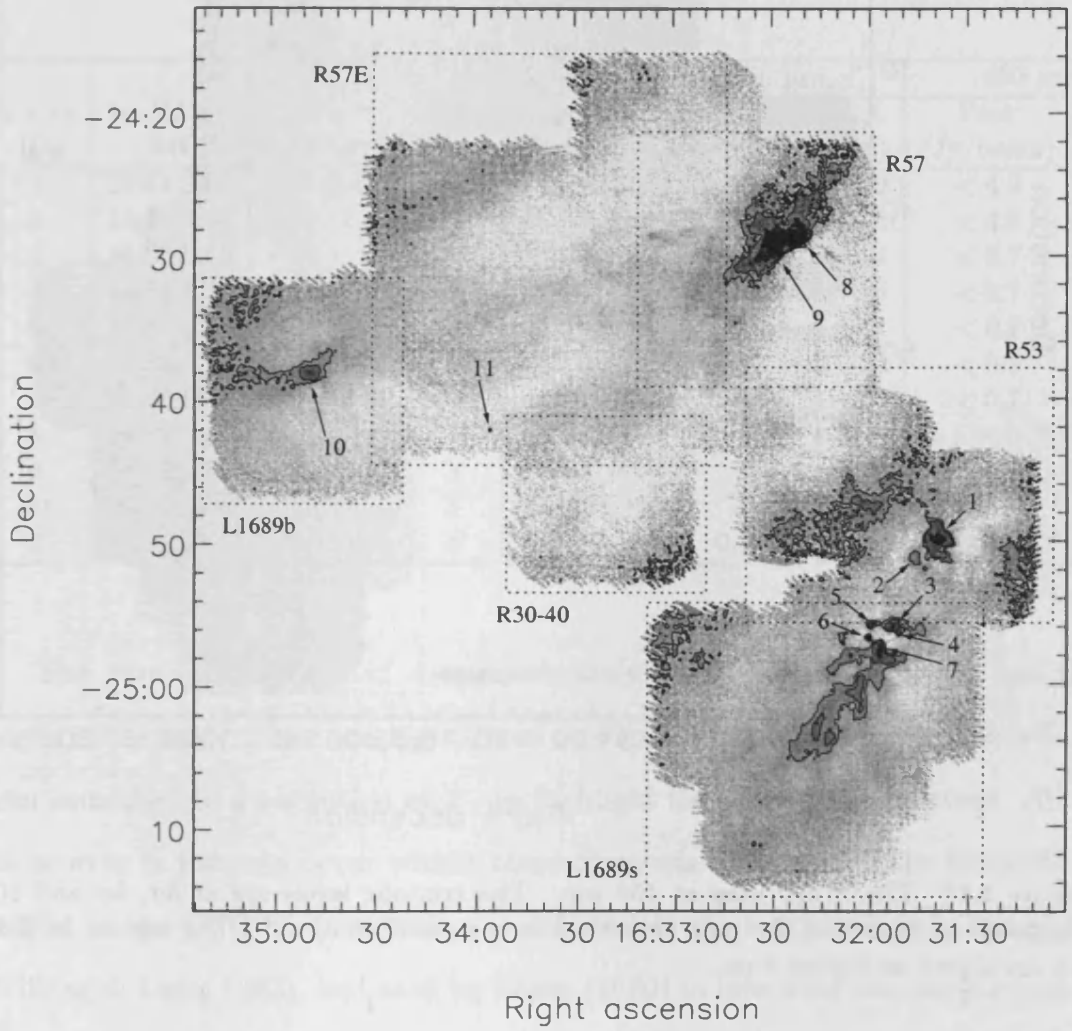

Figure 4.12: The L1689 map at 850 μm. The contour levels are at 3σ, 5σ, 10σ, 15σ, 20σ, 40σ and 80σ. Contours are based on the map smoothed to a resolution of $18''$. The regions in Table 4.5 are shown as dotted lines. The identified cores are marked on the map.

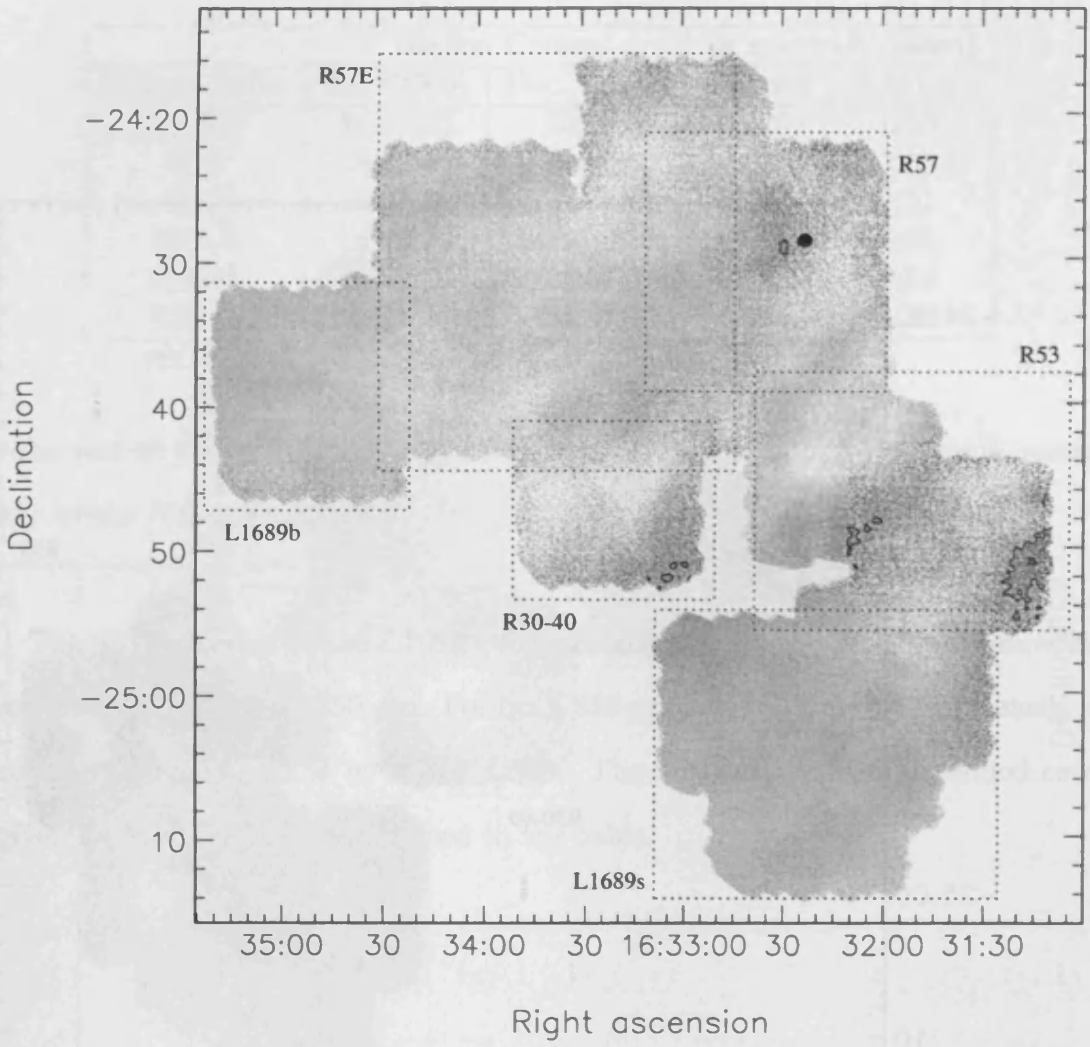

Figure 4.13: The L1689 map at 450 μm. The contour levels are at 3σ, 5σ and 10σ. Contours are based on the map smoothed to a resolution of $18''$. The regions in Table 4.5 are shown as dotted lines.

Table 4.6: The position and measured flux of each core in the L1689 maps, at 850 μm and 450μm. Column 4 indicates whether or not the core is extended in the 14″ 850 μm JCMT beam. The peak flux is quoted for unresolved sources (columns 6 and 8), and the integrated flux within an aperture is given for extended sources (columns 7 and 9). The aperture size used is given in column 5. 3σ upper limits are quoted for sources that are undetected at 450 μm.

Source ID	RA (2000)	Dec. (2000)	Ext.	Aperture diameter (arcsec)	850 μm		450 μm	
					Peak (Jy/beam)	Int. (Jy)	Peak (Jy/beam)	Int. (Jy)
1	16:31:39.0	−24:49:53	Y	151	–	8.9	< 4.9	–
2	16:31:46.4	−24:51:13	Y	58	–	0.8	< 4.9	–
3	16:31:53.5	−24:55:56	Y	59	–	1.4	< 0.7	–
4	16:31:52.0	−24:56:15	Y	29	–	0.5	< 0.7	–
5	16:31:59.9	−24:55:49	Y	44	–	0.4	< 0.7	–
6	16:32:01.0	−24:56:44	N	–	0.4	–	< 0.7	–
7	16:31:57.5	−24:57:39	Y	81	–	2.4	< 0.7	–
8	16:32:23.0	−24:28:40	Y	98	–	32.6	–	131
9	16:32:29.3	−24:29:13	Y	88	–	15.2	–	72
10	16:34:48.6	−24:38:00	Y	103	–	3.6	< 0.7	–
11	16:33:55.7	−24:42:06	N	–	0.1	–	< 0.8	–

The map is composed of 4 approximately parallel filaments, that run the length of the map. These are highlighted in Figure 4.14, where the contours have been smoothed to a resolution of 1′, to highlight the large scale structure. All of the sources in the map occur within these filaments. The axis of the filaments is parallel to the $C^{18}O$ filament that was detected in the neighbouring L1688 cloud (Wilking & Lada, 1983), and used by Loren (1989) to infer that the star formation in the ρ Ophiuchi cloud is triggered.

Filament 1 lies at the south-west of the map, and extends through the L1689S and R53 regions of the map. The filament appears to have fragmented into a number of objects, forming more than one object across the width. The degree of fragmentation appears to be more advanced at the north of the filament, where all of the cores detected in this filament are found.

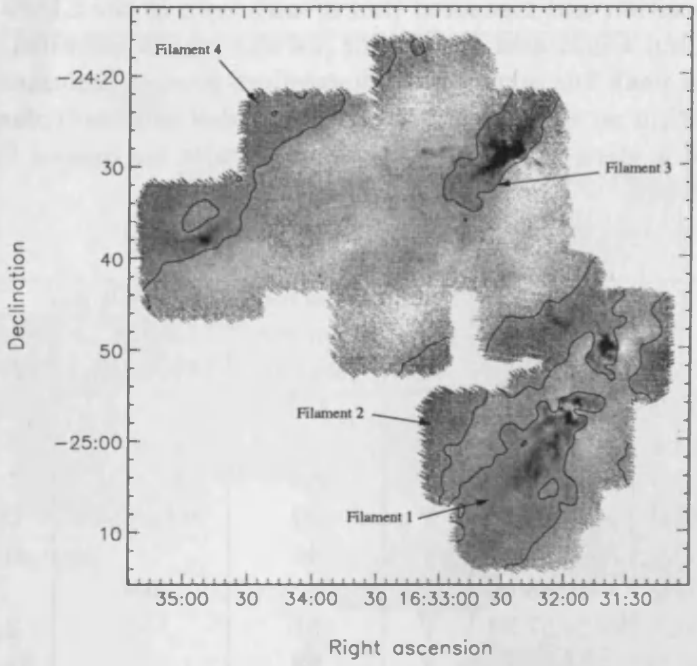

Figure 4.14: 850 μm scan-map of L1689, with contours placed to highlight the filaments.

Figure 4.15 shows this filament in more detail. The 6 cores in the filament have been labelled. Most of these objects are significantly extended in the JCMT beam, and have fairly complicated structure. Further south, the filament is significantly higher than the surrounding area and there is structure seen within it, but no condensations are detected.

Object #7 shown in Figure 4.15 is elongated in a north-south direction, and close inspection indicates that it may consist of more than one source. This source is also known as L1689SMM (Kirk, 2002). Figure 4.16 shows a slice across this object, and illustrates that though there are a number of density peaks along the ridge, they are not significant.

Filament 2 runs from the north-east corner of L1689S to close to Filament 1 near R53. Filament 2 has not been covered very well by the scan-mapping strategy.

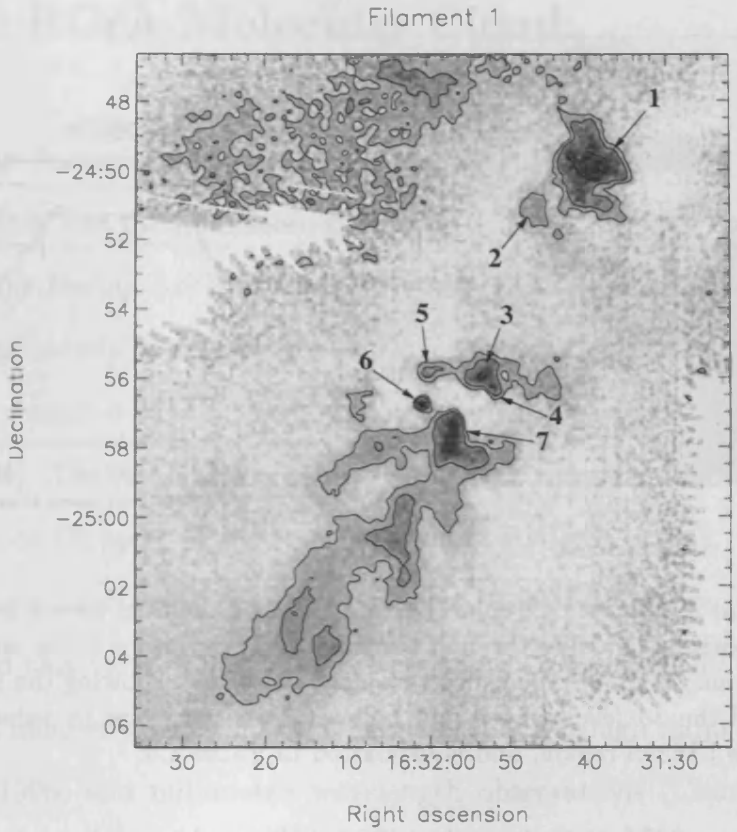

Figure 4.15: Enlarged view of Filament 1, showing the embedded cores.

There is an area that has not been mapped in the middle of the filament, and most of the area that was mapped was only covered once. In addition, the filament has mostly been caught on the edges of the scan-maps, where the noise is typically higher. As a result of these factors, the level of noise along the filament is higher than average. There are no sources detected in this filament, the region of highest flux density is found at RA (2000) = $16^{h}\,32^{m}\,03^{s}$, Dec. (2000) = $-24^{\circ}\,47'\,16''$.

Filament 3 extends from the north-west of the R57 region, in a south-east direction. The brightest source in this filament is the IRAS 16293-2422 binary protostar. The two components of the binary are separated by $5''$, and are unresolved in the JCMT beam at both wavelengths (Mundy et al., 1992). There is also

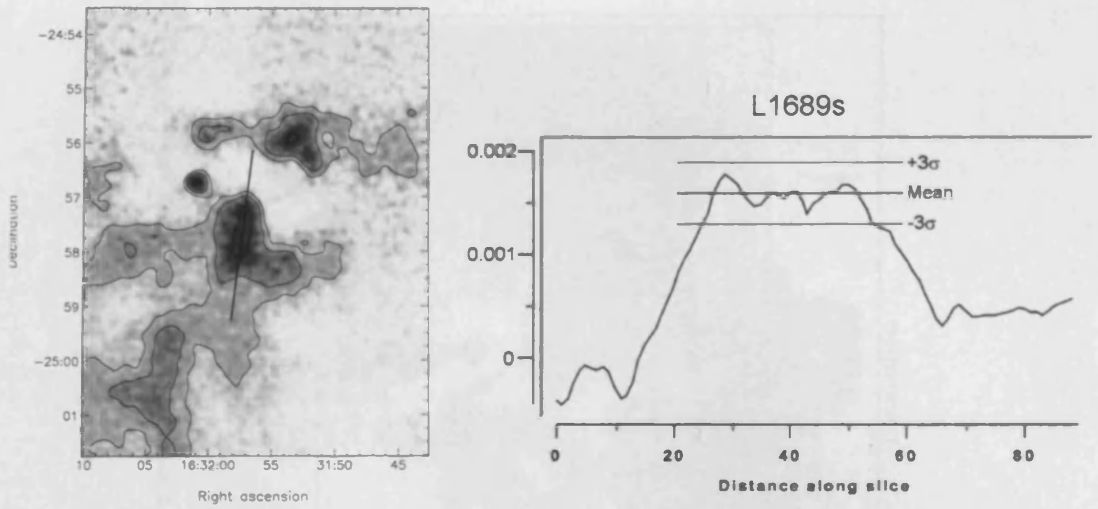

(a) (b)

Figure 4.16: (a) & (b). (a) An enlarged view of the elongated source #7 (L1689SMM), showing the position of a slice through the source. The contour levels are at 3σ, 5σ, 10σ, 15σ, 20σ, 40σ and 80σ. (b) The slice through the source, showing the mean level along the ridge, and the 3σ levels above and below this value. The 1σ value was calculated over the whole L1689S region, and is tabulated in Table 4.5.

a weaker source 90″ (approximately 14000 AU) to the south-west of IRAS 16293-2422. The filament is only detected in the north-west of the image, though if the line of the filament is extrapolated, a weak unresolved source (#11) is detected at RA (2000) = $16^{h}\,33^{m}\,55.7^{s}$, Dec. (2000) = $-24^{\circ}\,42'\,06''$.

Filament 4 extends from the L1689B region at the east of the map, in a north westerly direction. Like Filament 2, it skirts along the edge of the map, therefore the noise is higher than average. The only object detected in the filament is the L1689B prestellar core (#10), at RA (2000) = $16^{h}\,34^{m}\,48.6^{s}$, Dec. (2000) = $-24^{\circ}\,38'\,00''$. Filament 4 is the least well mapped of the four filaments. The evidence in favour of it being a real structure is that it is seen in more than one overlapping scan-map, and that the envelope of L1689B is elongated along the filament. These data are analysed and compared to previous surveys of the molecular cloud in Chapter 5.

4.4 The RCrA Molecular Cloud

The R Coronae Australis dark cloud is found at a distance of 170 pc (Knude & Hog, 1998) and is one of the closest star-forming regions to the sun. The cloud is centred on the Herbig Ae/Be star RCrA, which is the illumination source of a bright reflection nebula (NGC 6729), and from which the region takes its name. There are also a number of other bright young stars in the region (e.g. Vrba, Strom, & Strom, 1976a). The cloud was previously believed to have an unusually low star-forming efficiency (Vrba et al., 1976a; Marraco & Rydgren, 1981). The discovery of a cluster of young stars termed the Coronet (Taylor & Storey, 1984) close to RCrA, changed this view. The cloud is now known to be actively forming stars, and contains a number of embedded objects revealed through radio (Brown, 1987; Suters et al., 1996) and millimetre wavelength observations (Chini et al., 2003; Choi & Tatematsu, 2004).

4.4.1 Observations

Scan-map observations of the RCrA cloud were carried out on the nights of 2000 April 9^{th} – 11^{th}. The atmospheric conditions were the same as for the L1689 observations. The observation details are given in Table 4.7. The scan-maps were made in the same manner as for the L1689 scan-maps, with chop throws of 30″, 44″ and 68″ in RA and Dec. The data reduction was carried out using the same interactive procedures employed in the Orion B and L1689 reduction.

Table 4.7: The positions of each of the scan-maps made of the RCrA molecular cloud. The atmospheric conditions over the course of each night are indicated by the 225 GHz optical depth in column 5.

Region Name	Region Centre		UT Date	τ_{225GHz}
	RA (2000)	Dec. (2000)		
RCrA-A	19:01:50	−36:57:00	2000 Apr 09	0.06 - 0.07
RCrA-B	19:02:50	−37:06:00	2000 Apr 10	0.05 - 0.06
RCrA-C	19:03:50	−37:13:00	2000 Apr 11	0.05 - 0.06

4.4.2 Data

Figures 4.17 and 4.18 show the reduced data for the RCrA region. Each map is comprised of 3 adjacent scan-maps. The area covered is approximately 0.5 square degrees, which at the distance of RCrA is equal to ~ 0.8 pc^2. The three scan-maps are RCrA A, B and C, and are marked on Figures 4.17 and 4.18. The 1σ noise level for each of these regions is given in Table 4.8.

Table 4.8: Table showing the noise levels for each region of the RCrA maps

Region Name	Region Centre		1σ noise (Jy/beam)	
	RA (2000)	Dec. (2000)	850 μm	450 μm
RCrA-A	19:01:50	−36:57:00	0.040	0.84
RCrA-B	19:02:50	−37:06:00	0.031	0.43
RCrA-C	19:03:50	−37:13:00	0.033	0.74

The flux densities of the RCrA cores are given in Table 4.9. As for the Orion B and L1689 maps, the 450 μm data were smoothed to the resolution of the 850 μm data. For both 850 μm and 450 μm, the flux density of unresolved cores is quoted in Jy/14″ beam. The flux densities from extended cores are given for the aperture size quoted in the table. Cores that are undetected at 450 μm are given upper limits in units of Jy/14″ beam.

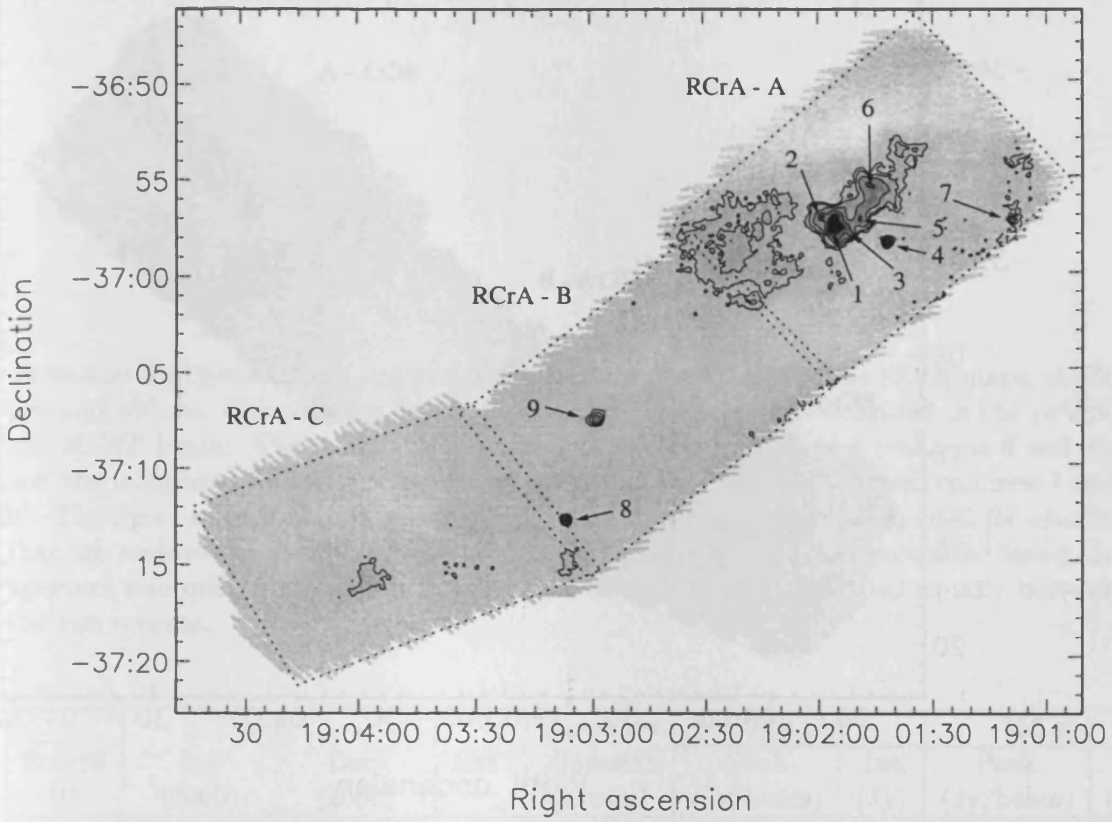

Figure 4.17: The RCrA map at 850 μm. The contour levels are at 3σ, 5σ, 10σ, 20σ, 40σ and 60σ. Contours are based on the map smoothed to a resolution of $18''$. The regions in Table 4.8 are shown as dotted lines. The identified cores are marked on the map.

The brightest feature in the two maps is source #1 at RA (2000) = $19^{h}\,01^{m}\,55.7^{s}$, Dec. (2000) = $-36°\,57'\,32''$. The 850 μm map indicates that this potentially consists of two or more sources. Figure 4.19 highlights this by showing a slice across the object. The two flux density peaks are separated by $20''$, which is equal to 2600 AU at the distance of RCrA. The peaks are significant at a level of 6σ. The 450 μm map is too noisy to confirm the dual nature of this object. The extended flux density is split according to the ratio of their peak flux density, which is equal. The northern source is also extended and therefore potentially made up of two unresolved objects, higher resolution data are required to confirm this.

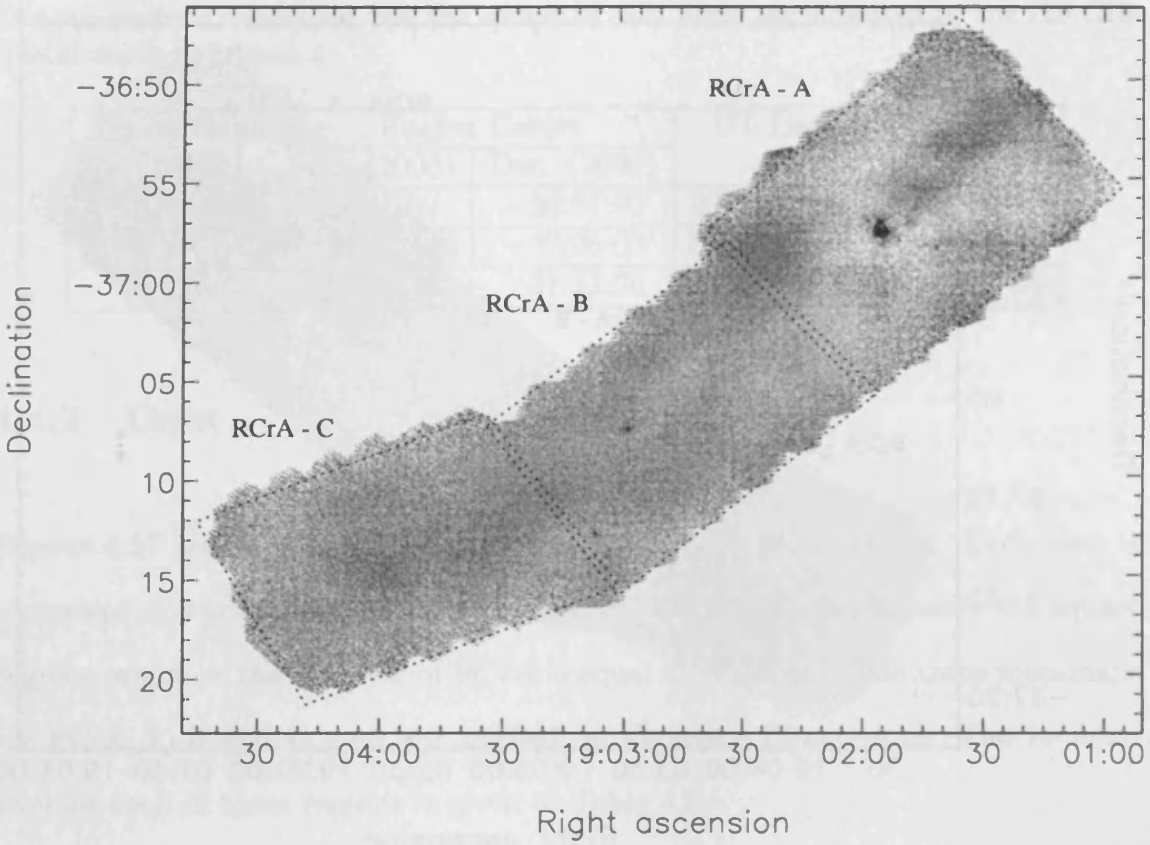

Figure 4.18: The RCrA map at 450 μm. The contour levels are at 3σ and 5σ. Contours are based on the map smoothed to a resolution of 18″. The regions in Table 4.8 are shown as dotted lines.

Source #1 is surrounded by a number of unresolved sources, and a filament extends north-west, containing two extended density peaks. There is another unresolved object to the west of the main clump. To the east of the main clump is an area of increased flux density, though no sources are detected within it.

The RCrA-B and RCrA-C regions show much less structure, with two marginally resolved sources (#8 & 9) in RCrA-B, and a small area of increased flux density in RCrA-C. With the exception of objects #5 and #7, all sources are detected at 450 μm. The nature of each of these sources is discussed in the following chapter.

Table 4.9: The position and measured flux density of each core in the RCrA maps, at 850 μm and 450μm. Column 4 indicates whether or not the core is extended in the 14″ 850 μm JCMT beam. The peak flux is quoted for unresolved sources (columns 6 and 8), and the integrated flux within an aperture is given for extended sources (columns 7 and 9). The aperture size used is given in column 5. 3σ upper limits are quoted for sources that are undetected at 450 μm. ‡The flux density for core #1 was measured using the aperture size quoted in column 5. The flux density was then divided equally between the two sources.

Source ID	RA (2000)	Dec. (2000)	Ext.	Aperture diameter (arcsec)	850 μm		450 μm	
					Peak (Jy/beam)	Int. (Jy)	Peak (Jy/beam)	Int. (Jy)
1a	19:01:55.6	−36:57:43	Y	88‡	–	14.3	–	33.2
1b	19:01:56.4	−36:57:27	Y	88‡	–	14.3	–	33.2
2	19:01:58.8	−36:57:07	N	–	1.6	–	4.4	–
3	19:01:51.1	−36:58:04	N	–	1.3	–	< 1.8	–
4	19:01:41.9	−36:58:27	N	–	1.6	–	5.5	–
5	19:01:49.0	−36:57:11	Y	26	–	1.7	–	2.5
6	19:01:46.4	−36:55:30	Y	27	–	1.9	–	7.0
7	19:01:09.1	−36:57:19	N	–	0.7	–	< 1.8	–
8	19:03:06.9	−37:12:50	Y	19	–	1.4	–	4.6
9	19:02:58.9	−37:07:37	Y	17	–	1.2	–	5.8

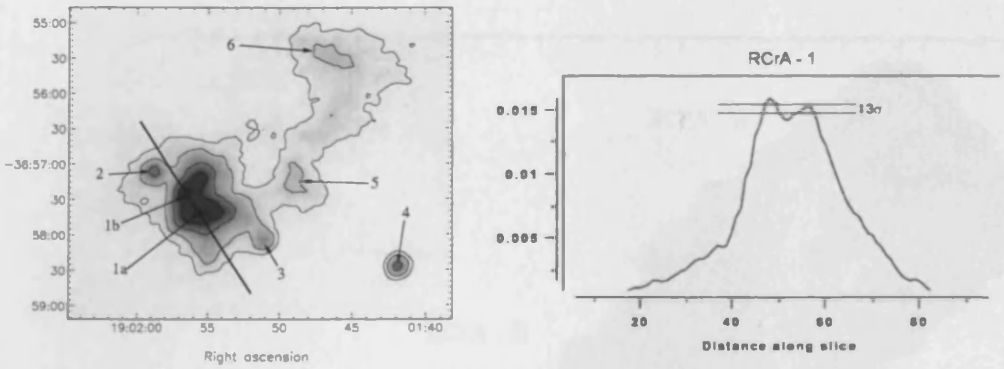

(a) (b)

Figure 4.19: (a) & (b). (a) An enlarged view of the central region of RCrA-A. The contours are placed at 10σ, 20σ, 40σ, 60σ and 75σ and the source ID numbers are included. (b) A slice across source #1, showing the profile of the object, along with the 3σ level calculated for the RCrA-A map.

4.5 Extracting Information

4.5.1 Viewing the Data

Once the data are reduced, they are in the form of a two dimensional grid (RA and Dec) with a third dimension containing the flux density information. There are many different ways to display this information, Figure 4.20(a) shows a grey-scale image where the brightness at each position corresponds to the flux density. This image contains the maximum information density as all of the information contained in the data is displayed. The spatial information in the map is well represented, for example it is easy to see the relative positions of different objects. However the flux density information displayed as a grey-scale is less clear and it is not easy to see the structures of objects and how they relate to each other. Displaying the grey-scale over a limited range as in Figure 4.20(b) can be useful, as it shows more detail in the region of interest.

Adding contours to a map is a common way to 'guide the eye' and allow

the viewer to easily visualise the differences between objects. This is shown in Figure 4.20(d) and can be very useful, though there are only a certain number of contours that can be displayed before the map looks cluttered. Also, the positions of the contours highlight some structural information whilst ignoring details that fall between the contours.

Replacing the grey-scale with a colour-scale (see Figure 4.20(c)) gives more contrast as more shades can be differentiated in a blue-green-yellow-red-white scale than with a grey-scale. This gives more insight into the structures present in the data, but can make comparing the heights of two points more difficult as the intensity scale is not linear. Also, the difference between two shades of blue may be seen as smaller than the difference between a blue and a green, though in reality the reverse could be true. This causes the position of the colour bands within the dynamic range to affect what the viewer sees.

These methods can be very useful as they are the easiest way of measuring the positions of objects in the data. However, to gain a better understanding of the structures within the data, it becomes necessary to discard some of the information in order to better display the information of interest. One way of doing this is to use a slice through an image. This discards one spatial dimension, allowing the flux density information to be displayed on the second axis. This is a very clear representation as it shows only a very small amount of information, and doesn't rely on a grey-scale. However, it can be unhelpful as too much information is thrown away. Figures 4.20(e) and 4.20(f) show how a filament extending from an object and bending round can appear to be a separate object when a viewed as a slice.

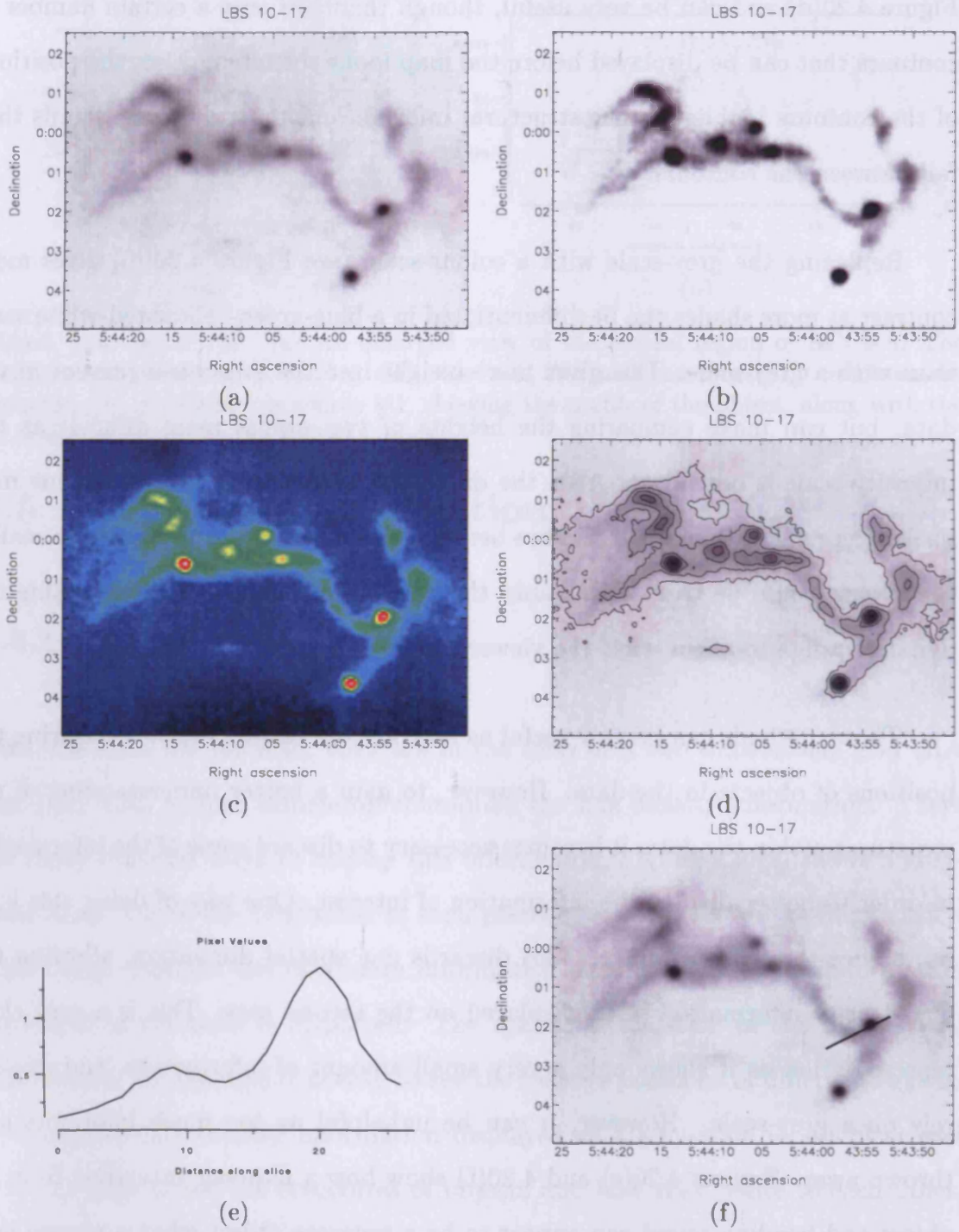

Figure 4.20: (a) to (f). Different representations of the LBS10-17 region, contrasting the different ways of viewing data. Grey-scale (a), grey-scale over a restricted dynamic range (b), colour-scale (c), contoured grey-scale (d) and slice (e) & (f).

What would be more useful would be a representation that combined the advantages of these different methods. One such way is to display the data as a 3D surface where flux density information is displayed as height. As shown in Figure 4.21, this surface can then be viewed from any angle. In this representation of the data, precise positional information is not immediately apparent as in the grey-scale image, and some information is not shown, but the true morphology is more evident. Examples of the usefulness of this technique are given in Section 4.5.2. Obviously the most effective way to view the data is to make use of all these different techniques, rather than relying on any one.

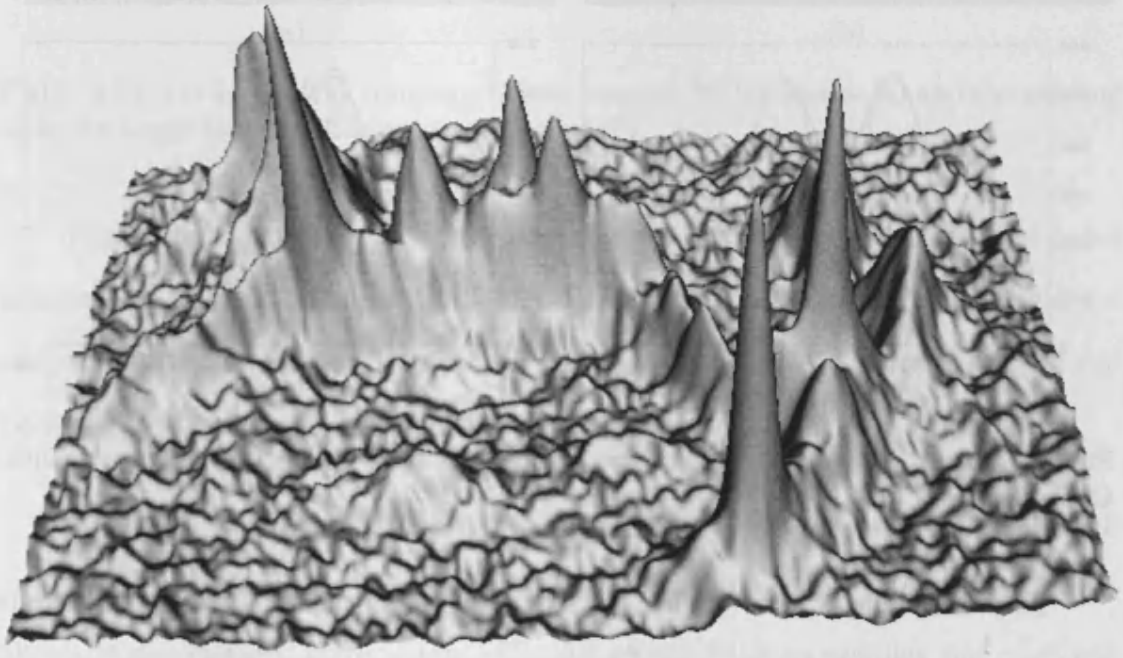

Figure 4.21: 3D surface representation of the LBS10-17 region.

4.5.2 Selection Criteria

If the data consist of isolated point-like sources, we can simply calibrate the map in Jy/beam and measure the peak flux of each source. Selecting which objects

are significant can be done simply by comparing the object's peak flux density to the local noise level. If the sources are not isolated, it becomes more difficult. A point-like source resembles the point spread function (PSF) of the beam, which can be approximated to a Gaussian. As two unresolved sources become closer, the two PSFs begin to overlap and we see the resultant of the two. This is illustrated in 1 dimension in Figure 4.22(a). Figure 4.22(b) shows how the resultant is more complicated if the two sources have unequal flux densities. The weaker source can appear to be a shoulder on the side of the brighter one. Fortunately our knowledge of the nature of the PSF allows us to fit the two convolved Gaussians and retrieve all of the information.

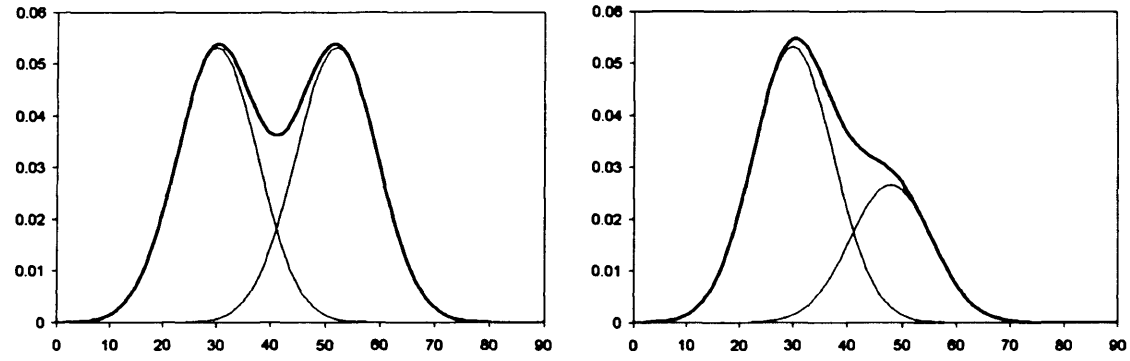

Figure 4.22: (a) & (b). The sum of two equally sized Gaussians (a), and two unequal Gaussians (b).

This technique works equally well with two dimensional Gaussians. Figure 4.23 shows the sum of two unequal Gaussians (a), and the resultant image once the larger Gaussian has been subtracted (b). The larger peak is removed by creating an image containing a single Gaussian with size and position equal to the large peak, and subtracting this from the image containing the sum of the two Gaussians.

We can apply this technique to the data, by observing a known point source such as Uranus in order to characterise the beam PSF, and then repeatedly subtracting the PSF from the brightest point in the target source map until the noise

level has been reached. A point to notice in Figure 4.22(b) is that the height of each peak is affected by a contribution from the other, and that the more significant effect is seen on the smaller of the two Gaussians.

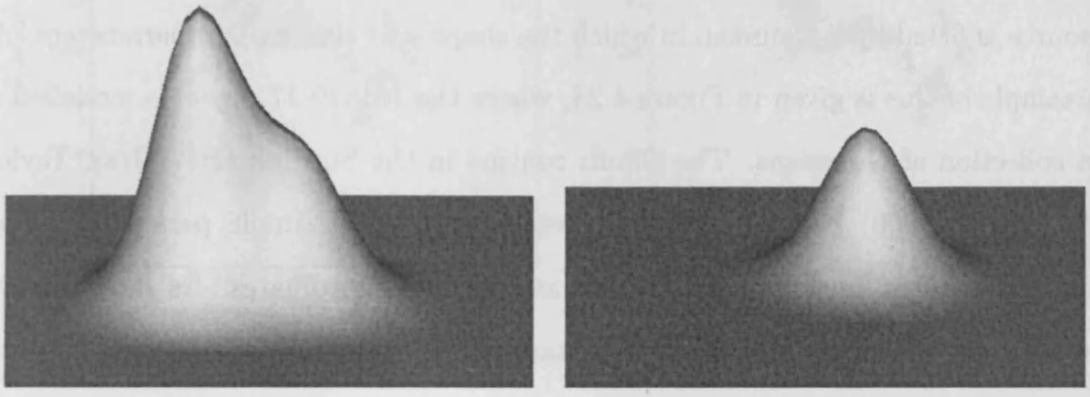

(a) (b)

Figure 4.23: (a) & (b). The resultant of two unequal 2D Gaussians (a) and the residual after the larger Gaussian has been subtracted (b).

This method can only be used if the sources in the data are unresolved point sources. If this is not the case and the objects are extended, then modelling them with the PSF of the beam is not appropriate as each extended source would not be modelled by a single PSF, but a central peak surrounded by a ring.

The size of the JCMT beam at 850 μm is approximately 14″. An object will only appear extended if the convolution of the beam and the angular size of the object is significantly larger than 14″. An object with an angular size of 8″ will be observed as having FWHM $\sqrt{(8''^{\,2} + 14''^{\,2})} \simeq 16''$. 16″ is probably the smallest angular size that can reliably be distinguished from 14″, therefore objects smaller than 8″ are effectively observed as point sources. At a distance of 400 pc (the approximate distance to Orion) 8″ subtends a distance of 3200 AU. In the nearer regions such as L1689, a spatially smaller object would appear extended. The majority of prestellar cores (Ward-Thompson et al., 1994) and protostars (Motte et al., 1998) have been observed to be significantly larger than 3200 AU, and it

is therefore unreasonable to make the assumption that all objects are unresolved. This method was therefore not used for the data presented here.

It is possible to use a similar method if the objects are extended, in which each source is fitted by a Gaussian in which the shape and size are free parameters. An example of this is given in Figure 4.24, where the LBS10-17 region is modelled as a collection of Gaussians. The Gaufit routine in the Starlink ESP (Gray, Taylor, & Privett, 2000) package was used, which employs a simple parameter search algorithm to fit an elliptical Gaussian at specified coordinates. As shown above, weak sources can be significantly contaminated with flux from nearby brighter sources, so it is necessary to remove the contribution from the brighter source, before fitting the weaker of the two.

The method described above can be useful for a number of reasons. In the simplest case, deciding whether or not a source is significant when it is very close to a brighter source can be difficult, and this is made much easier by removing the brighter source and considering only what is left. In addition, the parameters of the fit can be used to determine the flux density from an object in a number of ways. One method is to use the fit parameters P (the peak, calibrated in Jy/arcsec), FWHM_a and FWHM_b (the FWHM along the major and minor axes respectively) to calculate the flux density directly by numerically integrating the equation of a two dimensional Gaussian:

$$V_{int} = P \int_{-\infty}^{\infty} \int_{-\infty}^{\infty} \exp\left\{ -\left(\frac{1}{2}\right) \left[\left(\frac{x^2}{\sigma_a^2}\right) + \left(\frac{y^2}{\sigma_b^2}\right) \right] \right\} dxdy \qquad (4.1)$$

$$\sigma_a = 0.425 \times FWHM_a$$

$$\sigma_b = 0.425 \times FWHM_b$$

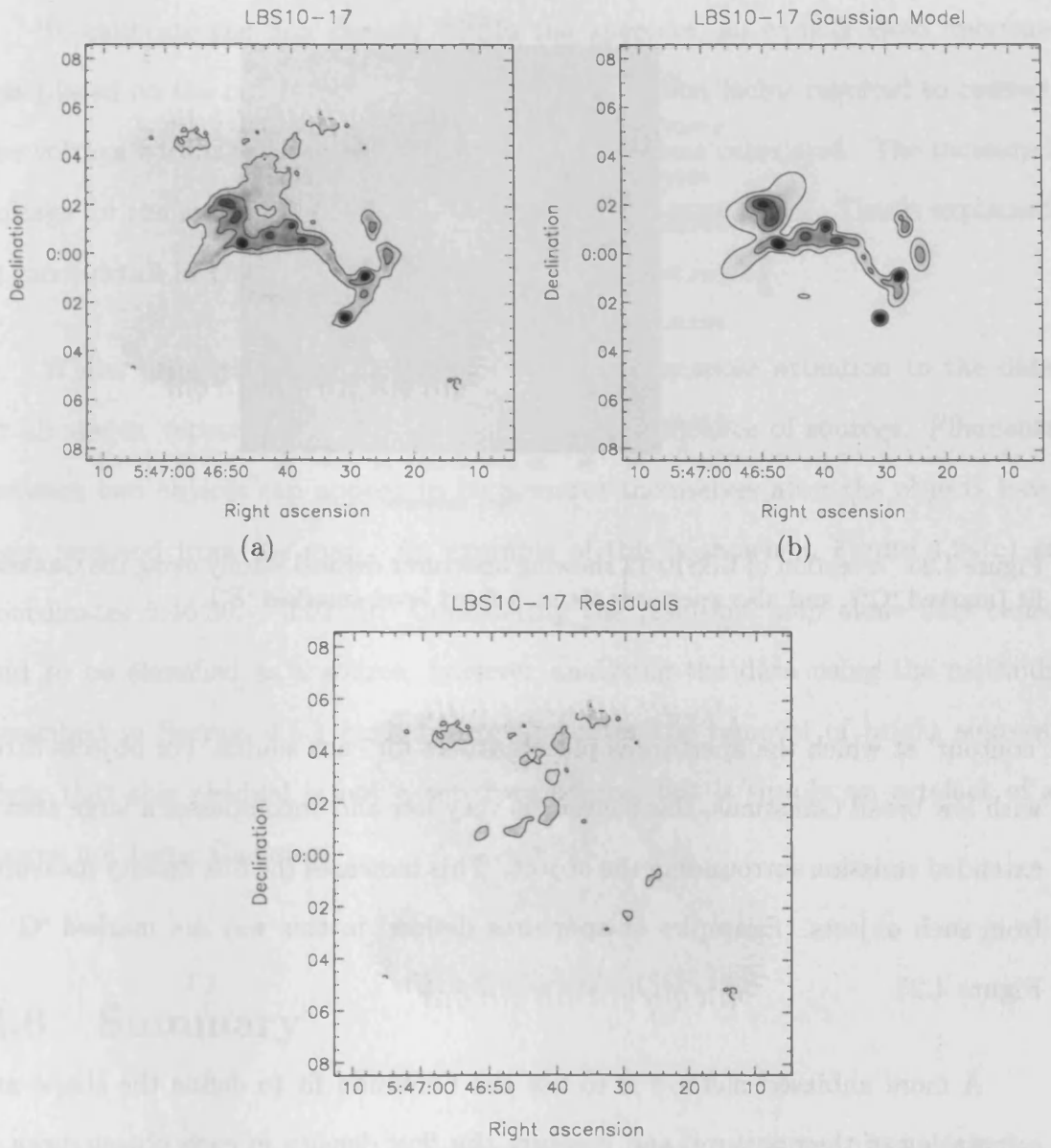

Figure 4.24: (a) to (c).The region LBS10-17 (a), the model based on a collection of Gaussians (b), the residuals after the model is subtracted from the data (c).

An alternative method is to remove nearby sources from the data that might contribute flux to an object, and place an elliptical aperture on the source with dimensions based on the fit parameters. One way to do this is to use the two FWHMs and their angle on the plane of the sky to define the shape, size and orientation of the aperture. An obvious consequence of this is that the flux density

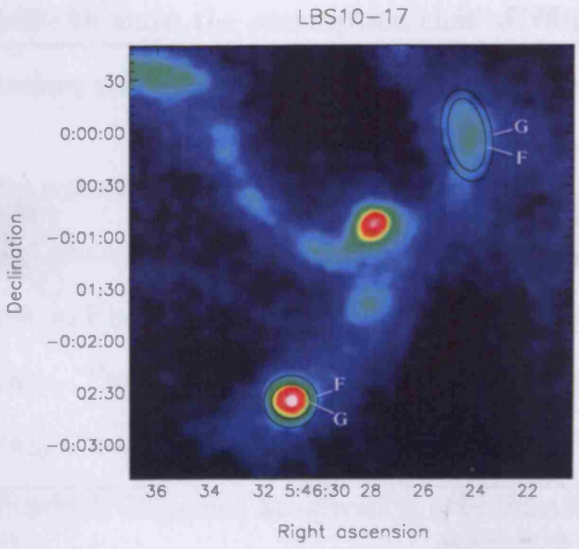

Figure 4.25: A section of LBS10-17 showing apertures defined wholly using the Gaussian fit (marked 'G'), and also apertures set at a fixed level (marked 'F').

'contour' at which the aperture is placed differs for each source. For objects fitted with low broad Gaussians, this contour is very low and encompasses a large area of extended emission surrounding the object. This increases the flux density measured from such objects. Examples of apertures defined in this way are marked 'G' in Figure 4.25.

A more unbiased method is to use the Gaussian fit to define the shape and orientation of the aperture, and measure the flux density in each object down to the same level. This level should be based on the point at which the object begins to merge into the surrounding extended emission. The apertures marked 'F' in Figure 4.25 are defined in this manner. Any errors introduced by the Gaussian fitting and by non-Gaussian shape of the source are minimised with this method. This is because the fit is used only to subtract the small contribution from the wings of sources near to the source being measured, and to determine the aspect ratio and orientation of the aperture.

To calibrate the flux density within the aperture, an equally sized aperture was placed on the calibrator source, and the conversion factor required to convert the voltage within the aperture to the correct flux was calculated. The measured voltage for the source can then be multiplied by the same factor. This is explained in more detail in Chapter 2.

Whilst using this method it is necessary to pay close attention to the data at all stages, especially when determining the significance of sources. Filaments between two objects can appear to be a source themselves after the objects have been removed from the map. An example of this is shown in Figure 4.24(c) at coordinates 5:46:30, −0:02:30. Considering the resultant map alone may cause this to be classified as a source, however analysing the data using the methods described in Section 4.5.1 both before and after the removal of bright sources, show that this residual is not a separate source, but is simply an artefact of a source not being Gaussian.

4.6 Summary

In this chapter I have introduced three molecular clouds, Orion B, L1689 and RCrA. I have described my scan-map observations of these regions and the data reduction. I have discussed the features in each of the maps. The flux density of each source at 850 μm and 450 μm has been tabulated. Finally, I have discussed a number of different ways of visualising the data, and different techniques for extracting information from the data. In the next chapter I will discuss the analysis of these data.

Chapter 5

Data Analysis of Orion B, L1689 and RCrA

5.1 Introduction

In this chapter I discuss the results of the scan-map observations of the Orion B, L1689 and RCrA molecular clouds. A literature search of each of the regions is undertaken, to identify any previously known objects that correspond to my submillimetre sources. For the Orion B map, there is a large enough number of sources to measure the mass function of the cores and also determine the clustering properties of the region. The L1689 SCUBA data are compared to the previous CO data and to the neighbouring and well studied cloud L1688, which lies at the centre of the ρ Ophiuchi complex. The analysis of the RCrA data, in comparison with previous data, allow one to classify the sources in the SCUBA data.

5.2 The Orion B Molecular Cloud

5.2.1 Young Stellar Objects

Figures 4.6 and 4.7 show a large number of density peaks. Some of these are known to have already begun the process of star formation. This is revealed in a number of ways. Some have molecular outflows. Molecular bipolar outflows appear to be ubiquitous phenomena in YSOs (see review by Bachiller, 1996). They are seen in emission from molecules such as CO, which are swept up and excited by the outflow. They are also sometimes seen as HH objects, which are visible in the optical and near infrared, due to emission from high temperature shocked gas.

Some protostars have associated cm radio sources. These can be understood as follows. Accreting material forms a shock front at the protostellar surface and is heated. Short wavelength radiation from this hot gas ionises atoms and molecules in the inner envelope, liberating electrons. The existence of a protostar can then be revealed at cm wavelengths by the free-free emission from these electrons (Bontemps et al., 1995). As protostars evolve and get hotter, their thermal emission peaks at shorter wavelengths, distinguishing them from colder prestellar objects.

We can therefore identify those cores in my data that have already formed protostars. Most of the cores detected in the LBS23 region of Orion B have already begun forming stars. Of the 9 sources, only 3 (#4, #5 and #9) are not previously identified protostars. Core #6 is the Class III protostar SSV61 (e.g. Gibb, 1999), which is detected at both infrared (Strom, Strom, & Vrba, 1976) and cm wavelengths (Bontemps et al., 1995; Gibb, 1999). Cores #1, #2 and #8 are the Class I protostars HH26IR, SSV59 and SSV63E/SSV63W respectively, which

are detected at infrared (Strom et al., 1976; Davis et al., 1997) and cm wavelengths (Bontemps et al., 1995; Gibb, 1999). They also drive molecular outflows, the shocks of which are detected in the ro-vibrational lines of H_2 (Jones et al., 1987; Gibb & Davis, 1997; Chrysostomou et al., 2000). Cores #3 and #7 are the Class 0 protostars HH25MMS and HH24MMS (Chini et al., 1993). These are detected at cm wavelengths (Bontemps et al., 1995; Gibb, 1999), but not in the infrared. They both drive molecular outflows (Bontemps, Ward-Thompson, & André, 1996; Chrysostomou et al., 2000), and have been designated as Class 0, based on the ratios of their sub-millimetre to bolometric luminosities (Ward-Thompson et al., 1995; Bontemps et al., 1995).

Core #10 (LBS17-H) has a molecular outflow, seen in CO and HCO^+ (Gibb & Little, 2000), though it has no infrared counterpart, and is not detected in the cm. It has therefore been designated as Class 0. Core #18 is located 12″ from a cm continuum source detected by Gibb (1999), though there is no detected outflow or point source visible in the infrared. The cm source is therefore probably a chance near alignment with a background source.

Cores #25 and #33 are associated with IRAS 05442-0000 and IRAS 05450+0019 (Launhardt et al., 1996; Motte et al., 2001). These sources are therefore assumed to have already formed protostars. The slope of their SED between 12 and 25 μm indicates that they are Class I objects. Core #41 is associated with the near infrared object SSV37 (Strom et al., 1976).

The brightest source in the map (core #55) is NGC2071IR, which is the source of a bipolar outflow that is seen in CO (Snell et al., 1984) in emission, and in OH in absorption (Ruiz et al., 1992). This small region contains a number of sources visible in the near infrared (Walther et al., 1993), of which eight (IRS1–8) lie within

the submillimetre peak. Walther et al. found that two sources (IRS4 and IRS6) were background sources, and one (IRS8) was a foreground object. The infrared emission from IRS5 consists solely of emission from shocked H_2, and is therefore probably caused by an outflow from a nearby young star. The other stars are all believed to be local to the region, two of which (IRS1 and IRS7) are undergoing mass loss and are the probable sources of the observed outflows.

Cores #53 and #54 lie along the path of the NGC 2071IR outflow, as shown in Figure 5.1. The possibility must therefore be considered that the observed continuum flux is significantly contaminated by molecular line emission. Chini et al. (2001) demonstrated that the 850 μm emission in the outflow of L1157 was contaminated by emission from the CO(3 – 2) transition, which lies within the 850 μm passband of SCUBA. The CO(6 – 5) transition falls within the 450 μm passband, though this transition has a much higher excitation temperature and is therefore less likely to be excited at the temperatures typically found in prestellar cores.

Braine et al. (1995) showed that the flux density due to line contamination F_{line} in a continuum band can be calculated from the integrated line intensity I using the following:

$$F_{line} = \frac{2k\nu^3}{c^3 \Delta\nu_{bol}} \Omega_{beam} I, \tag{5.1}$$

where k is the Boltzmann constant, ν is the frequency, c is the speed of light and $\Delta\nu_{bol}$ is the continuum filter bandwidth. Ω_{beam} is the beam integral given by:

$$\Omega_{beam} = \frac{2\pi\theta^2}{8 \ln 2}, \tag{5.2}$$

where θ is the telescope resolution in radians.

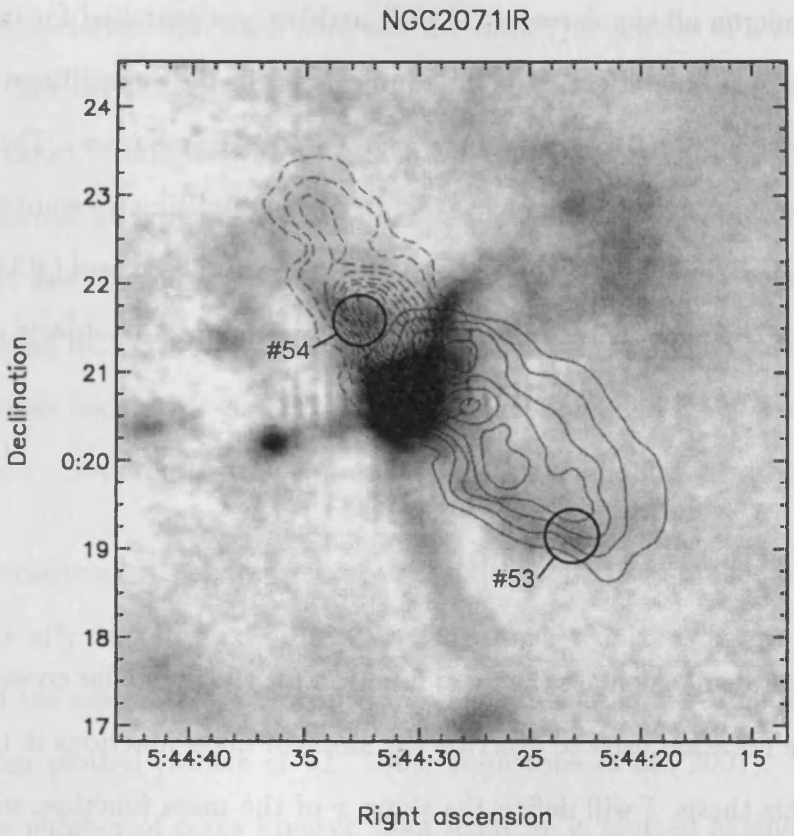

Figure 5.1: The NGC 2071IR source with the CO(2−1) outflow overlaid (Snell et al., 1984). Cores #53 and #54, which along the path of the outflow, are also plotted.

Chernin & Masson (1992) mapped the NGC 2071IR outflow using $CO(2-1)$ and $CO(3-2)$. They measured an integrated line intensity of ~ 450 Kkms^{-1} in CO(3−2). With a bandwidth and angular resolution of 30 GHz and 14″ respectively, the flux density detected by SCUBA due to $CO(3-2)$ emission is calculated to be 350 mJy/beam. This is $> 50\%$ of the total measured flux density at 850 μm. Cores #53 and #54 are therefore disregarded, as their mass cannot be reliably determined.

The CO(3−2) emission is observed to be 2 orders of magnitude weaker out of the outflow (Chernin & Masson, 1992), therefore the molecular line contamination in the other cores in this sample is assumed to be negligible.

The 2 micron all sky survey (2MASS) archive was searched for infrared point sources that were coincident with the sources seen in the submillimetre. Over the 0.2 square degree SCUBA map, there are 860 2MASS sources. The probability that an infrared source less than 7″ away from a submillimetre source is a chance alignment is less than 0.05%. Over the map, there are three cores (#33, #39, #41) with an infrared source within this radius. The remaining 42 objects are therefore assumed to be pre-stellar in nature.

5.2.2 Core Mass Function

In this section I will calculate the mass function for the prestellar cores in my Orion B data. The notation used to describe the slope of mass functions in the literature varies. In this thesis, I will define the slope x of the mass function, such that:

$$\frac{\mathrm{d}N}{\mathrm{d}\log M} \propto M^x, \tag{5.3}$$

where the term on the left gives the number of cores (or stars) in the interval $(\log M)$ to $(\log M + \mathrm{d}\log M)$. In this notation, the canonical slope for the high mass tail of the initial mass function (Salpeter, 1955) is given by $x = -1.35$. Some authors (e.g. Kroupa, 2001a) define the mass function as the number of stars per unit mass rather than the number of stars per unit log mass. The slope of such a function is then equal to $x - 1$.

Motte et al. (1998) mapped the ρ Ophiuchi molecular cloud at 1.3 mm using IRAM, and measured a mass function with a slope corresponding to $x = -1.5$ between 0.5 and 3 $M_\odot$, and a shallower slope of $x = -0.5$ between 0.1 and 0.5 $M_\odot$. This is qualitatively similar to the stellar initial mass function. From this,

Motte et al. concluded that each core was the direct progenitor of a star or stellar system, and that the initial mass function was determined by the fragmentation of a molecular cloud. Johnstone et al. (2000b) mapped the ρ Ophiuchi cloud at 850 μm, and measured an equivalent mass function. Core mass functions for the Orion B region have been formulated by Motte et al. (2001) and Johnstone et al. (2001) at 850 μm using SCUBA. The analysis used by both Motte et al. and Johnstone et al. differ from each other and from the analysis presented here. Their methods and results are compared to those presented in this thesis, later in this section.

When measuring a prestellar core mass function, the number of cores in a region is generally very limited. Therefore, the number of cores in any one bin can be small and the associated error quite significant. A cumulative mass function is therefore often plotted (Motte et al., 2001; Johnstone et al., 2001). In this type of graph, the number of cores greater than mass M is plotted against M. If the mass function is well described by a power-law, then the slope of a cumulative mass function is the same as that of the mass function, except when the core mass approaches the maximum mass. This is shown in Appendix D. The cumulative mass plot can therefore be useful in determining the slope of the high mass tail of the mass function. However, the position of the break in the mass function is less apparent.

To determine the core mass function, we need to calculate the mass of each core from its flux density. As discussed in Chapter 1, to determine the mass of an object from the thermal dust emission, assumptions must be made about the dust temperature and opacity, and also the distance to the region. I assume a dust opacity of 1.4 $\mathrm{cm^2 g^{-1}}$ (see Section 1.6.1), and a distance to the Orion B cloud of 400 pc (see Section 4.2). Gibb & Little (2000) fitted a greybody to SCUBA and IRAS data of the region, and found that the dust temperature lies between 9 and 20 K.

Harju, Walmsley, & Wouterloot (1993) mapped the cloud in NH_3, and determined a gas kinetic temperature of 15 K. I therefore assume a dust temperature of 15 K.

The mass I calculated for each core, M_N, is given in Table 5.1. To indicate whether or not the cores are gravitationally bound, the virial mass M_{vir} of each core was calculated. Using Equations 1.23 to 1.27, the virial mass can be calculated using:

$$M_{vir} = \frac{3\sigma^2 R}{G}. \tag{5.4}$$

This assumes a density profile of $\rho \propto r^{-2}$, as opposed to the uniform density sphere used in Equation 1.27. In each case, the radius of each core was determined as described in Section 4.5.2. The velocity dispersion σ was taken to be 0.68 kms^{-1}, as measured for the region using NH_3 (Jijina, Myers, & Adams, 1999). The mass of each core as a fraction of its virial mass is given in Table 5.1. In most cases, the core mass is typically greater than $0.3M_{vir}$.

The density profiles of prestellar cores are not generally $\rho \propto r^{-2}$ everywhere (Ward-Thompson et al., 1994), so this is no more than an approximate calculation. However, it indicates that the cores are close to gravitational equilibrium.

Figures 5.2 and 5.3 show the measured core mass function in both cumulative and standard forms respectively from my data. To take advantage of the improved statistics, the cumulative plot is used to determine the slope of the high mass side of the mass function. The best fit to this slope is $N(> M) \propto M^{-1.5}$, with minimum and maximum acceptable fits of $x = -1.2$ and -1.9 respectively. As is clear from Figure 5.3, the mass function has a maximum value at approximately 1 $M_\odot$, and decreases at higher masses as a fairly constant power-law. The noise level in the map leads to a minimum detectable mass at the 5σ level, of 0.2 $M_\odot$. The best fit slope and the sampling limit are shown on both plots. The plotted

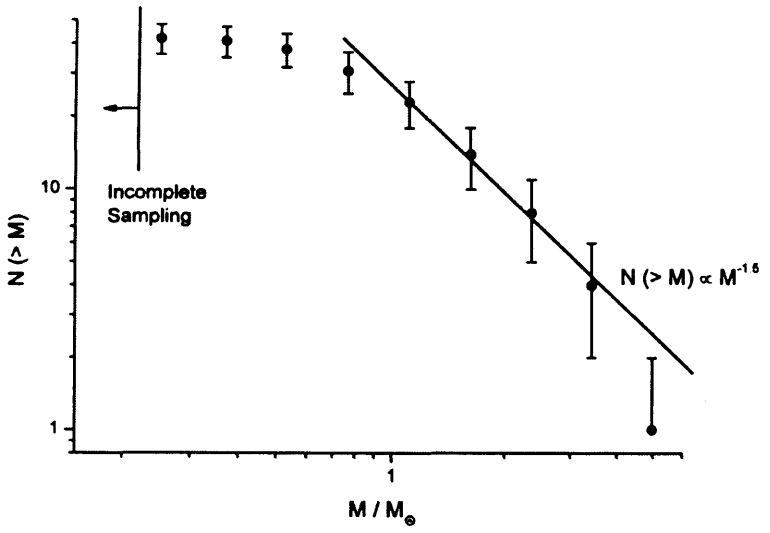

Figure 5.2: The cumulative core mass function for the prestellar cores in Orion B, based on my analysis. The bins have an equal spacing in $\log M$. The line of best fit for the high mass tail of the mass function is shown. The 5σ sampling limit is also plotted.

error bars in N are based on $\sqrt{N}$ statistics. Error bars in the mass coordinate are not plotted, because the uncertainty in mass arises predominantly from the conversion from flux density to mass. This uncertainty will affect all points by an equal factor, thus simply shifting the plot to the left or right without altering the slope. This makes the assumption that the dust temperature and mass opacity of each core is the same. If this is not the case, some scatter will be introduced in the mass coordinate. However, in order to quantify this effect, we would need to measure the temperature of each core, and also have a much greater understanding of the properties of the dust grains, and how these properties vary with density and temperature.

The systematic error in the flux density to mass conversion arises from uncertainties in the distance to the region, the dust temperature and the dust mass opacity. Taking worst-case estimates of these uncertainties to be 90 pc, 5 K and

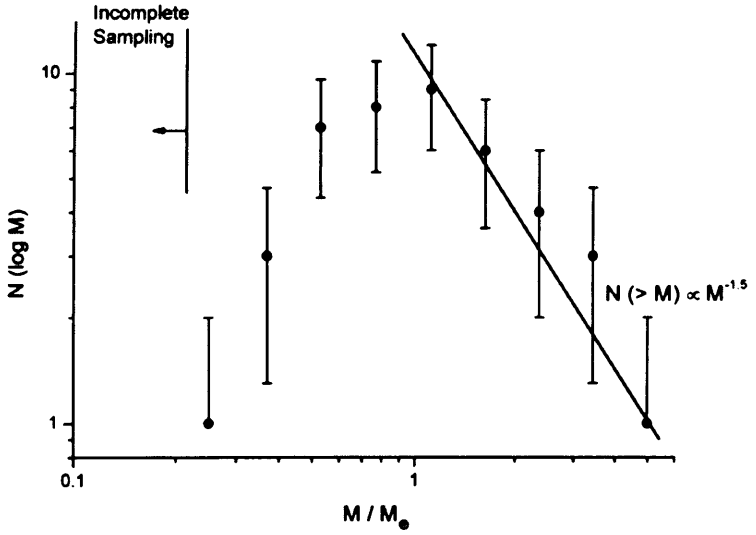

Figure 5.3: The core mass function for the prestellar cores in Orion B, based on my analysis. The bins have an equal spacing in $\log M$. The best fit line from Figure 5.2 is shown, and has a slope of $x = -1.5$. The 5σ sampling limit is also plotted.

0.4 cm^2g^{-1} respectively, the uncertainty in the mass estimate may be up to $\pm$ 75%.

The slope of the high mass side of the mass function is consistent with that of the initial mass function (IMF), which has a slope of approximately $x = -1.3$ to -1.5. The determination of this slope should be quite robust, as the random error in the measured flux density at 850 μm is quite low, with a calibration uncertainty of only $\sim$ 5%.

The break in the slope of the mass function lies at a higher mass ($\sim$ 1 $M_\odot$) than that of the IMF ($\sim$ 0.3 $M_\odot$). This is not a surprise because the efficiency of star formation for a core is expected to be less than unity. In addition, the total mass of the components of binary or higher multiple systems will be counted as a single core mass. This result was not found by Motte et al. (1998), who measured the core mass function in the ρ Ophiuchi molecular cloud. They concluded that the star formation efficiency of each core was very high, because the core mass

function they measured had a peak at approximately 0.1 $M_{\odot}$, whereas my peak is at ~ 1 $M_{\odot}$.

The uncertainty in the absolute mass estimates means that quantifying the extent to which the mass function is shifted relative to the initial mass function, is not possible.

To compare the measured core mass function to that of Johnstone et al. (2001) and Motte et al. (2001), it is helpful to first discuss their assumptions and reduction and analysis techniques. Johnstone et al. (2001) reduced their data using the matrix inversion technique discussed in Chapter 2. Before measuring the core masses, they removed any structure larger in scale than twice the largest chop throw, by convolving the map with a Gaussian and subtracting this from the data. They did this because the dual beam scan-mapping technique is not as sensitive to objects on large spatial scales, therefore they chose to remove all objects on these scales. Though this may remove low spatial frequency noise, it introduces artefacts that are manifested as negative bowls around bright sources.

I chose not to do this because the region is very clustered, and the technique removes some flux density from objects that are separated by less than the smoothing length used. The amount of flux density removed depends on the proximity and brightness of the nearby sources. Johnstone et al. determined the core masses using an automated clump finding algorithm, and visually inspected the results, removing a number as being misidentified noise.

Motte et al. (2001) reduced their data using automated scripts, and core masses were also extracted from the data using an automated procedure. The data presented here are the same as those published by Motte et al. (2001), though they

have been re-reduced from the raw data, and a different analysis method is used.

The three sets of results differ in a number of ways. The core identification by Johnstone et al. (2001) has produced similar results to my method, and generally, there is a one-to-one correspondence between the two sets of cores. In some regions of the map, their signal to noise ratio is higher, and they are able to identify cores that are not detected in my data. They include the known protostars discussed in Section 5.2.1. In calculating the prestellar core mass function, I do not believe this is useful, as the observations are only sensitive to the protostellar envelopes, and not the protostars themselves. The inclusion of these protostars could bias the mass function, as they are typically at a higher temperature and consequently brighter than the average core. Johnstone et al. also include a number of very extended objects that are much too low in mass to be gravitationally bound. Examples of these objects are located at coordinates RA (2000) = $5^h\,46^m\,34.5^s$, Dec. (2000) = $0°\,23'\,46''$. I have not included objects that I calculated to be unbound.

Motte et al. (2001) do not include the known protostars in their analysis and they exclude the LBS23 region. Their clump identification differs from both mine and that of Johnstone et al. (2001). There are a number of cases where Motte et al. identify two or three cores, which both Johnstone et al. and myself class as a single larger core. In some cases, these 'sub' cores are separated by a distance significantly smaller than that of the JCMT beam at 850 μm and hence I do not believe they are real.

In order to compare my results with those of Johnstone et al. and Motte et al. directly, the measured masses must be corrected for the different assumptions of dust temperature, opacity and the distance to the region. Motte et al. assumed a distance of 400 pc, a dust mass opacity of 1.0 cm^2g^{-1}, and a dust temperature

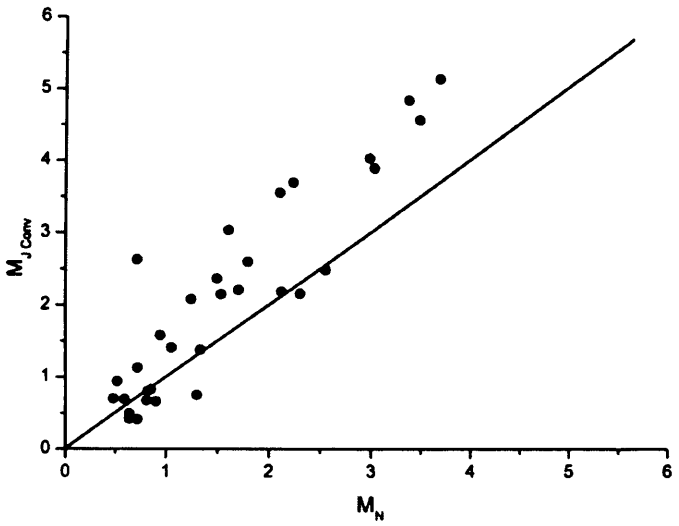

Figure 5.4: The relation between the core masses measured by Johnstone et al. (2001), and those measured by myself. The masses of Johnstone et al. have been normalised to my assumptions of distance, temperature and opacity. Generally, the masses measured by Johnstone et al. are systematically higher, indicating that they typically used a larger aperture size for measuring the flux densities, and may have included material from the clouds in which the cores are embedded.

of 15 K for prestellar objects and 20 – 30 K for protostellar objects. Johnstone et al. assumed a distance of 450 pc, and also used an opacity of 1.0 cm^2g^{-1}. They assumed a constant dust temperature of 30 K. The core masses are tabulated in Tables 5.1 and 5.2, which give the coordinates, type and mass for each of the cores identified by myself, Johnstone et al. and Motte et al. The masses calculated by Johnstone et al. and Motte et al., are given as quoted in the literature (M_J Quote and M_M Quote respectively), and also converted to account for the different assumptions (M_J Conv and M_M Conv respectively) — i.e.: the masses they would have calculated using my assumptions.

The corrected masses for Johnstone et al. (M_J Conv) and Motte et al. (M_M Conv) are compared to my calculated masses (M_N) in Figures 5.4 and 5.5 respectively. Generally M_J Conv is larger than M_N by a factor of 1.3. This is probably

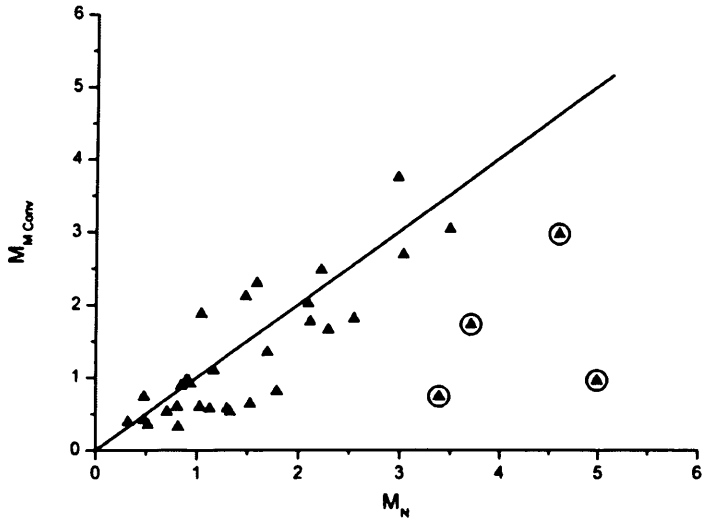

Figure 5.5: The relation between the core masses measured by Motte et al. (2001), and those measured by myself. The masses of Motte et al. have been normalised to my assumptions of distance, temperature and opacity. Good agreement can be seen in all cases except those that Motte et al. separated into sub-cores, but I treated as a single core (shown as circled triangles).

due to a difference in the size of apertures used. The fact that the relation is linear implies that both measurement techniques are self-consistent. Although there is less scatter in the relation between $M_{J\ \mathrm{Conv}}$ and M_N than between $M_{M\ \mathrm{Conv}}$ and M_N.

The most obvious feature in the relation between $M_{M\ \mathrm{Conv}}$ and M_N is the lack of objects with a high $M_{M\ \mathrm{Conv}}$. The cores with high values of M_N were split into a number of sub-cores by Motte et al. as discussed earlier. These points are circled in the Figure 5.5. If these inconsistent points are excluded, there is approximately a one-to-one correlation between $M_{M\ \mathrm{Conv}}$ and M_N, though there is still some residual scatter, indicating the order of magnitude of the flux density measurement errors.

Table 5.1: The core masses for each of the identified cores in Orion B. Column 4 indicates the object type (see Section 5.2.1). Column 5 gives the core mass as calculated by myself. The core mass as a fraction of the calculated virial mass is given in column 6. Where a core has also been identified by Johnstone et al. (2001) and/or Motte et al. (2001), the mass is given as quoted in the literature (columns 7 and 9), and normalised to my assumptions of distance, temperature and opacity (columns 8 and 10). Cores that have no ID in column 1 correspond to cores that are identified as a number of sub-cores by Motte et al., but not by myself or Johnstone et al.

ID	RA (2000)	Dec (2000)	Type	M_N ($M_\odot$)	Vir	M_J Quote ($M_\odot$)	M_J Conv ($M_\odot$)	M_M Quote ($M_\odot$)	M_M Conv ($M_\odot$)
1	05:46:03.7	−00:14:47	Protostellar	1.0	0.46	1.4	2.1	–	–
2	05:46:04.9	−00:14:20	Protostellar	1.1	0.66	1.3	2.0	–	–
3	05:46:07.4	−00:13:38	Protostellar	5.1	1.37	5.3	8.2	–	–
4	05:46:03.7	−00:12:12	Prestellar	0.7	0.46	0.3	0.4	–	–
5	05:46:10.1	−00:12:19	Prestellar	1.3	0.75	0.9	1.4	–	–
6	05:46:07.6	−00:11:52	Protostellar	1.1	0.62	1.2	1.9	–	–
7	05:46:08.5	−00:10:45	Protostellar	6.6	2.27	4.4	7.0	–	–
8	05:46:08.2	−00:10:03	Protostellar	1.6	0.84	1.8	2.8	–	–
9	05:46:06.1	−00:09:29	Prestellar	1.2	0.57	1.3	2.1	–	–
10	05:46:30.9	−00:02:35	Protostellar	4.3	1.53	2.7	4.3	6.0	8.6
11	05:46:28.1	−00:01:37	Prestellar	1.7	0.68	1.4	2.2	1.9	1.3
12	05:46:27.8	−00:00:52	Prestellar	3.5	1.36	2.9	4.6	4.3	3.0
13	05:46:24.1	−00:00:01	Prestellar	1.8	0.57	1.7	2.6	1.2	0.8
–	05:46:24.5	−00:00:22	–	–	–	–	–	0.4	0.3
–	05:46:24.6	+00:00:13	–	–	–	–	–	0.8	0.5
14	05:46:26.7	+00:01:08	Prestellar	1.6	0.66	1.9	3.0	3.3	2.3
15	05:46:27.4	+00:01:32	Prestellar	1.3	0.56	–	–	0.8	0.5
16	05:46:29.3	−00:01:09	Prestellar	1.0	0.54	–	–	0.9	0.6
17	05:46:32.5	−00:00:38	Prestellar	0.8	0.44	0.4	0.7	0.9	0.6
18	05:46:33.4	−00:00:11	Prestellar	0.8	0.40	0.5	0.8	0.5	0.3
–	05:46:33.5	−00:00:02	–	–	–	–	–	0.4	0.3
–	05:46:32.9	−00:00:23	–	–	–	–	–	0.3	0.2
19	05:46:35.1	+00:00:34	Prestellar	0.9	0.58	1.0	1.6	0.7	0.5
–	05:46:35.8	+00:00:33	–	–	–	–	–	0.7	0.5
20	05:46:37.7	+00:00:35	Prestellar	2.1	0.85	1.4	2.2	2.5	1.8
21	05:46:42.5	−00:01:43	Prestellar	0.5	0.26	0.5	0.7	0.6	0.4
22	05:46:40.5	+00:00:35	Prestellar	1.5	0.76	1.4	2.1	0.9	0.6
23	05:46:39.4	+00:01:11	Prestellar	2.3	0.93	1.4	2.2	2.4	1.7

Table 5.1: Continued.

ID	RA (2000)	Dec (2000)	Type	M_N ($M_\odot$)	Vir	M_J Quote ($M_\odot$)	M_J Conv ($M_\odot$)	M_M Quote ($M_\odot$)	M_M Conv ($M_\odot$)
24	05:46:42.9	+00:00:48	Prestellar	2.2	0.89	2.4	3.7	3.5	2.5
25	05:46:47.4	+00:00:26	Protostellar	4.2	1.38	3.1	4.8	1.4	3.1
26	05:46:48.2	+00:01:35	Prestellar	3.4	1.13	3.1	4.8	1.1	0.7
–	05:46:48.9	+00:01:22	–	–		–	–	1.0	0.7
27	05:46:49.9	+00:02:07	Prestellar	3.7	1.17	3.3	5.1	1.4	1.0
–	05:46:50.7	+00:02:07	–	–		–	–	1.1	0.8
28	05:46:40.3	+00:04:16	Prestellar	0.6	0.29	0.3	0.4	–	–
29	05:46:28.5	+00:04:26	Prestellar	0.6	0.28	0.3	0.5	–	–
30	05:46:36.3	+00:05:49	Prestellar	0.8	0.40	0.5	0.8	1.3	0.9
31	05:46:45.9	+00:07:17	Prestellar	5.0	1.11	3.9	6.1	1.4	1.0
–	05:46:46.1	+00:07:09	–	–		–	–	1.5	1.0
–	05:46:47.3	+00:07:27	–	–		–	–	1.1	0.7
32	05:46:51.9	+00:09:13	Prestellar	0.7	0.30	0.7	1.1	–	–
33	05:47:36.9	+00:20:07	Protostellar	2.2	0.71	–	–	0.6	1.4
34	05:47:32.6	+00:20:24	Prestellar	1.2	0.54	–	–	1.6	1.1
35	05:47:25.2	+00:18:49	Prestellar	0.5	0.25	–	–	1.1	0.7
36	05:47:24.9	+00:20:59	Prestellar	4.6	1.52	–	–	4.2	3.0
37	05:47:26.4	+00:20:48	Prestellar	1.1	0.78	–	–	0.8	0.6
38	05:47:26.2	+00:19:56	Prestellar	0.9	0.41	–	–	1.4	1.0
39	05:47:15.3	+00:18:42	Protostellar	0.7	0.41	1.7	2.6	0.8	0.5
40	05:47:16.0	+00:21:24	Prestellar	1.0	0.43	0.9	1.4	2.7	1.9
41	05:47:10.5	+00:21:14	Protostellar	2.7	1.09	1.2	1.9	1.1	2.5
42	05:47:12.4	+00:22:23	Prestellar	0.9	0.41	0.4	0.7	1.4	1.0
43	05:47:01.7	+00:18:00	Prestellar	2.1	0.75	2.3	3.6	2.9	2.0
44	05:47:06.8	+00:12:34	Prestellar	1.5	0.59	1.5	2.4	3.0	2.1
45	05:47:04.6	+00:14:59	Prestellar	2.5	0.55	1.6	2.5	2.6	1.8
46	05:47:10.6	+00:13:23	Prestellar	0.6	0.24	0.4	0.7	–	–
47	05:47:05.2	+00:13:29	Prestellar	0.5	0.22	0.6	0.9	0.5	0.4
48	05:46:28.2	+00:19:29	Prestellar	3.0	1.21	2.5	3.9	3.8	2.7
49	05:47:01.1	+00:26:19	Prestellar	3.0	1.08	2.6	4.0	5.3	3.8
50	05:47:07.8	+00:25:08	Prestellar	0.3	0.22	–	–	0.6	0.4
51	05:46:57.2	+00:23:56	Prestellar	1.3	0.64	0.5	0.8	0.8	0.6
52	05:46:59.1	+00:22:58	Prestellar	0.7	0.46	–	–	–	–
53	05:46:57.2	+00:20:11	Outflow	1.0	0.61	1.7	2.7	1.3	0.9
54	05:47:06.5	+00:22:35	Outflow	4.1	1.17	1.2	1.8	1.4	1.0
55	05:47:04.8	+00:21:45	Protostellar	57.4	7.60	30.3	47.5	9.2	52.4

Table 5.2: The core masses quoted by Johnstone et al. and/or Motte et al. that are not identified by myself. As in Table 5.1, core masses are given as quoted in the literature (columns 3 and 5), and normalised to my assumptions of distance, temperature and opacity (columns 4 and 6). Generally, the cores of Johnstone et al. are very extended and are not included in my list as I have calculated them not to be gravitationally bound, while those of Motte et al. are below my significance threshold.

RA	Dec	M_J Quote ($M_\odot$)	M_J Conv ($M_\odot$)	M_M Quote ($M_\odot$)	M_M Conv ($M_\odot$)
05:46:16.0	−00:00:44	0.3	0.5	–	–
05:46:17.4	+00:02:49	0.1	0.1	–	–
05:46:28.6	+00:21:10	1.2	1.9	–	–
05:46:29.2	+00:20:13	2.0	3.2	2.0	1.4
05:46:33.2	+00:27:22	0.5	0.8	–	–
05:46:34.2	+00:05:34	0.3	0.4	–	–
05:46:34.8	+00:24:37	1.1	1.7	–	–
05:46:37.6	+00:26:58	0.8	1.3	0.4	0.3
05:46:51.6	+00:00:01	0.6	0.9	0.4	0.3
05:46:54.2	+00:23:01	1.2	1.9	–	–
05:46:54.2	+00:23:58	0.7	1.0	–	–
05:46:54.4	−00:00:23	0.7	1.2	0.8	0.6
05:46:54.6	+00:23:34	0.8	1.3	1.3	0.9
05:46:57.8	+00:24:28	0.4	0.5	0.4	0.3
05:47:03.4	+00:20:10	0.7	1.1	–	–
05:47:05.0	+00:17:16	0.6	1.0	–	–
05:47:10.0	+00:15:58	0.2	0.4	–	–
05:47:10.0	+00:23:25	0.6	0.9	–	–
05:47:11.6	+00:23:04	0.4	0.6	–	–
05:47:11.8	+00:23:28	0.4	0.7	0.4	0.3
05:47:12.2	+00:15:37	0.2	0.3	–	–
05:47:17.0	+00:22:46	0.5	0.8	–	–
05:46:08.2	−00:12:26	0.6	0.9	–	–
05:46:06.2	−00:12:17	0.3	0.5	–	–
05:46:12.8	−00:09:50	0.7	1.2	–	–
05:46:13.4	−00:06:08	0.4	0.6	–	–
05:46:09.2	−00:05:50	0.4	0.6	–	–
05:46:13.8	−00:05:29	0.9	1.3	–	–
05:46:06.6	+00:01:07	0.1	0.1	–	–
05:46:23.6	−00:13:29	0.7	1.0	–	–

Table 5.2: Continued.

RA	Dec	M_J Quote ($M_\odot$)	M_J Conv ($M_\odot$)	M_M Quote ($M_\odot$)	M_M Conv ($M_\odot$)
05:46:59.8	+00:20:26	–	–	0.4	0.3
05:47:00.3	+00:20:35	–	–	0.5	0.3
05:47:01.1	+00:20:37	–	–	0.4	0.2
05:47:07.5	+00:22:46	–	–	0.6	0.4
05:47:08.2	+00:22:52	–	–	0.6	0.4
05:47:02.0	+00:20:45	–	–	0.7	0.5
05:46:49.7	+00:00:20	–	–	0.4	0.3
05:46:52.8	+00:01:48	–	–	0.4	0.3
05:46:39.1	+00:00:33	–	–	0.3	0.2
05:46:45.1	+00:00:18	–	–	0.6	0.4
05:46:28.5	+00:21:41	–	–	1.4	1.0
05:46:30.0	+00:19:52	–	–	0.7	0.5
05:47:35.1	+00:20:21	–	–	0.7	0.5
05:47:14.3	+00:21:30	–	–	0.3	0.2
05:47:17.2	+00:21:27	–	–	0.4	0.3
05:47:29.8	+00:20:39	–	–	0.9	0.6
05:47:02.7	+00:22:55	–	–	0.7	0.5
05:47:03.2	+00:19:40	–	–	0.3	0.2
05:47:03.3	+00:22:35	–	–	1.0	0.7
05:47:03.6	+00:19:54	–	–	0.3	0.2
05:47:03.6	+00:20:08	–	–	0.6	0.4
05:47:04.2	+00:20:23	–	–	0.4	0.2
05:47:10.7	+00:22:29	–	–	0.3	0.2
05:47:11.9	+00:22:45	–	–	0.4	0.3
05:46:58.2	+00:20:12	–	–	0.6	0.4

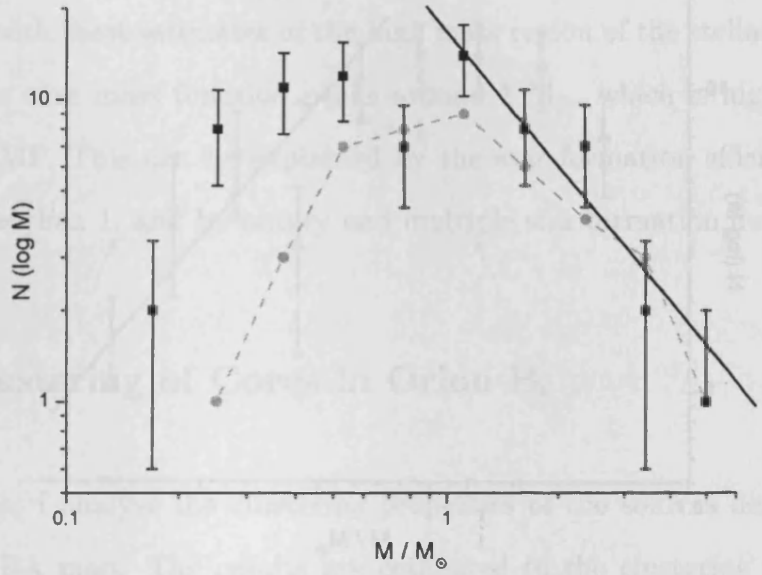

Figure 5.6: The core mass function based on the masses measured by Johnstone et al. (2001). The masses have been normalised to my assumptions of distance, temperature and opacity. The line of best fit to the data points above 1 $M_\odot$, which has a slope of $x = -1.5$ is shown. The mass function shown in Figure 5.3 is overlaid in grey.

Core mass functions based on the published data of Johnstone et al. (2001) and Motte et al. (2001) are plotted in Figures 5.6 and 5.7 respectively. The masses have been scaled to correspond to my masses by accounting for the different assumptions used, as discussed above.

Figure 5.6 shows that the mass function calculated by Johnstone et al. is approximately consistent with my mass function (overlaid in grey). The break in the function occurs at approximately 1 $M_\odot$ and the slope at the high mass side is consistent with $N(> M) \propto M^{-1.5}$. This fit is based on the cumulative mass function for these data. The fact that the slopes of the high mass side of the mass functions are approximately the same, indicates that the included protostellar envelopes have little effect on this region of the function. The notable difference

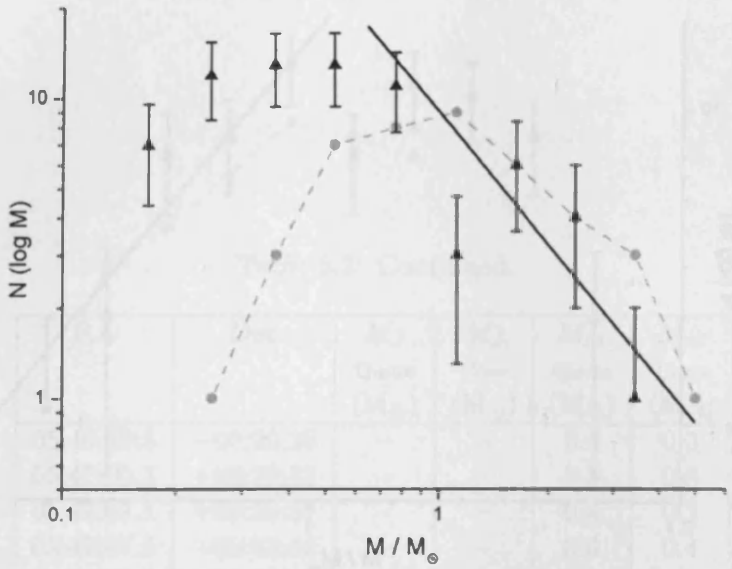

Figure 5.7: The core mass function based on the masses measured by Motte et al. (2001). The masses have been normalised to my assumptions of distance, temperature and opacity. The plotted line has a slope of $x = -1.5$, and is a good fit to the cumulative mass function. The mass function shown in Figure 5.3 is overlaid in grey.

between Figures 5.6 and 5.3 are the increased number of low mass cores found by Johnstone et al. These are more massive than my quoted sampling limit of 0.22 $M_{\odot}$. The reason they are not in my dataset is because they are both too extended and too low in mass to be bound cores.

The mass function of Motte et al. (2001) is shown in Figure 5.7. It is still consistent with my mass function, which is overlaid in grey, but shows a greater deal of discrepancy than we saw in Figure 5.6. This function peaks at a lower mass than Figure 5.3. This is expected, given that a number of high mass cores have been split up into lower mass sub-cores by Motte et al.

To summarise this section, I have calculated the prestellar core mass function for the submillimetre sources in the Orion B molecular cloud that are not known

to be protostellar in nature. The slope of the high mass tail of the mass function is consistent with most estimates of the high mass region of the stellar initial mass function. The core mass function peaks around 1 $M_{\odot}$, which is higher than the peak of the IMF. This can be explained by the star formation efficiency of each core being less than 1, and by binary and multiple star formation from each core.

5.2.3 Clustering of Cores in Orion B

In this section, I analyse the clustering properties of the sources detected in the 850 μm SCUBA map. The results are compared to the clustering properties of young stars that are still associated with their parent molecular cloud.

The majority of stars form in clusters (e.g. Gomez et al., 1993), and the way in which stars are clustered can give insight into the physics controlling their formation. Many researchers have studied the clustering of young pre-main-sequence (PMS) stars (e.g. Gomez et al., 1993; Larson, 1995; Simon, 1997). The scan-map data introduced in Chapter 4 shows that the prestellar cores and YSOs are obviously clustered. In this section, their clustering is analysed and compared to that of PMS stars from a number of regions. The advantage of studying the clustering of such young objects is that they have not yet had time to move far from their birthplace.

A number of methods have been employed to study the clustering properties of PMS stars in star-forming regions. Gomez et al. (1993) used a two-point angular correlation function to investigate the clustering of T-Tauri stars in the Taurus-Auriga molecular cloud. The two-point angular correlation function, $w(\theta)$, is defined in terms of the joint probability, δP, of finding two objects separated by

the angular distance θ (Peebles, 1980):

$$\delta P = N^2[1 + w(\theta)]\delta\Omega_1\delta\Omega_2. \tag{5.5}$$

Here, N is the mean surface density of objects and $\delta\Omega_1$ and $\delta\Omega_2$ are two elements of solid angle, separated by θ. $w(\theta)$ can be estimated by comparing the number of pairs of stars at each separation to an equivalent number calculated for an equal number of randomly placed objects within the map.

Gomez et al. (1993) used the estimator for $w(\theta)$ given by:

$$w(\theta) = \frac{N_{CC}(\theta)}{N_{RR}(\theta)} - 1, \tag{5.6}$$

where $N_{CC}(\theta)$, and $N_{RR}(\theta)$ are the number of object-object pairs and the number of random-random pairs respectively. They found that for Taurus, the stars are clustered, and the distribution of the stars could be fitted by a single power-law with an index of -1.2. This would indicate that the stars are clustered self-similarly, and that the clustering on this range of scales is caused by the same physical mechanism. They also found tentative evidence for a break in the slope of the power-law at a scale of approximately 0.05 pc.

An alternative method, that is both more rigorous, and more successful in handling smaller numbers of sources was proposed by Landy & Szalay (1993). They showed that the estimator for the correlation function, given by Equation 5.6, has a variance that is significantly higher than Poisson statistics would predict. They proposed an alternative method for calculating w(θ):

$$w(\theta) = \frac{N_{CC}(\theta) - 2N_{CR}(\theta) + N_{RR}(\theta)}{N_{RR}(\theta)}, \tag{5.7}$$

and showed that its variance was proportional to the statistical prediction, which is given by the following (Hewett, 1982):

$$\delta w(\theta) = \sqrt{\frac{1 + w(\theta)}{N_{CC}(\theta)}}. \tag{5.8}$$

Here, $N_{CC}(\theta)$ and $N_{RR}(\theta)$ are as in Equation 5.6, and $N_{CR}(\theta)$ is the number of object-random pairs. The three terms are normalised to account for a different number of real and random objects.

Larson (1995) combined the data of Gomez et al. (1993), with higher resolution data of the same region obtained by Simon (1992), Ghez et al. (1993) and Leinert et al. (1993). Larson plotted the data as the mean surface density of companions, which is related to the two-point angular correlation function, and is discussed below. This analysis confirmed the existence of the break in the slope at a scale of 0.04 pc, indicating that the star formation process is not scale-free. The data could be fitted by two power-laws, with slopes of -0.6 on scales larger than 0.04 pc, and -2 on scales shorter than this.

Larson (1995) noted that the break occurred at approximately the Jeans length, and suggested that on scales shorter than the break, the separations are between stars in bound systems. On larger scales, the distribution of separations represents the clustering of these systems.

Simon (1997) analysed new data for the Taurus-Auriga cloud, and carried out a similar analysis for the ρ Ophiuchi and the Orion Trapezium star-forming regions. He found that in all three regions, the mean surface density of companions is well represented by a two part power-law. In all cases except the Orion Trapezium cluster, the slopes of the power-laws are consistent with the results of Larson

(1995). The Trapezium cluster had a slope of -0.2 in the high separation regime. The position of the break in the slope for the three regions is very different, varying from 400 AU in the Orion Trapezium cluster, to 5000 AU in ρ Ophiuchi, and 12000 AU in Taurus-Auriga cloud. Simon concluded that the position of the break is not solely caused by the Jeans length in the cloud, but is influenced by other factors, such as the mean stellar density.

The only data regarding the clustering properties of PMS stars in Orion B was obtained by Nakajima et al. (1998), who found that between separations of $3.8'$ (0.4 pc) to $2.5°$ (17 pc), the data can be fitted with by $\Sigma_c(\theta) \propto \theta^{-0.7}$. At closer separations, the data cannot be fitted by a power-law.

The two-point angular correlation function was calculated using Equation 5.7 for the cores and protostars in my Orion B data. The result is given in Figure 5.8, which shows $w(\theta)$ plotted against $\log\theta$, from the resolution limit of the telescope to the maximum extent of the map. Each object in the map was used, regardless of whether or not a protostellar source has been identified, because the protostars are too young to have travelled far from their birthplace. The analysis was therefore based on 55 objects, which gave 2970 pairs. 250 objects were placed at random positions within the bounds of the map, therefore there were 13750 object-random pairs, and 62250 random-random pairs. The pairs were binned using annuli with logarithmically increasing radii. The error bars on the graph were calculated using Equation 5.8.

Figure 5.8 shows a positive correlation on small scales, indicating that the cores are clustered. To quantify this clustering, the data were plotted on a log-log

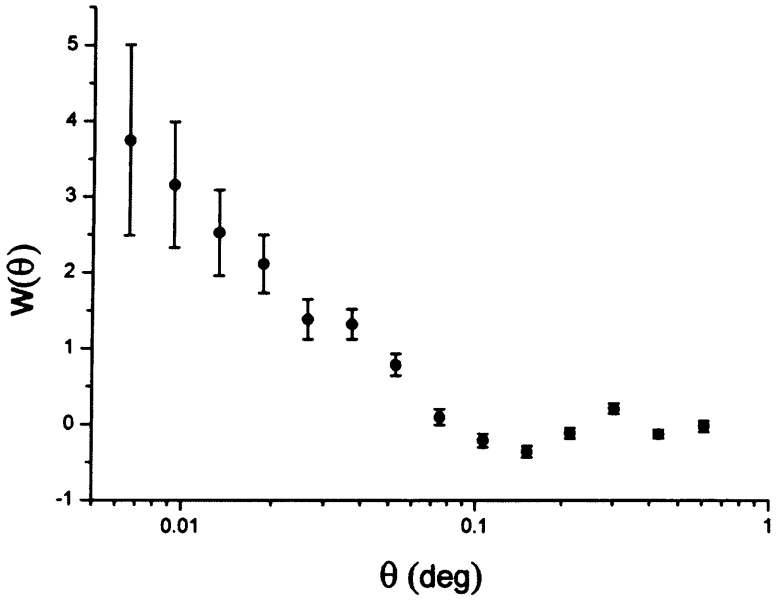

Figure 5.8: Figure showing the two-point angular correlation function for my Orion B cores, calculated using Equation 5.7. The graph clearly shows that the cores are clustered on scales smaller than $\sim 0.1°$.

scale in Figure 5.9. The data were fitted by a power-law of the form:

$$w(\theta) = \left(\frac{\theta}{\theta_0}\right)^{\alpha}, \tag{5.9}$$

where θ_0 is the characteristic clustering length scale. The best fit parameters of Equation 5.9 are $\theta_0 = 0.05°$ and $\alpha = -0.66$. This indicates that the cores are significantly clustered on scales smaller than $0.05°$, i.e. there is a higher probability of finding a pair of cores at a separations below this value than for a random distribution. At the distance of Orion, this corresponds to 0.35 pc. It should be borne in mind that the technique is insensitive to clustering on scales comparable with the map size (e.g. Simon, 1997). Given that my estimated θ_0 is smaller than the scale of the map, this appears to be a significant result.

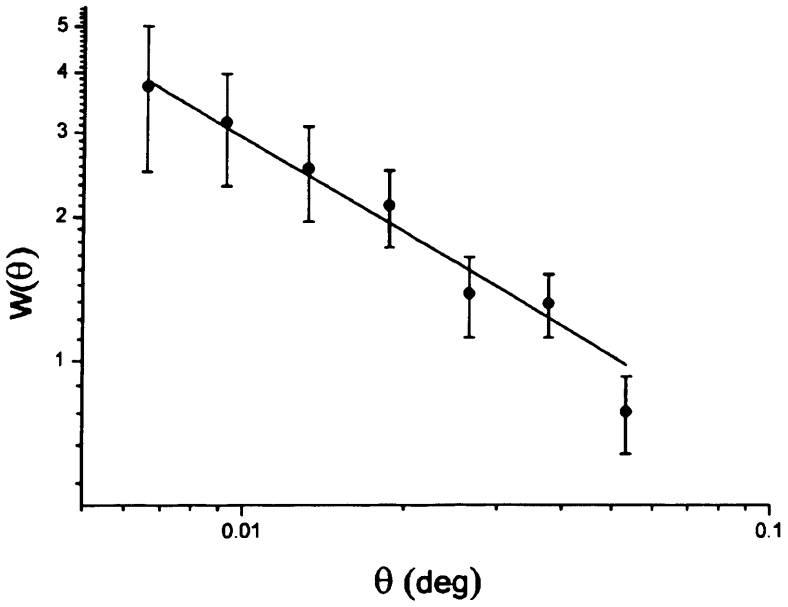

Figure 5.9: Figure showing the two-point angular correlation function in Figure 5.8, plotted on a log-log scale. The best fitted power-law is plotted.

The mean surface density of companions $\Sigma_c(\theta)$ can be more useful than the two-point angular correlation function (Larson, 1995), as it gives the actual surface density, rather than the excess density over a random distribution. It is calculated by measuring the number of core pairs at each separation, and dividing by the total number of objects (N_{cores}) and the area of the annulus:

$$\Sigma_c(\theta) = \frac{N_{CC}(\theta)}{N_{cores}\pi\left[\left(\theta + \frac{\Delta\theta}{2}\right)^2 - \left(\theta - \frac{\Delta\theta}{2}\right)^2\right]}. \tag{5.10}$$

$\Sigma_c(\theta)$ is related to the two-point angular correlation function by the following (Peebles, 1980):

$$\Sigma_c(\theta) = \frac{N_{cores}}{A}[1 + w(\theta)], \tag{5.11}$$

where A is the total area of the map.

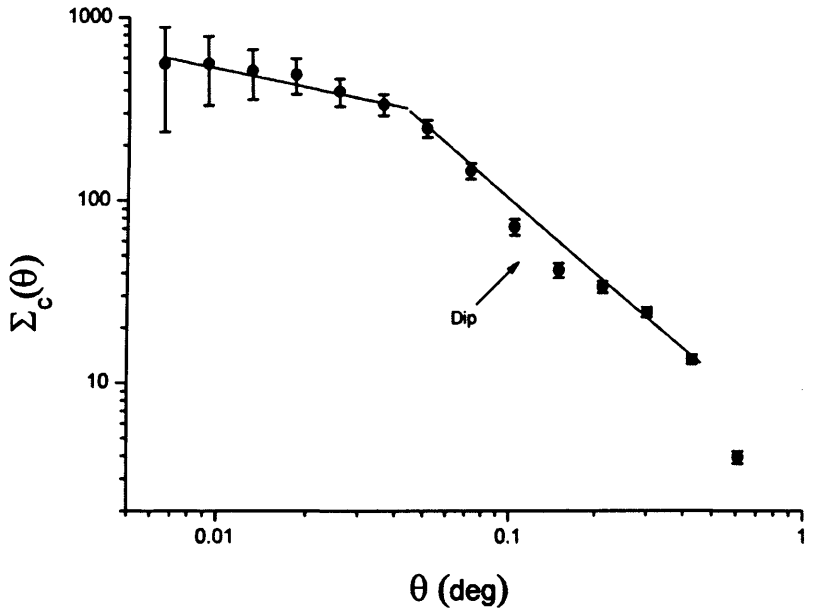

Figure 5.10: The mean surface density of companions for my Orion B cores, calculated using Equation 5.10. The error bars are calculated based on the square root of the number of pairs in each annular bin.

Figure 5.10 shows the mean surface density of companions calculated using Equation 5.10. As for Figure 5.8, the pairs were binned using annuli with logarithmically increasing radii, from the resolution limit, to the size of the map. The error bars on the graph are simply the $\sqrt{N}$ error in each annulus. The graph shows a number of features, the most obvious being that the data are not well fitted by a single power-law over their full range. This is an artefact of the limited scales that are reliably sampled by the data, and is explained more fully below. Secondly, there is a noticeable dip below the slope of the graph at $\theta = 0.1^\circ - 0.2^\circ$. This is due to the fact that the two groups of cores in LBS10-17 and LBS8 are smaller than this scale, and the distance between the groups is larger. There are therefore significantly fewer cores found in annuli with radii corresponding to this scale, than on both smaller scales (where core pairs from the same group are detected), and larger scales (where cores from the other group are picked up).

$\Sigma_c(\theta)$ can only be accurately measured for cores further away from the map boundary than the maximum annulus radius (θ_{max}). Any cores closer to the boundary than θ_{max} may have unseen companions, therefore $\Sigma_c(\theta)$ will be underestimated. This could explain why the curve in Figure 5.10 is not well fitted by a single power-law.

Bate, Clarke, & McCaughrean (1998) describe a number of methods for accounting for the missing cores. The simplest method is to select a subsample of cores such that none are closer to the map boundary than θ_{max}, and calculate $\Sigma_c(\theta)$ using this sub-sample. A disadvantage of this method is that a large amount of information is discarded. An alternative is to use the area of each annulus that falls within the map area, rather than the total area of the annulus. This area can be calculated either analytically, or using Monte Carlo methods.

As the number of cores in my sample is small, selecting a subset of the data is undesirable, because it leaves too few cores to obtain good statistics, therefore the area correction was applied. Given the complicated shape of the map, the areas of the annuli were calculated using the Monte Carlo method.

For each annulus size, the area of the annulus contained within the map was calculated for each core position. The average area for the annulus of that size was then used when calculating $\Sigma_c(\theta)$ for that scale (hereafter called $\Sigma_{c-corr}(\theta)$ when the correction is applied). For smaller values of θ, there are very few cores at a distance θ from the map boundary, therefore this method has no effect on the calculation, and $\Sigma_{c-corr}(\theta)$ is equal to $\Sigma_c(\theta)$. When θ approaches the size of a single scan-map, the average area of the annuli that falls outside the map becomes significant. The sizes of the annuli, together with the average area that falls inside the map boundary, are tabulated in Table 5.3. The table also contains the number

Table 5.3: Table giving the annular radii (columns 1 and 2), and the number of pairs with separations that fall within each annulus (column 3). Column 4 shows the mean surface density of companions, as calculated using Equation 5.10. Columns 5 and 6 give $\Sigma_c(\theta)$ and $\Sigma_{c-corr}(\theta)$ respectively. Column 6 gives the average fractional area of each annulus that is within the map.

Annular radii ($''$)		N_{CC}	$\Sigma_c(\theta)$	$\Sigma_{c-corr}(\theta)$	Area
Inner	Outer				
20.0	28.3	3	559	563	0.99
28.3	40.1	6	558	559	1.00
40.1	56.8	11	510	512	1.00
56.8	80.5	21	485	486	1.00
80.5	114.0	34	392	393	1.00
114.0	161.4	58	333	341	0.98
161.4	228.6	86	246	268	0.92
228.6	323.7	101	144	179	0.81
323.7	458.4	100	71	112	0.64
458.4	649.3	116	41	91	0.45
649.3	919.5	189	33	110	0.30
919.5	1302.3	276	24	137	0.18
1302.3	1844.3	305	13	152	0.09
1844.3	2612.0	179	4	161	0.02

of pairs at each separation, and the values of $\Sigma_c(\theta)$ and $\Sigma_{c-corr}(\theta)$.

Figure 5.11 shows the mean surface density of companions, corrected for annuli that fall partially outside the map. The effect of this correction is dramatic, and $\Sigma_{c-corr}(\theta)$ at large θ is increased by up to a factor of 10 from $\Sigma_c(\theta)$. This correction effectively makes the assumption that where the annulus falls outside the map boundary, it is populated with a density of cores equal to that within the map. At large separation, the correction will lead to a large overestimate in the number of pairs. This is because the mapped area is the central region of the Orion B molecular cloud, and the surface density of cores is likely to be higher here than outside the map. The calculation of $\Sigma_c(\theta)$ makes the assumption that there are no cores beyond the edge of the map, which is probably an underestimate. Therefore the estimation of $\Sigma_c(\theta)$ can only reliably be made where the results obtained using

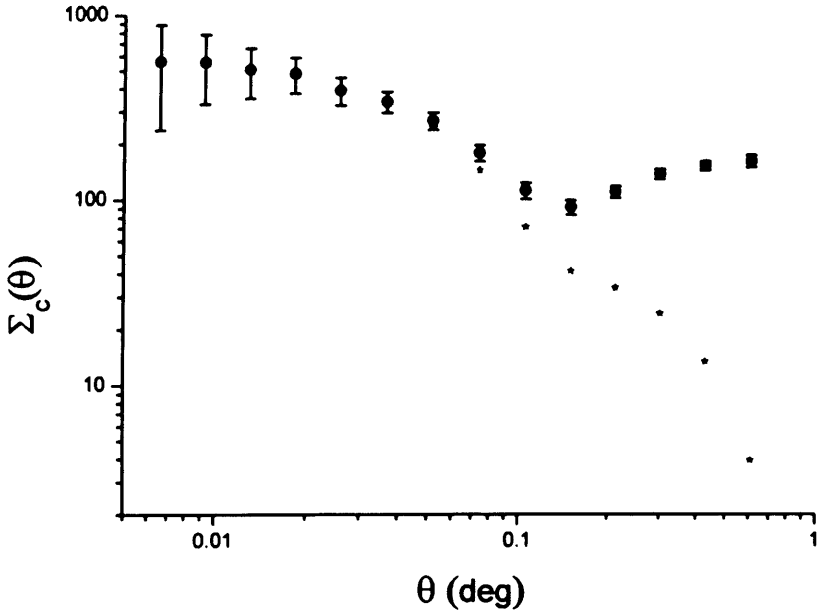

Figure 5.11: Figure showing the $\Sigma_{c-corr}(\theta)$ for the cores in my Orion B data (filled circles). The error bars are calculated based on the square root of the number of pairs in each annular bin. The grey stars indicate the uncorrected value of $\Sigma_c(\theta)$ for comparison, as plotted in Figure 5.10.

either of the two assumptions are consistent. This range of separations is from 20″ to 320″, which correspond to 0.04 pc and 0.6 pc respectively at the distance of Orion B.

Figure 5.12 shows the uncorrected mean surface density of companions for the separations that are reliable in this map shape and size. The data are clearly not well fitted by a single power-law. At separations below 0.04° (0.28 pc at a distance of 400 pc), the data are best fitted by a power-law with a slope −0.3. At larger separations, the data are best fitted by a power-law with a slope of −1.1. This indicates that the clustering on these scales does not occur in a scale free manner.

The steeper slope of −1.1 has the same origin as the 'dip' that is apparent in Figure 5.10, which has already been explained by the fact that the cores are

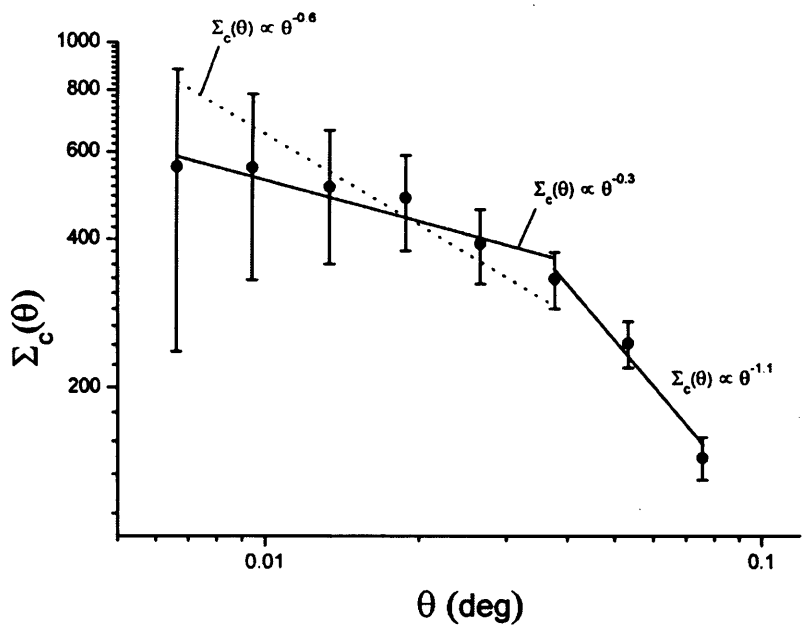

Figure 5.12: Figure showing the mean surface density of companions over the reliable scales, i.e. away from map edge effects. The best fit power-laws to the two regions of the graph are shown as solid lines. At separations smaller than 0.04° (0.28 pc), the data are fit by $\Sigma_c(\theta) \propto \theta^{-0.3}$. At separations larger than this, the best fit line is $\Sigma_c(\theta) \propto \theta^{-1.1}$. The steeper part of the graph can be explained by the finite size of each of the sub-clusters (0.04°).

located in two groups, which are found in LBS10-17 and LBS8. These groups are in the form of fragmenting filaments, with clear boundaries. These are therefore not scale free systems, and it is not surprising that the results find this. Hence we will ignore the slope of -1.1 and concentrate on the smaller separations.

The slope of -0.3 is flatter than the -0.6 that is usually found for PMS stars in the clustering regime. A power-law with a slope of -0.6 is plotted on Figure 5.12 as a dotted line. This line does fall within the 1σ statistical error bars, though it is a significantly poorer fit.

Interestingly, $\Sigma_c(\theta)$ measured for the young stars in the Orion Trapezium cluster at large separations, has a power-law slope of -0.2. This is more consistent

with the value of −0.3 I have calculated for the prestellar cores and protostars in Orion B. This suggests that clustering properties of the young stars are set at the prestellar stage, and also that the power-law slope of $\Sigma_c(\theta)$ is set by environmental effects, and as such, varies from region to region.

There is no evidence in the data for the break in the curve that signifies the change from the clustering to the multiplicity regimes. This is expected, because the break typically occurs on scales below the resolution limit of these data. The only previous data constraining the position of the break in the Orion B region is that it lies below 3.8′ (0.4 pc) (Nakajima et al., 1998). My data reduces this upper limit to 20″ (0.04 pc or 8000 AU).

To summarise and conclude this section, I have measured the mean surface density of companions for the prestellar cores and protostars in Orion B. The spatial scales that are reliably probed by the map are between 0.04 and 0.6 pc. At scales below 0.28 pc, $\Sigma_c(\theta)$ can be fitted by a single power-law with a best-fit slope of −0.3. This slope is smaller than the value of −0.6 that is typically found for PMS stars in the clustering regime, but is consistent with the value of −0.2 that is found in the Orion Trapezium cluster. However, the value of −0.6 is just consistent with my data at the extreme limits of the 1σ error bars (see Figure 5.12). Finally, my data have allowed the upper limit of the break between the multiplicity and the clustering regimes to be lowered from 0.4 pc to 0.04 pc. This is consistent with the values seen for YSOs.

5.3 The L1689 Molecular Cloud

In this section, I discuss the scan-map data for the L1689 molecular cloud. In Section 5.3.1 I discuss the nature of each of the sources using previous surveys of the region at different wavelengths. In Section 5.3.2, the SCUBA data are compared with molecular line maps of L1689 and the neighbouring L1688 cloud, and also millimetre continuum maps of L1688. The similarities and differences between the two clouds are discussed.

5.3.1 Young Stellar Objects

Figure 5.13 shows the map of the L1689 region with my 850 μm detected sources marked. In this section, I will discuss the identities of each of these detections.

Source #1 is a relatively bright object with no evidence of existing protostars. It shows some evidence of internal structure. Either side of the bright central core are what appear to be spiral arms. The diameter of the system is approximately 3′ (0.1 pc at a distance of 130 pc). There is also a second distinct core (#2) approximately 2′ from the centre of core #1. The proximity of the second core to #1 indicates that the more massive core may be undergoing fragmentation.

The relatively faint source #4 is the Class II object L1689-IRS5, which has been identified in the near and mid-infrared (Greene et al., 1994; Bontemps et al., 2001). Approximately 25″ north of this (0.015 pc at 130 pc), lies the brighter source #3, which has not been previously observed at other wavelengths. This object is therefore assumed to be prestellar in nature. Source #5 has also not been detected at other wavelengths, though its low mass (~ 0.05 $M_{\odot}$) and diffuse nature indicate

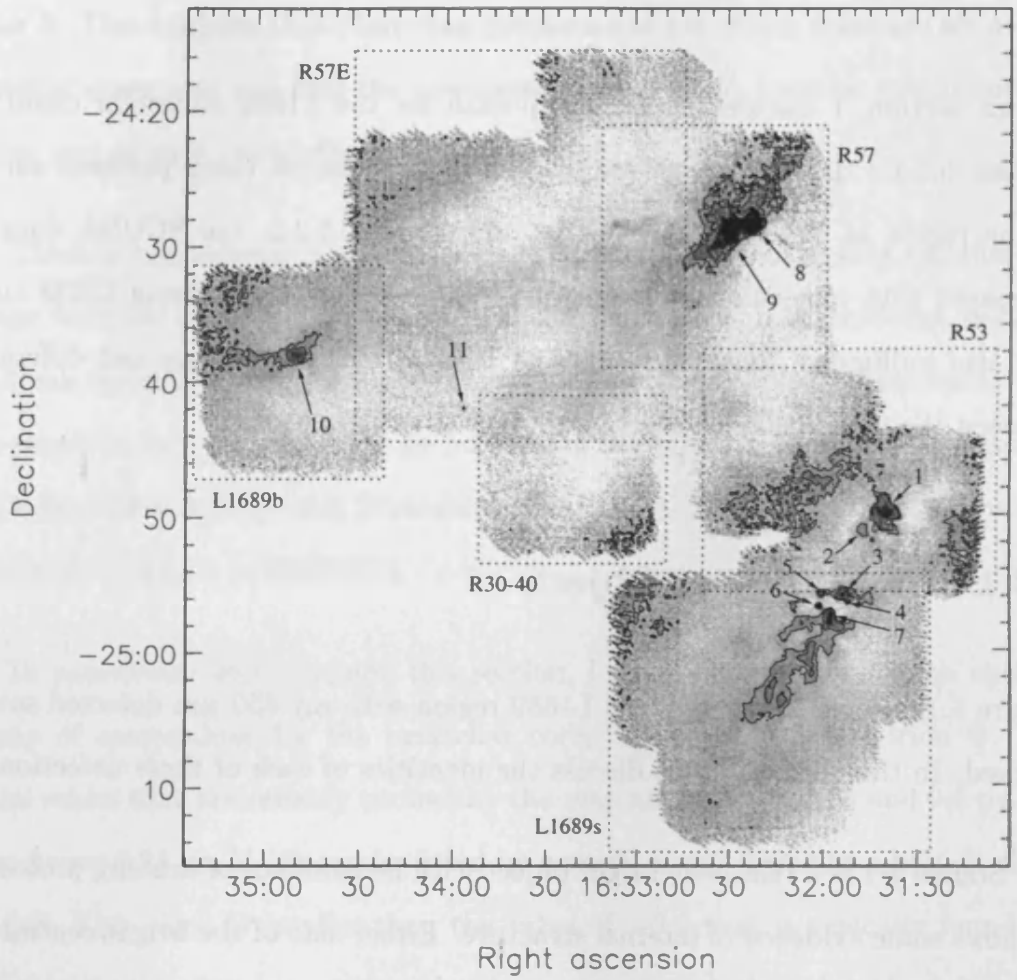

Figure 5.13: The L1689 map at 850 μm. The contour levels are at 3σ, 5σ, 10σ, 15σ, 20σ, 40σ and 80σ. Contours are based on the map smoothed to a resolution of $18''$. The identified cores are marked on the map.

that it may not be gravitationally bound.

Source #6 is the Class I object IRAS 16289-2450, which is also known as L1689-IRS6 (Greene et al., 1994; Bontemps et al., 2001). This object is centrally condensed in the submillimetre and no extended emission is detected. Source #7 is the prestellar core L1689SMM, which was mapped by Kirk (2002) using SCUBA in jiggle-map mode. As discussed in Chapter 4, the core is elongated in the direction

of the filament, though shows no evidence of fragmenting along its length. Both the morphology and flux density, measured from the scan-map, are consistent with the earlier jiggle-map. There is no evidence of a protostar at the centre. There is an abrupt gap in the filament between core #7 and the group of objects to the north (#3, #4 and #5). This could be caused by the gravitational collapse of the filament onto the cores, or the cavity could have been cleared by outflows from IRAS 16289-2450, which lies within the cavity.

The brightest source in the map is #8, which is the Class 0 protostar IRAS 16293-2422 (hereafter 16293). This object has been well studied at a number of wavelengths (e.g. Mundy et al., 1992; Ceccarelli et al., 1998; Castets et al., 2001), and is used as a secondary flux calibrator for submillimetre observations using SCUBA (Sandell, 1994). It is a proto-binary system, with two components (16293a & b) at a separation of approximately 800 AU (Mundy et al., 1992). Both objects are Class 0 protostars and are the sources of a quadrupolar molecular outflow, though 16293b shows no evidence of current outflow activity (Walker, Carlstrom, & Bieging, 1993). The two sources are unresolved in the 14″ JCMT beam.

Source #9 corresponds to the third object in the 16293 system, 16293E, which is located 86″ (0.05 pc) to the east of 16293. This object is also a Class 0, and the source of a molecular outflow (Castets et al., 2001). Assuming a temperature of 24 K for this source (Castets et al., 2001) gives an envelope mass of 1.0 ± 0.5 $M_{\odot}$ in an area of 0.06×0.05 pc.

Source #10 is the well studied prestellar core L1689B. This was one of the original starless ammonia cores mapped by Myers & Benson (1983) and subsequently determined to be prestellar in nature (Ward-Thompson et al., 1994). Subsequent mapping with the 1.3 mm MPIfR bolometer array at the IRAM telescope con-

firmed the results of the earlier survey (André et al., 1996), and provided a more detailed picture of the density profile of the core (see Section 1.3).

The morphology of L1689B, as shown in Figure 4.12, is elongated in a roughly east to west direction. This is consistent with the 1.3 mm map (André et al., 1996) and also a SCUBA jiggle-map of the core (Kirk, 2002). Kirk performed a greybody fit to the SED of L1689B between 90 μm and 1.3 mm using ISO, JCMT and IRAM data, and found a best-fit temperature of $11.9^{+0.7}_{-0.5}$ K. Using this temperature, together with a dust opacity of 1.4 cm^2g^{-1}, yields a mass for L1689B of 1.0 ± 0.4 $M_\odot$ in an area of 0.08×0.05 pc. This is consistent with the mass calculated by André et al. (1996) from the 1.3 mm dust emission for an equivalent sized aperture.

The final source (#11) lies 20″ (2600 AU) from a Class II protostar RX J1633.9-2442, which was identified through optical spectroscopy followup observations to a ROSAT (Röntgen Satellite) X-ray survey of ρ Ophiuchi (Martin et al., 1998). It is assumed that the submillimetre emission is associated with this source.

Table 5.4 summarises these results, and also gives the masses calculated from the 850 μm flux. The temperature of 12 K calculated for L1689B (Kirk, 2002) was used for all of the prestellar cores, and the $\kappa_{d,850\mu m}$ of 1.4 cm^2g^{-1} was used as discussed in Section 1.6.1. For Class 0 and I envelopes, the volume averaged dust temperature is assumed to be 30 K (André & Montmerle, 1994). A higher dust mass opacity of 1.9 cm^2g^{-1} was used, as recommended by Ossenkopf & Henning (1994) for higher density regions. This is consistent with the value used by André & Montmerle if a β of 1.3 is used to extrapolate from 1.3 mm. The dust temperature of Class II sources is also taken to be 30 K (André & Montmerle, 1994), though a higher still value of $\kappa_{d,850\mu m}$ is required, due to increased grain growth in the high

Table 5.4: The prestellar core and protostellar envelope masses for the sources in L1689. The region of the cloud that each source is associated with is included in column 4. This information is used in the following analysis. [‡1] IRAS 16293-2422 is known to be a binary system. [‡2] (Greene et al., 1994), [‡3] (Kirk, 2002), [‡4] (e.g. Mundy et al., 1992), [‡5] (Castets et al., 2001), [‡6] (André et al., 1996), [‡7] (Martin et al., 1998).

Source Name	Class	Mass ($M_\odot$)	^{13}CO region	Other Names
1	Pre	2.4	R53	
2	Pre	0.2	R53	
3	Pre	0.4	R55	
4	II	0.01	R55	L1689-IRS5[‡2]
5	Pre	0.1	R55	
6	I	0.02	R55	IRAS 16289-2450[‡2]
7	Pre	0.7	R55	L1689SMM[‡3]
8	0[‡1]	1.6	R57	IRAS 16293-2422[‡4]
9	0	0.8	R57	16293E[‡5]
10	Pre	1.0	R65	L1689B[‡6]
11	II	0.003	R65	RX J1633.9-2442[‡7]

density disks. Beckwith et al. (1990) recommend a $\kappa_{d,1.3mm} = 2.0$ cm^{2}g^{-1}, which corresponds to $\kappa_{d,850\mu m} = 3.5$ cm^{2}g^{-1} if β is equal to 1.3.

The temperature profile of 16293 makes calculating the dust mass from submillimetre observations problematic. Molecular line studies of molecules that adsorb to grain surfaces (e.g. Castets et al., 2001; Wakelam et al., 2004) indicate that the envelope of 16293 is composed of a hot core at a temperature of $\sim$ 100 K, surrounded by a cooler outer envelope at a temperature of 20 – 30 K. The hot inner core has an approximate size of 2″ (260 AU), and is therefore not resolved in the JCMT beam. Taking a temperature of 30 K, gives an envelope mass calculated from the 850 μm data of 1.6 ± 0.7 $M_\odot$ over an area of 0.07 × 0.06 pc. This is comparable with the estimated envelope mass calculated by Walker et al. (1993) from interferometric observations at 3 mm. However, the scale of the 3 mm map is comparable with the JCMT beam, therefore we would expect the combined (3 mm)

envelope masses to be comparable with the peak 850 μm flux density, rather than the integrated flux density. This implies that my values for either the temperature or the dust mass opacity (or both) may have been underestimated.

5.3.2 Comparisons with Previous Surveys

As discussed in Chapter 4, the submillimetre continuum sources in L1689 have all formed in filaments, the most clearly defined being Filament 1 (see Figure 4.14). Maps of L1688 made in $C^{18}O$ (Wilking & Lada, 1983) and ^{13}CO (Loren, 1989) have shown that the most of the CO is found in clumps that are connected by filaments. This filamentary structure is not restricted to the streamers that extend from L1688 and L1689 to the east, but is also seen in the larger clouds if data with restricted radial velocity are considered. Figure 5.14 compares the 850 μm data of L1689 with the ^{13}CO map considering only V_{LSR} between 4.68 kms^{-1} and 5.02 kms^{-1} (the full velocity range in the map is 2.98 - 5.70 kms^{-1}). As can clearly be seen, Filament 1 is detected both in the dust emission and in ^{13}CO. Filaments 3 and 4 are seen at velocities 3.32 - 3.66 kms^{-1}, though Filament 2 is not apparent in the ^{13}CO maps.

It is interesting to compare the L1688 and L1689 clouds, as they share the same environment, and are both the same distance away from the Sun, yet they do not share the same level of star formation activity. Loren (1989) calculated the mass L1688 and L1689 from the ^{13}CO map to be 1447 and 566 $M_{\odot}$ respectively, differing by a factor of 2.6. However, the area on the sky of L1688 (measured at the 6 K contour of the ^{13}CO maps — see Figure 4.9) is only 1.4 times larger than L1689. Assuming that the two clouds have approximately the same aspect ratio (which is probably a fair assumption, given their similar morphology), the volume

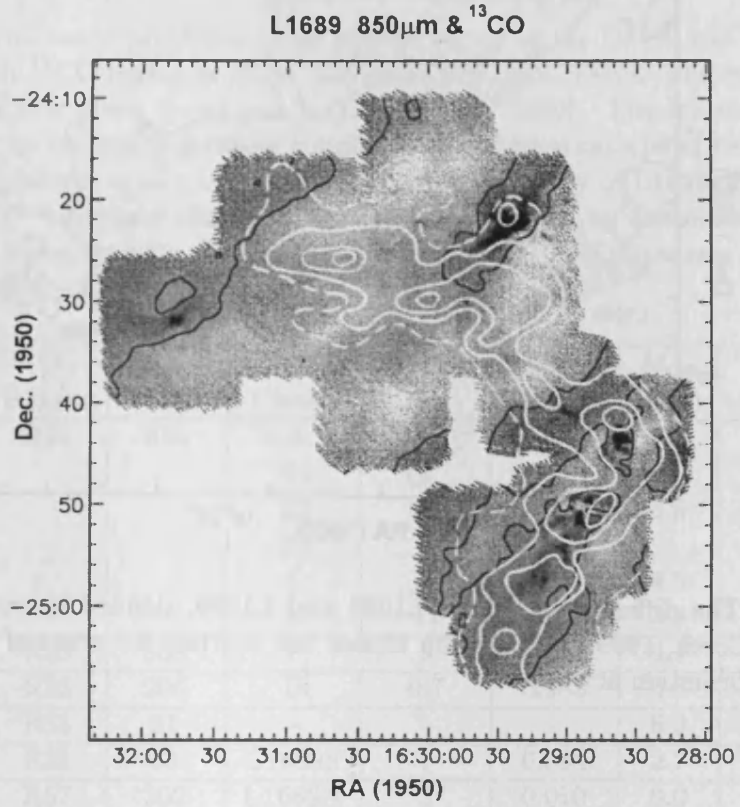

Figure 5.14: Composite map showing the 850 μm scan-map of L1689 as a grey-scale. The dark contours are based on the map smoothed to a resolution of 60″. The light contours are ^{13}CO emission with V_{SLR} 4.68 – 5.02 kms^{-1} (Loren, 1989), and give antenna temperatures $T_R^*(^{13}CO)$ of 2, 4, 6, 8, 10 and 12 K.

of L1688 is 1.7 times that of L1689. The average density of L1688 is therefore approximately 1.5 times larger than that of L1689. As a result of this, we might expect star formation in L1688 to proceed more rapidly.

Loren (1989) divided the two clouds into 89 different regions, which have a clear spatial or velocity separation. These regions are used in the following analysis to compare the star formation activity across the clouds. Figure 5.15 shows the region boundaries overlaid on the ^{13}CO contour map, with the names marked for the regions currently undergoing star formation.

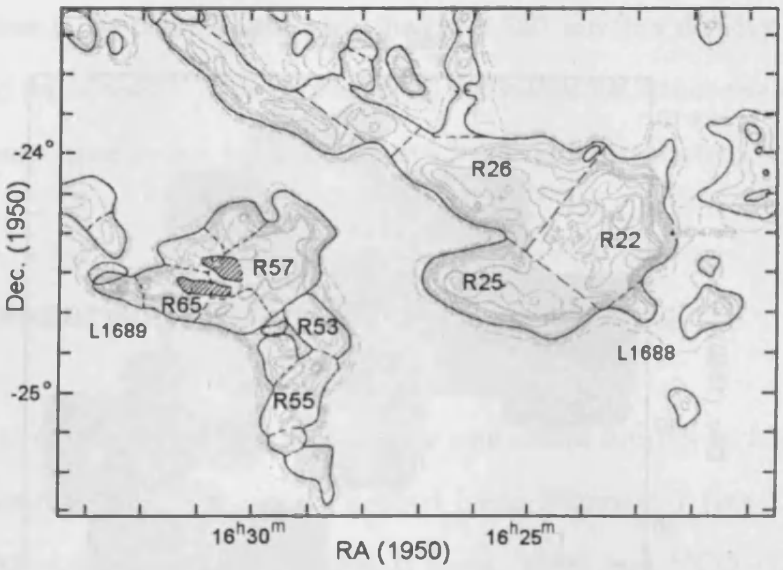

Figure 5.15: The different regions of L1688 and L1689, defined by spatial or velocity separations (Loren, 1989). The region names are marked for areas of the clouds with current star formation activity.

Loren et al. (1990) investigated differences in the star formation rates of the different regions of the ρ Ophiuchi cloud. To do this, they compared the total luminosity (L) of the young stars associated with each region, with the mass (M) of the gas, determined from the ^{13}CO measurements (Loren, 1989). They found that for L1688, the value of L/M is 1–2 orders of magnitude higher than for the neighbouring L1689. This method of estimating the star formation efficiency (SFE) is biased towards high mass stars. Loren et al. (1990) also calculated the ratio N/M, where N is the number of stars associated with each region. This estimate of the SFE is biased towards low mass stars. They again found that of all of the components of ρ Ophiuchi, L1688 has the highest SFE, though the difference between L1688 and L1689 is much less pronounced and may not be significant.

These methods are both probes of the past star formation activity in the two clouds. In order to compare the current activity, we can look at the mass of the

Table 5.5: The masses of prestellar cores in each region of the L1688 and L1689 clouds. The mass of each ^{13}CO region is given in column 3 (Loren, 1989). The mass of each of the DCO^+ clumps is given in column 5 (Loren et al., 1990). The masses of prestellar cores in each of the clumps is given in column 7. These were calculated using the IRAM survey of L1688 (Motte et al., 1998), and this SCUBA survey of L1689. For each ^{13}CO region, the DCO^+ mass and the prestellar mass are divided by the mass of the region (columns 6 and 8 respectively — for R22, the sum of the DCO^+ masses and prestellar core masses is used).

Cloud Name	^{13}CO Region	$M_{^{13}CO}$ ($M_\odot$)	DCO^+ Clump	M_{DCO+} ($M_\odot$)	$\frac{M_{DCO+}}{M_{^{13}CO}}$	M_{pre} ($M_\odot$)	$\frac{M_{pre}}{M_{^{13}CO}}$
L1688	R22	844	A	12	0.049	7.4	0.028
			B1	1		1.1	
			B2	6		6.6	
			B3	2		–	
			C	9		4.5	
			E	11		3.8	
	R25	368	F	9	0.024	0.4	0.001
	R26	206	D	0.7	0.003	0.6	0.003
L1689	R53	61	–	–	–	6.3	0.103
	R55	83	L1689S	7	0.084	2.7	0.033
	R57	202	L1689N	2	0.010	0.0	0.000
	R65	39	–	–	–	2.4	0.060

prestellar cores within each region of the two clouds, and compare that to the mass of the region measured using ^{13}CO (Loren, 1989). Motte et al. (1998) mapped the cold DCO^+ clumps in L1688 at a wavelength of 1.3 mm, with the IRAM 30 m telescope. They detected a number of dense cores, some of which were determined to be prestellar in nature by the lack of a central protostar.

Table 5.5 gives the mass of each cloud region, measured from the ^{13}CO emission (Loren, 1989), and also the mass of each of the DCO^+ clumps found within that region (Loren et al., 1990). The total mass of prestellar cores within each region (M_{pre}), is given in column 7. This is calculated from the millimetre dust emission for the L1688 cores (Motte et al., 1998), and from the submillimetre dust emission for the L1689 cores (my data).

In order to compare my prestellar core masses for L1689 with those for L1688, it is necessary to consider the assumptions used by Motte et al. They assumed a dust mass opacity ($\kappa_{d,1.3mm}$) of 0.5 cm^2g^{-1}, a distance to the region of 160 pc, and temperatures ranging from 12 - 20 K, depending on the local environment.

The masses of the prestellar cores in L1689, given in Table 5.5 were re-calculated to be consistent with these assumptions. A dust mass opacity ($\kappa_{d,850\mu m}$) of 0.9 cm^2g^{-1} was used, which is extrapolated from $\kappa_{d,1.3mm} = 0.5$ cm^2g^{-1}, assuming a β of 1.3 as discussed in Section 1.6.1. The core temperature of 12 K was not altered, as it is consistent with the temperature of 12 - 20 K used by Motte et al., given the lower number of luminous embedded stars (Loren et al., 1990).

The sensitivities of the millimetre and submillimetre surveys are not significantly different. The SCUBA map has a 1σ sensitivity of approximately 20 mJy/14″ beam, which corresponds to 0.009 $M_\odot$. The IRAM map has a 1σ sensitivity of 8 mJy/13″ beam, which corresponds to 0.006 $M_\odot$ at a temperature of 15 K.

Table 5.5 shows that the current star formation activity is highly variable across both clouds. R22 is currently the most active, forming 23 $M_\odot$ compared to ~ 0.5 $M_\odot$ in R25 and R26, and $\lesssim 6$ $M_\odot$ in the regions of L1689. This may be reasonably expected, as the R22 region is significantly more massive than the other regions. What is surprising is that the total mass of all of the prestellar cores in R22 is a lower percentage of the cloud mass than in most regions of L1689 (except R57 which has no detected prestellar cores). This indicates that per unit mass, L1689 is currently the more active of the two clouds. This conclusion contradicts that reached by Loren et al. (1990), which was based on previous star formation activity.

The two regions with the highest values of $M_{\rm pre}/M_{^{13}\rm CO}$ (R53 and R65) are the two regions that have no DCO^+ detection. Again this is surprising, because one of these regions contains the well studied prestellar core L1689B, which has no detected protostar, and has a well constrained temperature (Kirk, 2002), which is below the temperature that is required to dissociate DCO^+ (Loren et al., 1990). We would therefore expect L1689B to have the ideal conditions to contain DCO^+. This result indicates that DCO^+ clumps may not be as reliable a tracer of current star formation as was previously thought. The survey of L1688 carried out by Motte et al. (1998) was guided primarily by the DCO^+ clump positions and may therefore not have measured all of the current star formation activity of the cloud.

In conclusion, the L1689 cloud is currently forming stars at a comparable rate to L1688, when normalised to the total cloud mass. We would not expect this to be the case, because L1688 has a higher average density than L1689. This may be indicating that the rate of star formation is not being dominated by each cloud's self-gravity, which should be higher in the more dense L1688.

A possible alternative is that the star formation in both clouds could be being affected or even dominated by an external influence such as the Sco OB2 association, as originally suggested by Loren (1989). This is consistent with the observation that the majority of the star formation in both clouds is occurring at the edge of each cloud closest to the OB association. In addition, the streamers to the east of the clouds have a much smaller star formation rate. This hypothesis is strengthened because the star formation in both clouds is occurring in filaments that are perpendicular to the line of sight between each cloud and the OB association.

In addition, the filaments that are seen in the ^{13}CO observations of Loren have been detected in the submillimetre continuum, and contain all of the current star

formation activity.

5.4 The RCrA Molecular Cloud

In this section, I discuss the scan-map data of the RCrA cloud. The data are shown at 850 μm in Figure 5.16, on which the source numbers are marked. Unlike most of the objects detected in the Orion B and L1689 regions, the majority of the detections in the RCrA cloud correspond to known protostars. The most interesting source is #1, which is the brightest source in the map, and is composed of at least two and possibly three sources (see discussion in Section 4.4.2). A close up view of this source is given in Figure 5.17.

Chini et al. (2003) mapped the RCrA cloud at 1.2 mm with the SIMBA camera at the SEST telescope, which has a resolution of 24″. In order to compare the SIMBA data with my SCUBA data, Figure 5.18 shows the 850 μm SCUBA map in the vicinity of the brightest source, with the SIMBA data overlaid as a contour map (Chini et al., 2003). Other sources in the region are marked with stars and are discussed below.

In the immediate vicinity of the submillimetre peak lies the IRS 7 source, which was first detected in near infrared (Taylor & Storey, 1984). Centimetre radio observations revealed two sources (labelled on Figure 5.18 as VLA 10A and 10B), approximately equidistant from the IRS 7 infrared source (Brown, 1987). The authors interpreted the cm emission as being due to the interaction between a stellar wind from IRS 7 and a thick accretion disk.

Wilking et al. (1997) observed the region at 10 μm using the TIMMI camera

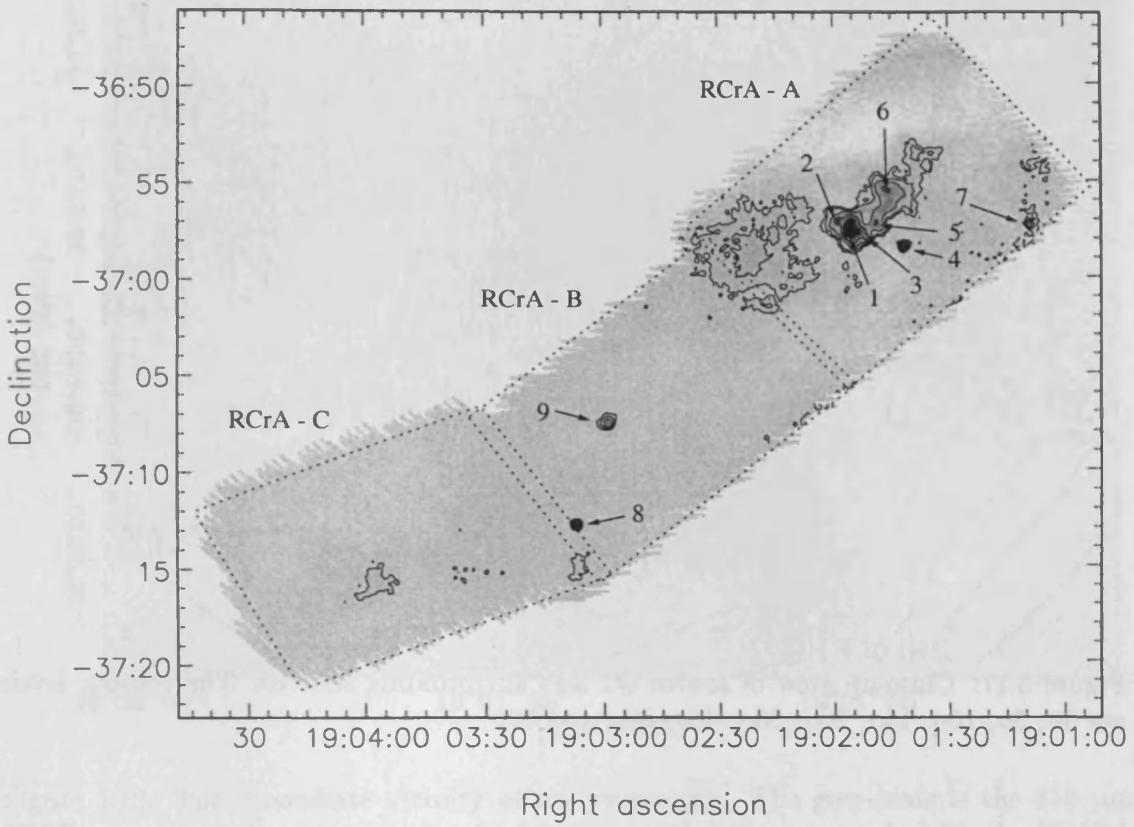

Figure 5.16: The RCrA map at 850 μm. The contour levels are 3σ, 5σ, 10σ, 20σ, 40σ and 60σ. Contours are based on the map smoothed to a resolution of $18''$. The regions in Table 4.8 are shown as dotted lines. The identified sources are marked on the map.

at the ESO 3.6 m telescope, and found that at this wavelength the object lies much closer to VLA 10A. The position of this detection is marked on Figure 5.18 as 'TIMMI'. The authors claim that the near infrared detection at the original position of IRS 7 is most likely to be reflection nebulosity, and they therefore refute the conclusion about the source made by Brown (1987). Instead, they claim that VLA 10A and the 10 μm source are the same deeply embedded protostar, while they state that VLA 10B is of an unknown nature.

The northern peak of the brightest source in the SCUBA map (#1b) is co-

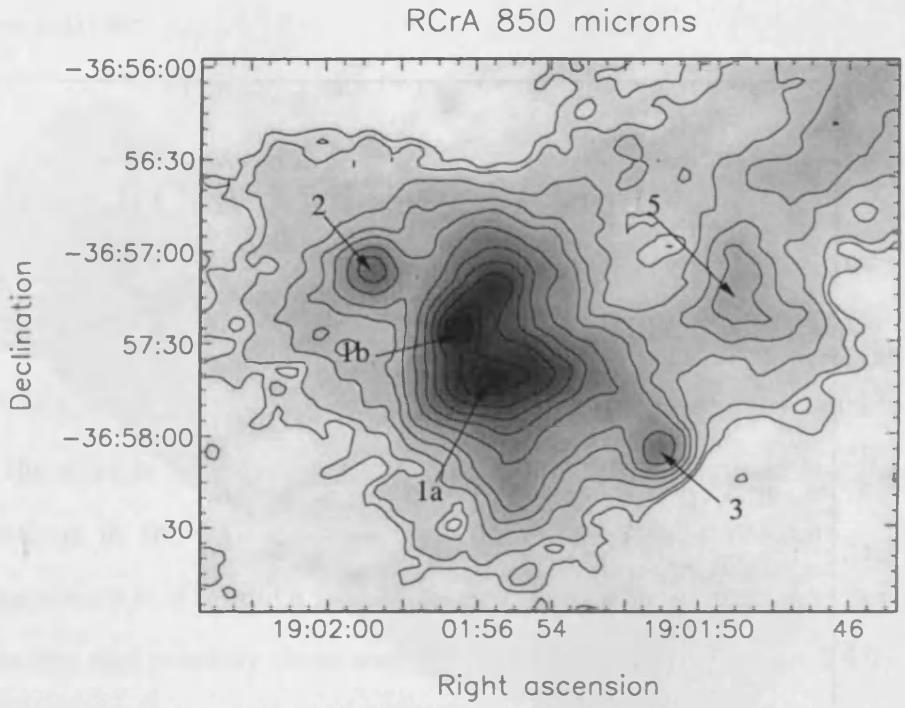

Figure 5.17: Close-up view of source #1 and surrounding sources. The contour levels are 3σ, 5σ, 10σ, 15σ, 20σ, 30σ, 40σ, 50σ and 60σ.

incident with VLA 10B. Therefore my source #1b is most likely a new Class 0 protostar. This conclusion is based on the object's large submillimetre flux, which traces a concentration of gas and dust, and the cm emission from VLA 10B, which reveals the presence of a protostellar object, embedded at the centre of the core. In addition, there have been no near or mid-infrared sources detected, which would indicate the presence of a more evolved protostar. This conclusion could be confirmed by the detection of a collimated outflow, centred on #1b. The southern peak (#1a) does not contain any infrared or centimetre sources, therefore it is more likely to be prestellar in nature.

The 1.2 mm continuum map of Chini et al. (2003), shows a similar morphology to my SCUBA data, featuring a strong peak — named MMS 13 by Chini et al. — between RCrA and TCrA. The two components of source #1 that are separated

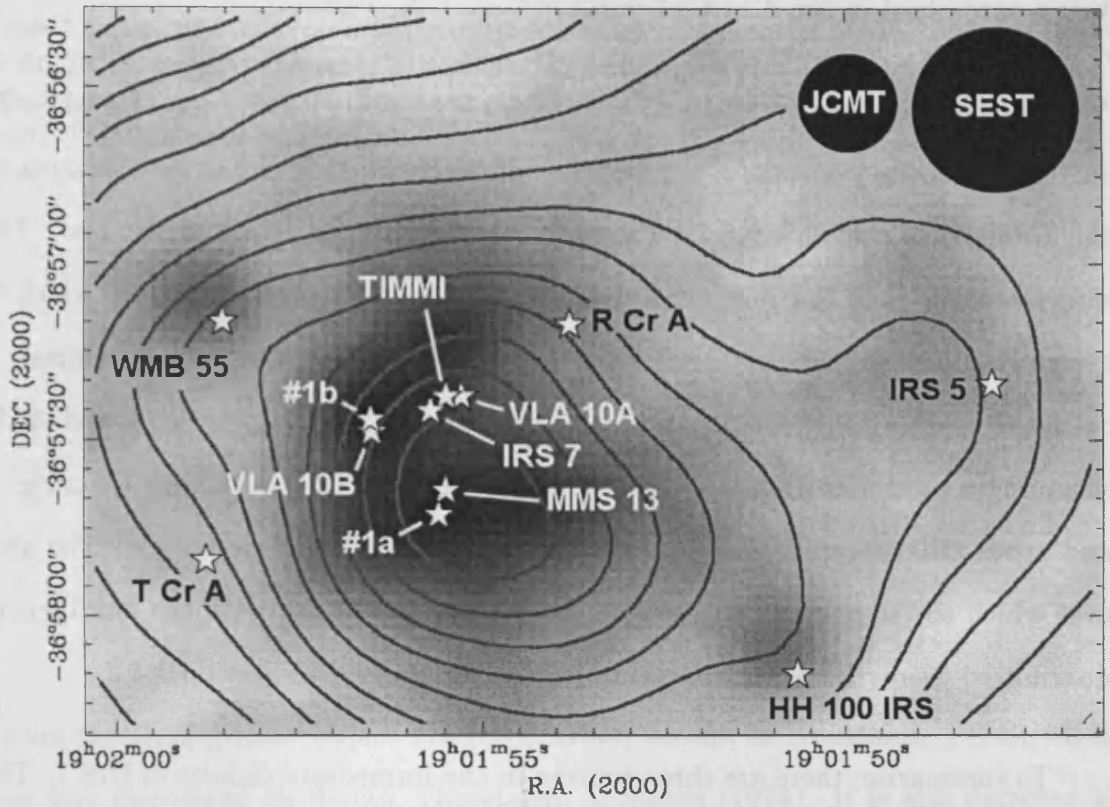

Figure 5.18: The immediate vicinity of my source #1. The grey-scale is the 850 μm SCUBA map and the contours are the 1.2 mm continuum map made with the SIMBA camera on the SEST telescope (Chini et al., 2003). The contour levels are 415 to 580 mJy/beam in steps of 55, then 690 to 1450 in steps of 190, and 1720 to 2800 in steps of 270 mJy/beam. The positions of relevant sources in the region are marked with stars, and discussed in the text. The JCMT and SEST beams are indicated at the top right of the figure.

by 20″ in my SCUBA data, are unresolved in the 24″ SIMBA beam. However, the 1.2 mm peak is centred on the SCUBA source #1a, instead of being centred on the composite of #1a and #1b. Therefore the SEDs of the two SCUBA sources seemingly have a different slope between 850 μm and 1.2 mm, with #1a having a shallower slope. This is consistent with #1a being prestellar and #1b being protostellar in nature, as the hotter protostellar envelope will have an SED that peaks at a shorter wavelength, and will therefore have a steeper slope between 850 μm and 1.2 mm. The slopes cannot easily be quantified, due to the two sources

being unresolved in the SIMBA beam.

Chini et al. classify MMS 13 as a Class 0 object with a mass of 5 $M_{\odot}$. To calculate this, they assume a temperature of 20 K. Making the same assumption, the total mass calculated from the SCUBA map is consistent with this. The interpretation that the flux density is partly due to a prestellar core, which is typically colder than a protostellar envelope, will increase the measured mass. I calculate masses of $3 - 7$ $M_{\odot}$ and $1.2 - 2$ $M_{\odot}$ respectively for #1a and #1b, assuming a prestellar dust temperature and opacity of $12 - 20$ K and 1.4 cm^2g^{-1}, and protostellar temperature and opacity of $20 - 30$ K and 1.9 cm^2g^{-1}. The area over which the total flux density is measured is 0.08×0.06, with the flux density distributed evenly between the two objects, as discussed in Section 4.4.2.

To summarise, there are three sources in the immediate vicinity of IRS 7. The cm source VLA 10A is the least embedded, and is the only source visible in the infrared. It has the weakest submillimetre flux, and is therefore associated with the least dust. I conclude that it is probably a Class I object. VLA 10B has only been detected at cm wavelengths (Brown, 1987) and in my 850 μm SCUBA data (source #1b). This object is probably a Class 0, as discussed above. The third source (#1a) is only detected in the submillimetre and at 1.2 mm (Chini et al., 2003), and is therefore probably prestellar in nature.

The majority of the other submillimetre sources in the region correspond to known YSOs. Source #2 is detected at 2 μm (Wilking et al., 1997) and shown on Figure 5.18 as 'WMB 55'. It is also seen as a shoulder on the side of MMS 13 in the 1.2 mm map of Chini et al. (2003), who suggested that it is a Class I object. Source #3 corresponds to the Coronet member IRS 1 (Taylor & Storey, 1984, see Section 4.4), which is also known as HH100 IRS. It is a Class I source that

Table 5.6: The prestellar core and protostellar envelope masses for the SCUBA detections in the RCrA map. ‡1 (Chini et al., 2003), ‡2 (Brown, 1987), ‡3 (Wilking et al., 1997), ‡4 (Taylor & Storey, 1984), ‡5 (Strom et al., 1974), ‡6 (Joy, 1945), ‡7 (e.g. Prato & Simon, 1997), ‡8 (Wilking et al., 1992).

Source Name	Class	Mass ($M_\odot$)	Other Names
1a	Pre	7	MMS 13‡1
1b	0	1.2	VLA10B‡2
2	I	0.13	WMB55‡3
3	I	0.11	IRS 1‡4, HH100 IRS‡5
4	I	0.14	IRS 2‡4
5	I	0.14	IRS 5‡4
6	Pre	0.9	MMS 10‡1
7	II	0.03	SCrA‡6
8	II	0.07	VVCrA‡7
9	I	0.10	IRAS 18595-3712‡8

drives the Herbig-Haro object HH100 (Strom, Strom, & Grasdalen, 1974), which was first discovered by Strom, Grasdalen, & Strom (1974). It is also detected at cm wavelengths (Brown, 1987). This source is also seen as a shoulder on the side of MMS 13 (Chini et al., 2003). Sources #4 and #5 coincide with the Class I Coronet members IRS 2 and IRS 5 respectively (Taylor & Storey, 1984; Wilking et al., 1997).

Source #6 has no indication of an embedded protostar, the only other detection of this source is at 1.2 mm by Chini et al. (2003), who claim that it is probably a deeply embedded protostar. This source is the least centrally condensed in the SCUBA map, and no cm radio source has been detected, therefore it is more likely that the object is prestellar in nature.

The sources #7 and #8 correspond to the T-Tauri stars SCrA and VVCrA respectively. SCrA was one of the original T-Tauri stars categorised by Joy (1945). It is a strong source at millimetre wavelengths (Reipurth et al., 1993; Chini et al.,

2003), and is the driving source of the Herbig-Haro object HH 82 (Strom et al., 1986). Both SCrA and VVCrA are close visual binaries with separations of 1.4″ and 1.9″ respectively (Prato & Simon, 1997). Source #9 coincides with the Class I protostar IRAS 18595-3712, which has also been detected in the near infrared (Wilking et al., 1992).

Table 5.6 summarises the results above and gives mass estimates of the prestellar cores and protostellar envelopes. The same assumptions are made about the temperature and dust mass opacity as in Section 5.3.1.

To conclude, I have mapped the R Coronae Australis molecular cloud at submillimetre wavelengths. I have discovered a new Class 0 object. This object is associated with a cm source which was previously of an unknown nature. I hypothesise that the cm emission arises from the accretion onto the protostellar surface. The protostar is separated by 0.01 pc from a second source that I hypothesise to be prestellar in nature. In addition, I have determined the envelope masses of a number of previously identified YSOs and identified two prestellar cores.

The summary and conclusions of this chapter are given in Chapter 6.

Chapter 6

Summary and Conclusions

6.1 Thesis Summary

Star formation is an extremely important process in its own right and it also has important consequences for many other aspects of astronomy. In this thesis I have presented an observational study of star formation.

In Chapter 1, I discussed our current understanding of the process of star formation. I looked at the observed properties of both protostars and their progenitors, prestellar cores. I discussed the implications that these observations have on our understanding about how stars are born in molecular clouds. I gave an overview of the different theories that attempt to explain how and why stars form with the properties that we observe. I also explained the different techniques I have employed to measure important parameters such as the masses of prestellar cores and protostellar envelopes, and the magnetic fields that could play a vital role in a star's formation. I then briefly described our current knowledge of the

stellar initial mass function, and explained why it is important that we understand what causes stars to form with this seemingly universal distribution of masses.

In Chapter 2, I introduced the telescope and instrumentation that were used to obtain the data presented in this thesis. I discussed the atmospheric conditions at the telescope and the strategies that are used to minimise their effect on the data. The different modes of data acquisition were described, including jiggle-mapping, scan-mapping and polarimetry. The data reduction process was described in detail, with emphasis on the reduction of scan-map and polarimetry data.

6.2 Magnetic Fields

In Chapter 3, I presented new polarimetry data for the prestellar core L183. I used these data, together with previously published polarimetry data of L1544, L43 and L183 (Ward-Thompson et al., 2000), to measure the dispersion of the magnetic field lines on the plane of the sky. The polarimetric map of L183 represents the deepest polarimetry map made to date of a prestellar core. The new data have confirmed the conclusions made by Ward-Thompson et al. (2000) that the magnetic field in the three cores is uniform in direction, and is offset significantly from the core's minor axis. The field direction and the core major axis for L1544 (measured north through east) are $23° \pm 3°$ and $-38° \pm 5°$ respectively. The offset is therefore $61° \pm 6°$. For L43, the field direction and major axis are $-21° \pm 2°$ and $-53° \pm 5°$ respectively, giving an offset of $32° \pm 6°$. For L183, the field direction and major axis are $27° \pm 3°$ and $-17° \pm 5°$ respectively, giving an offset of $44° \pm 6°$.

I showed that there are no theoretical models that can simultaneously fit all of the data for the L1544 prestellar core. The initially subcritical B_{UV} model

matches the mid-infrared absorption data of Bacmann et al. (2000) and the line of sight magnetic field strength measured using the Zeeman effect (Crutcher & Troland, 2000). It can also be argued to be consistent with the molecular line data of Williams et al. (1999). However, it is not consistent with the infall velocities measured by Tafalla et al. (1998), and the value of β is too low to agree with the data of Ward-Thompson et al. (2000). The $B_{UV-L1544}$ model fits the molecular line data of Tafalla et al. and Williams et al. and the magnetic field morphology measured by Ward-Thompson et al., but cannot reproduce the sharp edges seen in the infrared absorption data of Bacmann et al.

Using the measured dispersion of the polarisation vectors in each core, I have used the Chandrasekhar-Fermi technique to determine the magnetic field strength in the plane of the sky. For L1544, L43 and L183, this is equal to 110 $\pm$ 50, 140 $\pm$ 50 and 80 $\pm$ 25 μG respectively. These are larger than the typical line of sight field strengths measured using the Zeeman effect for cores of this mass. However, this is to be expected as the Zeeman observations preferentially sample lower density material. The mass to magnetic flux ratio for the three cores has been determined, and compared to the critical value for magnetic support. The mass to flux ratios (in units of the critical mass to flux ratio) for L1544, L43 and L183 are calculated to be 1.0 $\pm$ 1, 1.3 $\pm$ 1 and 3.1 $\pm$ 2 respectively. Therefore the cores are either approximately critical or marginally supercritical.

The result that the cores may be supercritical is consistent with the observations of infalling material towards L1544 and L183, and especially the evidence that in L1544 both the neutrals and the ions are undergoing infall (Tafalla et al., 1998). Crutcher (1999) compiled all of the Zeeman observations of molecular clouds carried out thus far. He found that the average mass to flux ratio was approximately twice the critical value. This is also consistent with the results presented here.

Ambipolar diffusion models predict the formation of a supercritical core after a period of quasi-static contraction. Our results can be made to be consistent with this picture. However, when other results are taken into consideration, one cannot rule out models that are dominated by turbulence, and are magnetically supercritical at all times (as discussed above). Ambipolar diffusion models predict that cores are subcritical earlier in their evolution. Observations of cores at this younger age might be able to distinguish between turbulent and ambipolar diffusion models.

The Chandrasekhar-Fermi technique has been shown to yield magnetic field strengths that are consistent with our current understanding of star formation, and to provide a way of measuring field strengths on a smaller scale than is possible with any other technique.

6.3 Molecular Clouds

In Chapter 4, I presented submillimetre continuum data of three molecular clouds, Orion B, L1689 and RCrA. I described my scan-map observations of these regions and the data reduction. I discussed the features in each of the maps and tabulated the flux density of each source at 850 μm and 450 μm. I discussed a number of different ways of visualising the data, and different techniques for extracting information from the data. In Chapter 5, I carried out a comparison with the literature data for Orion B, L1689 and RCrA.

6.3.1 Orion B

I measured the mass function of the prestellar cores in my Orion B data, and compared this to the stellar IMF, and to previously measured core mass functions for the region. I found that the core mass function for masses greater than 1 $M_{\odot}$ is best fitted by a power-law of slope -1.5, and is therefore consistent with estimates of the IMF in this mass range.

The core mass function peaks at approximately 1 $M_{\odot}$. This is higher than the peak of the IMF, which is typically located at $0.1-0.2$ $M_{\odot}$. This is easily explained, because many cores are expected to form binaries and higher multiple systems, and the star formation efficiency of each core is expected to be significantly less than unity.

Motte et al. (2001) and Johnstone et al. (2001) measured a core mass function with a characteristic mass similar to that of the IMF. This would appear to indicate that the majority of the mass of each core accretes onto the most massive star that is formed within it. This in turn suggests that a star's final mass is dictated by the fragmentation of the cloud, as opposed to mechanisms such as dynamical feedback or competitive accretion. However, I have found that the characteristic mass of the core mass function is significantly higher than that of the IMF. This suggests that a star's final mass is not simply dictated by the physics of fragmentation, and that alternative theories should not be ruled out.

I also measured the clustering properties of the sources in my Orion B map. I found that the cores are clustered on spatial scales less than 0.35 pc. Between 0.04 and 0.4 pc, the mean surface density of companions $\Sigma_c(\theta)$ is best fitted by a power-law of slope -0.3. This is consistent with the equivalent data calculated

for young stars in the Orion Trapezium cluster. It is less consistent with $\Sigma_c(\theta)$ measured for young stars in the Taurus and ρ Ophiuchi star-forming regions. I therefore conclude that the star formation process in Orion B is more similar to the rest of Orion than it is to other regions.

6.3.2 L1689

I compared my L1689 scan-map data to previous surveys of L1689 and the neighbouring L1688 cloud made using ^{13}CO and DCO^+, and also to a submillimetre continuum map of L1688. I showed that the star formation activity as a fraction of the total cloud mass in the two clouds was comparable. However, parts of L1689 have a higher percentage of the cloud mass in prestellar cores, indicating that they might be about to undergo significant star formation. I suggested that this was consistent with the star formation in the two clouds being dominated by external influences such as the Sco OB2 association.

6.3.3 RCrA

I compared my RCrA data to previous surveys of the region made at infrared and millimetre wavelengths. I have discovered a new Class 0 source. This object is associated with a cm source which was previously of an unknown nature. I hypothesise that the cm emission arises from the accretion onto the protostellar surface. There is a second submillimetre peak to the south of the Class 0 source that is just resolved in the JCMT beam. This source has only been previously detected at millimetre wavelengths. I therefore hypothesise that it is prestellar in nature.

6.4 Conclusions

I have mapped a number of molecular clouds in the submillimetre continuum. The Orion B cloud and L1689 show a number of similarities and differences. Both clouds show filamentary structure, with the majority of the star formation occurring within the filaments. The filaments in L1689 appear to have a coherent direction across the cloud and are also correlated with the filaments in the neighbouring L1688 cloud. Conversely, the filaments in Orion B appear to be oriented at random angles to each other. This could indicate that the dominant physics controlling the star formation in the two regions is different. A possible explanation for this is that the star formation in the ρ Ophiuchi complex is dominated by the influence of the Sco OB2 association, the closest members of which are located only 4 pc away. The Orion OB association by comparison is located over 30 pc from the Orion B molecular cloud. Perhaps this difference is the reason behind the differences in the two clouds.

The three molecular clouds for which I have data have different properties. Orion B is a region of massive star formation, and does not appear to be influenced by the surrounding environment. L1689 and L1688 are forming typically solar mass stars, and both clouds show evidence of triggered star formation. RCrA is a more isolated region and currently has a low star formation activity. The differences in star formation in the different regions can be explained by the various parameters and environment of each cloud.

I have measured the magnetic field strength of three prestellar cores. It appears that the magnetic field is important in the evolution of the cores, but may not be a dominant factor at this stage of their evolution. Finally there are currently no theoretical models of prestellar evolution that can fit all of the available data.

Clearly the problems of star formation will tax astronomers for many years to come. Currently the observations are constraining theoretical models in an unprecedented way. It appears that only models that can consider in detail every aspect of the physics of star-forming regions will stand a chance of explaining the burgeoning quantities of data produced by modern-day telescopes.

Appendix A

Convolution theory

Two functions $f(t)$ and $g(t)$, have Fourier transforms ($\mathcal{FT}$) $F(\nu)$ and $G(\nu)$, given by:

$$F(\nu) = \mathcal{F}[f(t)](\nu) \int_{-\infty}^{\infty} f(t) e^{-2\pi i \nu t} \mathrm{d}t, \tag{A.1}$$

$$G(\nu) = \mathcal{F}[g(t)](\nu) \int_{-\infty}^{\infty} g(t) e^{-2\pi i \nu t} \mathrm{d}t. \tag{A.2}$$

The convolution, or degree of overlap of these functions is given by:

$$\begin{aligned}
f(t) \otimes g(t) &= \int_{-\infty}^{\infty} g(\tau) f(t-\tau) \mathrm{d}\tau, && \text{(A.3)} \\
&= \int_{-\infty}^{\infty} g(\tau) \left[\int_{-\infty}^{\infty} F(\nu) e^{2\pi i \nu (t-\tau)} \mathrm{d}\nu \right] \mathrm{d}\tau, && \text{(A.4)} \\
&= \int_{-\infty}^{\infty} g(\tau) \left[\int_{-\infty}^{\infty} F(\nu) e^{2\pi i \nu t} e^{-2\pi i \nu \tau} \mathrm{d}\nu \right] \mathrm{d}\tau, && \text{(A.5)} \\
&= \int_{-\infty}^{\infty} F(\nu) \left[\int_{-\infty}^{\infty} g(\tau) e^{-2\pi i \nu \tau} \mathrm{d}\tau \right] e^{2\pi i \nu t} \mathrm{d}\nu, && \text{(A.6)} \\
&= \int_{-\infty}^{\infty} F(\nu) G(\nu) e^{2\pi i \nu t} \mathrm{d}\nu, && \text{(A.7)} \\
&= \mathcal{F}^{-1}[F(\nu) G(\nu)]. && \text{(A.8)}
\end{aligned}$$

Taking the $\mathcal{FT}$ of both sides:

$$\mathcal{F}[f(t) \otimes g(t)] = F(\nu)\ G(\nu) = \mathcal{F}[f(t)]\ \mathcal{F}[g(t)], \tag{A.9}$$

we find that the $\mathcal{FT}$ of a convolution of two functions is equal to the product of the $\mathcal{FT}$s of the two functions.

Appendix B

Matrix Inversion

A simple example of iterative matrix inversion is given for a one dimensional array, of length 30, with three non-zero values in the centre of the array.

```
S  = 0.0  0.0  0.0  0.0  0.0  8.0 10.0  2.0  0.0  0.0  0.0  0.0  0.0
```

The chop is simulated by creating two difference arrays, with chop throws of 4 and 6, such that:

$$D1_i = S_{i-2} - S_{i+2} \quad \text{(B.1)}$$

$$D2_i = S_{i-3} - S_{i+3} \quad \text{(B.2)}$$

```
D1 = 0.0  0.0  0.0 -8.0 -10.0 -2.0  0.0  8.0 10.0  2.0  0.0  0.0  0.0
D2 = 0.0  0.0 -8.0 -10.0 -2.0  0.0  0.0  0.0  8.0 10.0  2.0  0.0  0.0
```

To recover S from the two difference arrays, make an initial guess S1:

```
S1 = 0.0  0.0  0.0  0.0  0.0  0.0  0.0  0.0  0.0  0.0  0.0  0.0  0.0
```

The second estimate is made by calculating a new array S2 using S1, D1 and D2.

For each position in S2, two values from D1 are taken that are separated by the chop throw and centred on this position. The difference ($D1_{diff}$) between these values is then calculated. Two values from S1 are selected that are separated from the current position in each direction by the chop throw. These values are added

together to make $S1_{sum}$. The average is then calculated between $D1_{diff}$ and $S1_{sum}$. Call this value $D1_{av}$.

The same procedure is carried out for D2, and the average between $D1_{av}$ and $D2_{av}$ is calculated. This is the new estimate for S2 at this position, and is defined by Equation B.4. The process is iterated, using the previous estimate in place of S1.

$$\begin{aligned} S_{new,i}) &= [(D1_{i+2} - D1_{i-2}) + (S1_{i+4} + S1_{i+4}) \\ &+ (D2_{i+3} - D2_{i-3}) + (S1_{i+6} + S1_{i+6})]/4 \end{aligned} \tag{B.3}$$

The first few iterations are as follows:

```
S2 = -2.5 -2.5 -2.5 -0.5  0.0  8.0 10.0  2.0  0.0 -2.0 -2.5 -2.5 -2.5
S3 =  0.0  0.0  0.0 -1.0 -1.3  5.8  7.5  0.5 -1.3 -0.3  0.0  0.0  0.0
S4 = -1.4 -1.4 -1.4 -0.7 -0.5  7.9 10.0  1.6 -0.5 -1.2 -1.4 -1.4 -1.4
S5 = -0.2 -0.2 -0.2 -0.8 -0.9  6.7  8.6  1.0 -0.9 -0.4 -0.2 -0.2 -0.2
S6 = -0.9 -0.9 -0.9 -0.6 -0.5  7.7  9.8  1.6 -0.5 -0.9 -1.0 -1.0 -1.0
```

```
S35 = 0.0  0.0 -0.1  0.0 -0.1  7.9  9.9  1.9 -0.1 -0.1 -0.1 -0.1 -0.1
S36 = 0.0  0.0  0.0  0.0 -0.1  8.0  9.9  1.9 -0.1 -0.1 -0.1 -0.1 -0.1
S37 = 0.0  0.0  0.0  0.0  0.0  8.0 10.0  2.0 -0.1  0.0 -0.1  0.0  0.0
S38 = 0.0  0.0  0.0  0.0  0.0  8.0 10.0  2.0  0.0  0.0  0.0  0.0  0.0
```

After 38 iterations, the solution has converged to the correct value of S.

Appendix C

Stokes Parameters

As derived in Equations 2.24 to 2.30, The Stokes parameters are given by:

$$Q = I_p \cos 2\theta, \tag{C.1}$$
$$U = I_p \sin 2\theta, \tag{C.2}$$
$$I = I_p + I_u. \tag{C.3}$$

The polarised intensity (I_p) and the degree of polarisation (p) are therefore:

$$I_p = (Q^2 + U^2)^{0.5}, \tag{C.4}$$
$$p = (I_p/I). \tag{C.5}$$

It is convenient to define the normalised (or reduced) Stokes parameters q and u:

$$q = \frac{Q}{I}, \qquad u = \frac{U}{I}. \tag{C.6}$$

Using this notation, the degree of polarisation and polarised intensity are given by:

$$p = (q^2 + u^2)^{0.5}, \tag{C.7}$$
$$I_p = p \times I, \tag{C.8}$$

although as noted in Section 2.5.4, a debias term should be included to account for the errors in p not being normally distributed.

The variances in q and u are given by:

$$\begin{aligned}
\sigma_q^2 &= \left(\frac{\partial q}{\partial Q}\right)^2 \sigma_Q^2 + \left(\frac{\partial q}{\partial I}\right)^2 \sigma_I^2 \\
&= \left(\frac{1}{I}\right)^2 \sigma_Q^2 + \left(\frac{-Q}{I^2}\right)^2 \sigma_I^2 \\
&= \frac{\sigma_Q^2}{I^2} + \frac{\sigma_I^2 q^2}{I^2} \\
&= \frac{\sigma_I^2 q^2 + \sigma_Q^2}{I^2}. \qquad \text{(C.9)} \\
\sigma_u^2 &= \frac{\sigma_I^2 u^2 + \sigma_U^2}{I^2}. \qquad \text{(C.10)}
\end{aligned}$$

The variance in p is calculated as follows:

$$\begin{aligned}
\sigma_p^2 &= \left(\frac{\partial p}{\partial q}\right)^2 \sigma_q^2 + \left(\frac{\partial p}{\partial u}\right)^2 \sigma_u^2, \\
&= \left(\frac{q^2}{q^2+u^2}\right)^2 \sigma_q^2 + \left(\frac{u^2}{q^2+u^2}\right)^2 \sigma_q^2, \\
&= \frac{q^2\sigma_q^2 + u^2\sigma_u^2}{q^2+u^2}. \qquad \text{(C.11)}
\end{aligned}$$

Finally, the variance in I_p is given by:

$$\begin{aligned}
\sigma_{I_p}^2 &= \left(\frac{\partial I_p}{\partial p}\right)^2 \sigma_p^2 + \left(\frac{\partial I_p}{\partial I}\right)^2 \sigma_I^2, \\
&= I^2\sigma_p^2 + p^2\sigma_I^2. \qquad \text{(C.12)}
\end{aligned}$$

Appendix D

Cumulative Mass Function

If a mass function can be approximated to a power law, then the number of cores in the interval $\log M$ to $\log M + \mathrm{d}\log M$ is given by:

$$\frac{\mathrm{d}N}{\mathrm{d}\log M}\mathrm{d}\log M = kM^x\ \mathrm{d}\log M, \tag{D.1}$$

where k is a constant. Integrating Equation D.1 between $\log M$ and $\log M_{max}$ will give the number of stars with mass greater than M.

$$N(>M) = \int_{\log M}^{\log M_{max}} kM^x \mathrm{d}\log M. \tag{D.2}$$

Using the substituting $\mathrm{d}M/M = \mathrm{d}\log M$:

$$N(>M) = \int_M^{M_{max}} kM^x \frac{\mathrm{d}M}{M} = \int_M^{M_{max}} kM^{x-1}\mathrm{d}M. \tag{D.3}$$

Integrating this yields:

$$N(>M) = \left[\frac{kM^x}{x}\right]_M^{M_{max}} = \frac{k}{x}\{M_{max}^x - M^x\} \tag{D.4}$$

For negative values of x, the M_{max} term in Equation D.4 is negligible except when M approaches M_{max}.

Bibliography

Adams F. C., Asymptotic theory for the spatial distribution of protostellar emission, 1991, ApJ, 382, 544

Agladze N. I., Sievers A. J., Jones S. A., Burlitch J. M., Beckwith S. V. W., Reassesment of millimetre-wave absorption coefficients in interstellar silicate grains, 1994, Nature, 372, 243

Alves J. F., Lada C. J., Lada E. A., Internal structure of a cold dark molecular cloud inferred from the extinction of background starlight, 2001, Nature, 409, 159

Ambartsumian V. A., 1947, Stellar Evolution and Astrophysics. Armenian Acad. of Sci.

Anders E., Grevesse N., Abundances of the Elements: Meteoritic and Solar, 1989, Geochim. Cosmochim. Acta., 53, 197

André P., Montmerle T., From T Tauri stars to protostars: Circumstellar material and young stellar objects in the rho Ophiuchi cloud, 1994, ApJ, 420, 837

André P., Ward-Thompson D., Barsony M., From Prestellar Cores to Protostars: the Initial Conditions of Star Formation, 2000, Protostars and Planets IV, 59

André P., Ward-Thompson D., Motte F., Probing the initial conditions of star formation: the structure of the prestellar core L 1689B., 1996, A&A, 314, 625

André P., Ward-Thompson D., Barsony M., Submillimeter continuum observations of Rho Ophiuchi A - The candidate protostar VLA 1623 and prestellar clumps, 1993, ApJ, 406, 122

Archibald E. N., Jenness T., Holland W. S., Coulson I. M., Jessop N. E., Stevens J. A., Robson E. I., Tilanus R. P. J., Duncan W. D., Lightfoot J. F., On the atmospheric limitations of ground-based submillimetre astronomy using array receivers, 2002, MNRAS, 336, 1

Arons J., Max C. E., Hydromagnetic Waves in Molecular Clouds, 1975, ApJ, 196, L77

Axon D. J., Ellis R. S., A Catalogue of Linear Polarization Measurements for 5070 stars, 1976, MNRAS, 177, 499

Bachiller R., Bipolar Molecular Outflows from Young Stars and Protostars, 1996, ARA&A, 34, 111

Bacmann A., André P., Puget J.-L., Abergel A., Bontemps S., Ward-Thompson D., An ISOCAM absorption survey of the structure of pre-stellar cloud cores, 2000, A&A, 361, 555

Ballesteros-Paredes J., Klessen R. S., Vázquez-Semadeni E., Dynamic Cores in Hydrostatic Disguise, 2003, ApJ, 592, 188

Bate M. R., Clarke C. J., McCaughrean M. J., Interpreting the mean surface density of companions in star-forming regions, 1998, MNRAS, 297, 1163

Beckwith S. V. W., Sargent A. I., Chini R. S., Guesten R., A survey for circumstellar disks around young stellar objects, 1990, AJ, 99, 924

Beichman C. A., Myers P. C., Emerson J. P., Harris S., Mathieu R., Benson P. J., Jennings R. E., Candidate solar-type protostars in nearby molecular cloud cores, 1986, ApJ, 307, 337

Beichman C. A., Neugebauer G., Habing H. J., Clegg P. E., Chester T. J., Infrared astronomical satellite (IRAS) catalogs and atlases. Explanatory supplement, 1985, NASA STI/Recon Technical Report N, 85, 18898

Berry D. S., Gledhill T. M., 2001, POLPACK - Users's Manual - Starlink User Note 223.5

Bertout C., T Tauri South - A protostar?, 1983, A&A, 126, L1

Bertout C., Robichon N., Arenou F., Revisiting Hipparcos data for pre-main sequence stars, 1999, A&A, 352, 574

Bonnell I. A., Bate M. R., Clarke C. J., Pringle J. E., Competitive accretion in embedded stellar clusters, 2001, MNRAS, 323, 785

Bonnor W. B., Boyle's Law and gravitational instability, 1956, MNRAS, 116, 351

Bontemps S. et al., ISOCAM observations of the rho Ophiuchi cloud: Luminosity and mass functions of the pre-main sequence embedded cluster, 2001, A&A, 372, 173

Bontemps S., André P., Ward-Thompson D., Deep VLA serach for the youngest protostars: A Class 0 source in the HH24-26 region, 1995, A&A, 297, 98

Bontemps S., Andre P., Terebey S., Cabrit S., Evolution of outflow activity around low-mass embedded young stellar objects, 1996, A&A, 311, 858

Bontemps S., Ward-Thompson D., André P., Discovery of a jet emanating from the protostar HH 24 MMS., 1996, A&A, 314, 477

Braine J., Kruegel E., Sievers A., Wielebinski R., 1.3mm continuum emission in the late-type spiral NGC 4631. Dust in NGC 4631., 1995, A&A, 295, L55

Brown A., Radio emission from pre-main-sequence stars in Corona Australis, 1987, ApJ, 322, L31

Brown A. G. A., de Geus E. J., de Zeeuw P. T., The Orion OB1 association. 1: Stellar content, 1994, A&A, 289, 101

Caselli P., Benson P. J., Myers P. C., Tafalla M., Dense Cores in Dark Clouds. XIV. N_2H^+ (1-0) Maps of Dense Cloud Cores, 2002, ApJ, 572, 238

Castets A., Ceccarelli C., Loinard L., Caux E., Lefloch B., Multiple shocks around the low-luminosity protostar IRAS 16293-2422, 2001, A&A, 375, 40

Ceccarelli C., Caux E., White G. J., Molinari S., Furniss I., Liseau R., Nisini B., Saraceno P., Spinoglio L., Wolfire M., The far infrared line spectrum of the protostar IRAS 16293-2422, 1998, A&A, 331, 372

Chabrier G., Galactic Stellar and Substellar Initial Mass Function, 2003, PASP, 115, 763

Chandrasekhar S., Fermi E., Magnetic Fields in Spiral Arms., 1953, ApJ, 118, 113

Chen H., Grenfell T. G., Myers P. C., Hughes J. D., Comparison of Star Formation in Five Nearby Molecular Clouds, 1997, ApJ, 478, 295

Chen H., Myers P. C., Ladd E. F., Wood D. O. S., Bolometric temperature and young stars in the Taurus and Ophiuchus complexes, 1995, ApJ, 445, 377

Chernin L. M., Masson C. R., Extremely high velocity CO emission from NGC 2071, 1992, ApJ, 396, L35

Chini R., Kämpgen K., Reipurth B., Albrecht M., Kreysa E., Lemke R., Nielbock M., Reichertz L. A., Sievers A., Zylka R., SIMBA observations of the R Corona Australis molecular cloud, 2003, A&A, 409, 235

Chini R., Krugel E., Haslam C. G. T., Kreysa E., Lemke R., Reipurth B., Sievers A., Ward-Thompson D., Discovery of a Cold and Gravitationally Unstable Cloud Fragment, 1993, A&A, 272, L5

Chini R., Ward-Thompson D., Kirk J. M., Nielbock M., Reipurth B., Sievers A., Mm/Submm images of Herbig-Haro energy sources and candidate protostars, 2001, A&A, 369, 155

Choi M., Tatematsu K., High resolution millimeter imaging of the R Coronae Australis IRS 7 region, 2004, ApJ, 600, L55

Chrysostomou A., Hobson J., Davis C. J., Smith M. D., Berndsen A., High-resolution near-infrared observations of Herbig-Haro flows - I. H_2 imaging and proper motions, 2000, MNRAS, 314, 229

Ciolek G. E., Basu S., Consistency of Ambipolar Diffusion Models with Infall in the L1544 Protostellar Core, 2000, ApJ, 529, 925

Ciolek G. E., Mouschovias T. C., Ambipolar diffusion, interstellar dust, and the formation of cloud cores and protostars. 3: Typical axisymmetric solutions, 1994, ApJ, 425, 142

Ciolek G. E., Mouschovias T. C., Ambipolar Diffusion, Interstellar Dust, and the Formation of Cloud Cores and Protostars. IV. Effect of Ultraviolet Ionization and Magnetically Controlled Infall Rate, 1995, ApJ, 454, 194

Cohen M., Red and nebulous objects in dark clouds - A survey, 1980, AJ, 85, 29

Cowie L., Astronomy: Wrestling monsters in deep space, 2003, Nature, 422, 670

Crutcher R. M., Magnetic Fields in Molecular Clouds: Observations Confront Theory, 1999, ApJ, 520, 706

Crutcher R. M., Troland T. H., OH Zeeman Measurement of the Magnetic Field in the L1544 Core, 2000, ApJ, 537, L139

Crutcher R. M., Troland T. H., Goodman A. A., Heiles C., Kazes I., Myers P. C., OH Zeeman observations of dark clouds, 1993, ApJ, 407, 175

Crutcher R. M., Troland T. H., Lazareff B., Paubert G., Kazès I., Detection of the CN Zeeman Effect in Molecular Clouds, 1999, ApJ, 514, L121

Cudlip W., Furniss I., King K. J., Jennings R. E., Far infrared polarimetry of W51A and M42, 1982, MNRAS, 200, 1169

Davis C. J., Ray T. P., Eisloeffel J., Corcoran D., Near-IR imaging of the molecular outflows in HH24-26, L1634(HH240-241), L1660(HH72) and RNO15FIR., 1997, A&A, 324, 263

Davis L. J., Greenstein J. L., The Polarization of Starlight by Aligned Dust Grains., 1951, ApJ, 114, 206

Draine B. T., Lee H. M., Optical properties of interstellar graphite and silicate grains, 1984, ApJ, 285, 89

Dunne L., Eales S., Ivison R., Morgan H., Edmunds M., Type II supernovae as a significant source of interstellar dust, 2003, Nature, 424, 285

Eales S., Lilly S., Gear W., Dunne L., Bond J. R., Hammer F., Le Fèvre O., Crampton D., The Canada-UK Deep Submillimeter Survey: First Submillimeter Images, the Source Counts, and Resolution of the Background, 1999, ApJ, 515, 518

Eales S., Lilly S., Webb T., Dunne L., Gear W., Clements D., Yun M., The Canada-UK Deep Submillimeter Survey. IV. The Survey of the 14 Hour Field, 2000, AJ, 120, 2244

Ebert R., Über die Verdichtung von H I-Gebieten. Mit 5 Textabbildungen, 1955, Zeitschrift fur Astrophysics, 37, 217

Eisenhauer F., Quirrenbach A., Zinnecker H., Genzel R., Stellar Content of the Galactic Starburst Template NGC 3603 from Adaptive Optics Observations, 1998, ApJ, 498, 278

Elias J. H., A study of the Taurus dark cloud complex, 1978, ApJ, 224, 857

Elmegreen B. G., Star Formation in a Crossing Time, 2000, ApJ, 530, 277

Emerson D. T., 1995, in ASP Conf. Ser. 75: Multi-Feed Systems for Radio Telescopes, p. 309

Emerson D. T., Klein U., Haslam C. G. T., A multiple beam technique for overcoming atmospheric limitations to single-dish observations of extended radio sources, 1979, A&A, 76, 92

Fiedler R. A., Mouschovias T. C., Ambipolar diffusion and star formation: Formation and contraction of axisymmetric cloud cores. I - Formulation of the problem and method of solution, 1992, ApJ, 391, 199

Foster P. N., Chevalier R. A., Gravitational Collapse of an Isothermal Sphere, 1993, ApJ, 416, 303

Franco G. A. P., High latitude molecular clouds - Distances derived from accurate photometry, 1989, A&A, 223, 313

Garcia R. N., 1995, Ph.D. Thesis

Genzel R., Stutzki J., The Orion Molecular Cloud and star-forming region, 1989, ARA&A, 27, 41

Ghez A. M., Neugebauer G., Matthews K., The multiplicity of T Tauri stars in the star forming regions Taurus-Auriga and Ophiuchus-Scorpius: A 2.2 micron speckle imaging survey, 1993, AJ, 106, 2005

Gibb A. G., A VLA search for embedded young stellar objects and protostellar candidates in L1630, 1999, MNRAS, 304, 1

Gibb A. G., Davis C. J., 1997, in IAU Symp. 182: Herbig-Haro Flows and the Birth of Stars, p. 120P

Gibb A. G., Little L. T., Discovery of a dense bipolar outflow from a new class 0 protostar in NGC 2068/LBS 17, 2000, MNRAS, 313, 663

Glass I. S., An improved chopper for use in infrared photometry, 1972, The Observatory, 92, 140

Goldsmith P. F., Langer W. D., Molecular cooling and thermal balance of dense interstellar clouds, 1978, ApJ, 222, 881

Gomez M., Hartmann L., Kenyon S. J., Hewett R., On the spatial distribution of pre-main-sequence stars in Taurus, 1993, AJ, 105, 1927

Goodman A. A., Crutcher R. M., Heiles C., Myers P. C., Troland T. H., Measurement of magnetic field strength in the dark cloud Barnard 1, 1989, ApJ, 338, L61

Goodman A. A., Jones T. J., Lada E. A., Myers P. C., Does Near-Infrared Polarimetry Reveal the Magnetic Field in Cold Dark Clouds?, 1995, ApJ, 448, 748

Goodman A. A., Whittet D. C. B., A Point in Favor of the Superparamagnetic Grain Hypothesis, 1995, ApJ, 455, L181

Goodwin S. P., Whitworth A. P., Ward-Thompson D., 2004, A&A, in press

Gray N., Taylor M., Privett G., 2000, ESP - Extended Surface Photometry User's Manual - Starlink User Notes 180.5

Greaves J., 1999, SCUBA Imaging Polarimetry, Commissioning Report: 02/99, http://www.jach.hawaii.edu/JACpublic/JCMT/Continuum_observing/SCUBApol/reports/comm2/comm_850img.html

Greaves J., 2000, SCUBA Polarimeter Commissioning Report: 08/00, http://www.jach.hawaii.edu/JACdocs/JCMT/tr/001/89/comm99v2.html

Greaves J. S., Holland W. S., Jenness T., Chrysostomou A., Berry D. S., Murray A. G., Tamura M., Robson E. I., Ade P. A. R., Nartallo R., Stevens J. A., Momose M., Morino J.-I., Moriarty-Schieven G., Gannaway F., Haynes C. V., A submillimetre imaging polarimeter at the James Clerk Maxwell Telescope, 2003, MNRAS, 340, 353

Greene T. P., Wilking B. A., André P., Young E. T., Lada C. J., Further mid-infrared study of the rho Ophiuchi cloud young stellar population: Luminosities and masses of pre-main-sequence stars, 1994, ApJ, 434, 614

Gregersen E. M., Evans N. J., Mardones D., Myers P. C., Does Infall End before the Class I Stage?, 2000, ApJ, 533, 440

Gregersen E. M., Evans N. J., Zhou S., Choi M., New Protostellar Collapse Candidates: an HCO + Survey of the Class 0 Sources, 1997, ApJ, 484, 256

Hall J. S., Observations of the Polarized Light from Stars, 1949, Science, 109, 166

Harju J., Walmsley C. M., Wouterloot J. G. A., Ammonia clumps in the Orion and Cepheus clouds, 1993, A&AS, 98, 51

Hazell A. S., 1991, Ph.D. Thesis

Hecht E., 1998, Optics. Addison Wesley Longman, Inc.

Heitsch F., Zweibel E. G., Mac Low M., Li P., Norman M. L., Magnetic Field Diagnostics Based on Far-Infrared Polarimetry: Tests Using Numerical Simulations, 2001, ApJ, 561, 800

Henriksen R., Andre P., Bontemps S., Time-dependent accretion and ejection implied by pre-stellar density profiles., 1997, A&A, 323, 549

Herbig G. H., Radial velocities and spectral types of T Tauri stars, 1977, ApJ, 214, 747

Herbig G. H., Jones B. F., Large proper motions of the Herbig-Haro objects HH 1 and HH 2, 1981, AJ, 86, 1232

Hewett P. C., The estimation of galaxy angular correlation functions, 1982, MNRAS, 201, 867

Hildebrand R. H., The Determination of Cloud Masses and Dust Characteristics from Submillimetre Thermal Emission, 1983, QJRAS, 24, 267

Hildebrand R. H., Davidson J. A., Dotson J. L., Dowell C. D., Novak G., Vaillancourt J. E., A Primer on Far-Infrared Polarimetry, 2000, PASP, 112, 1215

Hildebrand R. H., Dragovan M., Novak G., Detection of submillimeter polarization in the Orion nebula, 1984, ApJ, 284, L51

Hildebrand R. H., Whitcomb S. E., Winston R., Stiening R. F., Harper D. A., Moseley S. H., Submillimeter photometry of extragalactic objects, 1977, ApJ, 216, 698

Hiltner W. A., Polarization of Light from Distant Stars by Interstellar Medium, 1949, Science, 109, 165

Holland W., Duncan W., Griffin M., 2002, in ASP Conf. Ser. 278: Single-Dish Radio Astronomy: Techniques and Applications, p. 463

Holland W. S., Greaves J. S., Zuckerman B., Webb R. A., McCarthy C., Coulson I. M., Walther D. M., Dent W. R. F., Gear W. K., Robson I., Submillimetre images of dusty debris around nearby stars., 1998, Nature, 392, 788

Holland W. S., Robson E. I., Gear W. K., Cunningham C. R., Lightfoot J. F., Jenness T., Ivison R. J., Stevens J. A., Ade P. A. R., Griffin M. J., Duncan W. D., Murphy J. A., Naylor D. A., SCUBA: a common-user submillimetre camera operating on the James Clerk Maxwell Telescope, 1999, MNRAS, 303, 659

Hunter C., The collapse of unstable isothermal spheres, 1977, ApJ, 218, 834

Jeans J. H., 1929, Astronomy and Cosmogony. Cambridge University Press

Jenness T., 2000, private communication

Jenness T., Lightfoot J. F., 2000, SURF User's manual - Starlink User Note 216.7

Jenness T., Lightfoot J. F., Holland W. S., 1998, in Proc. SPIE Vol. 3357, p. 548-558, Advanced Technology MMW, Radio, and Terahertz Telescopes, Thomas G. Phillips; Ed., p. 548

Jenness T., Stevens J. A., Archibald E. N., Economou F., Jessop N. E., Robson E. I., Towards the automated reduction and calibration of SCUBA data from the James Clerk Maxwell Telescope, 2002, MNRAS, 336, 14

Jessop N. E., Ward-Thompson D., A far-infrared survey of molecular cloud cores, 2000, MNRAS, 311, 63

Jijina J., Myers P. C., Adams F. C., Dense Cores Mapped in Ammonia: A Database, 1999, ApJS, 125, 161

Johnstone D., Fich M., Mitchell G. F., Moriarty-Schieven G., Large Area Mapping at 850 Microns. III. Analysis of the Clump Distribution in the Orion B Molecular Cloud, 2001, ApJ, 559, 307

Johnstone D., Wilson C. D., Moriarty-Schieven G., Giannakopoulou-Creighton J., Gregersen E., Large-Area Mapping at 850 Microns. I. Optimum Image Reconstruction from Chop Measurements, 2000a, ApJS, 131, 505

Johnstone D., Wilson C. D., Moriarty-Schieven G., Joncas G., Smith G., Gregersen E., Fich M., Large-Area Mapping at 850 Microns. II. Analysis of the Clump Distribution in the ρ Ophiuchi Molecular Cloud, 2000b, ApJ, 545, 327

Jones B. F., Cohen M., Wehinger P. A., Gehren T., Proper motions of Herbig-Haro objects. VIII - The region of NGC 2068, 1987, AJ, 94, 1260

Jones B. F., Herbig G. H., Proper motions of T Tauri variables and other stars associated with the Taurus-Auriga dark clouds, 1979, AJ, 84, 1872

Jones R. V., Spitzer L. J., Magnetic Alignment of Interstellar Grains, 1967, ApJ, 147, 943

Joy A. H., T Tauri Variable Stars., 1945, ApJ, 102, 168

Kirk J. M., 2002, Ph.D. Thesis

Knude J., Hog E., Interstellar reddening from the HIPPARCOS and TYCHO catalogues. I. Distances to nearby molecular clouds and star forming regions, 1998, A&A, 338, 897

Kroupa P., On the variation of the initial mass function, 2001a, MNRAS, 322, 231

Kroupa P., 2001b, in ASP Conf. Ser. 228: Dynamics of Star Clusters and the Milky Way, p. 187

Kroupa P., The Initial Mass Function of Stars: Evidence for Uniformity in Variable Systems, 2002, Science, 295, 82

Lada C. J., 1987, in IAU Symp. 115: Star Forming Regions, p. 1

Lada C. J., Wilking B. A., The nature of the embedded population in the Rho Ophiuchi dark cloud - Mid-infrared observations, 1984, ApJ, 287, 610

Ladd E. F., Adams F. C., Fuller G. A., Myers P. C., Casey S., Davidson J. A., Harper D. A., Padman R., Far-infrared and submillimeter wavelength observations of star-forming dense cores. II - Images, 1991, ApJ, 382, 555

Lai S., Crutcher R. M., Girart J. M., Rao R., Interferometric Mapping of Magnetic Fields in Star-forming Regions. I. W51 e1/e2 Molecular Cores, 2001, ApJ, 561, 864

Lai S., Crutcher R. M., Girart J. M., Rao R., Interferometric Mapping of Magnetic Fields in Star-forming Regions. II. NGC 2024 FIR 5, 2002, ApJ, 566, 925

Landy S. D., Szalay A. S., Bias and variance of angular correlation functions, 1993, ApJ, 412, 64

Larson R. B., Numerical calculations of the dynamics of collapsing proto-star, 1969, MNRAS, 145, 271

Larson R. B., Star formation in groups, 1995, MNRAS, 272, 213

Launhardt R., Mezger P. G., Haslam C. G. T., Kreysa E., Lemke R., Sievers A., Zylka R., Dust emission from star-forming regions. IV. Dense cores in the Orion B molecular cloud., 1996, A&A, 312, 569

Lazarian A., Goodman A. A., Myers P. C., On the Efficiency of Grain Alignment in Dark Clouds, 1997, ApJ, 490, 273

Leach R. W., Clemens D. P., Kane B. D., Barvainis R., Polarimetric mapping of Orion using MILLIPOL - Magnetic activity in BN/KL, 1991, ApJ, 370, 257

Lee C. W., Myers P. C., Tafalla M., A Survey for Infall Motions toward Starless Cores. II. CS (2-1) and N_2H^+ (1-0) Mapping Observations, 2001, ApJS, 136, 703

Lehtinen K., Mattila K., Lemke D., Juvela M., Prusti T., Laureijs R., Far infrared observations of pre-protostellar sources in Lynds 183, 2003, A&A, 398, 571

Leinert C., Zinnecker H., Weitzel N., Christou J., Ridgway S. T., Jameson R., Haas M., Lenzen R., A systematic search for young binaries in Taurus, 1993, A&A, 278, 129

Loren R. B., The cobwebs of Ophiuchus. I - Strands of (C-13)O - The mass distribution, 1989, ApJ, 338, 902

Loren R. B., Wootten A., Wilking B. A., Cold DCO(+) cores and protostars in the warm Rho Ophiuchi cloud, 1990, ApJ, 365, 269

Luhman K. L., Rieke G. H., Low-Mass Star Formation and the Initial Mass Function in the ρ Ophiuchi Cloud Core, 1999, ApJ, 525, 440

Lynds B. T., Catalogue of Dark Nebulae., 1962, ApJS, 7, 1

Mac Low M., Klessen R. S., Burkert A., Smith M. D., Kinetic Energy Decay Rates of Supersonic and Super-Alfvénic Turbulence in Star-Forming Clouds, 1998, Physical Review Letters, 80, 2754

Maddalena R. J., Thaddeus P., A large, cold, and unusual molecular cloud in Monoceros, 1985, ApJ, 294, 231

Marraco H. G., Rydgren A. E., On the distance and membership of the R CrA T association, 1981, AJ, 86, 62

Martín E. L., Brandner W., Bouvier J., Luhman K. L., Stauffer J., Basri G., Zapatero Osorio M. R., Barrado y Navascués D., Membership and Multiplicity among Very Low Mass Stars and Brown Dwarfs in the Pleiades Cluster, 2000, ApJ, 543, 299

Martin E. L., Montmerle T., Gregorio-Hetem J., Casanova S., Spectroscopic classification of X-ray selected stars in the rho Ophiuchi star-forming region and vicinity, 1998, MNRAS, 300, 733

Massey P., 1998, in ASP Conf. Ser. 142: The Stellar Initial Mass Function (38th Herstmonceux Conference), p. 17

Mathieu R. D., Myers P. C., Schild R. E., Benson P. J., Fuller G. A., L43 - an example of interaction between molecular outflows and dense cores, 1988, ApJ, 330, 385

Mathis J. S., Rumpl W., Nordsieck K. H., The size distribution of interstellar grains, 1977, ApJ, 217, 425

Matthews B. C., Wilson C. D., Fiege J. D., Magnetic Fields in Star-forming Molecular Clouds. II. The Depolarization Effect in the OMC-3 Filament of Orion A, 2001, ApJ, 562, 400

Matthews H., 2003, The James Clerk Maxwell Telescope: User Guide, http://www.jach.hawaii.edu/JACpublic/JCMT/User_documentation/Users_guide/guide/guide.html

Mattila K., Optical extinction and surface brightness observations of the dark nebulae LYNDS 134 and LYNDS 1778/1780, 1979, A&A, 78, 253

McGlynn T., 2003, Skyview, http://skyview.gsfc.nasa.gov/

Mestel L., Spitzer L., Star formation in magnetic dust clouds, 1956, MNRAS, 116, 503

Motte F., André P., The circumstellar environment of low-mass protostars: A millimeter continuum mapping survey, 2001, A&A, 365, 440

Motte F., André P., Neri R., The initial conditions of star formation in the rho Ophiuchi main cloud: wide-field millimeter continuum mapping, 1998, A&A, 336, 150

Motte F., André P., Ward-Thompson D., Bontemps S., A SCUBA survey of the NGC 2068/2071 protoclusters, 2001, A&A, 372, L41

Mouschovias T. C., Nonhomologous contraction and equilibria of self-gravitating, magnetic interstellar clouds embedded in an intercloud medium: Star formation. I Formulation of the problem and method of solution, 1976a, ApJ, 206, 753

Mouschovias T. C., Nonhomologous contraction and equilibria of self-gravitating, magnetic interstellar clouds embedded in an intercloud medium: Star formation. II - Results, 1976b, ApJ, 207, 141

Mouschovias T. C., Ambipolar diffusion in interstellar clouds - A new solution, 1979, ApJ, 228, 475

Mouschovias T. C., Ciolek G. E., 1999, in NATO ASIC Proc. 540: The Origin of Stars and Planetary Systems, p. 305

Mouschovias T. C., Spitzer L., Note on the collapse of magnetic interstellar clouds, 1976, ApJ, 210, 326

Mundy L. G., Wootten A., Wilking B. A., Blake G. A., Sargent A. I., IRAS 16293 - 2422 - A very young binary system?, 1992, ApJ, 385, 306

Myers P. C., Dense cores in dark clouds. III - Subsonic turbulence, 1983, ApJ, 270, 105

Myers P. C., Benson P. J., Dense cores in dark clouds. II - NH3 observations and star formation, 1983, ApJ, 266, 309

Myers P. C., Goodman A. A., Evidence for magnetic and virial equilibrium in molecular clouds, 1988, ApJ, 326, L27

Myers P. C., Goodman A. A., On the dispersion in direction of interstellar polarization, 1991, ApJ, 373, 509

Myers P. C., Linke R. A., Benson P. J., Dense cores in dark clouds. I - CO observations and column densities of high-extinction regions, 1983, ApJ, 264, 517

Najita J. R., Tiede G. P., Carr J. S., From Stars to Superplanets: The Low-Mass Initial Mass Function in the Young Cluster IC 348, 2000, ApJ, 541, 977

Nakajima Y., Tachihara K., Hanawa T., Nakano M., Clustering of Pre-Main-Sequence Stars in the Orion, Ophiuchus, Chamaeleon, Vela, and Lupus Star-forming Regions, 1998, ApJ, 497, 721

Nakano T., Nakamura T., Gravitational Instability of Magnetized Gaseous Disks 6, 1978, PASJ, 30, 671

Norman C. A., Ferrara A., The Turbulent Interstellar Medium: Generalizing to a Scale-dependent Phase Continuum, 1996, ApJ, 467, 280

Ossenkopf V., Henning T., Dust opacities for protostellar cores, 1994, A&A, 291, 943

Ostriker E. C., Gammie C. F., Stone J. M., Kinetic and Structural Evolution of Self-gravitating, Magnetized Clouds: 2.5-dimensional Simulations of Decaying Turbulence, 1999, ApJ, 513, 259

Ostriker E. C., Stone J. M., Gammie C. F., Density, Velocity, and Magnetic Field Structure in Turbulent Molecular Cloud Models, 2001, ApJ, 546, 980

Pagani L., Lagache G., Bacmann A., Motte F., Cambrésy L., Fich M., Teyssier D., Miville-Deschênes M.-A., Pardo J.-R., Apponi A. J., Stepnik B., L183 (L134N) Revisited. I. The very cold core and the ridge, 2003, A&A, 406, L59

Papoular R., The processing of infrared sky noise by chopping, nodding and filtering, 1983, A&A, 117, 46

Peebles P., 1980, The Large Scale Structure of the Universe. Princeton University Press

Pelletier G., Pudritz R. E., Hydromagnetic disk winds in young stellar objects and active galactic nuclei, 1992, ApJ, 394, 117

Penston M. V., Dynamics of self-gravitating gaseous spheres-III. Analytical results in the free-fall of isothermal cases, 1969, MNRAS, 144, 425

Phillips R., 2002, The James Clerk Maxwell Telescope (JCMT): A brief overview, http://www.jach.hawaii.edu/JACpublic/JCMT/About_JCMT/about_jcmt.html

Pierce-Price D. P., 2001, Ph.D. Thesis

Prato L., Simon M., Are Both Stars in a Classic T Tauri Binary Classic T Tauri Stars?, 1997, ApJ, 474, 455

Purcell E. M., Suprathermal rotation of interstellar grains, 1979, ApJ, 231, 404

Rao R., Crutcher R. M., Plambeck R. L., Wright M. C. H., High-Resolution Millimeter-Wave Mapping of Linearly Polarized Dust Emission: Magnetic Field Structure in Orion, 1998, ApJ, 502, L75

Redman M. P., Rawlings J. M. C., Nutter D. J., Ward-Thompson D., Williams D. A., Molecular gas freeze-out in the pre-stellar core L1689B, 2002, MNRAS, 337, L17

Reipurth B., Chini R., Krugel E., Kreysa E., Sievers A., Cold Dust around Herbig-Haro Energy Sources - a 1300-MICRON Survey, 1993, A&A, 273, 221

Ruiz A., Rodriguez L. F., Canto J., Mirabel I. F., High-velocity OH in absorption - A new tracer of shocked gas in outflows?, 1992, ApJ, 398, 139

Salpeter E. E., The Luminosity Function and Stellar Evolution., 1955, ApJ, 121, 161

Sandell G., Secondary calibrators at submillimeter wavelengths., 1994, MNRAS, 271, 75

Sandell G., 2002, Brightnesses of Secondary Calibrators for SCUBA, http://www.jach.hawaii.edu/JACpublic/JCMT/Continuum_observing/SCUBA/astronomy/calibration/calibrators_2.html

Sandell G., Jessop N., Jenness T., 2001, The SCUBA map reduction cookbook

Sault R. J., Killeen N. E. B., Zmuidzinas J., Loushin R., Analysis of Zeeman effect data in radio astronomy, 1990, ApJS, 74, 437

Schleuning D. A., Far-Infrared and Submillimeter Polarization of OMC-1: Evidence for Magnetically Regulated Star Formation, 1998, ApJ, 493, 811

Serkowski K., 1974, Methods of Experimental Physics, Vol. 12A. New York Academic Press

Shu F., Najita J., Ostriker E., Wilkin F., Ruden S., Lizano S., Magnetocentrifugally driven flows from young stars and disks. 1: A generalized model, 1994, ApJ, 429, 781

Shu F. H., Self-similar collapse of isothermal spheres and star formation, 1977, ApJ, 214, 488

Shu F. H., Adams F. C., Lizano S., Star formation in molecular clouds - Observation and theory, 1987, ARA&A, 25, 23

Simon M., 1992, in ASP Conf. Ser. 32: IAU Colloq. 135: Complementary Approaches to Double and Multiple Star Research, p. 41

Simon M., Clustering of Young Stars in Taurus, Ophiuchus, and the Orion Trapezium, 1997, ApJ, 482, L81

Snell R. L., Loren R. B., Plambeck R. L., Observations of CO in L1551 - Evidence for stellar wind driven shocks, 1980, ApJ, 239, L17

Snell R. L., Scoville N. Z., Sanders D. B., Erickson N. R., High-velocity molecular jets, 1984, ApJ, 284, 176

Sparks W. B., Axon D. J., Panoramic Polarimetry Data Analysis, 1999, PASP, 111, 1298

Stahler S. W., Shu F. H., Taam R. E., The evolution of protostars. I - Global formulation and results, 1980, ApJ, 241, 637

Stone J. M., Ostriker E. C., Gammie C. F., Dissipation in Compressible Magnetohydrodynamic Turbulence, 1998, ApJ, 508, L99

Strom K. M., Strom S. E., Grasdalen G. L., An infrared source associated with a Herbig-Haro object., 1974, ApJ, 187, 83

Strom K. M., Strom S. E., Vrba F. J., Infrared surveys of dark-cloud complexes. I. The LYNDS 1630 dark cloud., 1976, AJ, 81, 308

Strom K. M., Strom S. E., Wolff S. C., Morgan J., Wenz M., Optical manifestations of mass outflows from young stars - At atlas of CCD images of Herbig-Haro objects, 1986, ApJS, 62, 39

Strom S. E., Grasdalen G. L., Strom K. M., Infrared and optical observations of Herbig-Haro objects. ., 1974, ApJ, 191, 111

Suters M., Stewart R. T., Brown A., Zealey W., Variable Radio Sources in the Corona Australis Cloud, 1996, AJ, 111, 320

Tafalla M., Mardones D., Myers P. C., Caselli P., Bachiller R., Benson P. J., L1544: A Starless Dense Core with Extended Inward Motions, 1998, ApJ, 504, 900

Taylor K. N. R., Storey J. W. V., The Coronet, an obscured cluster adjacent to R Corona Austrina, 1984, MNRAS, 209, 5P

Velusamy T., Langer W. D., Outflow-infall interactions as a mechanism for terminating accretion in protostars., 1998, Nature, 392, 685

Verschuur G. L., Measurements of Magnetic Fields in Interstellar Clouds of Neutral Hydrogen, 1969, ApJ, 156, 861

Vrba F. J., Strom S. E., Strom K. M., Infrared surveys of dark- cloud complexes. III. The R CrA dark cloud., 1976a, AJ, 81, 317

Vrba F. J., Strom S. E., Strom K. M., Magnetic field structure in the vicinity of five dark cloud complexes, 1976b, AJ, 81, 958

Wakelam V., Castets A., Ceccarelli C., Lefloch B., Caux E., Pagani L., Sulphur-bearing species in the star forming region L1689N, 2004, A&A, 413, 609

Walker C. K., Carlstrom J. E., Bieging J. H., The IRAS 16293-2422 cloud core - A study of a young binary system, 1993, ApJ, 402, 655

Walker C. K., Lada C. J., Young E. T., Maloney P. R., Wilking B. A., Spectroscopic evidence for infall around an extraordinary IRAS source in Ophiuchus, 1986, ApJ, 309, L47

Walker R. J., Ward-Thompson D., Evans R., Leeks S. J., Ade P. A. R., Griffin M. J., Gear W. K., Kiernan B., Gannaway F. C., Rinehart S. A., Araujo H., 2003, in Millimeter and Submillimeter Detectors for Astronomy. Edited by Phillips, Thomas G.; Zmuidzinas, Jonas. Proceedings of the SPIE, Volume 4855, pp. 563-573 (2003)., p. 563

Walther D. M., Robson E. I., Aspin C., Dent W. R. F., JHKL Imaging and K Polarimetry of the Bipolar Outflow NGC 2071, 1993, ApJ, 418, 310

Ward-Thompson D., André P., Kirk J. M., The initial conditions of isolated star formation - V. ISOPHOT imaging and the temperature and energy balance of pre-stellar cores, 2002, MNRAS, 329, 257

Ward-Thompson D., Buckley H. D., Greaves J. S., Holland W. S., André P., Evidence for protostellar infall in NGC 1333-IRAS2., 1996, MNRAS, 281, L53

Ward-Thompson D., Chini R., Krugel E., André P., Bontemps S., A submillimetre study of the Class 0 protostar HH24MMS, 1995, MNRAS, 274, 1219

Ward-Thompson D., Kirk J. M., Crutcher R. M., Greaves J. S., Holland W. S., André P., First Observations of the Magnetic Field Geometry in Prestellar Cores, 2000, ApJ, 537, L135

Ward-Thompson D., Motte F., André P., The initial conditions of isolated star formation - III. Millimetre continuum mapping of pre-stellar cores, 1999, MNRAS, 305, 143

Ward-Thompson D., Scott P. F., Hills R. E., André P., A Submillimetre Continuum Survey of Pre Protostellar Cores, 1994, MNRAS, 268, 276

Ward-Thompson D. W., 1987, Ph.D. Thesis

Wardle J. F. C., Kronberg P. P., The linear polarization of quasi-stellar radio sources at 3.71 and 11.1 centimeters, 1974, ApJ, 194, 249

Webb T. M., Eales S. A., Lilly S. J., Clements D. L., Dunne L., Gear W. K., Ivison R. J., Flores H., Yun M., The Canada-UK Deep Submillimeter Survey. VI. The 3 Hour Field, 2003, ApJ, 587, 41

Weintraub D. A., Goodman A. A., Akeson R. L., Polarized Light from Star-Forming Regions, 2000, Protostars and Planets IV, 247

Whitcomb S. E., Gatley I., Hildebrand R. H., Keene J., Sellgren K., Werner M. W., Far-infrared properties of dust in the reflection nebula NGC 7023, 1981, ApJ, 246, 416

Whitworth A., Summers D., Self-similar condensation of spherically symmetric self-gravitating isothermal gas clouds, 1985, MNRAS, 214, 1

Whitworth A. P., Bhattal A. S., Francis N., Watkins S. J., Star formation and the singular isothermal sphere, 1996, MNRAS, 283, 1061

Whitworth A. P., Ward-Thompson D., An Empirical Model for Protostellar Collapse, 2001, ApJ, 547, 317

Wilking B. A., Greene T. P., Lada C. J., Meyer M. R., Young E. T., IRAS observations of young stellar objects in the Corona Australis dark cloud, 1992, ApJ, 397, 520

Wilking B. A., Lada C. J., The discovery of new embedded sources in the centrally condensed core of the Rho Ophiuchi dark cloud - The formation of a bound cluster, 1983, ApJ, 274, 698

Wilking B. A., Lada C. J., Young E. T., IRAS observations of the Rho Ophiuchi infrared cluster - Spectral energy distributions and luminosity function, 1989, ApJ, 340, 823

Wilking B. A., Lebofsky M. J., Kemp J. C., Rieke G. H., Infrared polarimetry in the Rho Ophiuchus dark cloud, 1979, AJ, 84, 199

Wilking B. A., McCaughrean M. J., Burton M. G., Giblin T., Rayner J. T., Zinnecker H., Deep Infrared Imaging of the R Coronae Australis Cloud Core, 1997, AJ, 114, 2029

Williams J. P., Blitz L., McKee C. F., The Structure and Evolution of Molecular Clouds: from Clumps to Cores to the IMF, 2000, Protostars and Planets IV, 97

Williams J. P., Myers P. C., Wilner D. J., di Francesco J., A High-Resolution Study of the Slowly Contracting, Starless Core L1544, 1999, ApJ, 513, L61

Wright E. L., Hinshaw G., Bennett C. L., Producing Megapixel Cosmic Microwave Background from Differential Radiometer Data, 1996, ApJ, 458, L53

Zhou S., In search of evidence for protostellar collapse - A systematic study of line formation in low-mass dense cores, 1992, ApJ, 394, 204

Zhou S., Evans N. J., Koempe C., Walmsley C. M., Evidence for protostellar collapse in B335, 1993, ApJ, 404, 232

Zuckerman B., Palmer P., Radio radiation from interstellar molecules, 1974, ARA&A, 12, 279